Multi-Scale Mathematical Models of Airway Epithelium to Facilitate Cystic Fibrosis Treatment

by

Florencio Serrano Castillo

B.S. Chemical Engineering, University of Arkansas at Fayetteville, 2014

Submitted to the Graduate Faculty of
the Swanson School of Engineering in partial fulfillment
of the requirements for the degree of

Doctor of Philosophy

University of Pittsburgh

2019

UNIVERSITY OF PITTSBURGH

SWANSON SCHOOL OF ENGINEERING

This dissertation was presented

by

Florencio Serrano Castillo

It was defended on

July 9th 2019

and approved by

Robert S. Parker, Ph.D., Professor, Department of Chemical and Petroleum Engineering

Timothy E. Corcoran, Ph.D., Associate Professor, Department of Medicine, Division of Pulmonary, Allergy, and Critical Care Medicine

Carol A. Bertrand, Ph.D., Research Assistant Professor, Department of Pediatrics

Michael M. Myerburg, M.D., Associate Professor, Department of Medicine, Division of Pulmonary, Allergy, and Critical Care Medicine

Ipsita Banerjee, Ph.D., Associate Professor, Department of Chemical and Petroleum Engineering

Dissertation Advisors: Robert S. Parker, Ph.D., Professor, Department of Chemical and Petroleum Engineering,

Timothy E. Corcoran, Ph.D., Associate Professor, Department of Medicine,Division of Pulmonary, Allergy, and Critical Care Medicine

Multi-Scale Mathematical Models of Airway Epithelium to Facilitate Cystic Fibrosis Treatment

Florencio Serrano Castillo, PhD

University of Pittsburgh, 2019

Cystic Fibrosis is a life-shortening, autosomal recessive disease caused by mutations in the Cystic Fibrosis Transmembrane Conductance Regulator (CFTR) gene. Cystic Fibrosis is the most common lethal genetic disorder among Caucasians, and occurs at a rate of 1 in every 3,400 births in the United States. The CFTR gene codes an anion channel expressed on the mucosal side of the epithelia of multiple organ systems, including the digestive tract, reproductive organs, pancreas, and airways. Loss of CFTR expression or function results in an osmotic imbalance due to defective ion and water transport. In the respiratory tract, this leads to airway surface liquid hyperabsorption and mucus dehydration causing decreased mucociliary clearance rates. Failure to clear mucus and other inhaled debris favors the development of mucus plugs and the prolonged colonization of harmful pathogens. These conditions lead to a sustained, unregulated inflammatory response that results in severe tissue damage and, ultimately, respiratory failure, the leading cause of Cystic Fibrosis mortality.

Cystic Fibrosis therapeutic development is largely dependent on the availability of model systems that can be used to test and optimize therapies ahead of clinical use. These systems include networks of interactive elements that can be overly complex to exhaustively explore experimentally. The work described here, focuses on the development of cell-scale, mechanistic, and biologically relevant mathematical models that provide information about the contribution of individual mechanisms to experimental outcomes.

The models were trained and validated with data obtained from human bronchial and nasal epithelial cell cultures from donors with Cystic Fibrosis, non-Cystic Fibrosis controls, and carriers of a single disease-causing allele. Within this context, we have use these models as tools to explore the underlying mechanisms behind Cystic Fibrosis pathophysiology not easily accessible experimentally. These predictions were further enhanced through the inclusion of similar estimates generated from separately developed models of *in vivo* lung-scale

function, as well as standard clinical measurements of airway function. Model predictions provide us with unique and novel parametric descriptions of mechanistic and physiological differences between the three populations and across multiple spatiotemporal scales. We envision using these models as means to facilitate the deployment of personalized treatment protocols, where cells sampled and cultured from individuals could be use to generate patient-specific *in silico* predictors of lung-scale disease state and therapeutic response.

Table of Contents

List of Tables

List of Figures

Preface

No debes permitirte estar encadenado al destino, ni ser un esclavo de tus genes. Los seres humanos pueden escoger que tipo de vida quieren vivir. Lo que es crucial es que escojas vivir... y que vivas. -Naomi Hunter, Metal Gear Solid

Esta disertación no es solo el resultado de mi ezfuerzo, sino mas bien es una reflección del apoyo de un vasto grupo de personas que decidieron creer en mí.

Esto incluye, por supuesto, a mis consejeros y mentores que me proveyeron con el patrocinio y la guianza necesaria para que pudiera alcanzar mis metas. Incluso en aquellos momentos cuando fuí mas terco y argumentativo de lo necesario.

Igulamente, incluye a todos mis amigos y compañeros que atraves de sus ocurrencias, consejos y alegrías hicieron de Pittsburgh mi hogar. No importa si fue mientras nos tomabamos un trago, bailabamos, conversabamos hacerca de algo banal, ó cuando me escuchaban quejarme de alguna tonteria; su apoyo siempre sera increiblemente agradecido. Los últimos cinco años hubieran sido miserables sin ustedes.

Y mas que nadie más, le dedico este trabajo a mis padres. Quienes nunca dudaron, nunca dieron excusas ni quejas, y nunca se rindieron. Ustedes han sido mis primeros y mis mejores porristas. Todo lo que he logrado y todo lo que lograré simpre se los deberé a ustedes.

You mustn't allow yourself to be chained to fate, to be ruled by your genes. Human beings can choose the kind of life that they want to live. What's important is that you choose life... and then live. -Naomi Hunter, Metal Gear Solid

This dissertation is not just the results of my work, but rather it is a reflection of the support of a vast group of people that decided to believe in me.

This group includes my mentors and advisors. You provided me the support and guidance I needed in order to reach my goals. Specially, in those moments when my stubbornness got the better of me.

It also includes my friends and classmates. Who through their advise, companionship and cheerfulness helped turn Pittsburgh into home. Regardless of if it was while we shared a drink, danced, talked about something silly, or while you listened to my complains, your support is truly appreciated. The last five years would have sucked without you all.

Most importantly, I dedicate my work to my parents. You never doubted, never complained or made excuses, and never gave up. You are my first and best cheerleaders. Everything I have accomplished, and anything else I may achieve will always be because of you.

1.0 Introduction

1.1 Airway Epithelial Structure and Function

Epithelia are inherently interfacial tissues. They exist ubiquitously across the entire body, and serve a myriad of different specialized functions depending on their location. The skin, for example, primarily serves as the outermost protective layer of the body. Stomach epithelia regulate pH and facilitates digestion; intestinal epithelia facilitate water and nutrient absorption; proximal tubules facilitate the secretion of excess solutes and fluids; while lung epithelia hydrate the airway and facilitate gas exchange during breathing.

Regardless of their various functions, all epithelial tissues share a general structural formula: a group of cells joined laterally through a junctional space that facilitates intercellular communications and establishes a tight, mesh-like layer. This conformation creates two distinct interfacial membranes: the apical (or mucosal) membrane that interacts with the lumen, and the basolateral (or serosal) membrane where the epithelium attaches to other tissue in the body. Figure 1.1 depicts the general structure of all epithelial tissues.

Transport in epithelial tissue can occur through transcellular pathways, or across the the paracellular pathway along the junctional space in between the cells. The paracellular pathway is delimited by tight junctions that connect the individual cells in the apical side and act as a physical boundary that regulates the permeability of the epithelial tissue. More permeant tight junctions lead to "leakier" tissue (*e.g.* airway, intestine), while the reverse (*e.g.* kidney, stomach) leads to significantly reduced paracellular liquid and solute transport. Changes in "leakiness" can therefore cause drastic differences in the hydraulic permeability, electrical resistance and conductivity of an epithelial tissue.

The characterization of epithelial transport has been historically complex [106]. Transcellular ionic permeability is traditionally assessed through electrophysiological measurements of channel and cellular conductivity. However, the membrane structure of the epithelia results in a more physiologically complex system than dispersed cells, and thus requires more technical nuance and careful examination.

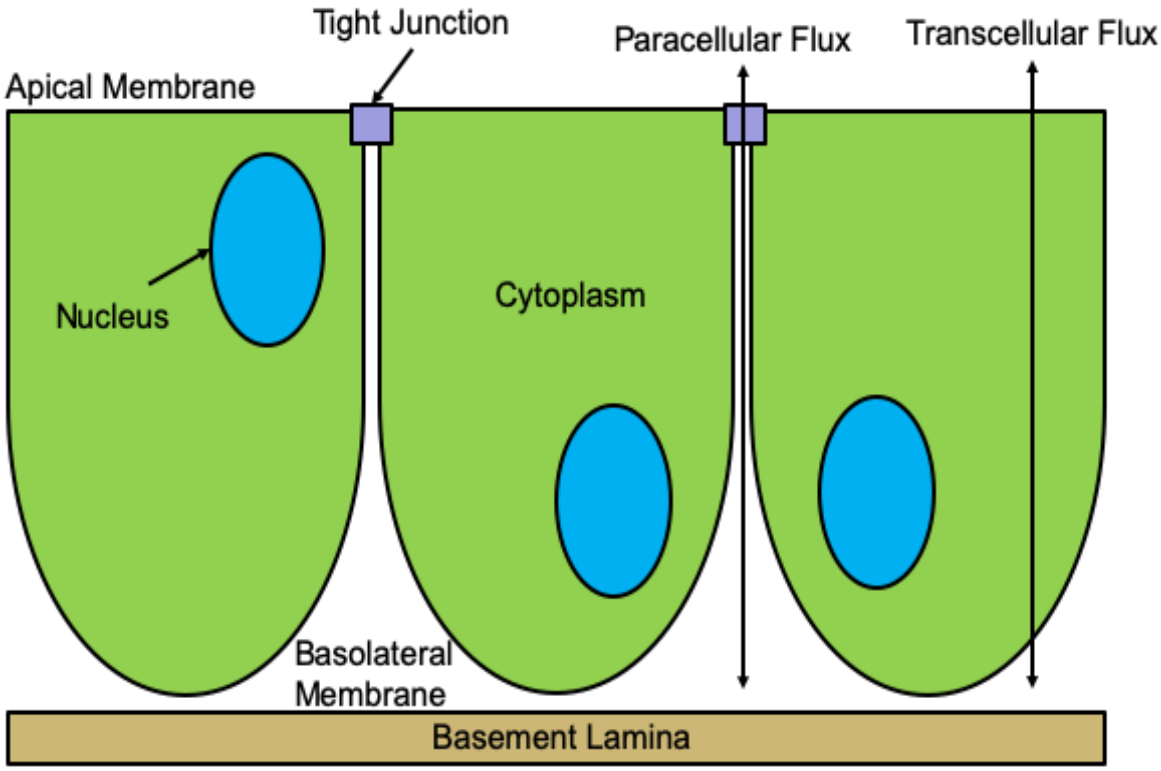

Figure 1.1: Diagram of the general structure of epithelial membranes. Epithelial cells adhere to a basement membrane of connective tissue. Transcellular transport occurs in all epithelia via channels and pumps in the apical and basolateral membranes. Paracellular transport occurs through the tight junctions.

1.2 Fundamentals of Human Airway Electrophysiology

When considering the transport of ions across a cellular membrane, the electrochemical potential ($\hat{\mu}$) represents the main driving force behind ionic transport. The total change in potential energy behind this transport ($\Delta\hat{\mu}$) is the resulting driving force after the inclusion of both the membrane potentials across the membrane (E_m) and the chemical potentials (μ). E_m is affected by the changes in the distribution of electrical charges across the membrane regardless of the chemical species, and is typically described through the Nernst equation. In contrast, μ is dependent on the concentrations ($[X_i]$) and activity coefficients (y_i) of each

species i in each compartment. If we considered a single-ion system, equation 1.1 defines $\Delta\hat{\mu}$, such that R is the gas constant, T is the temperature of the system, z is the valence of ion i, and F is the Faraday constant.

$$\Delta\hat{\mu} = \Delta\mu + zFE_m = RT\ln\left(\frac{[X_i]_{in}}{[X_i]_{out}}\right) + \frac{RT}{zF}\ln\left(\frac{[X_i]_{in}}{[X_i]_{out}}\right) \tag{1.1}$$

However, most biological systems of relevance are not single-ion systems. Therefore, depending on the molar and charge distribution and the permeability of the membrane to each individual ion, it is possible for the conditions that lead to electrical equilibrium ($V_m = 0$) to not also lead to chemical equilibrium ($\Delta\mu = 0$), and vice versa. For example, imagine a two reservoir system divided by a semipermeable membrane, where each compartment contains two ionic species (i and j) of the same valence. Each compartment has equimolar concentrations of each ion, but one compartment has a lower overall molarity. At time zero this system is in neither chemical nor electrical equilibrium. If we define the membrane to be permeable to both ions, then the system will reach equilibrium when the net change of ion transport is zero (*i.e.* both species become equimolar across the two compartments). However, if the membrane is only permeable to one species (i), electrochemical equilibrium is reached when the net transport of species i is zero. In other words, when the chemical gradient is offset by the charge distributions, without the need for species i to reach equimolar conditions across the two compartments.

This example highlights the need to account for the electrostatic contributions to ionic transport when dealing with polyionic solutions. In the case of airway epithelial electrophysiology, the electrolytes considered in the system are Na^+, Cl^-, and K^+. This redefines E_m through the Goldman-Hodgkins-Katz equation to account for the three different ionic species (equation 1.2), where P_i is the permeability of ion i, and V_m replaces the E_m in equation 1.1.

$$V_m = \frac{RT}{F}\ln\left(\frac{P_{Na}[Na^+_{out}] + P_K[K^+_{out}] + P_{Cl}[Cl^-_{in}]}{P_{Na}[Na^+_{in}] + P_K[K^+_{in}] + P_{Cl}[Cl^-_{out}]}\right) \tag{1.2}$$

In equation 1.1, the two terms on the right hand side can be described as the diffusive and electrical driving forces, respectively. From these expressions, Goldman derived the single-ion flux relationship across a cellular membrane, assuming a negligible membrane thickness and constant electromagnetic field [66], as shown in equation1.3. Here, Γ^+ and Γ^- are the upper and lower bounds on the feasible flux conductivities, respectively. It is clear from equation 1.3 that ionic transport is inherently nonlinear in biological systems. This also implies that common linear transport relationships such as Fick's law (chemical diffusion) or Ohm's law (electrical conductivity) cannot single-handedly described this type of transport, at least not under non-asymptotic behavior.

$$J_i = \frac{zF^2V_m}{RT}\left(\frac{\Gamma^+ - \Gamma^- \exp^{\frac{RTV_m}{F}}}{1 - \exp^{\frac{RTV_m}{F}}}\right) \tag{1.3}$$

Having defined a physically relevant way to described ionic transport across biological membranes, it is possible to extrapolate these flux equations to explain ionic transport dynamics in biological systems in a compartmental fashion. If, for example, we define our system to be a single cell, the intracellular molar dynamics for a solute i (N_i) can be described through an ordinary differential equation by considering the different influx and efflux pathways relevant to that cell, as seen in equation 1.4. There, A_C is the surface area of the cell membrane, and K is the vector of all distinct pathways that conduct solute i across the cell membrane. This general structure can be use to defined systems of transepithelial ion transport for multiple species across multiple pathways, expressed in distinct membranes.

$$\frac{dN_i}{dt} = A_c \sum_{\mathbf{K}} J_{i,k} \tag{1.4}$$

The Ussing Chamber can be applied to study individual membrane potentials. Figure 1.2 shows the simplest equivalent circuit diagram of the epithelial ion transport system. From this representation it is easily observed that the three general transport pathways (apical and basolateral membranes and the paracellular junction) are individual resistors that provide a measurable electrical effect and can be studied individually.

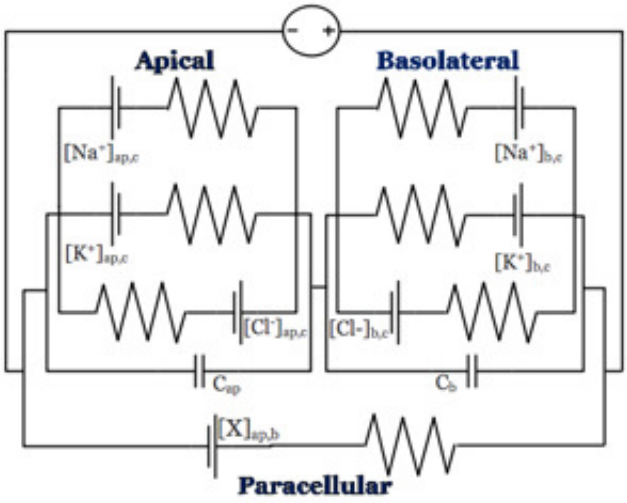

Figure 1.2: Diagram of the circuit abstraction of a epithelial monolayer. Ion channels and transporters are considered resistors that regulate ion displacement. The plasma membranes are taken to be slow-charging capacitors that inhibit flux of ions through non-physiological pathways, and the electrochemical potential for each ionic species is considered as a potential drop.

From this structure, we can derive an expression to assess the total epithelial resistance (R_T), as seen in equation 1.5. Here R_P and R_C represents the paracellular and cellular resistances, respectively. R_P is due to the occluding effect of junction proteins like actin, claudins, and connexins [36, 84].

$$\begin{aligned} R_T &= \left[\frac{1}{R_P} + \frac{1}{R_C}\right]^{-1} \\ &= \left[\frac{1}{R_P} + \frac{1}{R_{Ap} + R_{Bl}}\right]^{-1} \end{aligned} \tag{1.5}$$

The density and structure of these proteins is what largely determines the leakiness of an epithelial tissue type, where tighter epithelia have increased electrical resistance. The apical (R_{Ap}) and basolateral (R_{Bl}) resistances are related to the density of channels and

transporters in the apical and basolateral membranes, respectively. Higher densities and transport rates correlate with lower resistances. If we assumed a relatively even channel expression per surface area, the relatively smaller interfacial area of the lumen means the apical membrane acts as the transport limiting step. [84].

1.3 Cystic Fibrosis: A Multi-Scale Disease

Cystic Fibrosis (CF) is an autosomal recessive disease that arises from a defect in the Cystic Fibrosis Transmembrane Conductance Regulator (CFTR) gene [112]. It is the most common lethal recessive autosomal disease among populations of Caucasian descent, affecting around 70,000 patients worldwide, and with roughly 1,000 new cases diagnosed every year [58, 143]. CF is a systemic disease, affecting multiple organs, with the most deleterious effects taking place in the airways [141].

The CFTR gene codes for an anion channel expressed primarily on the apical membrane of epithelial cells [151]. The absence or dysfunction of this channel and the associated loss of Cl^- and HCO_3^- transport result in an electroosmotic imbalance of the epithelial membrane. These disruptions can have broad consequences in the homeostatic function of multiple tissues. For example, liquid hyperabsorption in the proximal ducts of the pancreas leads to a drastic increase in the viscosity of exocrine secretions, decreasing the flow of multiple digestive enzymes [101]. This build up induces a chronic inflammatory response, pancreatitis, which leads to pancreatic insufficiency ($\sim$ 90% of the CF population) [61]. In more severe cases, this also causes the destruction of islet cells, triggering the development of CF-related diabetes mellitus [61]. Similarly, liquid hyperabsorption in the intestines tends to manifest as Meconium ileus, a blockage of the small intestine during the infancy of CF patients [112]. Meconium ileus in patients with Cystic Fibrosis is widely accepted as the leading cause of bowel obstruction among newborns [185]. Similarly, congenital bilateral absence of the vas deferens is responsible for approximately 2% of cases of male infertility [107], see Figure 1.3.

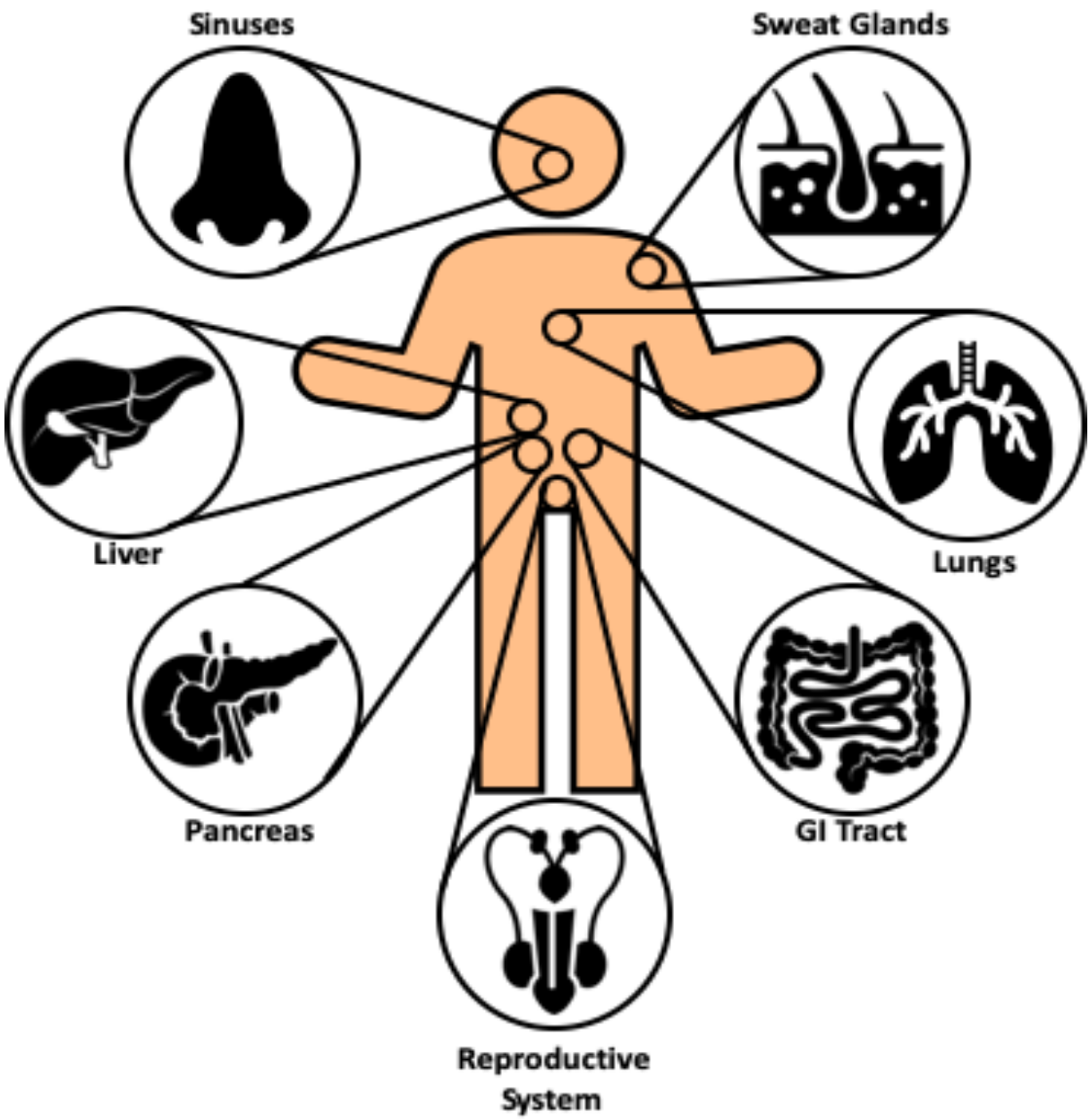

Figure 1.3: Description of primary organs affected by Cystic Fibrosis. The ubiquitous expression of CFTR across multiple epithelia leads to disruption in multiple organ systems.

However, the pathogenesis and the subsequent progression of CF airway disease, the primary cause of morbidity for patients with CF [179], is not entirely understood. General consensus suggests that lung disease starts to develop within the first few months of life for

human infants with Cystic Fibrosis. Much of this knowledge has been derived from physiological studies of neonatal CF animal models. These studies have highlighted the presence of multiple physiological hallmarks of CF airway disease, including airway malformation, dysfunctional MCC, increased airway surface liquid (ASL) acidity, dehydration of the periciliary liquid (PCL), and reduced pathogenic killing potential [23, 81, 88, 89, 148]. Furthermore, *in silico* predictions of lung-level mucocilliary clearance (MCC) and absorption (ABS) dynamics informed with radiological studies in pediatric patients with CF suggest a possible absorptive defect prior to adulthood [120].

1.3.1 Cystic Fibrosis Airway Disease

CF lung pathophysiology is characterized by liquid hyperabsorption, ASL depletion, and mucus accumulation. This, in turn, creates the perfect environment for opportunistic pathogens to thrive in, further compromising the integrity of the membrane and, possibly, reducing the MCC rate [111]. The inability to clear pathogens will then lead to a vicious cycle of chronic infection and further airway damage that eventually leads to premature respiratory failure (see Figure 1.4). These elements of CF progression have been identified and characterized through a multitude of methods, including *in vivo* functional lung imaging studies [15, 30], *in vitro* characterization of fully differentiated primary airway cell lines [32], and the development of multiple CF animal models, including ferret, mouse, pig, and rat [93, 188, 194]. These combined approaches have provided a wealth of knowledge regarding CF disease; they have also led to the development of multiple therapeutics that aim to both ameliorate symptoms and correct the underlying anion channel defect, nearly quadrupling of the average life expectancy of a person with CF over the last fifty years [114].

Most commonly, the progression of CF airway disease is tracked through longitudinal spirometric measurements. Forced expiratory volume in 1 second (FEV1) and the rate of pulmonary exacerbations (rate at which the patient requires hospitalization or treatment with IV antibiotics) are some of the primary outcomes in clinical trials of pulmonary therapies for CF [1, 53]. A decrease in FEV1 is indicative of a loss of lung function and the possible worsening of bronchial obstruction [157, 162]. However, the rate of progression of

CF airway disease can vary significantly. For instance, one study of 4,923 CF patients aged 6 to 17 in the US and Canada from 1994 to 2005 tried to estimate mean rates of change of %FEV1. The study found several factors predictive of increased decline in FEV1 across age-stratified groups, including age, gender (female), presence of crackles, FEV1 baseline, as well as *pseudomonas aeruginosa* colonization, amount of sputum production, and use of antibiotic to treat pulmonary exacerbation among all the groups [97].

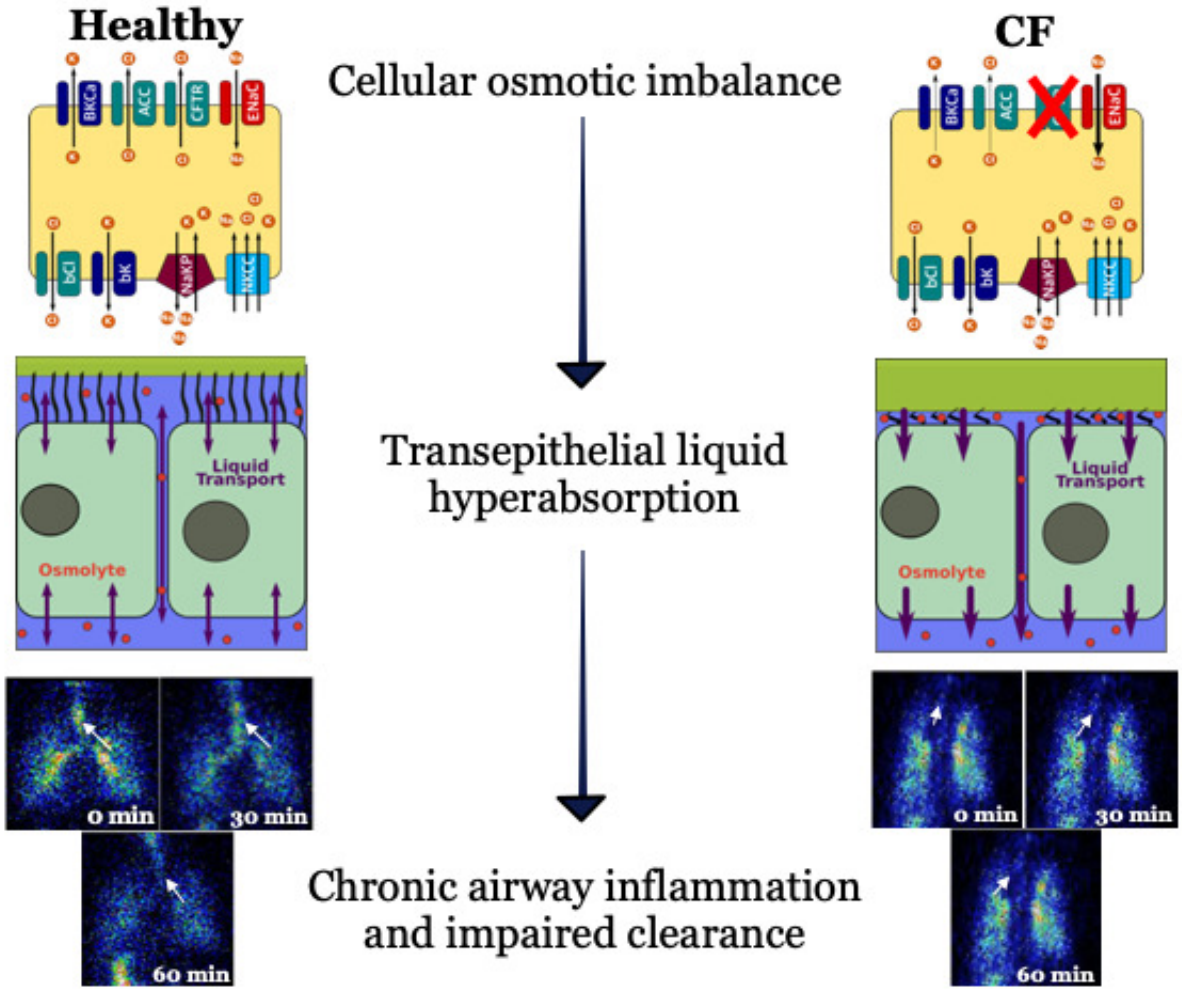

Figure 1.4: Flowchart depicting the multi-scale nature of disease progression in Cystic Fibrosis, starting from the underlying genetic mutation and leading to osmotic imbalances, airway obstruction, chronic inflammation, and eventual respiratory failure.

However, the multi-scale, complex, and highly heterogeneous nature of the disease makes it particularly difficult to study. As a genetic disease, CF disease phenotype is obviously related to the genotype of patients, but the relationship between a patient's CFTR genotype and their phenotype is not clear. In fact, recent studies have shown that CF disease phenotype is related to more than just CFTR genotype. Genome-wide association studies have linked five non-CFTR gene loci that display significant correlation with variations in CF airway disease severity [5, 35], response to CFTR-targeted therapeutics [34, 182], and the incidence rates of other CF comorbidities [67]. Furthermore, these studies have helped identify meaningful variations of DNA methylation patterns present within previously identified modifier genes of CF lung disease severity [115]. There is significant work left to do in order to understand the full scope of CF airway disease pathophysiology across the different physiological scales.

1.3.2 Cell Level Pathophysiology

At its most basic level, Cystic Fibrosis is a disease that disrupts the normal ion transport functions of the cell. In healthy tissue, water, ions, and other solutes are transported in and out of cells through a complex network of active and passive pathways, with the goal of regulating and controlling several aspects of intracellular and pericellular function [190]. In epithelial cells, this network is particularly complex due to the polarized conformation that these cells adopt. Epithelial cells differentiate as membranes made of adjacent cells that develop distinct potential differences across each end of the cellular compartment. The intracellular compartment acts as a central reservoir that interacts with both the basolateral (serosal) and apical (lumenal) compartments through the transport of ion, water, and other molecules across each respective membrane. Similarly, the apical and basolateral sides can also interact through the paracellular pathway. The highly dynamic nature of the airway, as well as the unique liquid/air interface at which these cells operate, makes them particularly difficult to characterize.

The cystic fibrosis transmembrane conductance regulator (CFTR) is a transmembrane anion channel that, under regular circumstances, is known to favor the secretion of Cl^-

and HCO_3^- ions. CFTR is also involved, either directly or indirectly, in the regulation of other ion channels and transporters, including the epithelial sodium channel (ENaC) [76], the solute carrier family 26 member 9 (SLC26A9) [8], and aquaporin 3 (AQP3) [90, 171]. In CF, CFTR is absent or dysfunctional. In the airway, this eliminates a key pathway for apical Cl^- secretion, and creates an electroosmotic imbalance that favors the hyperabsorption of water from the lumenal to the serosal compartment.

Airway epithelium includes apical chloride transport as facilitated by both CFTR and alternative channels, such as calcium-activated chloride channels (CaCCs) and SLC26A9 [8, 9, 84]. Apical Na^+ and K^+ transport occurs through ENaC and the large conductance Ca^{2+} activated K^+ (BKCa) channels, respectively [84]. Basolateral Na^+, Cl^-, and K^+ transport occurs primarily through mechanisms including the Sodium-Potassium-2-Chloride (NaKCC) co-transporter and Na^+-K^+-ATPase, as well as a series of basolateral Cl^- and K^+ channel and co-transporters [84]. Water transport will also occur through multiple aquaporin channels expressed at the apical, AQP5, and the basolateral, AQP4 and AQP3, membranes [200]. Paracellular transport of all major ionic and nonionic solutes is also relevant [32, 84, 211].

The reduction in Cl^- secretion and overactive Na^+ absorption generates osmotic conditions that cause dehydration of the ASL, including the periciliary liquid layer (PCL) and mucus layer [190]. The Cl^-, Na^+, and K^+ concentrations act as the primary regulators of lumenal composition and volume [190, 198]. Water transport is also affected in CF. Passive water and solute transport also occurs in the paracellular space and is regulated by osmolarity and tight junction integrity [56, 128]. *In vitro* studies have shown that tight junctions chronically exposed to cytokine profiles common to the CF airway exhibit profound changes to their ion and liquid permeability [36]. Similarly, apical mucus accumulation has been shown to affect transepithelial solute permeabilities [110]. A comparison of ASL conditions between healthy and CF airway epithelium is depicted in Figure 1.5.

The absence, or dysfunction, of CFTR at the apical membrane also affects several components of the upstream protein maturation cascade. For example, cells expressing ΔF508 CFTR, the most common CF-causing genetic mutation, can't produce fully maturated CFTR. The immature protein fails to clear one of several maturation checkpoints along this cascade and gets tagged for degradation. This accumulation of misfolded protein may

create a strain on the translational and protein maturation apparatus [156]. This strain can in turn affect the expression of other proteins. Studies have shown decreased levels of the soft palate, lung, and nasal epithelium clone 1 (SPLUNC1) in chronic CF disease [19, 71]. SPLUNC1 binds to ENaC, inhibiting its activation, thus, suggesting that the reduction of SPLUNC1 in chronic CF may contribute to the increased Na^+ flux typical of CF [184]. A similar mechanism has been proposed to explain the role of defective CFTR protein in the dysregulation of SLC26A9 through the Na^+/H^+ Exchange Regulatory Co-factor (NHERF1) [8].

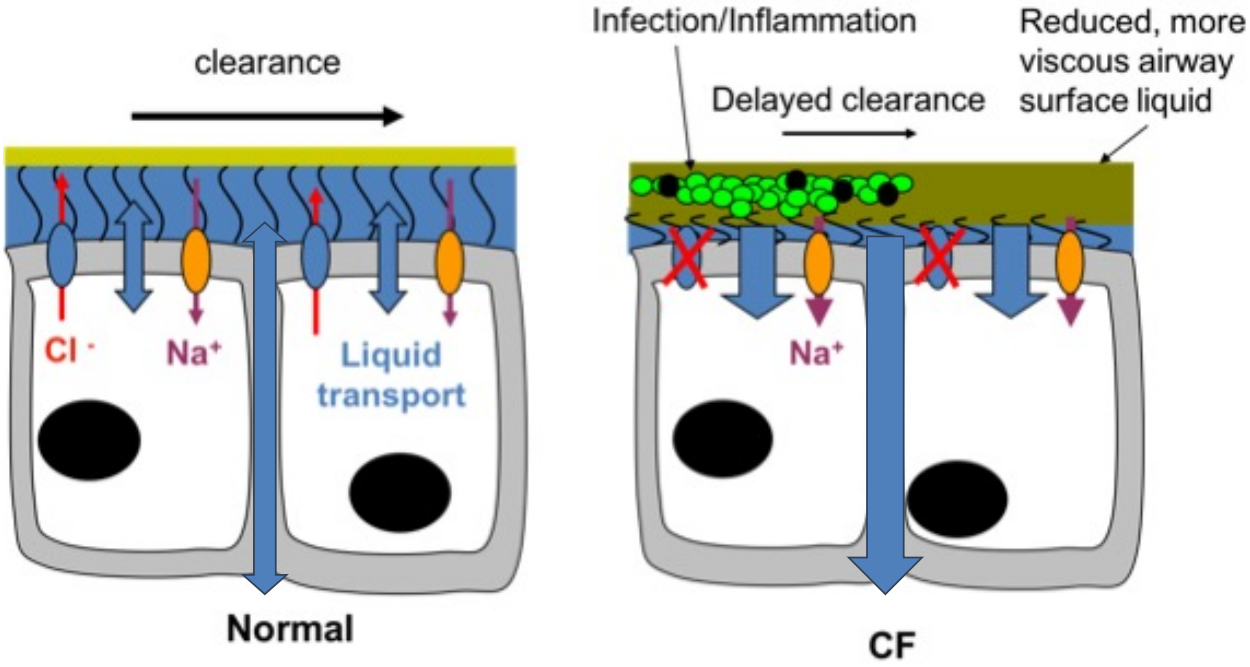

Figure 1.5: Normal PCL and MCC homeostatic behavior is maintained with normal function levels of CFTR at the apical membrane of the airway epithelium (left). In CF (right) ASL hyperabsorption due to the absence of CFTR and subsequent dysregulation of electrolyte balance causes mucus dehydration, and thickening, leading to chronic infections and subsequent inflammation and tissue damage [119].

1.3.3 System Level Pathophysiology

The liquid hyperabsorptive phenotype described in *in vitro* studies of CF cell cultures is reflected in several organ level phenotypes. For example, the increased concentration and/or differential production of different MUC proteins in the airway's lumen alters the rheological properties of mucus, making its clearance more challenging [79, 190]. Similarly, PCL dehydration leads to ciliary stasis, which further prevents the elimination of mucus, as well as the clearance of any inhaled pathogens or debris. These functional changes in the airway create the perfect conditions for pathogenic colonization, which over the lifetime of patients with CF leads to advanced airway damage and eventual respiratory failure.

CF airway disease is the primary cause of CF-related patient mortality [112]. The progression of airway disease is traditionally measured through spirometric tests [1, 53]. These techniques, however, lack the resolution necessary to better understand the pathophysiological changes occurring within the airway. CT studies have been used to provide insight into the structural changes that occur as a consequence of airway obstruction and disease progression [42]. Similarly, functional imaging through nuclear scans of the clearance of inhaled radio-labeled pharmaceutical probes has been used to assess temporal changes of MCC along the airway tree. This method commonly uses Tc^{99m} Sulfur Colloid (Tc-SC) as the probe. Tc-SC is a large particle designed to be too large for it to be absorbed across the lung epithelium (see Figure 1.6 left panel), so a decrease in background- and decay-corrected signal across the particular region of interest is attributed to MCC of the inhaled Tc-SC.

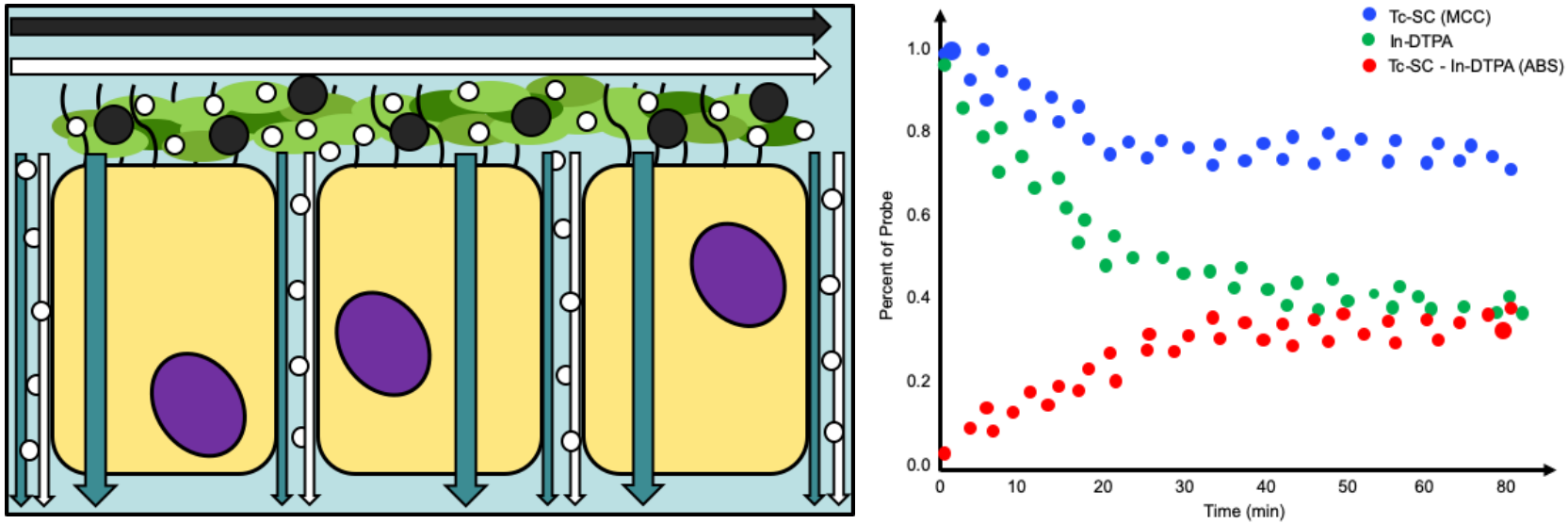

Figure 1.6: Left panel: Tc-SC, and DTPA are delivered to the airways via inhaled aerosol. Both probes are cleared through MCC at the same rate, however, only the smaller of the probes, DTPA, can also be absorbed through the epithelium. Right panel: DTPA retention (green) can be subtracted from the Tc-SC retention (blue) to calculate the amount of absorption (red). Modified from Markovetz, *et al* [120].

MCC measurements have been extended through the use of an additional radiopharmaceutical, In^{111}-DTPA (In-DTPA). DTPA is a small molecule, relative to Tc-SC, that can be absorbed through the epithelial membrane's paracellular pathways, as well as being cleared through MCC (see Figure 1.6 left panel) [33, 111]. The size difference between DTPA and Tc-SC is of great importance. It is assumed that the two molecules are cleared at identical MCC rates, meaning any difference in In-DTPA and Tc-SC retention curves is due to absorption of In-DTPA across the airway epithelium, see Figure 1.6. Furthermore, In-DTPA absorption has been shown to be directly proportional to *in vitro* liquid absorption measurements in primary human bronchial epithelial (HBE) cell cultures, as well as being increased in CF HBE cultures compared to non-CF HBE cultures [33, 111]. In-DTPA absorption measurements (ABS) have been used as a surrogate biomarker of system level liquid absorption as they are affected by both the paracellular component of liquid absorption and likely by tight junction integrity. Consequentially, ABS measurements can be used to show increased liquid absorption rates in patients with CF[33, 111, 120]. They also have the potential to be used as an experimental assessment of airway hydration and the effect that different therapeutic agents have on the absorption defect present in patients with CF.

At the system scale, MCC also acts as a host defense mechanisms against inhaled pathogens [14]. In CF patients, the possible reduced efficacy, or absence, of MCC function allows for opportunistic pathogens to colonize the airways and establish perennial biofilms [109, 118]. The immune system responds to this chronic invasion with a strong, unregulated inflammatory response characterized by a prolonged accumulation of neutrophils, high proteolytic activity and elevated levels of multiple cytokines and chemokines [36, 87]. The nature of this exaggerated inflammatory response is not entirely understood, and multiple mechanisms have been suggested in the literature. For example, TRPA1 Ca^{+} channels, among other functions, facilitate the fine-tuning of expression levels of multiple transcription factors relevant within the inflammatory cascade, and have been shown to have highly different expression levels in primary cells harvested from CF patients [152]. Similarly, CFTR is thought to play a direct role in the immune function of the epithelium [87]. This might also explain why several inflammatory mechanisms such as the IL17/TH17 signalling cascade and neutrophilic chemotaxis appear to be dysregulated in CF patients [6, 127]. The

persistence of this type of inflammatory response results in tissue damage, epithelial fibrosis, and bronchiectasis [6, 36, 51].

1.4 Mathematical Modeling of the Airway across Biological Scales: A Cystic Fibrosis Case study

As described so far, CF affects a wide variety of functions with vastly different spatiotemporal scales. Similarly, current therapies for CF span all pathophysiological scales from inhaled antibiotics to combat chronic airway infections, inhaled osmotic agents that transiently rehydrate the ASL and promote MCC, as well as small molecules that target CFTR and attempt to restore and potentiate its functionality [53, 126, 162, 195, 196]. Many of these approaches show high degrees of variability across the patients. It is true that some of this variability is to be expected given a disease that can be caused by approximately 281 unique genetic mutations, affecting different aspects of CFTR structure and function [25]. However, this also highlights a clear need to better understand the consequent pathophysiological differences that are likely to also play a role. In other words, there is an importance of establishing coherent protocols of longitudinal personalized care that properly address the unique needs of all CF patients.

It is important to point out that the multi-scale nature of CF presents a series of important challenges when attempting to identify possible biomarkers that can reliably inform the relationship between cell or tissue level function and system-level clinical outcomes. Mathematical models have gained significant interest within this field and present a novel alternative to study the complex biophysics of CF airway physiology. Through the inclusion of available experimental data, as well as relevant biological and clinical knowledge, mathematical models are designed to abstract the mechanisms responsible for different aspects of airway function by deconstructing experimental outcomes into physiologically meaningful components. From there, they provide a simple, reusable platform for experimentation and to parametric descriptions and dynamic estimates of important system components. From an engineering perspective, these model predictions and analysis can be combined with tradi-

tional process control and design techniques in order to better address the unique challenges of clinical applications.

The primary goal of process control is to maintain desired process operation conditions in light of external perturbations. Translating this into medicine, the desired operating condition would be to maintain or achieve stable patient health in the presence of various disturbances such as trauma, disease or even clinical intervention. Traditionally, medicine has operated as an open loop system where the physician manually closes the loop by making treatment decisions informed by patient examination and charts. However, the inherent complexities of all biological systems can produce unexpected deviations that obfuscate their behavior and response to intervention. A fundamental assumption of this methodology is that physicians' decisions are accurate most of the time, but are usually based on linear disease-treatment expectations that could be improved if personalized, model-based predictions of patient response to treatment are available to support clinical actions. A proposed work flow for such a framework is shown in Figure 1.7.

In this framework, final treatment decisions are solely in the hands of the physician, but they are informed by rigorous, quantitative predictions of a course of therapy that is optimal within measurement error and timing. Thus, mathematical models are effectively used as a supplementary experimental tool, not unlike a mass spectrometer or CT-scan, to generate valuable insights derived from experimental conditions that are either too expensive, impractical, or unethical to carry out in the laboratory or clinic [134]. These ideas have been explored in a number of medical application, such as: cancer chemotherapy and neutropenia [57, 72, 80]; glucose control in diabetes and critical care [95, 96, 105, 146, 166, 202]; sepsis [45, 219]; and CF [120, 174, 176].

1.4.1 Cellular Scale: Ion and Liquid Transport

There have been multiple attempts to mathematically model different aspects of cell physiology relevant to CF disease, particularly liquid and ion transport. Among these, it is important to mention the seminal work of David E. Goldman who, in 1943, published the first comprehensive mathematical description of the relationship between the electrical and

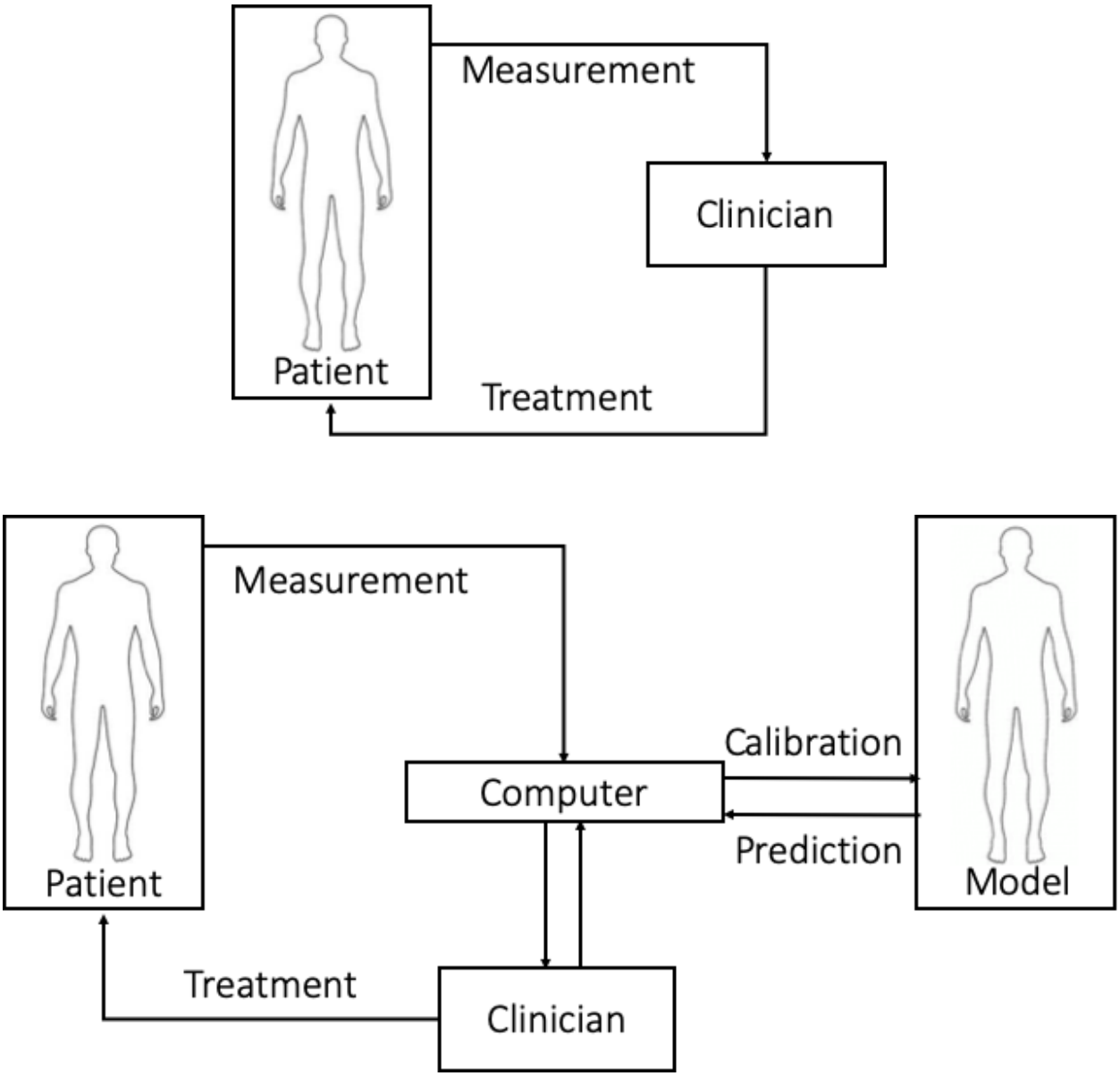

Figure 1.7: Top: Standard-of-care Physician-Patient treatment feedback loop. Bottom: A clinical decision support system for treatment using model-informed physician decisions for patient care.

chemical natures of transmembrane ion flux [66]. This mathematical description has become a cornerstone of mathematical modelling across multiple fields including neuroscience, cardiology, and more recently, epithelial electrophysiology. The first work attempting to model the dynamics of airway epithelium ion transport was published by Cook and Young [29], and quickly followed by Hartmann and Verkman [75]. Both models presented slight variations of the airway epithelium based on its electrochemical driving forces, but failed to described the impact that liquid transport would have on the system [29, 75]. Novotny and Jakobssen [136] published the first work to describe the interaction between ion and liquid transport. This model was expanded by Falkenberg and Jakobssen to include the possible effect that pH regulation would have on ion flux [54]. The expanded model included almost every major channel expressed in the airway, but suffered from numerical instability problems over timeframes relevant to system-level analysis [54]. Similarly, models developed by Warren *et al* [207], and Herschlag *et al* [78] attempted to describe the effect that Ca^{2+} and purinergic signals, respectively, have on ASL homeostasis, but suffered from similar numerical issues. More recently, Garcia *et al* [62], and O'Donoghue *et al* [138] developed similar models of HBE to identify electrochemical transport parameters in CF and non-CF cell cultures. These models have been used to assess the different electrophysiological trends present under flooded conditions. Lastly, Sandefur *et al* improved upon the model developed by Garcia and colleagues to include a simplified version of purinergic and Ca^{2+} signalling and its role within ion and fluid transport across the epithelium [168].

1.4.2 Organ Scale: Clearance Dynamics

At the system level, the human airway has inspired a myriad of models that have attempted to described different aspects of its physiology. Some examples include models that attempt to mathematically describe the structure of the bronchial tree [21, 55], gas exchange [104, 108] and its role in multiple chemical interactions [86], as well as linking disease states with mathematically generated structural differences [49]. More generally, Burrowes and colleagues published a comprehensive multiscale description of lung physiology that attempts to provide insight into possible strategies to provide a mathematical bridge between cellular

and organ function [22]. In the realm of CF, mathematical models describing the pathophysiology behind the MCC and absorptive defects of the disease have taken precedence. Sturm modeled the MCC mechanism as a set of stochastic differential equations that describe the clearance of particles through a geometric abstraction of the airway. This model succeeds in capturing decreased MCC rates in CF, but fails to identify an exact mechanism [183]. Similarly, Kuratova *et. al* developed a model that successfully described the potential role that mucus rheology plays on the reduced MCC in CF patients [100]. Lastly, Markovetz and colleagues developed a compartment-based model that follows a pharmacokinetics-type approach to describe the MCC and liquid absorption of both CF and non-CF subjects. Their model suggests the presence of areas of diminished MCC rate in patients with CF, as well as the transient rescue of these areas with inhaled osmotic therapy [120].

1.5 Dissertation Overview

The work described in this manuscript outlines the first steps in the development of a platform for the use of biophysically-inspired mathematical models of cell and tissue airway physiology to improve our understanding of disease pathophysiology and treatment decisions, eventually leading to the establishment of a framework for personalized treatment of CF.

Airway epithelial electrophysiology represents a complex system to model biophysically. There exist several experimental techniques that allow for the characterization of the governing mechanisms. However, they cannot provide simultaneous information about the individual dynamics of multiple network elements without the need to significantly perturb the nature of the epithelium.

With this in mind, **Chapter 2** focuses on the development and validation of a generalized, compartment-based model describing the mechanisms involved in primary human airway epithelial cell cultures under common experimental conditions. The model allows for the exploration of key interactive elements of the epithelial network, the description of electrochemical ion transport, and the system's response to common pharmacological stimuli. The chemical and electrical components of the system required the inclusion of both alge-

braic and differential states resulting in a largely non linear and heavily constrained model with a discontinuous parameter space that spans multiple orders of magnitude. This also leads to a high degree of parameter correlation due to tightly coupled transport dynamics and pathway complexity. The model development process was further complicated by the inherent data sparsity of the experimental results used to inform the model. **Chapter 2** also describes the development of a parameter space exploration algorithm that combines the robustness of a large scale, non linear optimizer, with the necessary reliability to satisfy the constraints of our system. This algorithm was used to establish a simple, iterable workflow where experimental data from primary cell cultures were used to inform the generation of parametric distributions describing the population level physiology of both CF and non-CF *in vitro* populations.

Lastly, **Chapter 2** outlines two applications of this model: (1) the generation of parametric descriptions of the pharmacodynamic profile of CF HBE cell cultures following the treatment with common CFTR corrector and potentiators; and (2) the evaluation and characterization of physiological differences between two different *in vitro* models of CF, HBEs and human nasal epithelial (HNE) cell cultures.

The lumenal side of airway epithelium is commonly lubricated by a "thin film", a small volume of liquid called the airway surface liquid (ASL). The ASL is composed of a complex mixture of protein, electrolytes, water, and other solutes that profoundly affect the function of the epithelium. In CF, the ASL is severely depleted. **Chapter 3** develops a thin film variation of the electrophysiology model described in **Chapter 2** that includes mechanisms involved in the regulation of ASL homeostasis and paracellular solute and liquid transport, allowing us to explore airway epithelial dynamics more akin to tissue level function.

Modeling the phenomena that underlie the regulation of ASL volume would provide critical insights into the mechanisms that play a major role in the pathophysiology of CF. A three compartment model will represent the dynamic volumes of the cells, the ASL, and the basolateral bath. Both *in vivo* and *in vitro* ASL volumes were osmotically controlled via the directed transport of solutes and liquid fluxes, both transcellularly and paracellularly.

Our model provides a novel platform to evaluate data obtained from patient-matched *in vitro* experiments analogous to commonly used *in vivo* measurements of airway function in

CF; thus proving a first step towards a multi-scale, personalized medicine platform in CF, see figure 1.8. Furthermore, this allows us to longitudinally assess liquid transport dysregulation and therapeutic response to treatment strategies like inhaled osmotic therapies.

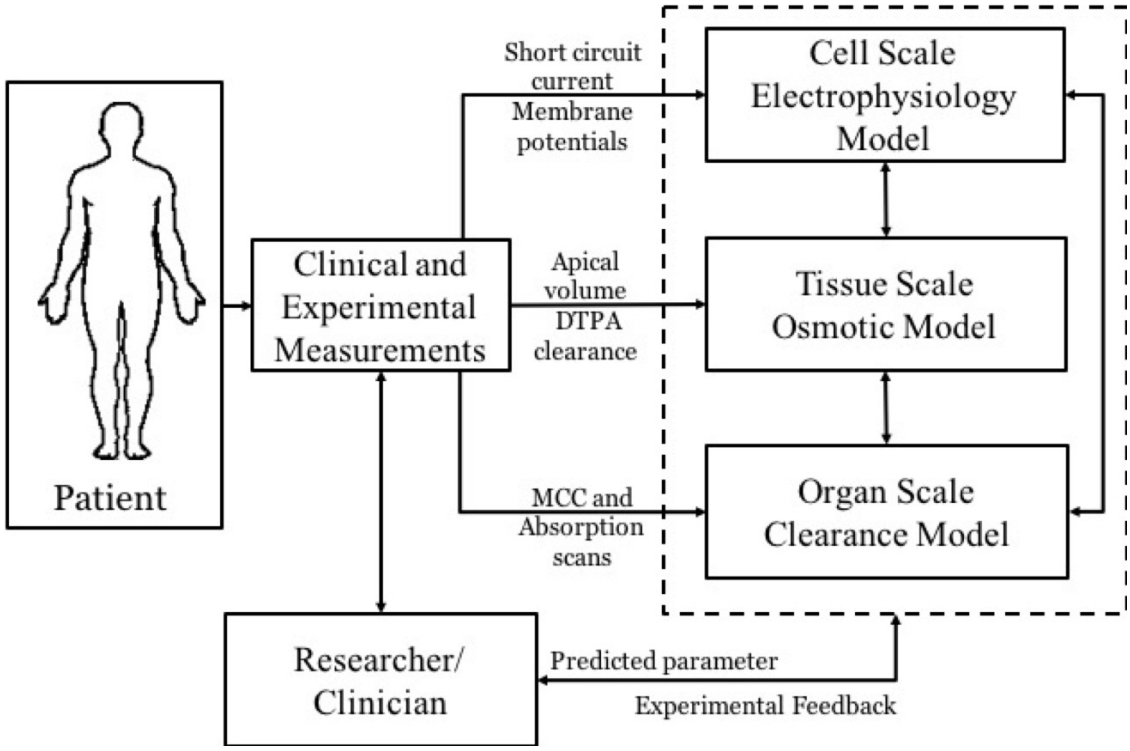

Figure 1.8: A clinical decision support system for treatment design using model-informed physician decisions for patient care.

Chapter 4 incorporates the mechanistic and parametric descriptions generated from the models in **Chapter 2** and **Chapter 3** with *in vitro* and *in vivo* measurements. This work highlights the development and implementation of a database that identifies novel relationships between *in silico* predictions of airway physiology, common cell and tissue level experimental assessments, and organ-level clinical data obtained from individuals with CF lung disease, carriers of a single CFTR mutations, and healthy controls.

The three groups provided samples of HNE cells, performed a nuclear imaging study to measure MCC and DTPA/airway surface liquid absorption (ABS), an *in vivo* pulmonary function test, and inert gas washout studies. CF subjects also performed a second ABS/MCC

imaging day that included inhalation of osmotic agents in order to characterize their therapeutic response. This data set was used to develop patient-specific descriptions that helped us identify key physiological differences across all three cohorts. These differences provided valuable insight into the high degree of variability seen among patients with CF.

Similarly, we leveraged this information to identify parameters that correlate dynamics observed during *in vitro* experiments with organ-level behavior. Under the current paradigm of CF airway pathogenesis and disease progression, sustained restoration of airway hydration and MCC will prevent chronic infections and decrease the incidence of inflammation, potentially halting disease progression. Therefore, the establishment of clear, minimally-invasive strategies to assess individualized therapeutic response could represent a breakthrough in CF treatment.

2.0 Compartment-based model of human airway epithelial electrophysiology under Ussing chamber conditions

2.1 Introduction

Healthy epithelial tissue maintains a very tightly regulated electrochemical balance of Na^+, Cl^-, and K^+ ions across the polarized membrane. Due to the ionic nature of their cargo, chemical and electrical forces simultaneously drive these processes. These electrolytes, along with water and other molecules, are transported through a complex network of trancellular and paracelluar pathways to maintain physiologically homeostatic concentration gradients between the apical, intracellular, and basolateral compartments for each electrolyte.

Herein we present a generalized, cell-scale, compartment-based model of ion and liquid transport across the human airway epithelium that uses volume regulation and electrophysiological data from primary airway epithelial cells to quantitate parameter values. Our goal in developing this model is to better resolve the specific physiological mechanisms that contribute to CF disease pathophysiology. We believe that the mechanism-specific predictions that our model generates can provide valuable insights that streamline the design of more specific experimental protocols, as well as potentially help in the evaluation of the therapeutic efficacy. The challenge is to construct a mathematical representation of the physiology that can resolve the underlying mechanisms and their interactions.

In CF epithelial tissue, the absence or dysfunction of CFTR affects multiple interactive elements of the airway epithelium electrophysiological network. The loss of Cl^- secretion across the apical membrane leads to cell and tissue-level dysregulation and ASL hyperabsorption. Characterization of the possible mechanisms responsible for this type of multi-scale pathophysiological linkage is inherently difficult. These difficulties are further compounded in epithelial cell lines when we attempt to emulate realistic airway conditions.

Several experimental techniques allow for the characterization of the interactions governing such mechanisms. However, they generally cannot provide simultaneous information about the individual dynamics of multiple network elements without perturbing the condi-

tions of the epithelial membrane. A relevant mathematical description of cell-scale epithelial physiology requires the inclusion of key mechanisms that regulate ion and liquid transport

2.2 Methods and Protocols

2.2.1 Cell Culture

This study used primary HBE cell cultures harvested from non-CF (13 donors, n=70 filters), and CF (9 donors, n=37 filters) subjects, and HNE cell cultures from non-CF (11 donors, n=44 filters), CF (11 donors, n=34 filters), and carriers (3 donors, n=8 filters). The HBE cells were cultured from excess pathological tissue removed after lung transplantation and organ donation under a protocol approved by the University of Pittsburgh Investigational Review Board (UPIRB), as described previously [43]. The non-CF donors presented with different airway pathologies but were deemed homozygous for wild-type CFTR. All HNE samples were obtained from either healthy individuals over 18 years of age with no known history of airway pathology or smoking and a %FEV1 greater than 70%, patients with a genetically verified CF diagnosis, or the biological parents of these CF patients, accordingly. All donors of HNE samples were screened for CF-causing mutations and their respective group assignment verified. The HNE samples were collected under a protocol approved by the UPIRB. For more detailed information about the cell culture protocol see Appendix A.

2.2.2 Ussing Chamber

Primary airway epithelial monolayers cultured on filter supports (0.33-cm^2 Costar Transwell filters) were mounted in Ussing chambers, and the cultures were continuously short circuited with a VCC MC6 automatic voltage clamp (Physiologic Instruments, San Diego, CA) in order to measure their transepithelial short-circuit current (I_{SC}). Transepithelial resistance (TER), an indicator of monolayer integrity, was measured by applying a $2mV$ bipolar pulse every $90s$ at the start and end of the experiments and calculated using Ohms law. A TER measurement of $200\Omega cm^2$ was used as a minimum threshold for inclusion of

a I_{SC} trace into the training data set, and $150\Omega cm^2$ for validation experiments. Ringers solution composed of 115 mM NaCl, 25 mM $NaHCO_3$, 5 mM KCl, 10 mM HEPES, 1 mM $MgCl_2$, 1.5 mM $CaCl_2$, and 5 mM glucose was used to fill both the apical and basolateral chambers for experiments containing bicarbonate. Chambers were constantly gassed with a mixture of 95% O_2 and 5% CO_2, which guarantees proper mixing and maintains extracellular pH at 7.4. For bicarbonate-free experiments, $NaHCO_3$ was replaced with 25 mM of Na-Gluconate, pH was adjusted with NaOH to 7.4, and chambers were gassed with air. All experiments were performed at 37 C. Following voltage clamping and chamber flooding, the I_{SC} was allowed to stabilize until a steady state was reached ($\sim 10 - 30min$). Depending on the experiment, different stimulants or blockers of ion transporters/channels were added to either the apical or basolateral chambers: Amiloride ($10\mu M$, added apically) to block the flow of Na+ through ENaC; Forskolin ($10, \mu M$, added basolaterally) to stimulate the flow of Cl- through CFTR; Bumetanide ($10\mu M$, added basolaterally) to inhibit the flux through the basolateral Na^+-K^+-2 Cl^- co-transporter (NKCC); and CF Inhibitor-172 ($10\mu M$, added apically) to block the CFTR-related current. Sufficient time was given to allow for a new steady state to be reached after each addition.

2.2.3 Model Development

In the human airway apical Cl^- transport is facilitated by both CFTR and alternative Cl^- channels (ACC), such as calcium-activated chloride channels (CaCCs) and SLC26A9 [84, 94, 138]. Apical Na^+ and K^+ transport occurs through ENaC and the large conductance Ca^{2+} activated K^+ channel (BKCa), respectively [84, 130, 142, 209]. Basolateral Na^+, Cl^-, and K^+ transport occurs primarily through mechanisms including the Na^+- K^+-2Cl^- co-transporter (NKCC) and Na^+-K^+-ATPase (NaKP), as well as a series of basolateral Cl^-, and K^+ channel [84]. Water transport will also occur through multiple aquaporin channels expressed at the apical (AQP5) and the basolateral (AQP4 and AQP3) membrane [84, 200].

In an Ussing Chamber (UC) experiment, the apical and basolateral compartments are filled with predetermined solutions designed to mimic physiological electrolyte concentrations. Due to their relatively high volume, when compared to the intracellular space, these

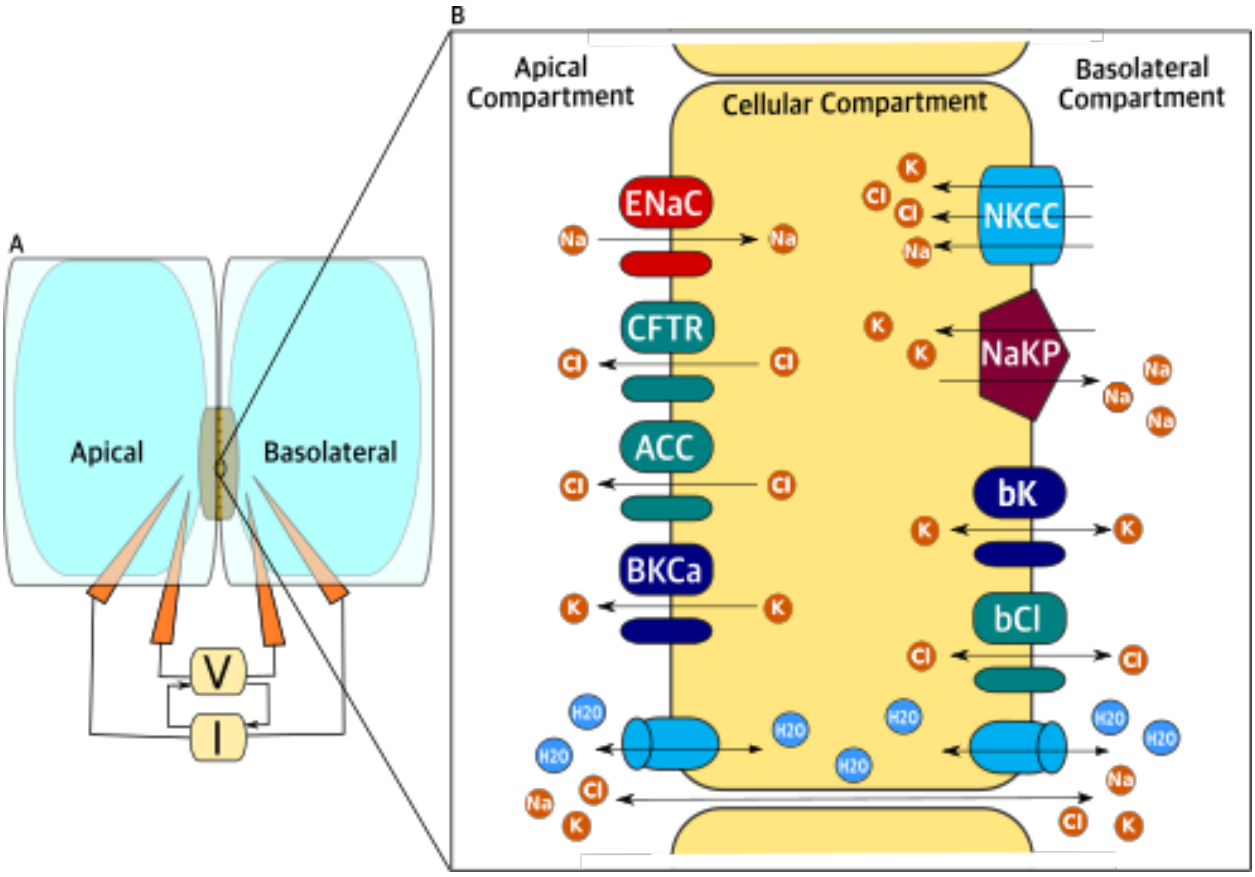

Figure 2.1: Schematic of a standard Ussing chamber (UC) set up, and the corresponding model abstraction of the airway epithelial cell culture insert used to measure short-circuit currents. In the UC, the cell monolayers are located in between two large volume reservoirs representing the apical and basolateral compartments. These compartments each hold approximately 4,000 times the volume capacity of the entire monolayer volume. Cells in the monolayer have been differentiated under air/liquid interface conditions and maintained consistent transepithelial resistance. The zoomed area describes the major contributors to solute and liquid transport across the airway epithelium represented in the model equations. Cellular volume and electrolyte concentrations dynamically respond to changes in electroosmotic driving forces.

compartments can be mathematically modelled as infinite reservoirs, and thus need not be included in the mass balances (Figure 2.1A). Therefore, transport of water between the cellular and apical (Ap) or basolateral (Bl) compartments is driven solely by the osmotic pressure difference, $\Delta\pi_{C,M}$, as described in Equation 2.1.

$$\Delta\pi_{C,M} = \sum_k \gamma_k \frac{n_{k,C}}{V_C} - Osm_M \tag{2.1}$$

Here, M is a set variable the includes both the Ap and Bl membranes, $n_{k,c}$ and V_C are the number of moles of solute k present in the cellular compartment, C, and the volume of the same compartment, respectively. γ_k is the osmotic coefficient associated with solute k. Osm_M is the osmolarity of either the apical or basolateral compartment as defined by the solutions simulated in the model. From this relation, we can then describe the intracellular volume (V_C) dynamics as:

$$\frac{dV_C}{dt} = V_m \sum_j (L_{PM}\Delta\pi_{i,j}) \tag{2.2}$$

Here, L_{PM} is the hydraulic permeability of the membrane separating compartments i and j, and V_w is the molar volume of water. In our cell cultures, the basolateral membrane is at least 10-fold larger than the apical membrane because basolateral transport begins immediately adjacent to tight junctions in the lateral intercellular space. As such, we allow hydraulic permeabilities of the basolateral membrane to be an order of magnitude greater than the apical membrane ($L_{PB} = 10L_{PA}$), similar to values previously reported in literature [123].

Our model abstracts the transepithelial ion transport network as an electrical circuit. This assumption allows us to describe ion channels as resistors that modulate flux and membranes as slow charging capacitors that inhibit the transit of ions, unless through a channel or transporter. Changes to the apical and basolateral membrane potentials due

to ion movement are considered instantaneous and are thus modeled algebraically. For ion channels, each flux is defined by Goldman's rectification equation [66].

$$J_{i\to j} = \frac{z_X F P_Y E_{i/j}}{RT\left(e^{\frac{z_X F P_Y E_{i/j}}{RT}} - 1\right)}\left([X]_i - [X]_j\, e^{\frac{z_X F P_Y E_{i/j}}{RT}}\right) \tag{2.3}$$

Here, i and j represent the two compartments involved in the flux, T is the system's temperature, F is the Faraday constant, R is the ideal gas constant, P_Y is the estimated permeability of channel Y, $E_{i/j}$ is the membrane potential between compartments i and j, z_X is the valence of electrolyte X, and $[X]_i$ and $[X]_j$ are the electrolyte concentrations in compartments i and j, respectively.

In the case of transporters and ionic pumps, the molar flux is calculated as a series of Hill terms that modify the estimated maximum flux with predetermined stoichiometry and directionality, based on known physiological data [54, 136].

$$J_{i\to j} = \frac{n J_Y^{max} A}{\prod\left(\frac{[X]_{50}^i}{[X]_j} + 1\right)^h} \tag{2.4}$$

Here, n refers to the stoichiometric coefficient associated with each ion X for the respective transporter, J_Y^{max} is the estimated maximum flux per ion for transporter Y, $[X]_{50}^i$ is the required concentration of electrolyte X present in compartment i to achieve half of the maximum flux, $[X]_i$ is the current concentration of electrolyte X in compartment i, h is the Hill coefficient associated with ion X, and A is the area of the relevant membrane.

From the individual channel and transporter ionic fluxes, J_Y, we can calculate the electrical current, I_Y, generated by the displacement of ion X through transporter Y, such that:

$$I_Y = z_x F J_Y \tag{2.5}$$

Where F represents Faradays constant. It should be noted that currents are only calculated for ion channels and electrogenic transporters (transporters with inbalanced charge

displacement). Based on the model schematic given in Figure 2.1 B, we established the equations governing liquid and solute transport in airway epithelia by defining an open mass balance around the cellular compartment. Solute transport occurs via passive transport down an electroosmotic gradient and by active, or facilitated, transport into and out of the cell. Thus, changes in intracellular electrolyte concentrations for a given ion is described:

$$\frac{dX_c}{dt} = \sum_Y J_Y + \sum_G n_x J_{act,G} \tag{2.6}$$

Here, X_C is the intracellular concentration for ion X,J_Y is the ionic flux through ion channel Y at time t, $J_{act,M}$ is the flux due to an ionic pump or co-transporter, G, that does not follow necessarily follow the electroosmotic gradient, and n_x is any ion-specific stoichiometry associated with G.

From the the relation between ion flux and current described in Equation 2.5, we can describe the total apical, I_{Ap}, and basolateral, I_{Bl}, currents based on the ion channels and transporters included at each membrane (Figure 2.1B), as follows:

$$I_{Ap} = I_{ENaC} + I_{CFTR} + I_{ACC} + I_{BKCa} \tag{2.7}$$

$$I_{Bl} = I_{bCl} + I_{bK} - I_{NaKP} \tag{2.8}$$

Lastly, these expressions are used to establish algebraic constraints that are used to simulate the zero millivolts clamped transepithelial voltage, E_t, conditions of the UC and estimate the apical, E_{Ap}, and basolateral, E_{Bl}, voltages, see equations 2.9 and 2.10.

$$I_{Ap} - I_{Bl} \approx 0 \tag{2.9}$$

$$E_{Ap} + E_{Bl} = E_t \approx 0 \tag{2.10}$$

The model is able to predict intracellular electrolyte concentration changes in response to treated with channel blockers and stimulants (see Figure 2.2, left panel), as well as predict apical and basolateral potentials of equal magnitude but opposite value (see Figure 2.2, right panel), thus simulating the voltage clamp conditions of the UC.

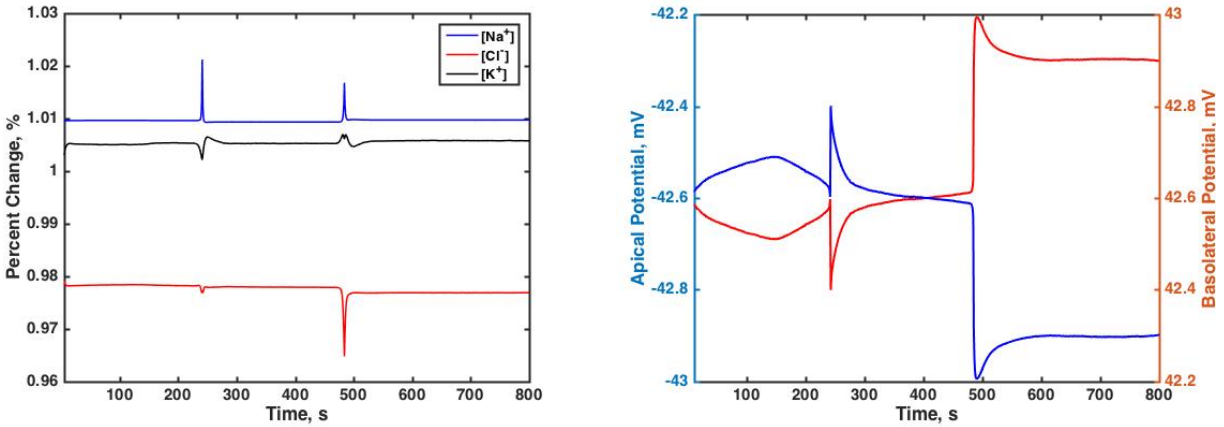

Figure 2.2: Percent change in electrolyte concentration (Left), and predicted apical and basolateral potentials (Right) for a representative model simulation.

2.2.4 Parameter Estimation

The model was implemented in Pyomo, an open source, Python-based, object-oriented modeling framework designed for the formulation and analysis of mathematical models for complex optimization problems [73, 74]. Pyomo combines the advantages of a full-featured programming language like Python and extends them to include the optimization capabilities of traditional algebraic modeling languages. In particular, our model takes advantage of methodology designed for the handling of generalized disjunctive programming and integration of dynamic differential/algebraic systems [73, 133]. Pyomo also includes a built-in interface with multiple numerical optimizers. This work was carried out using Interior Point Optimizer (IPOpt). IPOpt is an open source, large-scale optimization package designed to find the local solution of optimization problems with nonlinear and/or non-convex objective

and pathway-constraint functions [203]. Both Pyomo and IPOpt are freely available online (http://www.pyomo.org/installation/, https://projects.coin-or.org/Ipopt, respectively).

The complex nature of the epithelial membrane's ion and liquid transport network, and its response within the UC poses a fairly difficult numerical problem to model. The need to include both differential equations to model ion and water flux dynamics, and algebraic pathway constraints to properly describe the electrical component of transport, results in a nonlinear, highly stiff system with a discontinuous parameter hyperspace spanning multiple orders of magnitude. These characteristics make it prohibitive to implement our model using standard gradient-based optimization algorithms. Figure 2.3 summarizes the key differences faced when estimating parameters for pathway-constrained models.

In order to address this, we developed an algorithm that uses a combination of a Latin Hypercube (LHC) sampling scheme, and an *a priori* feasibility check to pre-screen potential initial parametric guesses to determine if they are located within a physiologically plausible region of the parametric hyperspace. LHC sampling is preferable for these types of applications because it guarantees a broader coverage of the parameter hyperspace by imposing thresholds for how close two sampled points can be [145, 159, 160]. The algorithm verifies the numerical feasibility of these guesses through the estimation and evaluation of model constraints at time zero, and excludes parameter sets that either fail to converge (based on a goodness of fit, Equation 2.11) or produce biophysically invalid results (based on a feasibility criterion, Equation 2.12). The approved guesses are then used to initialize a full implementation of the model previously described. 2.4 shows the summary work flow of this algorithm.

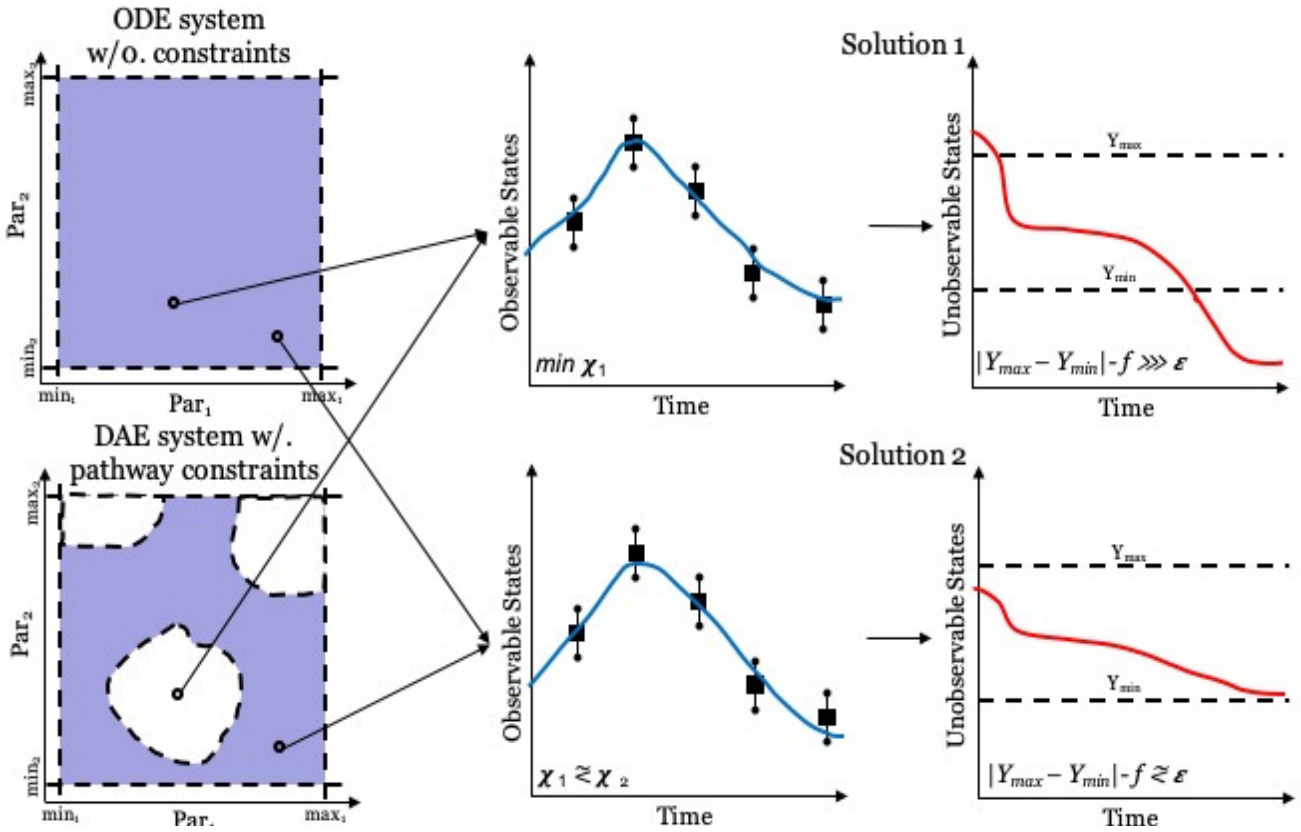

Figure 2.3: Summary of parameter estimation differences for differential algebraic equation (DAE) systems relative to traditional ordinary differential equations (ODE) systems. An ODE system (Top row) parameter estimation schemes converge when the simulated observable states approached the available data set, essentially minimizing an objective function χ. This, however, does not guarantee that unobservable states will remain within physiologically meaningful ranges, since the model is dynamically unconstrained. DAE pathway constraint models (Bottom row) include both χ and a feasibility criterion, ϵ, that guarantee the model minimizes the error but also satisfies pathway constraints imposed on it. This can lead to a trade-off in goodness of fit for overall system feasibility.

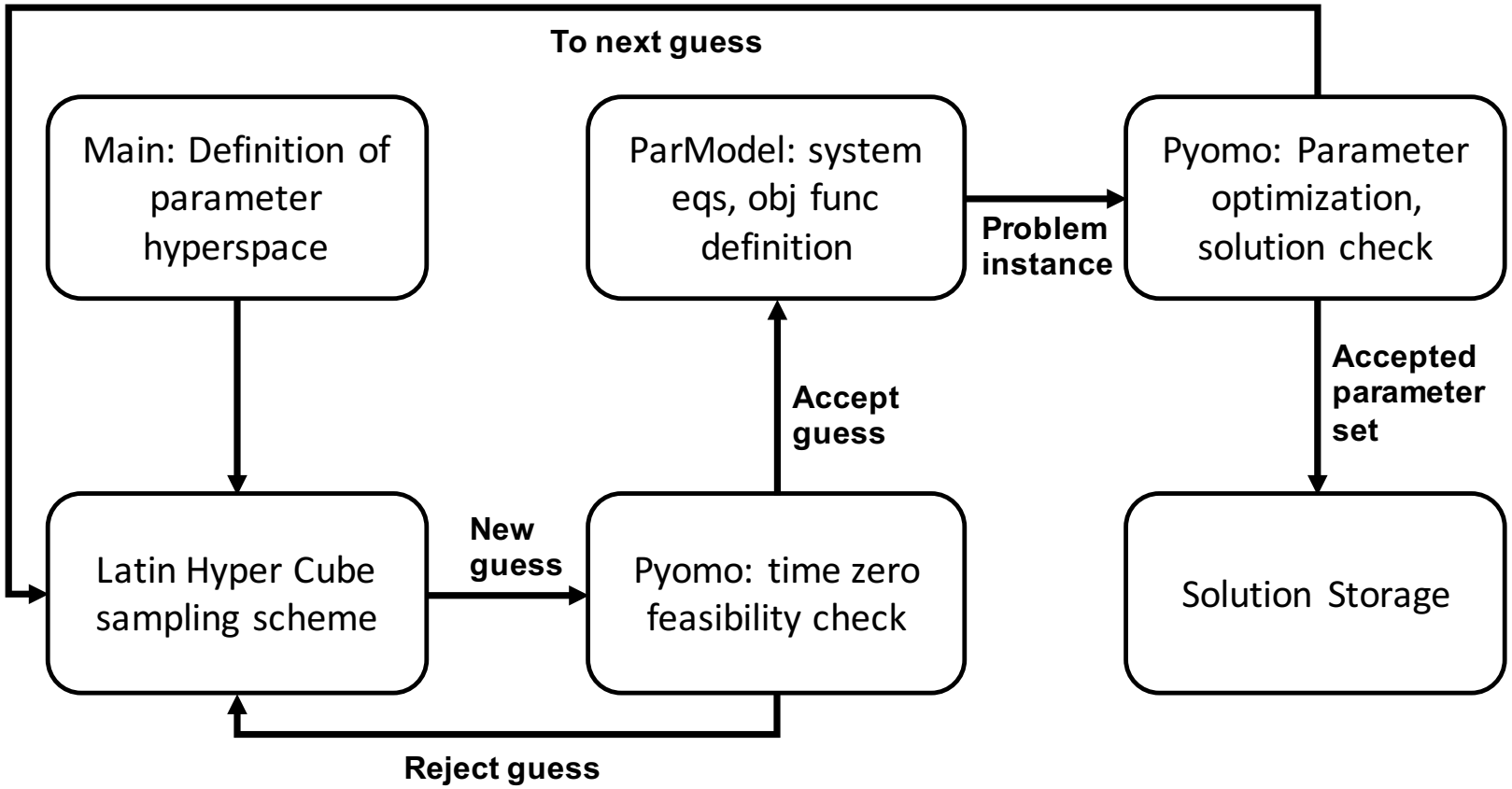

Figure 2.4: Workflow diagram describing the psudocode for the parametric search algorithm we developed. The diagram highlights the importance of incorporating a feasibility check prior to the optimization run in order to guarantee that physical constrains are met at time zero, while still sampling large portions of the physiological parameter space.

The objective function (χ^2) is a mathematical representation of the agreement of experimental data with observable predicted by the model. This model uses the weighted sum of squared residuals as our objective function, defined as:

$$\chi^2(\theta) = \sum_{k=1}^{m} \sum_{i=1}^{d} \left(\frac{y^*_{k,i} - y_k(, t_i)}{\sigma^*_{k,i}} \right)^2 \tag{2.11}$$

Here, $y^*_{k,i}$ refers to the I_{SC} data point recorded for each individual filter for donor k, measured at time point t_i, $\sigma^*_{k,i}$ denotes the standard error of the mean for all filters from donor k recorded at the same time point, and $y_k(\theta, t_i)$ is the corresponding model-simulated value of $y_{k,i}$ as predicted by a given parameters set, θ. The objective function will be minimized according to:

$$\begin{aligned} \hat{\theta} =& argmin\left\{\chi^2(\theta)\right\} \\ s.\ t.\ f_{min} \leq& f(X, \theta, t, X_0) \leq f_{max} \\ and\ \theta_{min} \leq& \theta \leq \theta_{max} \end{aligned} \tag{2.12}$$

Here $\hat{\theta}$ represent the parameter values that corresponds to the identified local solution to the optimization problem, f the constraints functions as defined in the Model Development section, θ are free model parameters, and $f_{min/max}$ and $\theta_{min/max}$ are the lower and upper bounds defined for all constraint function and free parameters.

This algorithm was designed to establish a simple, iterable work flow, where experimental data from primary HBE and HNE cell cultures are used to inform the generation of parametric distributions describing the population level physiology of both CF and non-CF cell cultures. Constant values for cellular volume regulation, electrolyte-transporter affinities, and other airway epithelium physiology descriptors were obtained from literature and previously models of human airway electrophysiology [54, 62, 123, 138, 168, 174, 209, 211], for more details please see Table S3.

2.3 Results

2.3.1 Model Validation against known experimental outcomes

The algebraic nature of many of the system components, and the lack of direct experimental data for any of the states describing intracellular dynamics, restricts our ability to validate some of the model predictions. To address this issue, we chose to validate the model through the simulation of known experimental protocols, and compare the results with known trends found in literature. This can be done through the assessment of changes in the model-predicted permeabilities of different transporters that should correlate to changes in either the expression levels or functionality of the same channels.

2.3.1.1 Evaluation of *in vitro* pharmacodynamic response to CFTR modulators

CF HBE cultures (p=1, n=3) were treated with VX809 or a vehicle control for 24, 72, 120, 168, 240, or 336 hours. Short circuit current (I_{SC}) measurements were collected to assess CFTR channel activity. This was done in order to establish the optimal treatment protocol to maximize cell culture response to modulator therapy. Results showed a steady dose-dependent response profile to the magnitude of $\Delta I_{Forskolin}$ stimulated response up to 120 hrs of chronic VX809 treatment. Treatment beyond this threshold, resulted in a complete loss of the modulator's corrective action. The lack of response to CFTR stimulation after 120 hours + of VX809 treatment is likely due to DMSO poisoning. DMSO is used to dissolve the correctors, and its prolonged exposure can be cytotoxic. See Figure 2.5.

We verified the model's ability to describe the rescue of mutated CFTR I_{SC} through treatment with small molecule correctors and potentiators. The model was informed with UC data from CF HBE cell cultures (n = 5, filters = 20) treated with a vehicle control (DMSO), or with the combination of corrector (VX809) for 24 hours and potentiator (VX770) during the UC recording. CFTR rescue was simulated by opening the permitted parameter range for predicted CFTR permeability in the model. Figure 2.6 shows the changes in predicted parameters between the two groups. A slight, but significant, increase in CFTR permeability was predicted, as well as a nominal increase in ACC permeability. This is

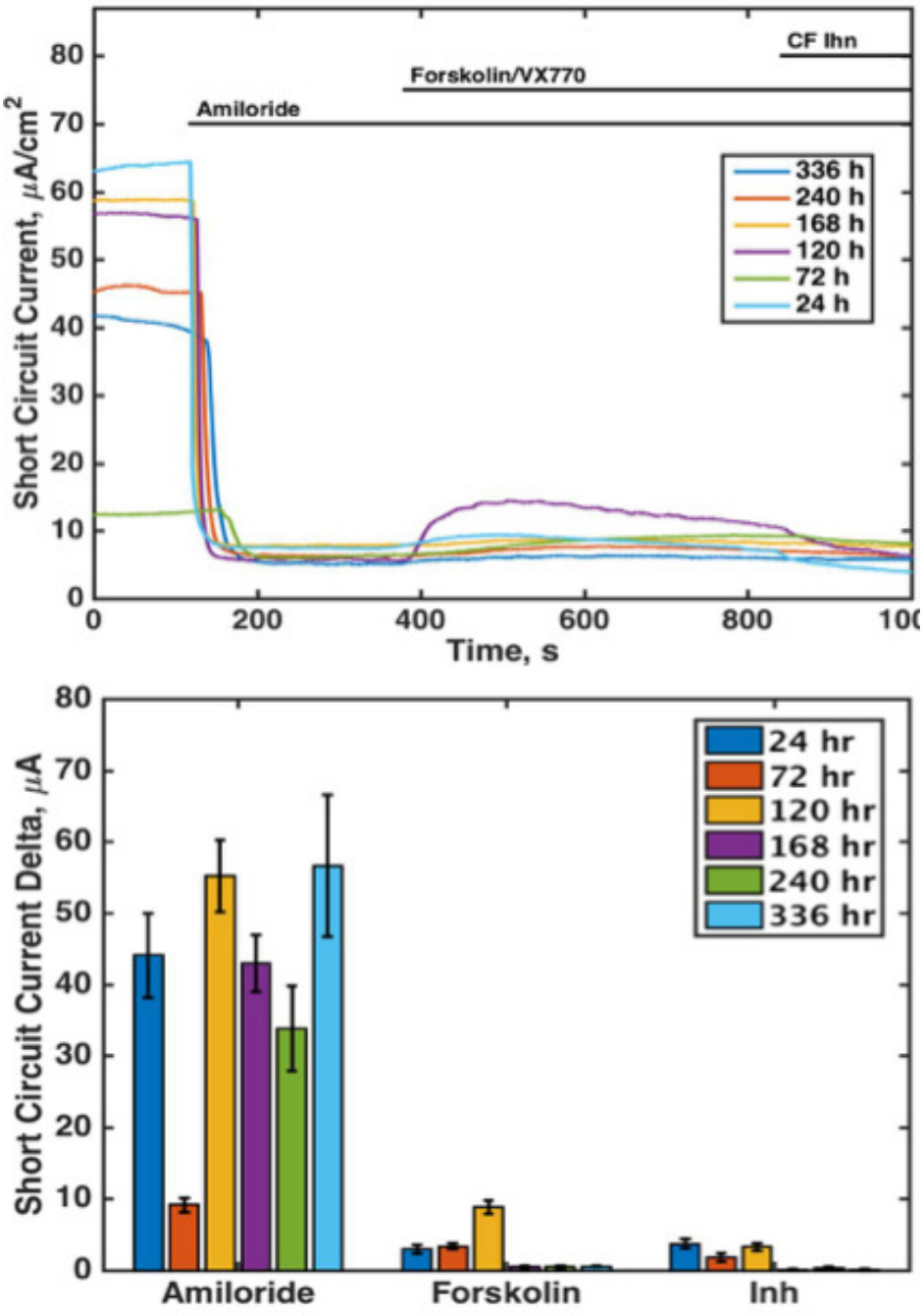

Figure 2.5: (Top) Ussing Chamber I_{SC} traces for $\Delta F508$ homozygous CF HBE cell cultures treated for 24, 72, 120, 168, 240, and 336 hours with a CFTR corrector (VX809), and acutely with a CFTR potentiator (VX770). (Bottom) Bar plots showing the summary of the change in I_{SC} measured following the addition of Amiloride, Foskoling+VX770 and CFInh172.

of particular interest due to recent findings from our collaborators that suggest mutations affecting the trafficking of CFTR to the plasma membrane may also affect the trafficking of SLC26A9 [8]. SLC26A9 is an anion channel expressed in the apical membrane of HBEs believed to be constitutively active in non-CF HBEs, whose function is found to be absent in CF HBE cell cultures[8, 9]. ENaC and BKCa showed no meaningful parametric difference between the two groups.

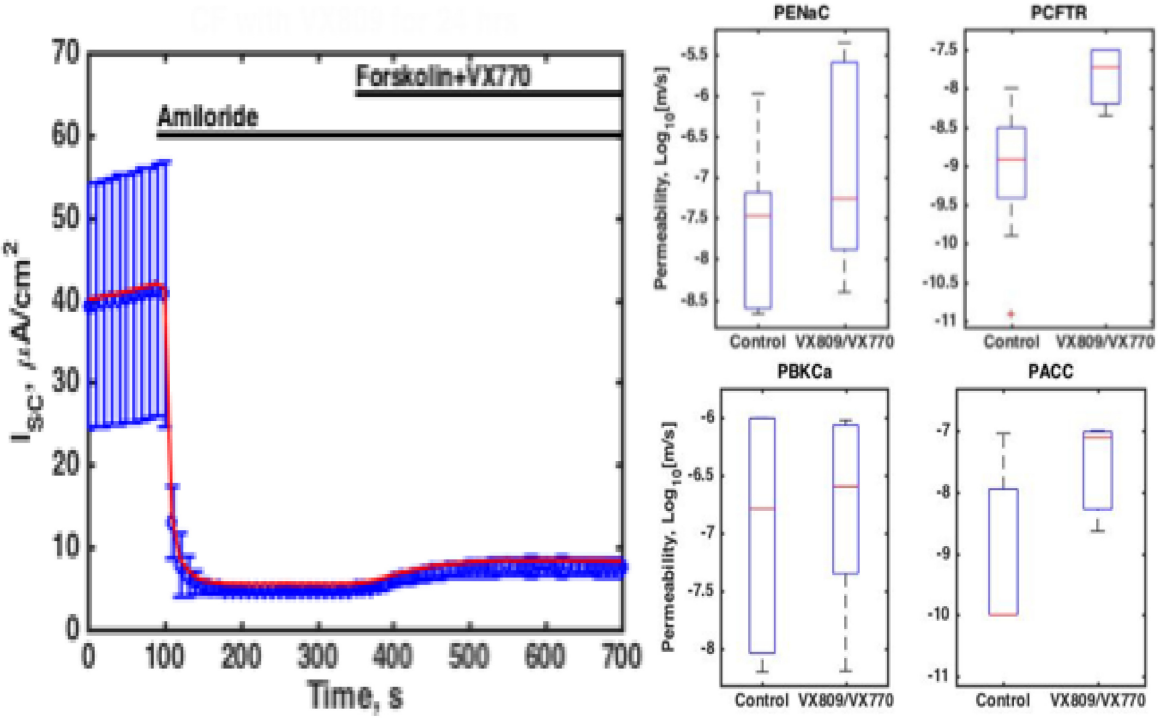

Figure 2.6: Model-predicted parameter changes for (Left) Short-circuit trace model predictions for CF HBE cell cultures (n = 5, filters = 20) treated with corrector and potentiator (VX809 72 hrs, and acute VX770), or vehicle control (DMSO). (Right) ENaC, CFTR, BKCa, and ACC permeabilities generated from Ussing Chamber data. Predicted CFTR and ACC permeabilities showed statistically significant changes between control and corrector treatments ($p < 0.01$).

2.3.1.2 Parameter predictions in response to $TGF - \beta 1$ We also wanted to test the ability of the model to predict changes in the molar flux of different channels as a result

of treatment with compounds believed to affect multiple members of the electrophysiology network. Over the last few years, there has been increased evidence that the cytokine $TGF-\beta1$ plays a significant role in the regulation of ion channels expressed in the airway epithelial. $TGF-\beta1$ is known to be elevated in CF patients, and single nucleotide polymorphisms in $TGF-\beta1$ gene have been linked to increased severity of lung disease [50]. More recently, $TGF-\beta1$ has been shown to limit BKCa function through the downregulation of LRRC26y, and auxiliary protein believed to be responsible for facilitating BKCa's function in non-excitable cells by lowering its Ca^{+2} activation thresholds [94, 213]. Similar results have been shown for TMEM16A, a Ca^{+2}-activated Cl^- channel expressed in the apical membrane of airway epithelia [187], and perhaps more relevant, for CFTR [180].

In order to explore this problem, we informed our model with data obtained from UC traces of non-CF HBE cell cultures (n = 5, filters = 18) treated with $TGF-\beta1$, or vehicle control for 24 hrs. This data was graciously provided by Dr. Agnes Swiatecka-Urban. Through our analysis, we assume that any regulatory changes induced by $TGF-\beta1$ have reached steady state, and that any changes to the new state through the length of the UC recording are negligible. Figure 2.7 shows significant decrease to the predicted molar flow across CFTR, ACC, BKCa, and ENaC. These changes are in agreement with literature trends for CFTR, and BKCa. $TGF-\beta1$ also appears to have decreased the overall I_{sc} baseline of the cell, which would explain the drastic decreased in Na^+ flow through ENaC. TER measurements were not significantly different between the control and $TGF-\beta1$ treated groups.

2.3.2 Characterizing the Electrophysiology of Primary Human Bronchial and Nasal Epithelia, an *In Vitro* and *In Silico* Approach

Primary human bronchial epithelial (HBE) cell cultures serve as a well-established experimental *in vitro* model of airway physiology. Most Cystic Fibrosis (CF) related studies with primary cell cultures have been performed in differentiated HBE cultures, which show the same ion and liquid transport defects as the CF airway [32, 138, 195]. However, HBE cultures are typically sourced from donated lungs not suited for transplantation, or from

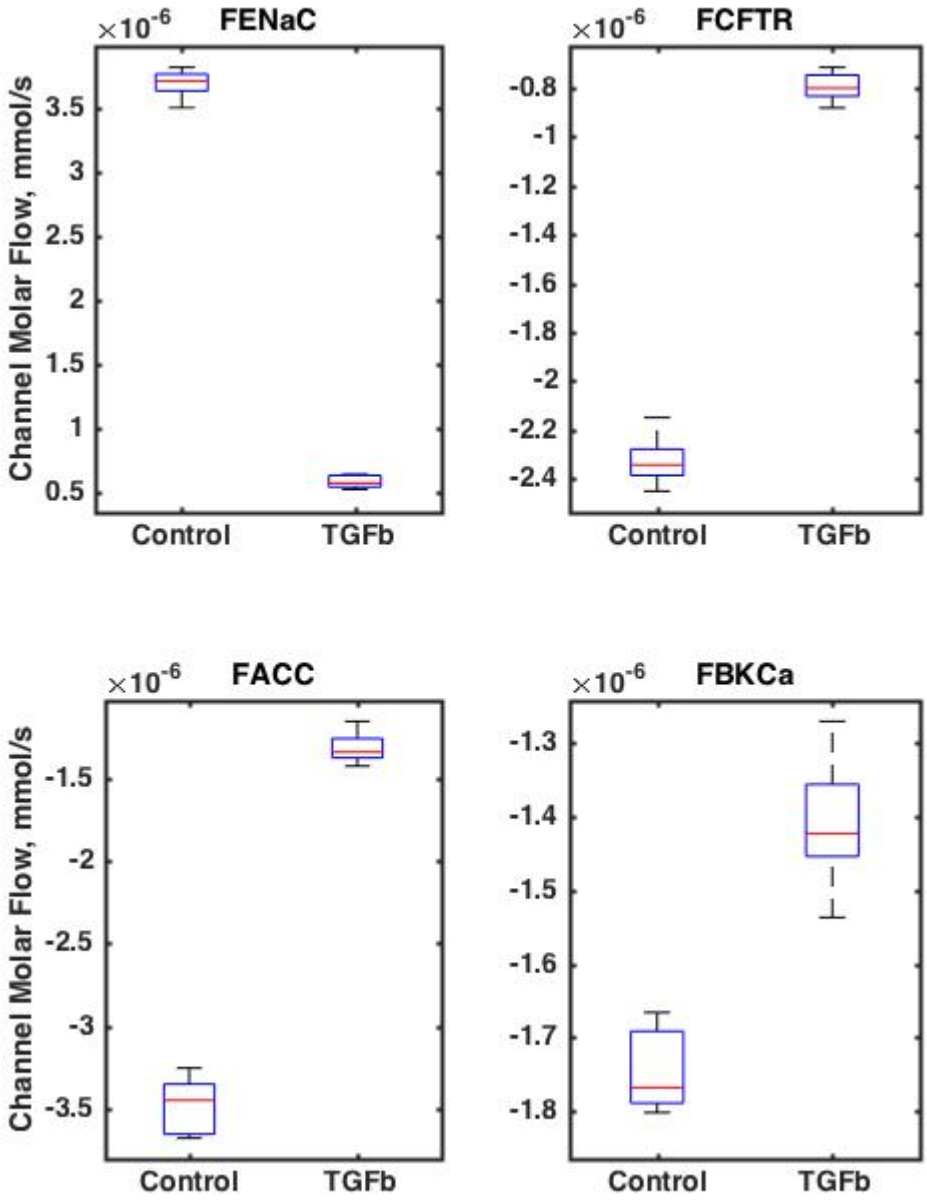

Figure 2.7: Model-predicted molar flux changes for ENaC, CFTR, ACC, and BKCa generated from Ussing Chamber data from HBE cell cultures (n = 5, filters = 18) treated $TGF\beta 1$, or vehicle control for 24 hrs. A flux's sign represents directionality, such that a positive flux means influx, and a negative flux means secretion.

explanted lungs of patients diagnosed with advance airway disease. This reality presents two main challenges: (1) it is not well understood whether HBE cells retain any physiological abnormality due to the underlying disease state; (2) access to explanted lung tissue is limited and can represent an insurmountable limitation to laboratories. These concerns are particularly relevant in CF, where samples are harvested from CF patients with advance airway disease, who are in need of a lung transplant, and may not provide a good representation of the physiology of patients with less progressed disease states.

Primary human nasal epithelial (HNE) cell cultures are a novel, and exciting, *in vitro* model of airway physiology. HNEs can be differentiated and cultured in a similar manner to HBEs and display anatomical markers similar to those of HBE cells like ciliation, mucus secretion, and ion and liquid transport [41, 113, 125, 129, 208, 211]. HNEs can be harvested through minimally-invasive nasal brushings from donors with no history of airway pathologies, making them a better control for the study of disease-specific physiological changes [129]. In CF specifically, HNEs can be harvested from individual patients at all stages of disease progression and allow for analogous *in vitro* measurements to those obtained from *in vivo* level measurements such as functional imaging scans and nasal potential difference (NPD).

Airway disease in CF is characterized by lung infection, inflammation, and impaired mucociliary clearance arising from depletion of the airway surface liquid (ASL). This occurs due to improper liquid and solute transport caused by absence or dysfunction of the Cystic Fibrosis Transmembrane Conductance Regulator (CFTR) [151]. CFTR is a transmembrane anion channel that under normal circumstances is known to secrete Cl- and HCO3- ions in epithelial tissue [189]. Its disruption eliminates a key pathway for apical Cl- secretion and creates an electroosmotic imbalance that favors the hyper-absorption of water from the luminal to the serosal compartment. CFTR is also involved, either directly or indirectly, in the regulation of other ion channels and transporters, including the epithelial sodium channel (ENaC) [76], the solute carrier family 26 member 9 (SLC26A9) [8, 9], and aquaporin 3 (AQP3) [90, 171]. However, the exhaustive analysis of these cell-system interactions is experimentally complex and necessitates the use of reliable models of airway physiology, in particular transepithelial ion transport dynamics.

In this study, we have performed electrophysiological measurements of ion transport dynamics on fully differentiated epithelium monolayers harvested and cultured from primary bronchial and nasal epithelial samples. The study included three genotypic groups: (1) patients with a genetically confirmed CF diagnosis, (2) carriers of a single CF-causing mutation, and (3) subjects homozygous for wild-type CFTR with no history of airway disease. These cultures were used to assess ion transport dynamics under Ussing Chamber (UC) conditions and for the subsequent development of a generalized, biophysically-inspired, mathematical model of ion transport dynamics across the human airway epithelium. The model is constructed to be a representation of cell electrophysiology that can resolve the underlying individual ionic fluxes, while guaranteeing the adherence to biological and physical constraints relevant to the system. Values obtained from model simulation recapitulate experimental findings of transepithelial ionic transport. This combination of experimental and computational characterization methodologies provides an avenue to increase data resolution through the estimation of physiologically-meaningful parameters that describe processes not measurable experimentally, thereby allowing us to identify and characterize possible underlying electrophysiological differences between distinct culture groups due to either cell type or CFTR genotype.

2.3.2.1 HNE and HBE show different electrophysiological dynamics Analysis of the UC traces revealed that non-CF and CF HNE cell cultures followed similar electrophysiological trends with respected to each other and to their HBE counterparts, but overall current magnitudes appeared to be distinct to each cell type. A full breakdown of these electrophysiological studies can be found in Figure 2.8 and Table 2.1. In HNEs, I_{SC} prior to any drug addition ($I_{Baseline}$, $\mu A/cm^2$) is statistically equivalent between CF (Figure2.8B) and non-CF (Figure2.8A) cultures, but did show a nominal decrease in CF ($p = 0.285$).

I_{SC} was increased in CF HNE (Figure 2.8B) vs. CF HBE (Figure 2.8E) ($p = 0.005$). In Non-CF, there was a trend towards a decrease in HNE vs HBE ($p = 0.061$). The same trends are observed when comparing Amiloride-sensitive current ($\Delta I_{Amiloride}$, $\mu A/cm^2$), a typical marker of ENaC-associated Na^+ transport, between non-CF and CF cell cultures in HNEs ($p = 0.578$) and HBEs ($p = 5.9x10^{-10}$). I_{SC} current response to Foskolin ($\Delta I_{Forkolin}$,

$\mu A/cm^2$), a common *in vitro* measurement of CFTR transport activity, was different between non-CF and CF in HNE ($p = 9.6x10^{-13}$) and HBE ($p = 1.9x10^{-20}$) cell cultures, as would be expected. As well as between non-CF ($p = 3.9x10^{-12}$), but not CF ($p = 0.304$) across the two cell types. The exact same trends as $\Delta I_{Forkolin}$ apply to post-Foskolin, Bumetanide-sensitive current drop ($\Delta I_{Bumetanide}$, $\mu A/cm^2$) (Non-CF vs. CF, HNE: $p = 0.032$, HBE: $p = 6.3x10^{-20}$; HBE vs. HNE, Non-CF: $p = 2.6x10^{-17}$, CF: $p = 0.331$). It is interesting to point out that the percent of $\Delta I_{Forkolin}$ inhibited by Bumetanide is more than 3 times greater in Non-CF HBEs than Non-CF HNEs ($\sim 75\%$ vs. $\sim 21\%$). Together, these results suggest possible differences in the electrophysiology profiles of Non-CF HBE and HNE cellular cultures, particularly with regards to the transcellular transport of Cl^-.

Our study also included UC traces from HNE cultures harvested from 5 parent donors carrying a single CF-causing mutation ($wt/\Delta F508 = 4$, $wt/2481insA = 1$, Table 2.1, Figure 2.8C). These revealed possible differences between the electrophysiological profiles of carriers relative to both non-CF and CF HNE cell cultures. In particular, carriers exhibited decreased $I_{baseline}$ and $\Delta I_{Amiloride}$ currents (Table 2.1, $p \ll 0.01$, compared to both CF and non-CF), approximately a 50% decrease in $\Delta I_{Forkolin}$ relative to non-CF cell cultures ($p = 1.43x10^{-3}$), and an increased in the percent of $\Delta I_{Forkolin}$ inhibited by Bumetanide relative to non-CF ($\sim 59\%$ vs. $\sim 21\%$, $p = 0.003$). No meaningful TER difference was observed between any of the groups (Table 2.1, $p \geq 0.25$).

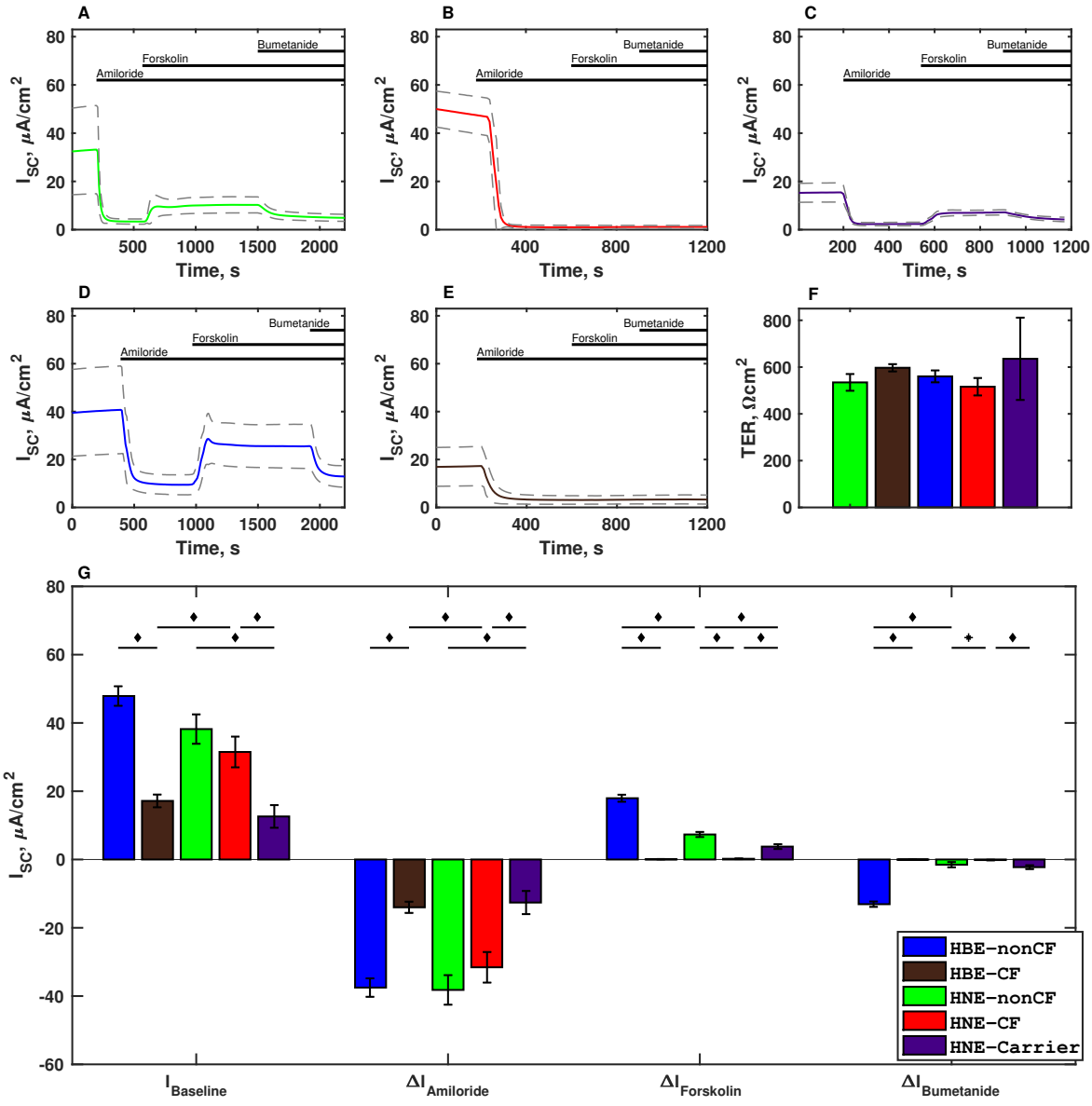

Figure 2.8: Cultures stratified by CFTR genotype and cell type. In sections A-E, the thick lines near the top denote drug additions, used to calculate their respective ΔI_{SC}. Solid lines represent mean population trace after correcting for addition times, and dotted lines represent the $\pm$ SEM for the population: A) non-CF HNE (green), B) CF HNE (red), C) Carrier HNE (purple), D) non-CF HBE (blue), and E) CF HBE (brown). F) Bar graph showing the population mean ($\pm$ SEM) for transepithelial resistances (TER). G) Bar graphs showing I_{SC} measurement means ($\pm$ SEM). Unpaired t-test to establish statistical significance,$* < 0.05$ and $\bullet < 0.01$.

Table 2.1: Summary of statistical analysis for the comparison of electrophysiology for HNEs and HBE cell cultures, stratified by their CFTR genotypes: healthy donors (non-CF, wt/wt, n = 13), carriers of a single CF-causing mutation (Carrier, wt/non-wt, n = 5) and patients with CF (CF, non-wt/non-wt, n = 14). Mean (± SEM) were calculated from all filters in a given group. At least 3 filters were used for each line included in the data set. Unpaired t-tests were used to compare and establish statistical significance across all different possible pairings. I_{SC} are shown in $\mu A/cm^2$ and TER in Ωcm^2.

	HBE			**HNE**						**HBE vs. HNE**	
	non-CF	CF	non-CF vs. CF	non-CF	CF	Carrier	non-CF vs. CF	non-CF vs. Carrier	CF vs. Carrier	non-CF	CF
$I_{Baseline}$ **(± SEM)**	47.88 (± 2.86)	17.16 (± 1.87)	$3.1\text{x}10^{-13}$	38.20 (± 4.31)	31.50 (± 4.50)	12.61 (± 3.32)	0.285	$2.12\text{x}10^{-5}$	$1.60\text{x}10^{-3}$	0.061	0.005
$\Delta I_{Amiloride}$ **(± SEM)**	-37.51 (± 2.70)	-14.00 (± 1.64)	$5.9\text{x}10^{-10}$	-34.40 (± 4.33)	-29.74 (± 4.48)	-9.80 (± 3.39)	0.578	$4.68\text{x}10^{-5}$	$9.93\text{x}10^{-4}$	0.546	0.002
$\Delta I_{Forskolin}$ **(± SEM)**	17.95 (± 1.03)	0.088 (± 0.06)	$1.9\text{x}10^{-20}$	7.33 (± 0.75)	0.21 (± 0.10)	3.78 (± 0.70)	$9.6\text{x}10^{-13}$	$1.43\text{x}10^{-3}$	$3.44\text{x}10^{-4}$	$3.9\text{x}10^{-12}$	0.304
$\Delta I_{Bumetanide}$ **(± SEM)**	-13.09 (± 0.79)	0.051 (± 0.03)	$6.3\text{x}10^{-20}$	-1.52 (± 0.76)	0.16 (± 0.10)	-2.24 (± 0.56)	0.032	0.455	$1.42\text{x}10^{-3}$	$2.6\text{x}10^{-17}$	0.331
TER **(± SEM)**	534.46 (± 35.8)	597.02 (± 15.6)	0.372	560.24 (± 25.5)	516.02 (± 37.3)	735.36 (± 176)	0.413	0.345	0.246	0.384	0.541

2.3.2.2 The mathematical model captures population ion transport dynamics in HBE and HNE samples

In order to describe differences between the electrophysiological dynamics among these groups, the data obtained from the UC studies were used to inform a mathematical model of ion and liquid transport under UC conditions, as described in Methods and Materials. We first examined whether model simulations were able to predict the transepithelial transport dynamics of all cell cultures, regardless of cell type or CFTR genotypic makeup.

Donor specific model predictions were obtained by fitting the model using the optimization scheme described in Equation 2.8 and 2.9, for all individual cell cultures measured from a single primary cell line. Parity plots comparing the model-predicted and experimental measurements for all cell types were generated (Figure 2.9). Individual dots represent the experimental data from one filter at one time point plotted against the model prediction for that cell line at the same simulated time. Root mean square error ($RMSE$) and R^2 values were calculated and reported in order to assess the ability of the model to describe ion transport dynamics of all cell groups within the constraints defined. The plots demonstrated good agreement between the model and experimental data for both cell types, regardless of CFTR genotype.

Next, parameter fits obtained from the simulations described above where analyzed and summarized in Table 2.2. Calculated means from all parameter distributions suggest significant differences between HBE and HNE model-predicted permeabilities for several transport pathways. Since the predicted parameter sets are not constructed from a population level fit, but rather from donor-specific parametric fits, the resulting distributions are non-normal and can present apparent multimodalities. In order to address this, 2-sample Kolmogorov-Smirnov test, a non-parametric test of the likelihood of two sample sets belonging to the sample distribution, was used to compare the corresponding distributions between non-CF HBE and HNE cell cultures (Figure 2.10 A). The distributions showed meaningful changes in mean model-predicted permeabilities (m/s) for ENaC ($p = 2.67\text{x}10^{-4}$), CFTR ($p = 1.32\text{x}10^{-4}$), BKCa ($p = 7.24\text{x}10^{-3}$), bCl ($p = 9.56\text{x}10^{-4}$), and the maximal flux (mol/m^2s) for NaKP ($p = 0.0412$). ACC, PbK and NKCC display similar mean predicted values between the

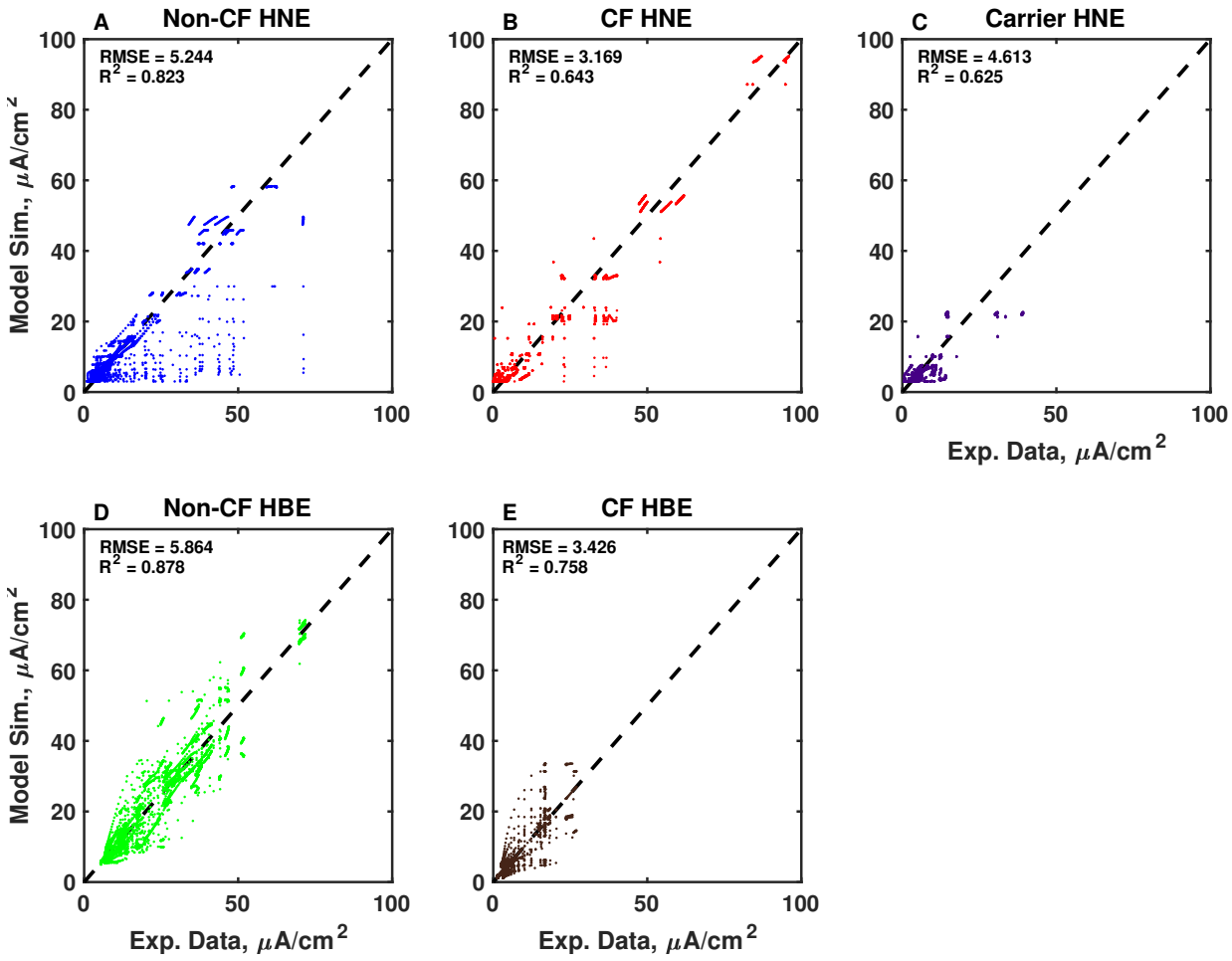

Figure 2.9: Parity plots comparing measured Ussing chamber data to cell-line specific model fits against all 5 groups of cells: (A) non-CF HNE (green); (B) CF HNE (red); (C) Carrier HNE (purple); (D) non-CF HBE (blue); (E) CF HBE (brown). Black dashed line represents a perfect model fit. Cell-line specific model predictions were obtained by fitting the model using a sum of square errors objective function with an variance-weighted simultaneous fit of all individual cell cultures in any given cell line. Individual dots represent the experimental data from one filter at one time point plotted against model prediction for that cell line . Root mean square error (RMSE) and R^2 values are reported for the parity between observed and simulated values for all cell groups.

Table 2.2: Summary of averaged population-level best fit parameters for CF, non-CF and carrier cell cultures in HBE and HNE groups. Model includes pathway constraints that satisfy the biophysical conditions of the Ussing Chamber system (*e.g.* electroneutrality, voltage clamping). Logarithmic, variance-weighted, nonlinear least-squares was used as the objective function. Model parameters were estimated via LHS/IPOpt optimization for model training. Abbreviations include ENaC (P_{ENaC}), CFTR (P_{CFTR}) BKCa (P_{BKCa}), alternative Cl^- channels (P_{ACC}), basolateral Cl^- (P_{bCl}) and basolateral K^+ (P_K) permeabilities in m/s, as well as the maximum fluxes through the basolateral Na^+-K^+-$2Cl^-$ co-transporter (J_{NKCC}) and Na^+-K^+-ATPase (J_{NaKP}) in mol/m^2s.

Cell Type/ CFTR genotype		P_{ENaC} **x10^{-7}**	P_{CFTR} **x10^{-7}**	P_{ACC} **x10^{-8}**	P_{BKCa} **x10^{-8}**	P_{bCl} **x10^{-8}**	P_{bK} **x10^{-8}**	J_{NKCC} **x10^{-7}**	J_{NaKP} **x10^{-7}**
HBE	**non-CF**	26.92	19.54	5.31	26.7	4.59	4.39	1.02	9.97
	CF	33.4	-	1.96	9.73	0.95	4.30	0.20	6.37
	non-CF	1.29	0.78	6.30	19.9	9.10	5.01	0.79	5.01
HNE	**CF**	9.46	-	0.43	21.1	0.68	2.52	0.10	0.31
	Carrier	9.82	0.054	0.38	39.1	4.51	2.44	0.10	5.81

two groups. In order to further explore these changes, joint parametric plots were generated between P_{bCl} and P_{ENaC}, P_{CFTR}, P_{BKCa}, or J_{NaKP} (Figure 2.10 B-E, respectively). These plots revealed an increased in the predicted basolateral Cl^- permeability in non-CF HNEs relative to their HBE counterparts. The observed change in PbCl correlates with changes observed in ENaC, CFTR and BKCa as well. When these trends are taken into consideration alongside the differences in $\Delta I_{Forkolin}$ and $\Delta I_{Bumetanide}$ observed between non-CF HBEs and HNEs in Figure 2.8 A, these predictions suggest HBEs and HNEs transport Cl^- at distinct homeostatic rates in the absence of a Cl^- gradient.

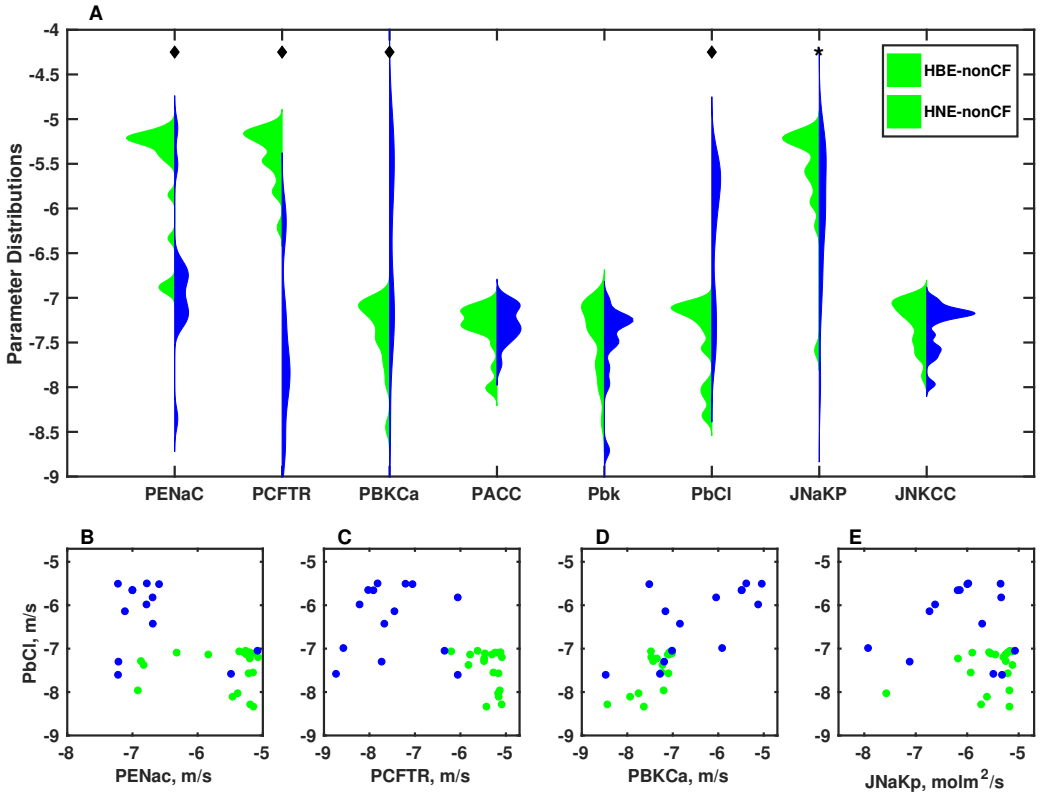

Figure 2.10: Plots summarizing the model-predicted parameter distributions for non-CF HBE (blue) and HNE (green) cell cultures. (A) Split violin plots for predicted distributions for all free parameter in the model. A 2-sample Kolmogorov-Smirnov test was used to compare the predicted distributions for each parameter between the two groups. $*$: $p < 0.05$, $\bullet$: $p < 0.01$. (B-E) Joint parametric scatter plots of the subject-specific, model-predicted parameters that showed statistically significant distributions between non-CF HBEs (blue) and HNEs (green). P_{bCl} vs. (B) P_{ENaC}, (C) P_{CFTR}, (D) P_{BKCa}, or (E) J_{NaKP}. All plots are on a base 10 logarithmic scale to better demonstrate the parametric shift between the two populations.

2.3.2.3 Basolateral Cl^- transport is different between HBEs and HNEs As a way to explore any potential differences in the basolateral Cl^- transport between HBEs and HNEs and attempt to validate model predictions, a series of experiments were designed to explore the role of NKCC in Cl^- intake. UC traces for non-CF HBE and HNE filters (N = 3, n $\geq$ 7) were measured with two different drug addition sequences. For the first set of runs, the addition sequence was as follows: (1) Amiloride (blocks ENaC), (2) Forskolin (stimulates CFTR), (3) CFIhn172 (blocks CFTR), and (4) bumetanide (blocks NKCC). In the second set, Amiloride is still added first, followed by Bumetanide, Forskolin and CFIhn172, in that order. The first sequence represents a fairly standard UC experiment run designed to provides information about the baseline function levels for both cell types. The second addition sequence was designed to explore the ability of the cells to move Cl^- following the inhibition of NKCC Cl^- intake. A graphical summary of this protocol can be found Figure 2.11.

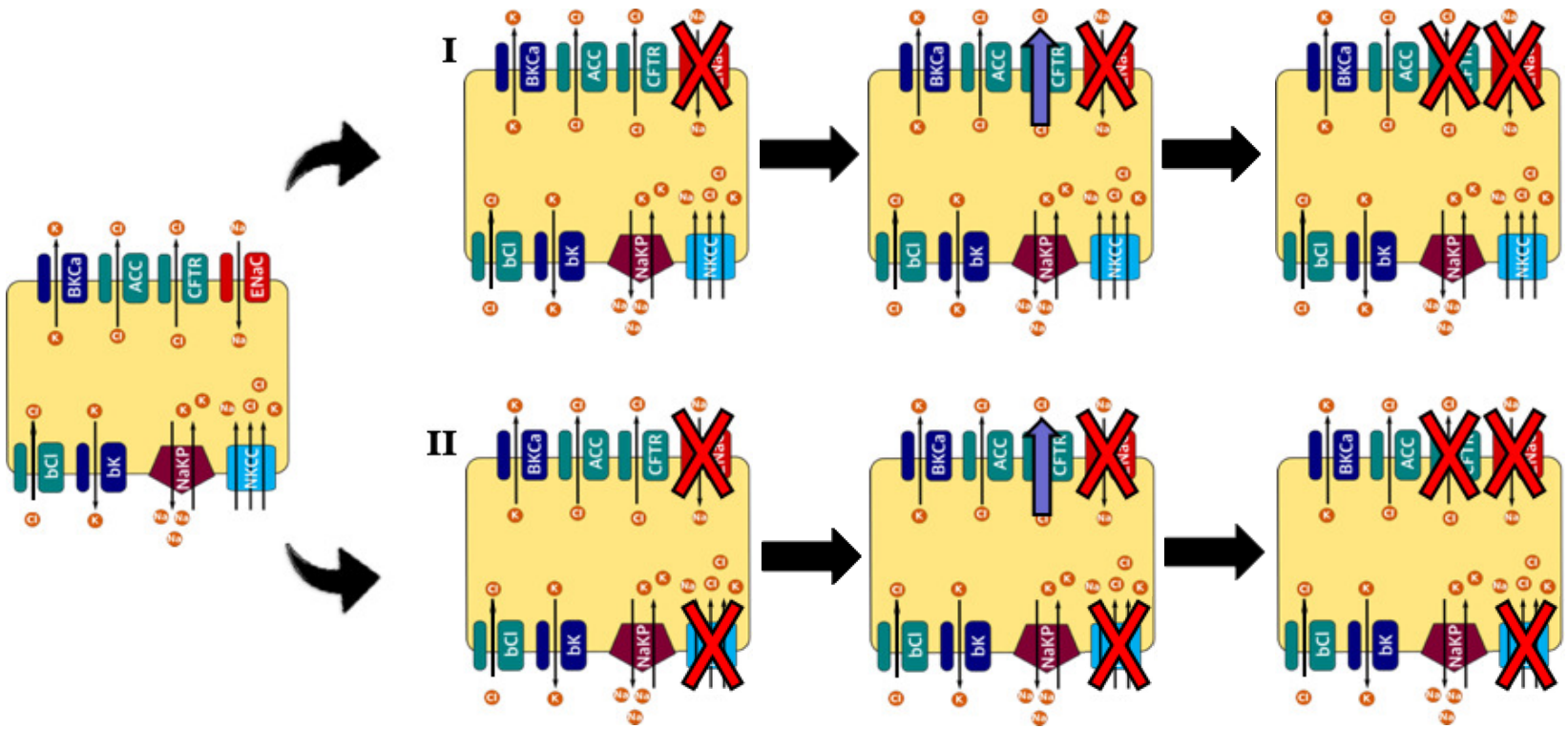

Figure 2.11: Protocol of Experiments to explore the role of the Na^+-K^+-$2Cl^-$ co-transporter in HNE and HBE cell cultures. I. the addition sequence was as follows: (1) Amiloride (blocks ENaC), (2) Forskolin (stimulates CFTR), (3) CFIhn172 (blocks CFTR), and (4) bumetanide (blocks NKCC). II. Amiloride is still added first, followed by Bumetanide, Forskolin and CFIhn172, in that order. The first sequence represents a fairly standard UC experiment run designed to provides information about the baseline function levels for both cell types. The second addition sequence was designed to explore the cells ability to move Cl^- following the inhibition of NKCC Cl^- intake.

Figure 2.12 shows representative I_{SC} traces of non-CF HBE (A, B) and HNE (C, D) for the two conditions listed above, respectively. Comparison between these conditions for the same cell type showed that treatment with Bumetanide prior to the stimulation of CFTR results in significant inhibition of $\Delta I_{Forkolin}$ for both non-CF HBE (-Bumetanide: 18.99±5.30, +Bumetanide: 8.03±1.50; $p = 1.93x10-3$) and HNE cell cultures (-Bumetanide: 9.62 ± 2.06, +Bumetanide: 5.27 ± 1.66, $p = 0.043$). Furthermore, when Bumetanide is added prior to Forskolin, HBE cultures showed a statistically higher mean percent inhibition of $\Delta I_{Forkolin}$ than HNEs relative to baseline $\Delta I_{Forkolin}$ measurements (HBE: $\sim 57.7\%$ vs. HNE: $\sim 45.2\%$, $p = 1.34x10 - 2$). Figure 2.12 E shows bar plots summarizing the mean (± SEM) from $\Delta I_{Forkolin}$ measurements from non-CF HNEs and HBEs under both experimental conditions.

2.3.2.4 Bicarbonate is essential for HNE Cl^- transport In order to further explore the mechanism behind the Cl- transport differences we have described, non-CF HBE and HNE (N = 3, n = 8) UC experiments were run to assess the role that bicarbonate, HCO_3^-, transport has on electrophysiology dynamics. These experiments either included or removed HCO_3^- from the extracellular solutions and used the following drug addition sequence: (1) Amiloride, (2) Bumetanide, (3) Forskolin, (4) CF Ihn172. Figure 2.13 shows representative I_{SC} traces of non-CF HBE (A) and HNE (B) for the two conditions listed above. Comparison between these conditions for the same cell type showed that removing HCO_3^- and blocking NKCC significantly reduces the $\Delta I_{Forkolin}$ and $\Delta I_{CFIhn172}$ relative to baseline measurements in non-CF HNEs ($\Delta I_{Forkolin}$; +HCO_3^-: 1.69±0.65, -HCO_3^-: 0.23±0.05; $p = 2.64x10-4$), but not for their HBE counterparts ($\Delta I_{Forkolin}$; +HCO_3^-: 6.79 ± 2.63, -HCO_3^-: 5.63 ± 0.92; $p = 0.134$) (Figure 2.13 A-D. Similarly, we explored the effect that the addition of Bumetanide and the removal of HCO_3^- has on CF HNE cell cultures treated with a CFTR corrector and potentiator combo. The results showed no meaningful change in $\Delta I_{Forkolin}$ between three conditions tested (-Bumetanide/+ HCO_3^-: 4.01 ± 0.02; +Bumetanide/+ HCO_3^-: 4.61 ± 0.01; +Bumetanide/- HCO_3^-: 5.62 ± 1.42). The addition of Bumetanide or removal of HCO_3^- both effectively abolished $\Delta I_{CFIhn172}$ measurements (-Bumetanide/+ HCO_3^-: -7.94 ± 0.79; +Bumetanide/+ HCO_3^-: -1.28 ± 0.01; +Bumetanide/- HCO_3^-: -1.16 ± 0.03)(Figure 2.14).

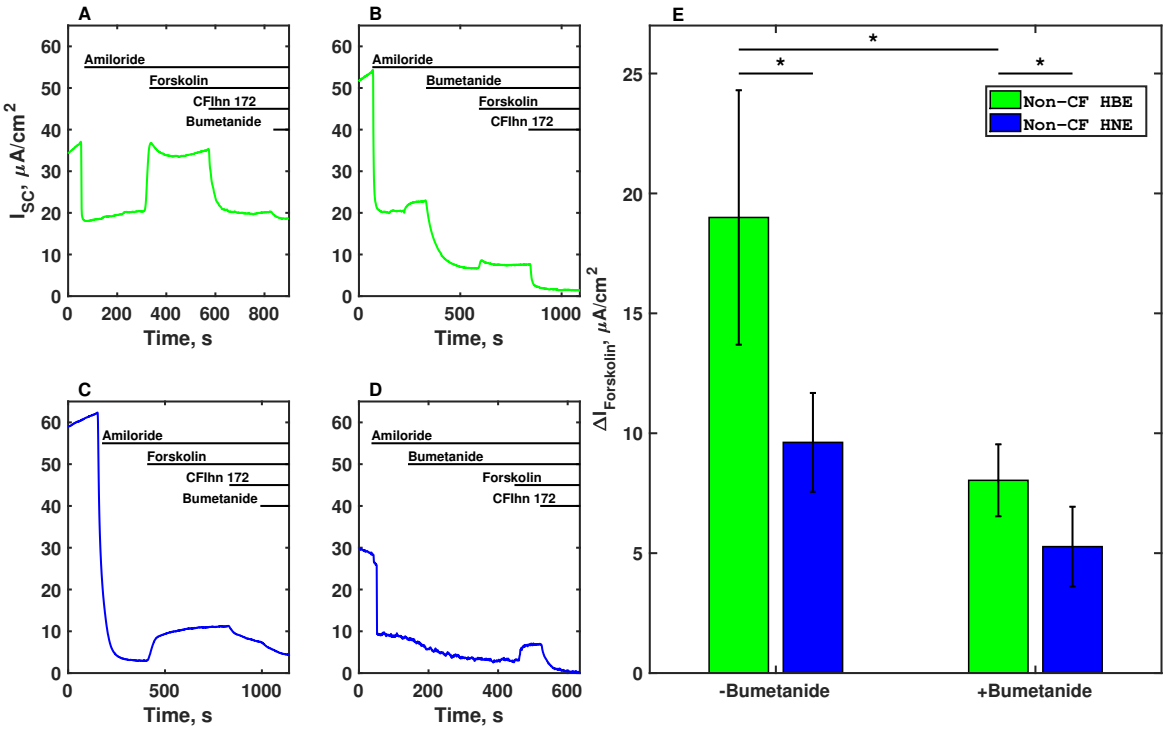

Figure 2.12: Summary of Ussing Chamber experiments designed for validation of model predictions. (A-D): representative short circuit current traces for HBE (A-B) and HNE (C-D) non-CF cell cultures (N = 3, n = 7, per cell type per experiment type). Plots on the left (A, C) were treated acutely with the following pharmacological addition: (1) Amiloride (blocks ENaC), (2) Forskolin (stimulates CFTR), (3) CFIhn172 (blocks CFTR), and (4) Bumetanide (blocks NKCC). Plots on the right (B, D) were treated acutely with the following pharmacological addition: (1) Amiloride (blocks ENaC), (2) bumetanide (blocks NKCC), (3) Forskolin (stimulates CFTR), and (4) CFIhn172 (blocks CFTR). (E) Bar graphs showing measured $\Delta I_{Forskolin}, \mu A/cm^2 (\pm SEM)$ per cell type per addition sequence. Student t-test was used to established statistical significance between the different groups. $* : p < 0.05$.

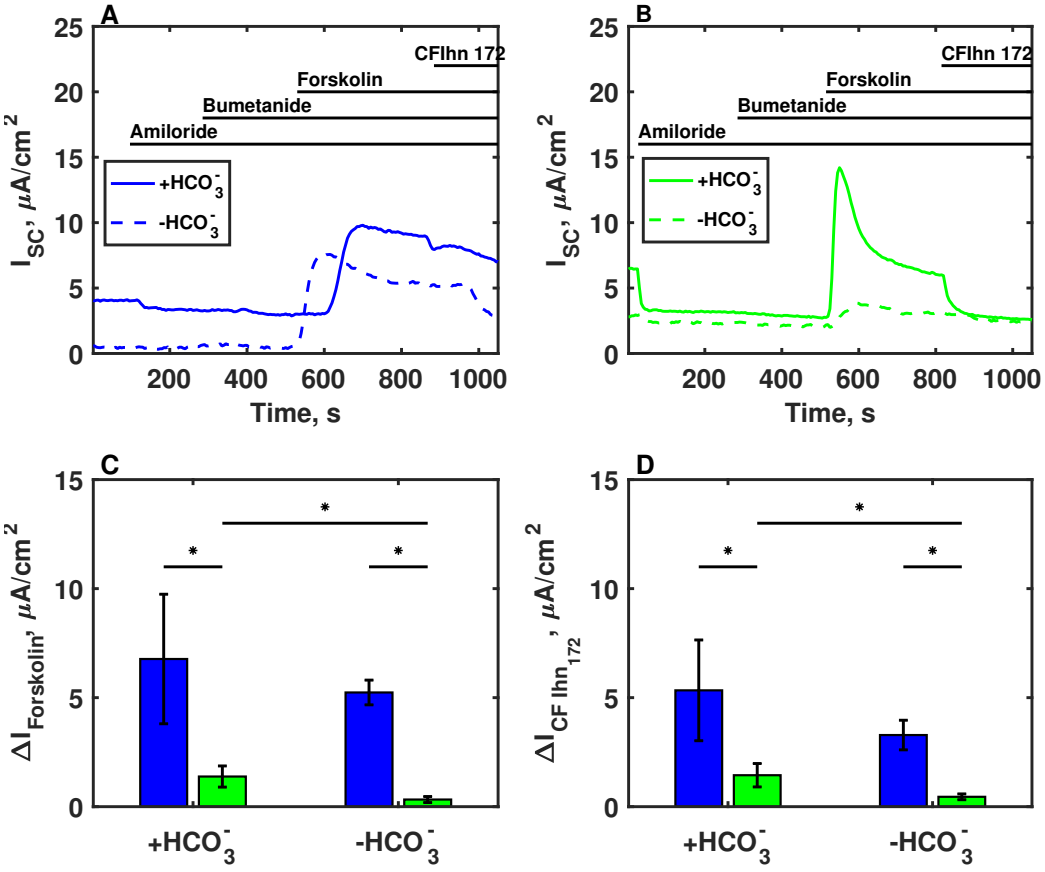

Figure 2.13: Summary of Ussing Chamber experiments to asses effect of bicarbonate ion, HCO_3^-, on airway epithelial Cl- transport. (A) Representative short circuit current traces for non-CF HBE cell cultures. (B) Representative short circuit current traces for non-CF HNE cell cultures. Solid lines represent filters treated with Bumetanide and with HCO_3^- in the extracellular solution. Dashed lines represent filters treated with Bumetanide in the absence of HCO_3^- in the extracellular solution. (C) Bar graphs showing $\Delta I_{Forkolin}$ ($\mu A/cm^2 \pm SEM$) for non-CF HBEs and HNEs measured under the two conditions described above. (E) Bar graphs showing $\Delta I_{CFIhn172}$ ($\mu A/cm^2 \pm SEM$) for non-CF HBEs and HNEs measured under the two conditions described above. Student t-test was used to established statistical significance between the different groups. $* : p < 0.05$. Three different primary lines were used for each experimental condition (N = 3, n = 8).

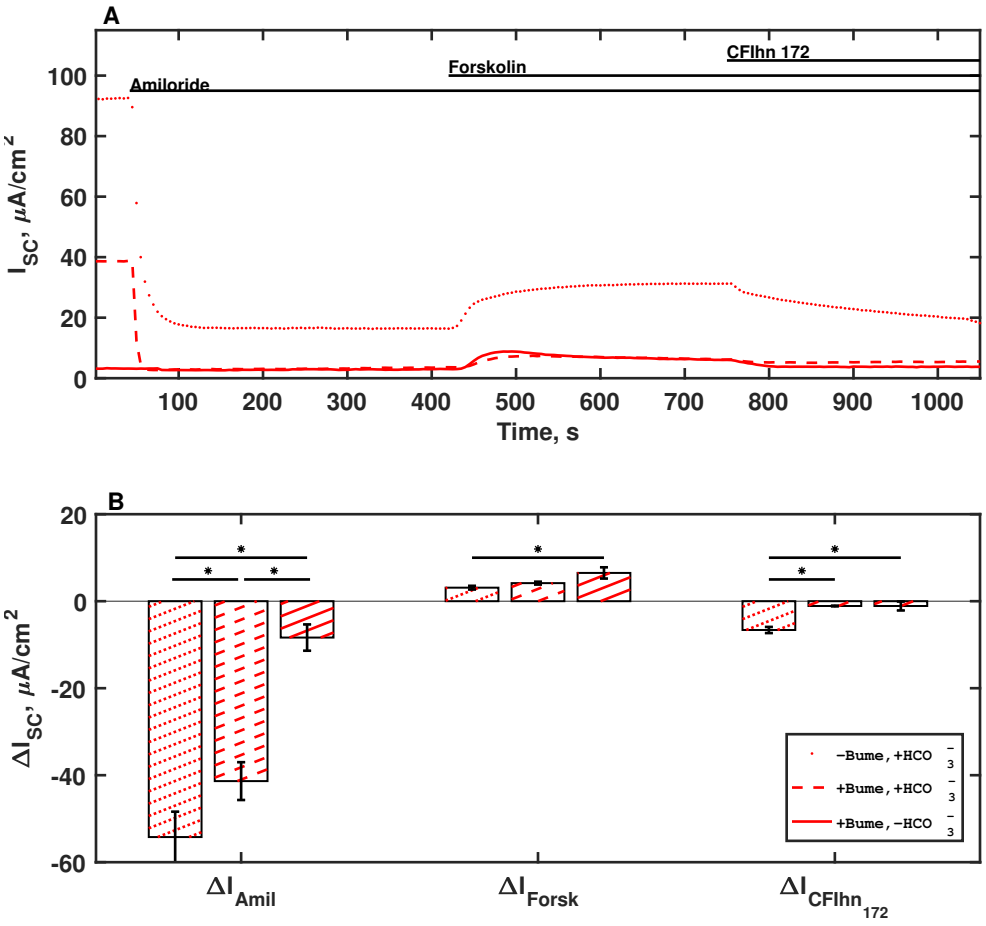

Figure 2.14: Summary of UC experiments to assess effect of Bumetanide treatment and bicarbonate ion, HCO_3^-, on airway epithelial Cl^- transport of primary CF HNE cell cultures. Cell cultures were treated with VX809, a CFTR corrector (10 μM) for 48 hours prior to experiment. Following addition sequence was used: (1) Amiloride, (2) Bumetanide or nothing, (3) Forskolin and VX770 (5 μM, CFTR potentiator), and (4) CFIhn172. (A) Representative I_{SC} traces.Dotted line represents filters with no Bumetanide added and with HCO_3^- present in the extracellular solution. Dashed lines represent filters treated with Bumetanide with HCO_3^- . Solid lines represent filters treated with Bumetanide in the absence of HCO_3^-. (B) Bar graphs showing $\Delta I_{Amiloride}$, $\Delta I_{Forskolin}$, and $\Delta I_{CFIhn172}$ ($\mu A/cm^2 \pm SEM$) measured under the conditions described above. Student t-test was used to compare the different groups. $* : p < 0.05$. Three different primary lines were used per experimental condition (N = 3, n = 7).

2.4 Discussion

HNEs represent a novel and exciting new model for the study of airway physiology and pathologies. This is particularly underscored in a study by Tosoni and colleagues that measured TER, transepithelial voltage, and calculated equivalent currents from 137 pseudostratified HNE cultures from 18 healthy donors [193]. Their study validated the feasibility of HNEs as a platform for common *in vitro* studies performed in other primary epithelial models like HBEs. However, it also found significant inter-patient variability with positively-skewed log normal distributions for all three measurements, suggesting the importance of initial cell line specific baseline measurements as a set point for framing experimental results [193]. In spite of their potential, the extent to which HNE electrophysiology may differ from that of HBE cultures has yet to be fully characterized. Studies on ENaC expression and functional levels in the nasal tissue, as well as the potential clinical relevance of these measurements, serve as a great example. A study that sampled tissue from the airways of patients undergoing a lung lobectomy showed that nasal tissue expressed markedly different mRNA levels of the $\alpha-$ and $\gamma-$subunits of ENaC when compared to bronchial and peripheral lung biopsies [140]. Similar studies have also found that these expression levels are correlated with Benzamil-sensitive NPD measurements and $\Delta I_{Amiloride}$ measured from nasal mucosa tissue samples, *in vivo* and *in vitro* measurements of ENaC function, respectively. This suggests a change in the homeostatic functional levels of ENaC as a function of depth along the airway tree (*i.e.* nasal cavity vs. bronchi) [144, 216].

In an effort to develop a consistent electrophysiological dataset to asses these type of differences, fully differentiated HBE and HNE cultures were used to perform transepithelial short-circuit electrophysiology studies under UC conditions as described previously. Data demonstrated that HNE filters present statistically significant decreases in $\Delta I_{Forskolin}$ and $\Delta I_{Bumatanide}$ with respect to HBE filters under the same conditions. $\Delta I_{Forskolin}$ is a commonly used marker of *in vitro* CFTR function, as well as the common *in vitro* endpoint for CFTR corrector and potentiator efficacy in CF. The concurrent change in both the magnitude of$\Delta I_{Bumetanide}$ and the percent of $\Delta I_{Forskolin}$ inhibited by Bumetanide suggest significant differences in the overall Cl^- transport dynamics exercised by each cell type. In fact, the

observed differences in $I_{Baseline}$ ($p = 0.06$) between the two cell types, while not significant, do support the notion of varied electrophysiology dynamics between the two cell types (Figure 2.8 A, D-E).

In order to further explore these observations, this dataset was used to inform a biophysically inspired model of airway epithelium electrophysiology (Figure 2.1 B). The model accurately recapitulated I_{sc} for all five groups (Figure 2.9 A-E). Interrogation of model mechanisms corroborated the different ionic flux dynamics, particularly an overall reduced transepithelial Cl^- secretion in HNEs. The model predicted a shift in the basolateral Cl^- permeabilities and fluxes between HBEs and HNEs. Specifically, subject-specific parameter sets were used to generate possible parameter distributions for each cell type. These distributions showed a significant decrease in J_{NKCC} and P_{CFTR}, and an increase in P_{bCl} for non-CF HNEs relative to their HBE counterparts (Figure 2.10 A). UC experiments looking at $\Delta I_{Forskolin}$ in the presence or absence of Bumetanide revealed a significantly higher inhibitory effect in HBEs than HNEs (Figure 2.12 A-E), supporting the previously described model findings.

Differences in CFTR function between nasal and lung airways have not been well described and may affect CF pathophysiology. A previous study of CFTR expression and function levels did not find any significant differences in I_{SC} measurements between HNEs and HBEs regardless of CFTR genotype in the presence of a large serosal to mucosal Cl^- gradient [153]. (It is important to note that a Cl^- gradient could induce a saturated transport mechanism, where the increased transport driving force inherently changes the homeostatic behavior of the epithelium.) A separate study that looked at patient-matched, non-CF HBE and HNE cultures found a linear relation between the CFTR-related I_{SC} measurements, but the relation does not appear to follow parity, which possibly indicates distinct functional levels [17]. An earlier study also supports this claim in cultures from donors homozygous for wild-type CFTR but reported TER measurements below $100\Omega cm^2$ for most of their samples [113]. Together these findings support the notion of distinct Cl^- transport dynamics for the nasal and bronchial epithelia.

In order to further explore this possibility, and to identify a possible mechanism behind this shift, we evaluated the effect that pre-Forskolin treatment with Bumetanide, and the

removal of HCO_3^- from the extracellular solution has on HBEs and HNEs UC dynamics. These experiments showed that while HBE cells do show a non-significant decrease in the $\Delta I_{Forskolin}$ and $\Delta I_{CFIhn172}$, relative to baseline, HNEs showed almost no current response to either pharmacological event (Figure 2.13 A-B) in the absence of HCO_3^-. This indicates that HCO_3^- plays a more important role in Cl^- transport in HNEs than HBEs. Together, these findings point to an increase in Cl^- flux linked to HCO_3^- in HNEs relative to baseline levels in HBEs.

Anion (Cl^- and HCO_3^-) transport has been of great interest in the study of airway epithelium, particularly with regards to submucosal glands in bronchi [44]. Single cell and monolayer electrophysiology studies in Calu-3 cells have shown that basolateral transport of HCO_3^- accounts for a large portion of basolateral Cl^- loading and that under voltage clamp conditions the lumen favors the secretion of HCO_3^- as oppose to Cl^- [172, 175]. In fact, similar studies suggest a possible anion exchange mechanism where the simultaneous influx of Na^+ and HCO_3^- through basolateral SLC4A4 (NBC) transporters leads to a corresponding basolateral Cl^- influx and HCO_3^- efflux through SLC4A2 (AE2)[99]. AE2 is a Cl^--HCO_3^- anion exchanger, and NBC is a unidirectional Na^+-HCO_3^- co-transporter; both are believed to be expressed in the airway epithelium [84]. This mechanism has been shown to be serosal Bumetanide insensitive, Forskolin-stimulated, electrogenic, serosal DNDS (a potent inhibitor of NBC) sensitive, serosal Na^+ dependent, and favored under depolarized basolateral potential conditions ($E_{Bl} \approx -40mV$) [44, 175].

Apical permeabilization studies confirmed electrogenicity due to unequivalent Na^+-HCO_3^- intake through NBC, with an estimated 2:1 stoichiometry[99, 175]. Similarly, the stable knock-down of AE2 in the same system abolished Cl^-/HCO_3^- basolateral exchange and increased the fraction of $\Delta I_{Forskolin}$ sensitive to Bumetanide, suggesting a reversal to an NKCC-dominated basolateral Cl^-intake profile [85]. Lastly, activation of basolateral Ca^{2+}-activated CTX-sensitive K^+ channels (hIK) with I-BIO (a sustained intracellular Ca^{2+} stimulant), hyperpolarized the basolateral potential, diminished HCO_3^- intake and increased the fraction of NKCC contribution to basolateral Cl^- intake [18].

Other studies have described similar mechanisms. Murine models deficient for NKCC exhibit a compensatory, HCO_3^--mediated Cl^- transport pathway in both airway and gut ep-

ithelia [44, 65, 204]. Even more relevant is a different study that performed UC measurements under isosmotic and HCO_3^- free conditions on nasal tissue samples obtained from 9 non-CF patients and observed low (less than $2\mu A/cm^2$) I_{SC} measurements following treatment with cAMP and IBMX, commonly used stimulants of CFTR [167]. This further suggests that lack of HCO_3^- may be sufficient to abolish transepithelial Cl^- transport in nasal epithelia.

We hypothesize that the increased basolateral Cl^- flux predicted by the model is linked to AE following a similar electrogenic transport rate through NBC, as the one described above. It is important to mentioned that due to the anion agnostic nature of our model, these types of anion transport would be predicted as an increase in the bCl and CFTR permeabilities (Table 2.2), with a possible decrease of the overall flux through NKCC. This is further confirmed by the decreased in the fraction of $\Delta I_{Forskolin}$ inhibited by Bumetanide in HNEs relative to HBEs and the near total inhibition of $\Delta I_{Amiloride}$ and $\Delta I_{Forskolin}$, following the removal of HCO_3^-, but not following treatment with Bumetanide (in the $\Delta I_{Forskolin}$ case).

CFTR expression and functional levels in HNEs have been linked to several commonly used clinical markers of airway function in CF. More recently, a study found that apical expression levels of CFTR in HNEs correlate to lung disease progression in CF, as measured by %FEV1 [197]. Similarly, HNEs harvested from patients with CF and treated with CFTR correctors and potentiators showed that changes in their $\Delta I_{Forskolin}$ strongly correlates with changes in the Forskolin-stimulated NPD and %FEV1 in patients undergoing analogous treatments [153]. And perhaps more importantly, cells harvested from nasal brushings have been used to identify significant H^+ and HCO_3^- transport rate differences between chronic rhinosinusitis (CRS) patients with and without CF [27].

We also assessed whether treatment with Bumetanide or removal of HCO_3^- affected the response of CF HNEs cell culture CFTR correctors and potentiators in 3 $\Delta F508$ homozygous lines. The results showed that Bumetanide decreased both the $\Delta I_{Forskolin}$ and $\Delta I_{CFIhn172}$ of CF HNEs. However, no meaningful difference was observed between the experiments with and without HCO_3^- (Figure 2.14 A-B). In fact, Bumetanide inhibited all the $\Delta I_{Forskolin}$ when added following the CFTR stimulant, suggesting NKCC dominates basolateral Cl^- intake.

It is possible that the absence of any basolateral Cl^- transport is sufficient to inhibit the action of the correctors, due to limited rescue levels of CFTR relative to wild type levels of

function. However, there have been significant studies that have looked at the effect that CFTR variants have on the relative Cl^- and HCO_3^- permeabilities the channel. Seminal work by Reddy and colleagues, for example, identified distinct Cl^-:HCO_3^- CFTR selectivity in a CF human sweat gland epithelium model [161]. They showed $\Delta F508/R117H$ lost nearly all Cl^- conductance but retained significant HCO_3^- conductance, while $\Delta F508$ homozygous cultures lost both conductances [161]. It should be noted that the latter CFTR variant combination is associated with a low likelihood of causing CF (www.cftr2.org/r117h). Other studies have also showed that CFTR variants can impair HCO_3^- transport by disrupting CFTR regulation through the WNK1-SPAK pathway [101]. Specifically, they showed that loss of HCO_3^- is linked with higher incidence of CRS, pancreatitis and vas deferens abnormalities, even in the absence of CF airway disease [101].

Lastly, and perhaps most relevant, recently presented work by Bridges and colleagues has identified remarkable differences in the ability of correctors to restore HCO_3^- function. Polarized cultures of FRT cells expressing $\Delta F508$ CFTR showed no meaningful difference in $\Delta I_{Forskolin}$ in the presence or absence of a serosal-to-mucosal HCO_3^- gradient. Cells expressing $G551D$ or $S549R$ showed higher response in the presence of the same HCO_3^- gradient, with $G551D$ cells responding nearly as well as when exposed to an equivalent Cl^- gradient [173]. The distinct selectivity and permeability described by different variants could explain the shift from HCO_3^- to NKCC driven basolateral Cl^- transport observed between Non-CF and CF HNEs (Figures2.13 and 2.14). Specifically, the analysis must be expanded to include cultures from a broad range of CFTR variants in order to validate the proposed mechanism. Figure 2.15 summarizes this proposed mechanism. However, more detailed studies are needed in order to fully explore the role that basic electrophysiological differences between HBEs and HNEs can have in the electrophysiological profiles observed in CF HNEs .

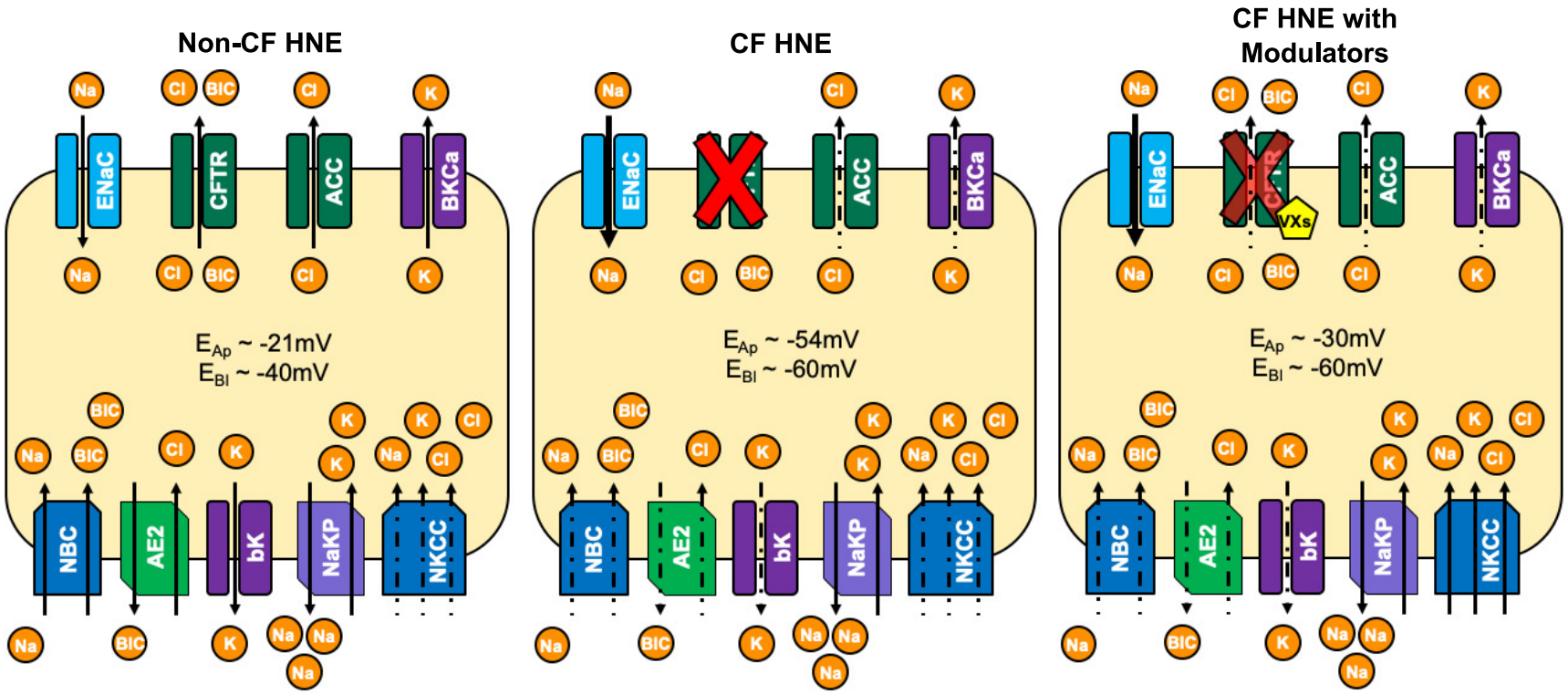

Figure 2.15: Outline of proposed mechanism for anion transport in Non-CF and CF HNEs. Combined results from *in vitro* and *in silico* experiments revealed a possible shift in basolateral anion transport. Non-CF HNEs revealed a HCO_3^--dependent, and Bumetanide insensitive transport profile. CF HNEs treated with a CFTR modulator combination (VX770/VX809) revealed a shift that favors basolateral Cl^- intake through NKCC transport. Model results suggest that this shift could be caused by a change in the transmembrane potential as a result of loss of CFTR function and the indirect effect that it has on other neighboring ion channels.

Similarly, basic UC studies performed on HNE cultures harvested from subjects with a CF carrier genotype (wt/non-wt) showed markedly distinct electrophysiology profiles versus either CF or non-CF HNEs, including lower $I_{Baseline}$,$\Delta I_{Amiloride}$, and $\Delta I_{Forskolin}$ (Figure 2.8 B, Table 2.1). HNE carrier data also yielded distinct model-predicted parameters, with predictions for ENaC, ACC, NKCC and bK trending to values similar to those predicted for CF-subjects, the NaKP flux staying similar to that of non-CF, and values for CFTR and bCl splitting the difference between non-CF and CF predictions (Table2.2). All subjects showed greater than 60% inhibition of $\Delta I_{Forskolin}$ by Bumetanide in the presence of physiological HCO_3^- levels. Once again, this suggests, a possible shift towards a more NKCC-dominated basolateral Cl^- intake than their Non-CF counterparts. It is important to point out that this study only included data from 5 distinct carrier subjects (4 with a Δ F508/wt genotype and 1 with a 2184$insA$/wt genotype).

Previously published studies have found a link between CFTR mutations and incidence of CRS [206]. Another study, specifically found that carriers of a CF-causing mutation have a higher prevalence of CRS than normal [205]. In fact, multiple studies have found links between the incidence of common CF comorbidities like nasal polyps, bronchiectasis, and pancreatitis and CF-causing mutations, even in the absence of a formal CF diagnosis [24, 28, 150, 177]. Together, these suggest an underlying electrophysiological difference between carriers and non-CF individuals that, while not severe enough to cause CF, can disrupt the healthy function of the epithelia. More studies are needed to further explore the extent of any physiological difference and to better understand the link between CFTR mutations and possible clinical manifestations. These studies are currently underway.

3.0 A Quantitative System Pharmacology Model of Cystic Fibrosis Liquid and Solute Transport Dynamics across Primary Human Nasal Epithelia

Cystic Fibrosis (CF) is a life-shortening, autosomal recessive disease caused by mutations in the Cystic Fibrosis Transmembrane Conductance Regulator (CFTR) gene. CF is the most common lethal genetic disorder among Caucasians and occurs at a rate of 1 in every 3,400 births in the United States affecting approximately 70,000 patients worldwide [192]. The CFTR gene codes for an anion channel (also referred to as CFTR) expressed on the mucosal side of the epithelium of multiple organ systems, including the pancreas, intestine, reproductive organs, and airway [142]. Loss of CFTR expression or function results in an osmotic imbalance due to defective ion transport. In the respiratory tract, these conditions cause airway surface liquid (ASL) hyperabsorption, mucus dehydration, and depressed mucociliary clearance (MCC). Mucostasis leads to chronic infection and a sustained and unregulated inflammatory response that causes bronchiectasis and respiratory failure, the leading cause of CF mortality.

Fundamentally, CF is a disease driven by dysregulation of transepithelial ion and water transport. In healthy epithelia, water, ions, and other solutes are transported across the epithelium via paracellular and transcellular mechanisms [190]. Water transport is primarily driven by osmotic forces across tight junctions or through water channels on the plasma membrane of epithelial cells [199]. Ions and some small molecules are transported transcellularly through active or passive fluxes linked to a multitude of ion channels and co-transporters [84]. Solute transport also occurs in the paracellular space, and it is mediated by both diffusive and convective transport [110]. Cl^-, Na^+, and K^+ concentrations are the main determinants of ASL and cellular volume regulation [190, 198]. In CF, deficient or absent CFTR causes decreased Cl^- and $HCO3^-$ secretion [12, 151]. In CF, dysfunctional CFTR or its downstream physiological effects have been shown to either directly or indirectly disrupt the normal functions of multiple known members of the epithelial electrophysiology network, including the epithelial sodium channel (ENaC) [130], the solute carrier family 26 member 9 (SLC26A9) [8], aquaporin 3 (AQP3) [90, 171], and some gap and tight junction

proteins [18, 19]. The combined effect of these disruptions leads to a homeostatic imbalance that favors the hyperabsorption of ASL.

Electrophysiological measurements are taken using an Ussing Chamber (UC) to study ion and liquid transport dynamics at the airway epithelium. The UC allows for the measurement of the whole-membrane, transepithelial short-circuit current, which provides a direct link to ion transport dynamics under conditions where the epithelium interfaces two static, relatively infinite liquid and ion reservoirs. This technique has been particularly useful in CF, where UC recordings are commonly used to study disease pathophysiology and assess the efficacy of novel CFTR modulators [8, 52, 195]. Several mathematical models have been published that explore the electrophysiological dynamics of the airway epithelium under conditions similar to those of the UC, where apical liquid volume far exceeds physiological conditions. These models have either focused on general descriptions of airway epithelia function [54, 62, 135, 136]or explored possible functional differences between CF and non-CF cell cultures [138, 174]. However, the ASL has a much smaller volume under physiological conditions and is often described as a highly dynamic, thin-film volume responsible for epithelial hydration. Thus the conditions assumed in these previous models may limit their applicability to predict ASL dynamics under physiological, or thin film conditions, or those associated with ASL dehydration , a hallmark of CF pathophysiology [30, 32, 110, 120]. More recently, Sandefur et al. published an extended model that accounts for thin-film conditions of the airway and includes cellular regulation through both Ca2+ and purinergic signals over a physiologically-relevant time period [168]. However, it does not account for all paracellular transport mechanisms or provide a meaningful and scalable metric to extrapolate model predictions to clinical measurements.

Here we present a detailed model characterizing the pathways for liquid and solute transport within the CF airway. The model is informed with data generated from primary human nasal epithelial (HNE) cell cultures harvested from subjects who performed concurrent airway function tests. Contributions of both convective and diffusive paracellular transport on epithelial dynamics are described. In particular, the model includes expressions to track the transport of the radiopharmaceutical Technetium 99m-Diethylenetriamine Pentaacetic Acid (Tc-DTPA), an *in vitro* analogue of the in vivo functional imaging probe Indium 111-DTPA

(In-DTPA), which is used to measure small molecule absorption across the airway epithelium [110]. Radiolabeled DTPA can only move through the paracellular pathway, and its absorption rate characterizes paracellular flows and tight junction integrity. Radiolabeled DTPA absorption is increased in the lungs of patients with CF [30, 110, 120], and in primary human bronchial epithelial (HBE) CF cell cultures where it is strongly correlated with ASL absorption [110]. Functional imaging scans measuring In-DTPA absorption were developed with the goal of detecting changes in liquid absorption in the CF airway —a key indication of therapeutic efficacy.

These types of in vitro to in vivo relations are of particular relevance in the study of CF. Primary cell cultures have played an unusually important role in therapeutic development within this disease, which lacks an easily accessible, reliable animal model that can recapitulate human airway physiology, disease pathogenesis, and the genotypic variety observed in humans [102, 170]. Biophysically-inspired computational models can further facilitate this process by providing a physiologically-grounded bridge between novel cell culture based experimental measurements and commonly used clinical indicators of CF pathophysiology and therapeutic efficacy. The work presented here, an *in silico* model that leverages knowledge obtained from a parallel assessment of cell and organ level physiology, serves as a first step in this direction. On a longer timeframe, this can yield a platform where in vitro measurements sets can be used to informed data-driven, validated *in silico* model and generate patient-tailored and phenotype-based analyses of this trans-scale disease.

3.1 Materials and Methods

3.1.1 Cell culture

HNE cells, collected under a protocol approved by the University of Pittsburgh Institutional Review Board (clinicaltrial.gov number NCT02947126), were cultured from samples obtained from minimally-invasive nasal brushings of donors. Donors either had no history of lung disease and who were not carriers of the 144 most common CFTR mutations associated

with CF disease, or had a genetically-confirmed CF diagnosis. In brief, cells were expanded using conditionally reprogrammed cells, allowing for their passaging without loss of quality decline [121, 131]. Following sufficient expansion (80-90% confluency), the cells were seeded onto 0.33-cm2 filters (0.4-m pore size, Corning- Costar Transwell Collagen T-cols, Acton, MA, USA). After 24 hours, apical media was removed, and cell cultures were maintained at an air-liquid interface (ALI) thereafter. Basolateral media was changed 3 times weekly. Filters were maintained for at least 4 weeks under ALI conditions and demonstrated active cilia, an indicator of successful epithelial differentiation, before testing [43, 131]. For more detailed information about the cell culture protocol see **Appendix A**. This study used filters cultured from primary HNE cells from CF (14 subjects, n=36 filters) and non-CF donors (14 subjects, n=48 filters). For a general summary of the subject demographics and basic general experimental results see Table 3.1.

Table 3.1: HNE donor information and summary measurements. This includes in vitro ASL and Tc- DTPA total absorption from healthy donors (wt/wt) and donors with CF (non-wt/non-wt) following either an isotonic or an hypertonic stimuli. Experimental measurements are reported as the percent (%) change over 24 hours . For ASL measurements, a positive values signals a net liquid absorption, and a negative value represents a net liquid secretion over the same time period. Means (± SEM) were calculated from all individual cell cultures from each group. N represents the number of individual primary cell lines used for each experimental set up.

ID	**Group Size**	**Age**	**Sex**	**Genotype**	**Isotonic Ringers**		**Hypertonic Ringers**	
					ASL	**Tc-DTPA**	**ASL**	**Tc-DTPA**
					%± **SEM**	%± **SEM**	%± **SEM**	%± **SEM**
				ΔF508/ΔF508 (4)	N = 14		N = 7	
CF	14	38	M	ΔF598/other (8)	83.2	61.2	-23.4	34.4
		(±7.4)	(8)	other/other (2)	± 0.09	± 8.3	± 10.9	± 6.3
					N = 14		N = 6	
non-CF	14	28	M	wt/wt	64.2	37.5	-110.2	36.5
		(±0.4)	(9)		± 0.06	± 8.1	± 15.2	± 2.9

3.1.2 In vitro ASL and paracellular transport clearance studies

ASL volume and Tc-DTPA apical retention were measured during the 24 h following the addition of 0.01mCi/ml Tc-DTPA in 10 μL of isotonic Ringer's solution (IR) (115 mM NaCl, 25 mM $NaHCO_3$, 5 mM KCl, 10 mM HEPES, 1 mM $MgCl_2$, 1.5 mM $CaCl_2$, and 5 mM glucose) to the apical surface of the HNE cell cultures (Figure 3.1A). Tc-DTPA radioactivity was measured in the ASL and cell layer by removing the filter from the media and briefly placing it in a well counter. Results were decay and background corrected, normalized by starting counts, and fitted to exponential curves to generate clearance rates [30, 110]. Plates containing HNE cells cultures were imaged with an optical scanner (Epson V500, Epson Corporation, Long Beach, CA, USA). ASL volume was measured using a previously described optical method [76]. These images were then analyzed using an image analysis algorithm implemented in ImageJ (https://imagej.nih.gov/ij/, NIH, Bethesda, MD, USA) [76]. The algorithm utilizes the radial refraction patterns induced as transmitted light passes through the meniscus of the ASL layer to predict a liquid volume from an experimentally determined calibration curve. A diagram detailing the experimental setup for these studies can be found in Figure 3.1A. In order to explore the behavior of HNE cell cultures under osmotic stimuli, these studies were also performed following the apical addition of Tc-DTPA in 10μL of hypertonic Ringer's solution (isotonic + 200mM NaCl) (HR).

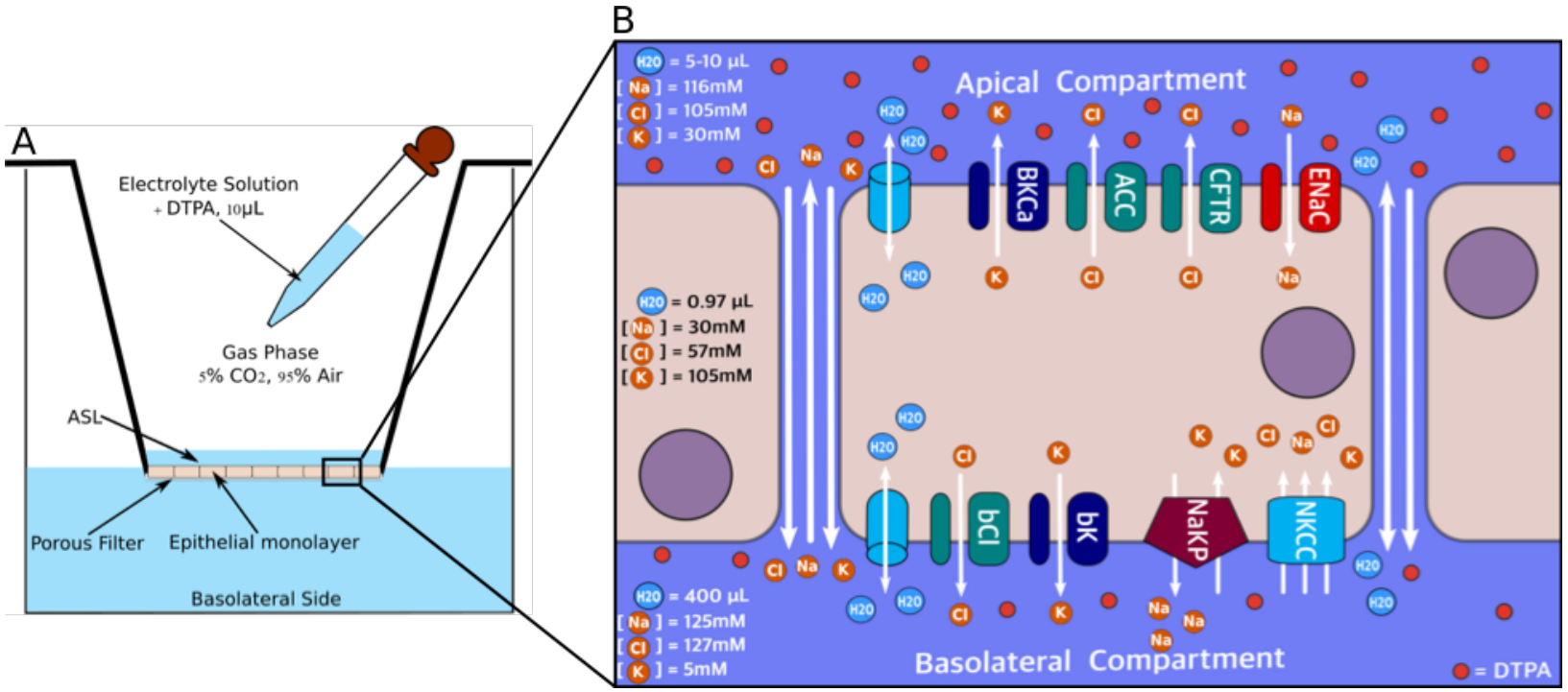

Figure 3.1: (A) Schematic of human nasal epithelial (HNE) cell culture experimental conditions. The HNE membrane was seeded and allowed to differentiate on porous supports in the presence of epithelial differentiation media (basolateral side) and a 5% CO_2/95% O_2 gas mixture (apical side). Membranes naturally develop an ASL volume. At the beginning of the experiments, $10\mu L$ of Ringers solution and Tc-DTPA were added. Tc-DTPA retention (in counts) and ASL volume (in μL) were measured at 0, 2, 4, 6, 8, 12, and 24 h following the volumetric stimulus. The zoomed area (B) shows the major contributors to solute and liquid transport across the airway epithelium represented in the model equations.

3.1.3 Model Structure and Development

Based on the model schematic in Figure 3.1 B, we have developed a system of ordinary differential equations (ODEs) governing liquid and solute transport in HNE cell cultures. HNE cultures are grown at an ALI to mimic physiological conditions in the human airway as closely as possible. In order to accurately describe the dynamic behavior of this system, three compartments are included:

1. the cellular (C) compartment, which accounts for the total intracellular volume across the entire epithelial monolayer ($\sim 0.5 - 1.5\mu L$)
2. the apical (Ap) compartment consisting of the naturally occurring ASL ($\sim 0 - 25\mu L$)
3. the larger basolateral (Bl) compartment, which contains cell culture media ($\sim 400\mu L$)

These compartments interface each other in the transport of water, electrolytes, and other solutes through a complex network of ion channels, transporters, and junction proteins across both the paracellular and transcellular pathways [84]. The model includes mathematical expressions characterizing the different transport mechanisms of water, Na^+, Cl^-, K^+, and Tc-DTPA between all three compartments, as well as the electrical potential across both the apical and basolateral membranes. A compartmental description of the model fluxes and compartments can be found in Figure 3.2.

The model describes the geometry and dimensions of HNE cell cultures based on the assumption that they are composed of cell monolayers, with individual cells having the shape of rectangular prisms adjacent to one another over the entire filter plane. Accordingly, the model definitions of effective surface area for all tight junctions (A_{TJ}), and apical (A_{Ap}) and basolateral (A_{Bl}) membranes are as follows: A_{TJ} is taken to be the cross-sectional area of the total filter area ($A_F = 0.33cm^2$) occupied by tight junctions. A_{Ap} is the remaining part of A_F once A_{TJ} is subtracted. Lastly, A_{Bl} is taken to include both the basal reflection of A_{Ap} and the lateral membrane lining the paracellular space, starting immediately below the tight junctions. Previous work from our lab has shown that when the number of cells in a filter is sufficiently large (as is the case in fully differentiated cell cultures with physiologically-meaningful transepithelial resistance) [119], the following relationship exists:

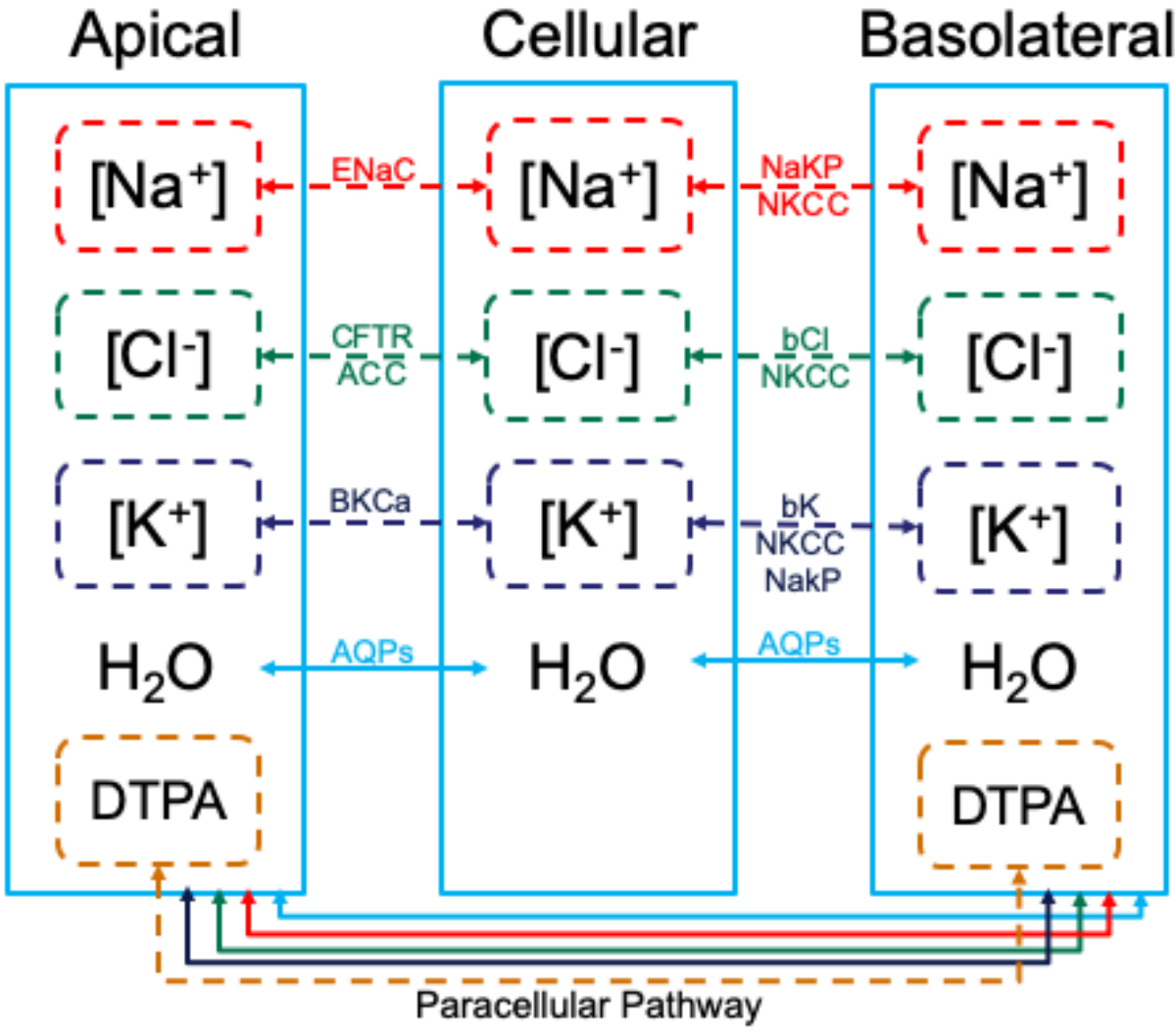

Figure 3.2: Compartmental model diagram that highlights the different pathways that affect transcellular and paracellular solute and fluid transport. Model allows for the apical, basolateral, and cellular volume and electrolyte concentrations to dynamically respond to changes in electroosmotic driving forces (ion channels) and facilitated ion transport (co-transporters). The model also includes paracellular transport of solutes (ions and Tc-DTPA) through both diffusion and convection, and osmotically driven water flux through both the trans- and paracellular pathways.

$$A_{T,J} = A_F \frac{2A_{TJ,1}}{A_{C,1}} \tag{3.1}$$

Here $A_{TJ,1}$ and $A_{C,1}$ are the areas of a single tight junction section and cell, respectively, calculated from tight junctions cross-sectional length (average separation between two individual cells, $L_{TJ} = 60nm$) and a single cell average square face length ($L_C = 8\mu m$) [119]. Initial monolayer volume (V_C) was estimated from cell height (h_c) predictions under the aforementioned geometrical basis and assuming constant total epithelial membrane area [62, 168]. However, V_c, and thus h_c, vary dynamically in response to volumetric and osmotic effects, allowing the monolayer to regulate cellular solute concentration and membrane polarization in response to stimuli [123]. In order to model this behavior, the transport of water between any two compartments ($i \rightarrow j$) is driven solely by osmotic pressure difference, $\Delta\pi_{i,j}$.

$$\Delta\pi_{i,j} = \sum_k \left(\gamma_k \frac{n_{k,i}}{V_i}\right) - \sum_k \left(\gamma_k \frac{n_{k,j}}{V_j}\right) \tag{3.2}$$

In this expression, $n_{k,i}$ is the number of moles of solute, k, which is divided by the volume of compartment i and multiplied by osmotic coefficient γ_k. Volume changes in all compartments can thus be caused by water transport across the paracellular pathway, or either of the epithelial membranes, and can be described as:

$$\frac{dV_i}{dt} = V_m \sum_{i,j \neq i} P^w_{i,j} \Delta\pi_{i,j} \tag{3.3}$$

Here, i refers to any of the three compartments, $P^w_{i,j}$ is the water permeability between compartment i and j, and V_M is the molar volume of water ($0.018\frac{L}{mol}$).

The model accounts for the transport of both ionic (Na^+, Cl^-, K^+) and uncharged (Tc-DTPA) solutes. Tc-DTPA can only move between the Ap and Bl compartments through the paracellular space. All ionic solutes can move both paracellularly and transcellularly. In transcellular flux, ion transport can occur via passive transport through an ion channel

down an electroosmotic gradient, facilitated transport through a co-transporter, or by active transport through ion pumps. For ion channels, the directionality and driving force include both the chemical and electrical components and are defined by Goldman's constant field equation [66]. In the case of transporters and ionic pumps, the molar flux is calculated as a series of Hill terms that modify maximal solute fluxes with predetermined stoichiometry and directionality based on relevant ionic concentrations in the source compartment at any given time [54, 136]. Through model-estimated permeabilities (ion channels) and maximal fluxes (co-transporters), these terms are used to describe the dynamics for each individual transport pathway.

In the paracellular space, we include the transport of solutes through both diffusive and convective means. It is important to note that the model applies the same paracellular transport mechanisms to both ionic and uncharged solutes. With this in mind, we can describe the diffusive (J_{diff}) and convective (J_{conv}) components of paracellular solute transport as follows:

$$J_{diff} = P^{k}_{Ap,Bl} \left[k\right]_{Ap,Bl} \tag{3.4}$$

$$J_{conv} = \left[k\right]_{i} \frac{dV_{Ap \leftrightarrow Bl}}{dt} \tag{3.5}$$

Here, $P^{k}_{Ap,Bl}$ represents the paracellular permeability of solute k, $\Delta[k]_{Ap,Bl}$ and $\frac{dV_{Ap \leftrightarrow Bl}}{dt}$ are the concentration gradient of solute k and the water flux between the Ap and Bl compartments, respectively, as determined by the orientation of $\Delta\pi_{Ap,Bl}$, see Equation 3.2. From these expressions, we can describe a closed system mass balance for any solute, k_i, throughout the three compartments as:

$$\frac{dk_{Ap}}{dt} = -\sum_{Y}^{C,Ap} J_y + J_{diff} + J_{conv} \tag{3.6}$$

$$\frac{dk_{C}}{dt} = \sum_{Y}^{C,Ap} J_y + \sum_{Y}^{C,Bl} J_y + \sum_{L} n_k J_{act,L} \tag{3.7}$$

$$\frac{dk_{Bl}}{dt} = -\sum_{Y}^{C,Bl} J_y - \sum_{L} n_k J_{act,L} - J_{diff} - J_{conv} \tag{3.8}$$

Here, $\frac{dk_i}{dt}$ is the change of solute k in compartment i, $\sum_{Y}^{C,i} J_Y$ is the summation of all the ion channel (Y) fluxes between the C and either the Ap or Bl compartments, and $\sum_L n_k J_{act,L}$ is the summation of any co-transporter (L) flux multiplied by their respective stoichiometric coefficient, n_k. Notice that this last term is only present between the C and Bl compartments due to the lack of significant facilitated or active ion transport between the Ap and C compartments in airway epithelial cells [84]. Individual ionic currents, I_Y, are calculated for all electrogenic ionic fluxes, J_Y, such that the relation between ion flux and current can be described as:

$$I_Y = z_k F J_Y \tag{3.9}$$

Here z_k is the ionic charge of solute k, and F refers to Faradays constant. These currents are used to derive dynamic expressions for the membrane potential across both membranes, such that:

$$\frac{dE_{Ap}}{dt} = C_{Ap}^{-1} A_{Ap} \left(-\sum_{Y}^{Ap} I_Y + \sum_{k}^{P} I_k \right) \tag{3.10}$$

$$\frac{dE_{Bl}}{dt} = C_{Bl}^{-1} A_{Bl} \left(-\sum_{Y}^{Bl} I_Y + \sum_{k}^{P} I_k \right) \tag{3.11}$$

Here E_i and C_i are the either the apical or basolateral membrane potentials and capacitances per area, respectively for compartment i. Where $i \in \{Ap, Bl\}$. Membrane capacitances are considered constants for both membranes, and are based on previously reported values [39].

3.1.4 Parameter Estimation

Model training and estimation of the 15 free parameters in the model were carried out via our affine-invariant ensemble of samplers with parallel tempering Markov Chain Monte Carlo (APT-MCMC) algorithm, a C++-implemented, Python-wrapped parameter optimization tool for systems of ODEs [218]. APT-MCMC is open-source and publicly available online (https://gitlab.com/liangzha/APT-MCMC). APT-MCMC estimates parameter values by leveraging the dynamic nature of MCMC algorithms to sample a user-defined parametric hyperspace. The algorithm deploys distinct, yet parallelly executed, chains of samplers that explore different temperatures or levels of the models objective space. The samplers are implemented to efficiently search regions of highly correlated parametric distributions, a common occurrence in biologically-inspired mathematical models [68]. Each level is defined with varying thermodynamic energies, and permits the inter-chain exchange of information regarding goodness of fit, thus providing information about the breadth and depth of the objective space [70, 83]. APT-MCMC has been successfully implemented for optimization of a clinically-relevant mathematical model of coagulopathies in trauma patients [154].

In our simulations, a logarithmically-transformed sum-of-squared errors objective function (χ^2) was defined between simulation predictions and ASL volume (fitted in mL) and DTPA absorption data (fitted as retention in hundreds of thousands of counts to scale it suitably versus ASL volume), such that:

$$\chi^2(\theta) = \sum_{x=1}^{n} \sum_{p=1}^{m} \sum_{i=1}^{d} \left(\log X^*_{x,p,i} - \log X_x\left(\theta, t_i\right) \right)^2 \tag{3.12}$$

Here, $X^*_{x,p,i}$ refers to the data point recorded for the observable states (ASL or Tc-DTPA) x, for each individual filter for donor p, measured at time point t_i. $X_x(\theta, t_i)$ is the corresponding model-simulated value of each state as predicted by a given parameter set, θ. The objective function was optimized according to equation 3.13.

$$\begin{gathered} \hat{\theta} = argmin\left\{\chi^2(\theta)\right\} \\ s.\ t.\ X_x = f(X, \theta, t, X_0) \\ and\ \theta_{min} \leq \theta \leq \theta_{max} \end{gathered} \tag{3.13}$$

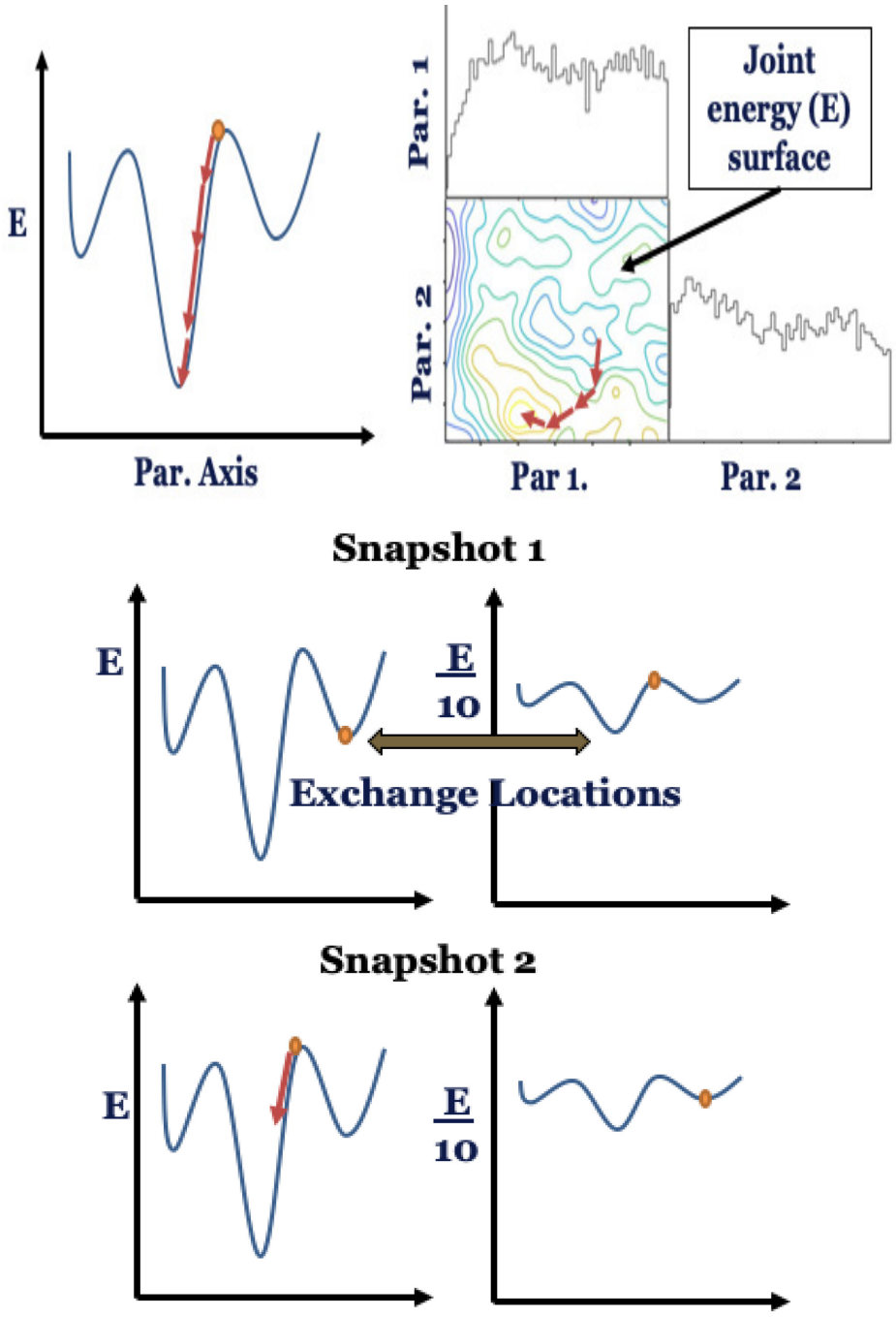

Figure 3.3: APT-MCMC uses Markov Chain Monte Carlo techniques to dynamically sample parameter hyperspace by efficiently searching highly multimodal objective function surfaces (Top). It implements parallel tempering and affine ensemble sampler techniques to allow for breadth and depth of parameter space characterization (bottom). Modified from Zhang, *et al* [218].

Here, $\hat{\theta}$ represents the parameter values that correspond to the identified solution to the optimization problem, f is the user-defined ODE system, θ is the set of free parameters, X and X_0 are the states and their respective initial conditions, and θ_{min} and θ_{max} are the set of lower and upper bounds for all free parameters. It should be noted that predicted parametric distributions do not have a normality condition imposed on them; hence, they should not be analyzed as such. This distinction is due to the multidimensional nature of our parameter set, and to APT-MCMC not requiring a strict statistical prior to all predicted distributions in order to converge. These conditions then necessitate the use of a non-parametric statistical test like 2-sample Kolmogorov-Smirnov to compare distributions between the two population without the need to assume normality.

Since the model is trained with a dataset that primarily informs paracellular fluxes and transcellular water transport, and in an effort to limit exploration within a biologically-meaningful parametric region, parameter ranges for ion channels and transporters were estimated from a the results of the UC of airway epithelial electrophysiology under flooded conditions for both non-CF and CF cell cultures shown in Chapter 2 [174]. A list of all free parameters used in the model, and their respective parametric ranges, can be found in Table 3.2. Constant values for cellular volume regulation, electrolyte-transporter affinities, and other airway epithelial physiology descriptors were obtained from literature and previously published models of human airway electrophysiology [54, 62, 123, 138, 169, 181, 209, 210].

3.2 Results

3.2.1 In vitro ASL and Tc-DTPA transport across healthy and CF HNEs

$10\mu L$ of IR solution and DTPA were added to the apical side of non-CF and CF HNE cell cultures as described in the Methods section and shown in Figure 3.1 A. Data demonstrated that CF cultures had decreased ASL volumes (μL) at the start of the experiment ($t = 0h$) relative to non-CF cultures (10.01 ± 1.38 vs. 15.35 ± 0.95, respectively; $p = 0.0019$ by student

Table 3.2: Model parameters were estimated using APT-MCMC, a separate log-space, non-linear least-squares objective function for each population (Non-CF, CF), as described in section 3.1.4. Model includes 15 free parameters describing ion and water permeabilities through both transcellular and paracellular pathways. The permeability of CFTR was assumed to be negligible in the CF case. $*$: $p < 0.05$ comparing CF to non-CF through Kolmogorov-Smirnov test. Initial ranges for ion channels and transporter permeabilities parametric exploration were based on a previously published model of airway electrophysiology under Ussing Chamber conditions [174].

Parameter	**Units**	**Non-CF**	**CF**	**Axis**	**Definition**
P^*_{wca}	$\mu m/min$	1.41x10^4	3.33x10^4	10200-18000	Water permeability, trans-apical
P^*_{wcb}	$\mu m/min$	1.31x10^4	3.46x10^4	8000-18000	Water permeability, trans-basolateral
P_{wab}	$\mu m/min$	0.97x10^5	1.0x10^5	72000-120000	Water permeability, paracellular
P^*_{ENaC}	$\mu m/min$	2.303	3.359	0.6-6	ENaC permeability
P_{CFTR}	$\mu m/min$	2.209	-	0.6-6	CFTR permeability
P^*_{ACC}	$\mu m/min$	2.584	0.759	0.6-6	ACC permeability
P_{BKCa}	$\mu m/min$	0.862	0.962	0.6-6	BKCa permeability
P_{bK}	$\mu m/min$	4.094	3.312	0.6-6	bK permeability
P_{bCl}	$\mu m/min$	3.597	2.821	0.6-6	bCl permeability
P_{pna}	$\mu m/min$	2.909	3.199	0.6-6	Na^+ paracellular permeability
P_{pcl}	$\mu m/min$	2.597	2.566	0.6-6	Cl^- paracellular permeability
P_{pk}	$\mu m/min$	3.151	3.037	0.6-6	K^+ paracellular permeability
P^*_{pdt}	$\mu m/min$	7.850	8.485	6-10	Tc-DTPA permeability
J_{NKCC}	$mmol/m^2min$	33.51	32.83	6-60	Max NKCC molar flux
J_{NaKP}	$mmol/m^2min$	29.84	30.44	6-60	Max NaKP molar flux

t-test), indicative of the characteristic dehydration of CF ASL (Figure 3.3A). CF samples also showed a significantly depressed ASL volume 24 hours after the initial volumetric challenge (1.68 ± 0.38 vs. 5.49 ± 0.90, respectively; $p = 0.0027$). Percent Tc-DTPA absorption over 24 hours was significantly increased in the CF case relative to non-CF (55.40 ± 3.66 vs. 33.51 ± 3.41, respectively; $p = 7.16x10^{-4}$), as shown in Figure 3.3 B. Previous studies have demonstrated increased rates of DTPA absorption in primary CF HBE cell cultures and in the lungs of CF patients [32, 111, 119]. Previous studies have also shown that there is a strong correlation between ASL volume and Tc-DTPA absorption in non-CF HBE cultures [32]. In an effort to further corroborate these observations in HNE, total ASL and Tc-DTPA absorption were calculated from each subject-specific set of cultures and correlated (Pearsonss r), see Figure 3.3 C. The analysis confirmed that for non-CF cell cultures, ASL volume and Tc-DTPA absorption are strongly correlated ($r = 0.79$). A similar analysis for CF cell cultures showed the breakdown of this relationship due to increased Tc-DTPA clearance.

3.2.2 Transcellular water transport drives Cystic Fibrosis pathophysiology

Model simulations were able to capture the absorption dynamics of the ASL and Tc-DTPA, for both CF and non-CF cell cultures, using identical structure, as shown in Figure 3.5. The model-predicted apical volume and Tc-DTPA trajectories were within the standard error of the mean for all time points in both cases. Population-level parameter distributions were generated for all free parameters listed in Table 2, according to the procedure described in section 3.1.4. Comparisons between the model-predicted distributions of CF and non-CF cultures were performed using a 2-sample, unpaired Kolmogorov-Smirnov (2-KS) test. The model predicts that CF cultures, relative to non-CF cultures, have increased apical (P_{wac}: $3.33x10^{-4}$ vs. $1.41x10^{-4}$, respectively; $p = 4.329x10^{-9}$) and basolateral (P_{wcb}: $3.46x10^{-4}$ vs. $1.31x10^{-4}$, respectively; $p = 7.583x10^{-8}$) water permeabilities (Figure 3.6A, B). On the other hand, paracellular water permeability was similar in CF and non-CF cultures (P_{wab}: $1.02x10^{-5}$ vs. $0.97x10^{-5}$; $p = 0.936$) (Figure 3.5C). These results suggest that transcellular water transport is responsible for the hyperabsorptive phenotype observed in CF cell cultures.

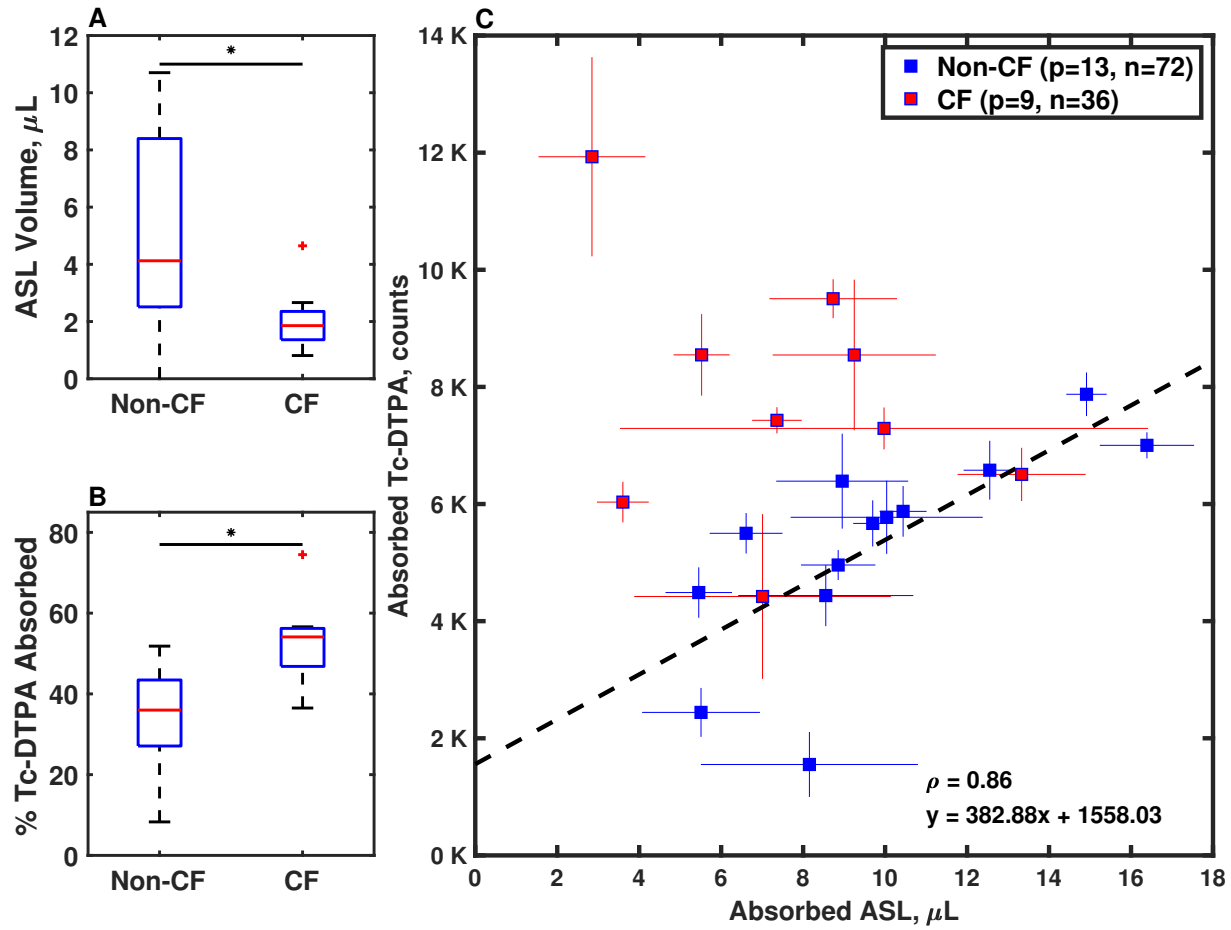

Figure 3.4: Summary of ASL and Tc-DTPA absorption profiles for non-CF and CF HNE cell cultures. (A) Final ASL volume 24 h following the addition of 10 μL of isotonic Ringers solution and Tc-DTPA. CF cultures demonstrated a significantly decreased final ASL volume relative to non-CF cell cultures ($p = 0.0027$). (B) Percent Tc-DTPA absorbed.CF cell cultures had higher Tc-DTPA absorption rates than non-CF cultures ($p = 9.708\text{x}10^{-4}$). (C) Comparison plot showing the relationship between Tc-DTPA absorbed (thousands of counts) and ASL volume absorbed (μL) for both non-CF (13 patients, 72 filters, blue squares) and CF (9 patients, 36 filters, red squares) 24 h after the initial volumetric challenge. The dashed line represents the linear regression for non-CF cultures which shows strong correlation between the measurements. CF cultures show a significant upwards deflection relative to the fitted line, suggesting an increased rate of Tc-DTPA absorption independent of liquid movement (diffusive component). Comparisons by unpaired t-test. Statistical significance is indicated as $*$.

Furthermore, the model predicted a statistically significant increase in the paracellular Tc-DTPA permeability for the CF relative to non-CF groups (P_{pdt}: 8.48 vs.7.85, respectively; $p = 0.0376$; Figure 3.6D). It is important to notice that there is significant overlap between the numerical range of the two distributions. In other words, while the two distributions have distinct shapes, they will lead to similar transport rates on average. This suggests that while it is likely for CF individuals to exhibit higher Tc-DTPA diffusion transport rates than the average non-CF cell culture, the increase is not due to morphological differences (i.e. permeabilities) in the tight junctions of the two populations. This is further confirmed by the lack of any statistical difference in the paracellular permeabilities of the electrolytes (P_{pNa}, P_{pCl}, P_{pK}) predicted between the two groups (Figure 3.7). The model also estimated that CF cultures exhibit significantly increased ENaC permeability, P_{ENaC}, and decreased constitutively active (i.e. not CFTR) chloride channel permeability, P_{ACC}, which correlates to observations from the literature (Figure 3.7) [138, 209].

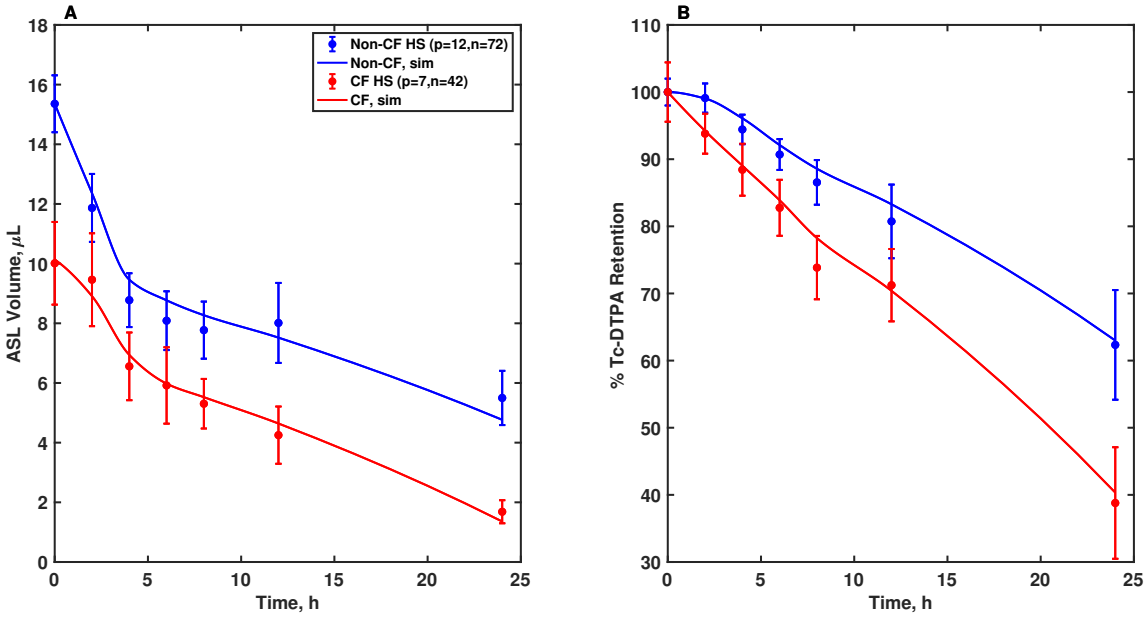

Figure 3.5: Best-fit model trajectories (solid lines) and experimental data (error bars; population mean ± SEM) from HNE cell cultures following the apical addition of $10\mu L$ of Isotonic Ringers with Tc-DTPA to 12 non-CF (72 filters) and 7 CF (42 filters) lines. (A) CF lines have lower ASL volumes than non-CF lines at the start and end of the experiment (p<1x10-4). Total predicted volume absorbed is $9.85 \pm 0.934\mu L$ (64.2%) in the non-CF lines and $8.33 \pm 0.886\mu L$ (83.2%) in the CF lines. Non-CF cells rapidly return to homeostatic ASL volumes ($t = 4-12h$), whereas CF cells exhibit a more prolonged absorption profile. (B) CF cultures displayed consistently higher Tc-DTPA absorption rates ($p < 1\text{x}10^{-4}$) vs. non-CF. Model-estimated DTPA clearance is 37.7% in non-CF cells compared to 61.2% in CF after 24 hrs.

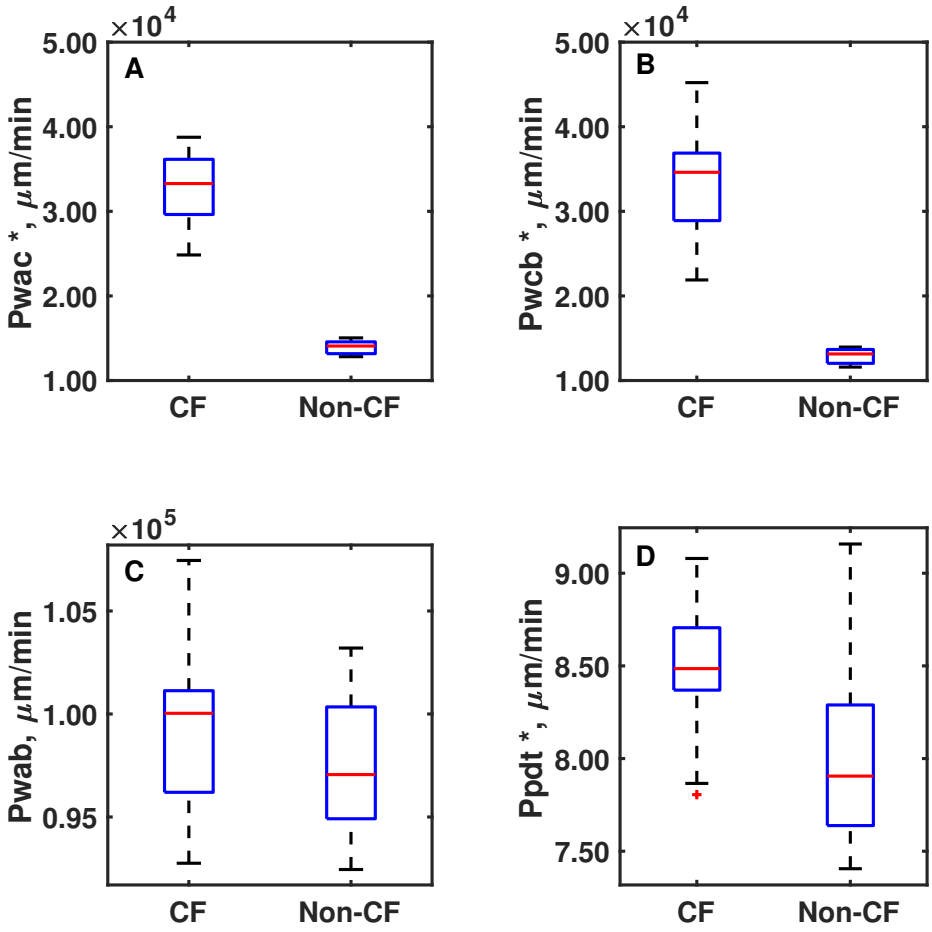

Figure 3.6: Comparison plot of the model-predicted distributions of water permeability (A: apical, B: basolateral, C: paracellular) and DTPA permeability (D) for both CF and non-CF cell cultures. $\star$ denotes significant differences between CF and non-CF distributions by a 2-sample Kolmogorov-Smirnov test. Model predicts that both the apical and basolateral water permeabilities (P_{wac} and P_{wcb}, respectively) are increased in CF cultures vs. non-CF cultures ($p = 4.329\text{x}10^{-9}$ and $p = 7.583\text{x}10^{-8}$). However, paracellular water permeability is similar between the two population ($p = 0.936$). Tc-DTPA permeability is increased in CF ($p = 0.0376$).

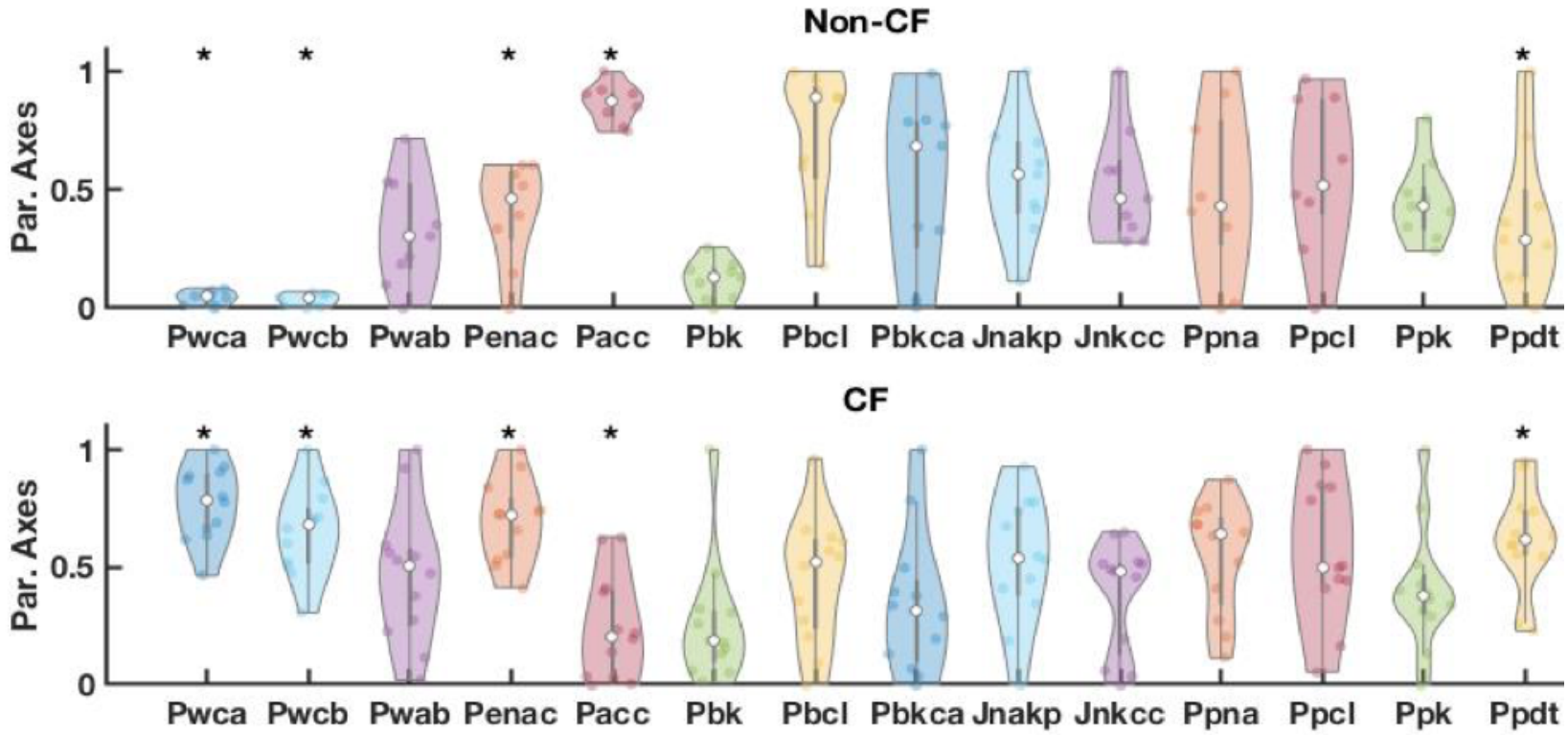

Figure 3.7: Summary plot for all model-generated parametric distributions for both the CF and non-CF groups. Combined distributions' minima and maxima were obtained for each parameter from both groups, and used to generate normalized representations for ease of visualization. Distribution difference between the two groups was determined for each parameter by 2-sample Kolmogorov-Smirnov test, and shown as ($\star$) for parameters with a $p < 0.05$

The predicted parametric distributions will not all necessarily be normal; and therefore, should not be analyzed as such. This distinction is due to the multidimensional nature of our parameter set, and to APT-MCMC not requiring a strict prior to all predicted distributions in order to converge. These conditions then necessitate the use of a non-parametric statistical test like 2-sample Kolmogorov-Smirnov to compare distributions between the two population without the need to assume normality.

3.2.3 Comparison of DTPA Convection and Diffusion

Since Tc- DTPA can only move through the paracellular space, the equation describing apical Tc-DTPA counts ($DTPA_{Ap}$), contains no active or passive flux terms into or out of the cell. Thus, the transport equation reduces to:

$$\frac{dDTPA_{Ap}}{dt} = J_{diff} + J_{conv} = -P_{DTPA_{A,B}} \left(\frac{DTPA_{Ap}}{V_{Ap}} - \frac{DTPA_{Bl}}{V_{Bl}} \right) + \frac{DTPA_{Ap}}{V_{Ap}} \left(\frac{dV_{Ap}}{dt} \right) \tag{3.14}$$

The equation for basolateral Tc-DTPA counts ($DTPA_{Bl}$) has opposite directionality but equivalent structure to Equation 3.14, as the two are linked by a mass balance. Each flux term on the right-hand side of Equation 3.14 was integrated individually for the 100 best parameter sets obtained after fitting. The cumulative percent Tc-DTPA absorbed via diffusion was calculated at every experimentally-measured time point for both CF and non-CF cultures. The model predicts that over a period of 24 hours, CF cultures on average clear 61.9% Tc-DTPA through diffusion, a significantly higher amount when compared to non-CF cultures ($49.7\%, p = 1.034x10^{-4}$; see Figure 3.8). It should be noted that the percent of Tc-DTPA clearance due to convection will simply be the complementary fraction. Thus, the $\sim 40\%$DTPA absorption estimated as due to convection in CF HNE is similar to experimental values previously reported in CF HBE [110].

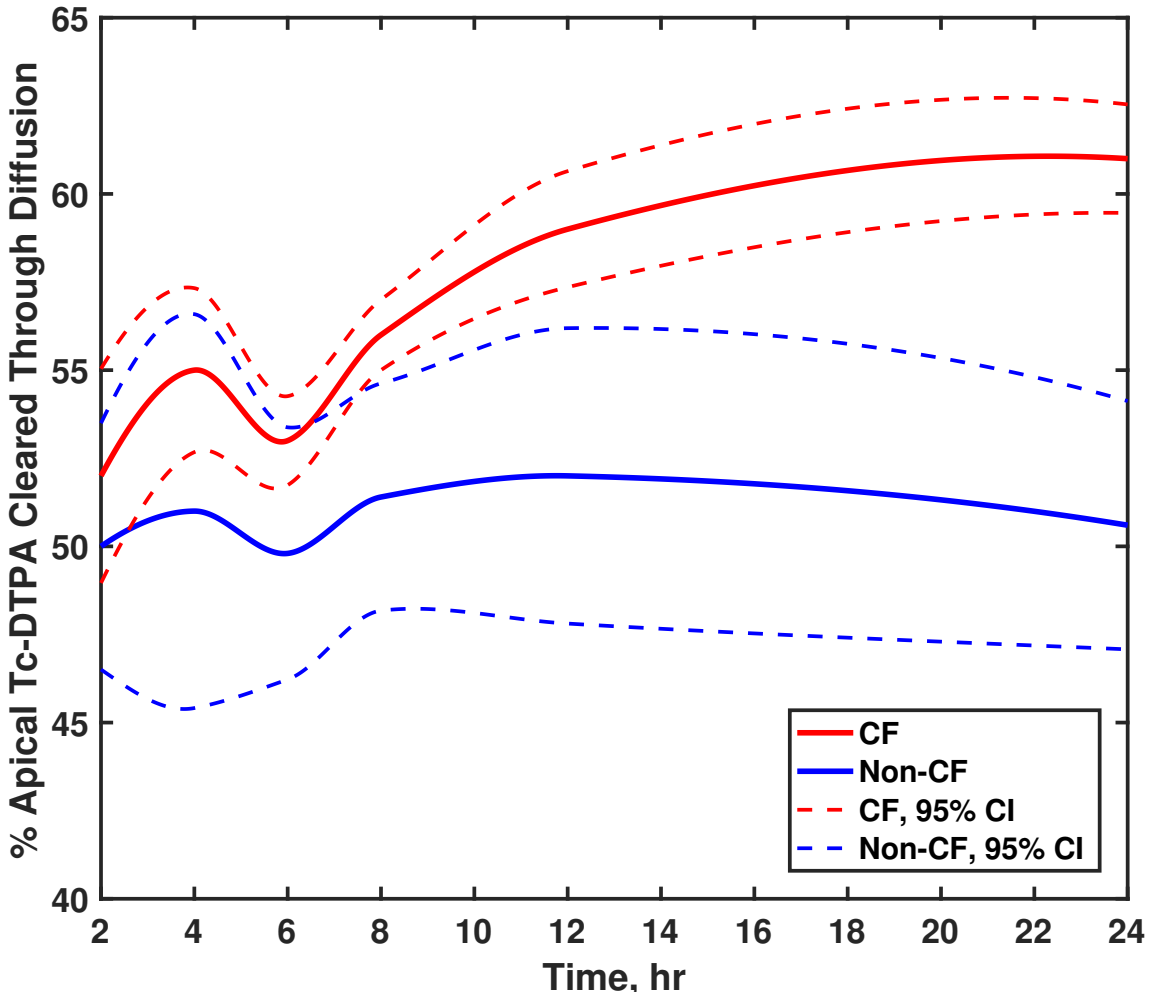

Figure 3.8: Model-predicted percent of Tc- DTPA cleared through diffusion for CF and non-CF HNE cell cultures following the apical addition of $10\mu L$ of isotonic Ringers solutions and Tc-DTPA (diffusion + convection = 100%). Model predicts CF cultures (red) on average clear 61.9% Tc-DTPA through diffusion, a significantly higher amount when compared to non-CF cultures (blue, 50.6%, by student t-test $p = 1.034x10^{-4}$) over a period of $24h$. Solid lines are the mean percent and dashed lines are the 95% confidence intervals. Both measures are calculated from simulations generated from the top 100 parameter sets (based on goodness of fit).

3.2.4 Experimental Validation: Hypertonic Ringers as a Case Study

In order to test the ability of the model to capture different experimental conditions, the model was used to simulate the results from a test data set. The test data set consisted of non-CF (6 subjects, 22 filters) and CF (5 subjects, 22 filters) ASL and Tc-DTPA retention curves over a period of 24 hours following the treatment with HR solution. The increased osmolarity of HR solution, relative to IR, is due to NaCl. Based on its high NaCl proportion, HR may be thought of as a surrogate for hypertonic saline which is a common inhaled osmotic therapy given to CF patients [46]. The addition of HR to both CF and non-CF HNE reverses liquid hyperabsorption, inducing apical volume swelling and arresting paracellular convection of Tc-DTPA. Paracellular diffusion of Tc-DTPA does continue under these circumstances. In the non-CF case, liquid secretion resulted in an initial ASL increase, and peak volume was reached approximately 2 hours into the experiment, after which ASL volume began to be absorbed, possibly re-introducing paracellular convection (Figure 3.9). However, the relatively stable apical Tc-DTPA retention suggests the majority of water transport occurs transcellularly at this stage (Figure 3.9). ASL volume showed minimal changes after 8 hours (Figure 3.9. This implies the observed Tc-DTPA profiles over 8 hours represent a strictly diffusive regime (Figure 3.9). In the CF case, HR also induced epithelial fluid secretion. However, the cultures showed a significantly reduced rate of ASL reabsorption (Figure 3.9). Tc-DTPA absorption rates were diminished and remained statistically similar to corresponding rates in the non-CF case for most of the experiments (Figure 3.9), further suggesting a change in the diffusive driving force for Tc-DTPA.

Validation simulations were carried out by changing *in silico* experimental conditions to match those of the testing data set (initial ASL volume, Tc-DTPA counts and electrolyte concentrations), while keeping parameter sets the same as those estimated from the training data set (IR conditions) for each group. The model demonstrates good agreement between predictions and data, even in the case of ASL volume where transport dynamics are quite different (fluid secretion instead of absorption) relative to the training set. In particular, the model successfully captures the initial rise of ASL volume followed by a slower correction to steady state for both CF and non-CF cultures, as well as the observed increase of apical

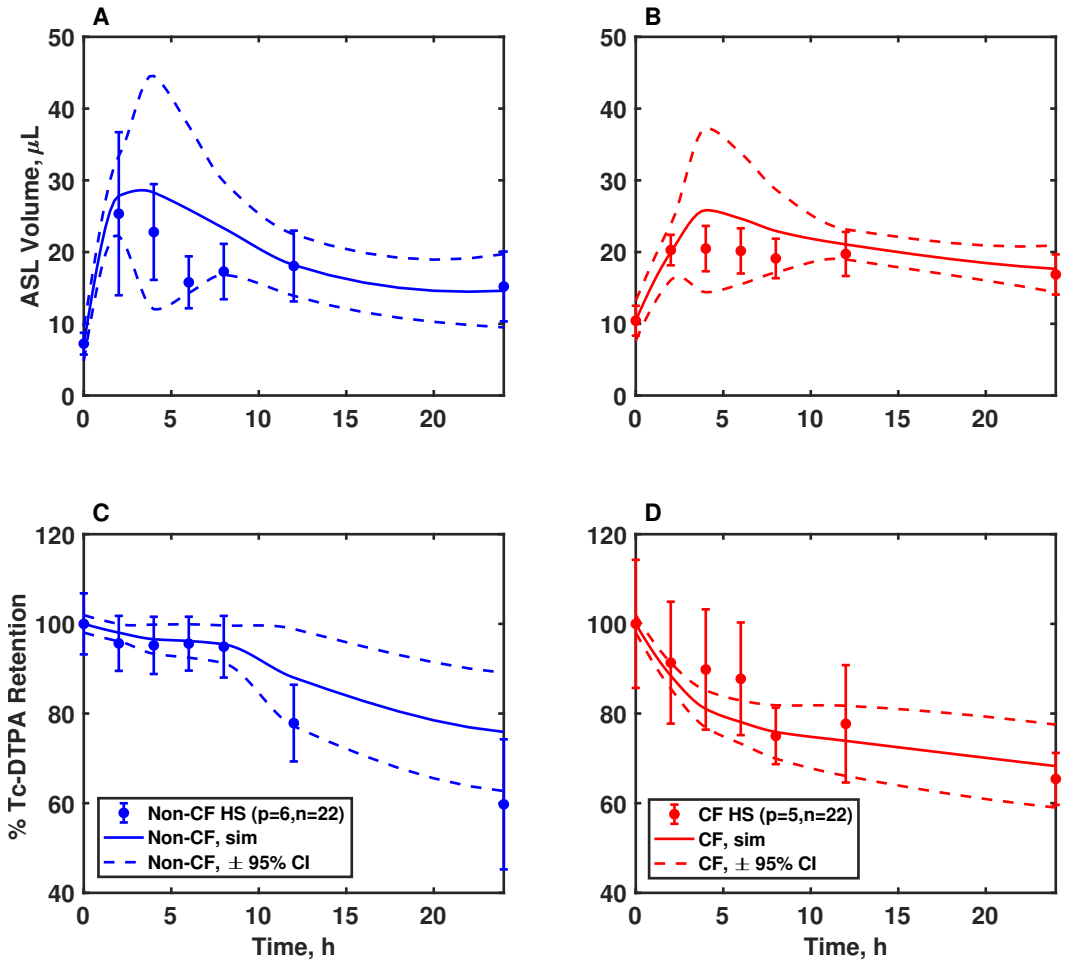

Figure 3.9: Model predictions demonstrate good agreement with experimental data from a validation data set. Testing data was from non-CF (6 patients, 22 filters, blue squares) and CF (5 patients, 22 filters, red squares) cultures and included ASL and Tc-DTPA retention curves following the treatment with HR solution. Validation simulations were carried out by changing *in silico* experimental conditions (initial ASL volume, apical electrolyte/Tc-DTPA concentrations (HR = IR $+200mM$ NaCl)) to match those of the testing dataset, and using the top 100 parameter sets for CF and non-CF groups estimated from the training data set (IR conditions). There is good agreement between model prediction and data, even though transport dynamics are quite different from the training conditions (fluid secretion instead of absorption). In particular, the model successfully captures the initial rise of ASL volume with HR followed by a slower correction to steady state for both CF and non-CF cultures and an observed increase in apical Tc-DTPA retention for CF cultures, relative to the training data set (IR, Figure 3.5). Error bars represent mean experimental data ± SEM.

Tc-DTPA retention for CF cultures. However, the model under-predicts the rate of ASL volume re-absorption immediately following the ASL peak volume (Figure 3.9). The absence or possible delay of this resorptive behavior suggests a possible shift in water permeability as a function of osmotic stimuli in the non-CF and CF cultures that cannot be described without reparametrization. In an effort to validate this we harvested whole cell protein from both CF and Non-CF HNE cell cultures after 0, 4, and 12hr of apical HR treatments (Figure 3.10). The blot revealed an increase in whole cell AQP5 protein expression for both non-CF and CF HNE cultures following osmotic stimuli. This type of response to osmotic stimuli has been observed in other types of epithelial tissues under similar conditions and time frames [77, 220].

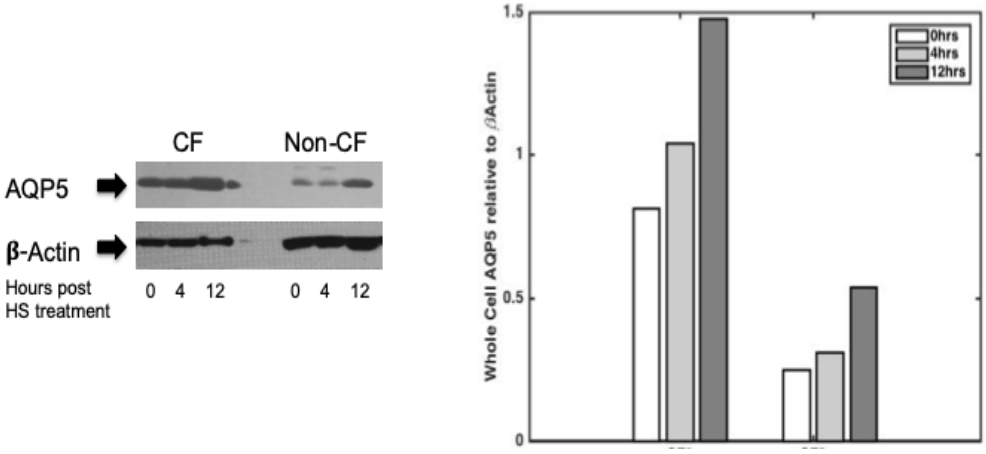

Figure 3.10: (Left) Whole cells western blots obtained from 1 cell line each (6 filters per time point) from the CF and Non-CF HNE groups with no treatment (time zero) and following 4 and 12 hours of apical treatment with hypertonic Ringer's. Blots were probed against AQP5, and β-actin as a reference protein to normalize the results. (Right) Bar plots summarizing the relative changes in whole cell AQP5 protein expression over time.

3.2.5 ASL dehydration drives increased Tc-DTPA transport in CF HNEs

The training data set was used to compare ASL and Tc-DTPA end point behaviors between the IR and HR conditions, thus allowing the verification of model predictions. First,

we compared the percent apical Tc-DTPA cleared 24 hours after the HR osmotic challenge for both CF and non-CF HNE cultures (Figure 3.11A). HR significantly reduced the percent of Tc-DTPA absorption relative to IR in CF cultures ($p = 2.003x10^{-4}$), but HR did not affect Tc-DTPA retention in the non-CF (p=0.934) cultures. Since the bulk of convective flux is stopped under these conditions, we explored changes in the diffusive driving force. In Figure 3.11B, we calculated the fold change in apical Tc-DTPA concentration as a function of time for HR studies relative to the IR studies. In the CF cultures, apical concentration of Tc-DTPA was significantly reduced with HR relative to IR, much more so than for non-CF cultures (maximum fold change: ~ 7 vs. ~ 3, CF vs. non-CF; $p = 1.092x10^{-4}$). This reveals that the observed hyperabsorption of Tc-DTPA in CF cultures (Figure 3.4A) is likely due to depressed apical volume, leading to a consistently higher diffusive driving force relative to non-CF cultures. Lastly, total change in ASL volume and Tc-DTPA absorption were calculated from each donor in the testing data set (HR conditions) and tested for correlation (Figure 3.11C). The analysis revealed the loss of the strong correlation previously observed for non-CF cultures under IR conditions (r=0.09 vs.r=0.86 (Figure 3.11C), p = 0.83). Since the cornerstone of this relationship is the now osmotically depressed convective Tc-DTPA transport, its absence further confirms the amplifying effect that ASL dehydration has on diffusive Tc-DTPA transport in CF cells.

3.3 Discussion

The model presented herein accurately captures ASL and Tc-DTPA dynamics within biologically-meaningful parametric ranges allowing for a mechanistic exploration of the physiological differences between CF and non-CF epithelia. The trajectories also highlight differences in absorption kinetics between the non-CF and CF cultures. Non-CF cells rapidly reabsorbed liquid and return to homeostasis while CF cells demonstrated a slower rate, but longer duration, of liquid absorption that ultimately leads to a decreased standing apical volume. In addition to good dynamic agreement between model output and experimental data, the parameters agreed well with those found in literature. The total epithelium water

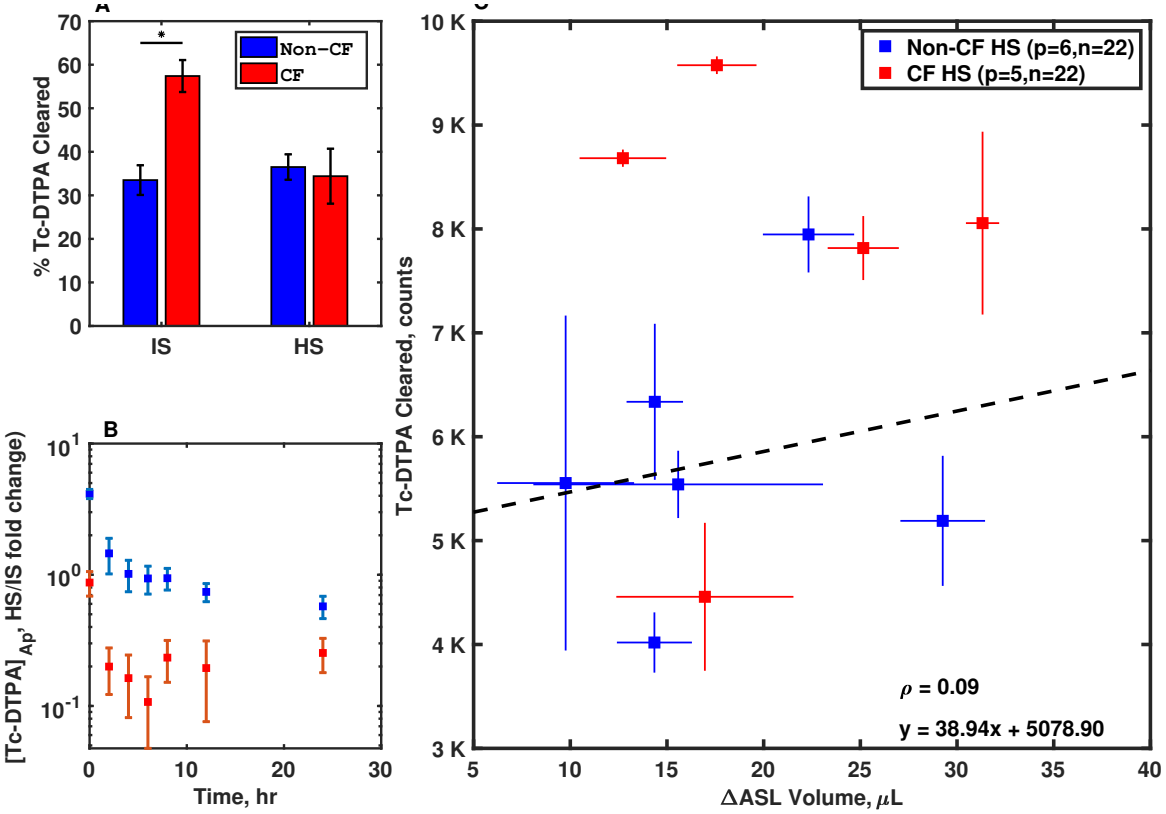

Figure 3.11: Summary of ASL and Tc-DTPA clearance for non-CF and CF HNE cell cultures following the apical addition of $10\mu L$ of Hypertonic Ringers solutions (isotonic +200 NaCl mM) and Tc-DTPA. (A) Percent apical Tc-DTPA cleared 24 h after the HR osmotic challenge for both CF and non-CF HNE cultures. It shows that HR significantly reduces the percent of Tc-DTPA absorbed relative to IR in CF ($p = 2.003x10^{-4}$), but not in non-CF ($p = 0.934$) cultures. Comparisons by unpaired t-test, $*$: $p < 0.05$. (B) Apical Tc-DTPA concentration as a function of time calculated as the fold change in HR relative to the IR. This reveals that the observed hyperabsorption of Tc-DTPA in CF cultures is likely due depressed apical volume, leading to a consistently higher driving force relative to non-CF cultures ($p = 1.092x10^{-4}$). (C) Comparison plot showing the relationship between Tc-DTPA absorbed (thousands of counts) and ASL volume absorbed (μL) for both non-CF (6 patients, 22 filters, blue squares) and CF (5 patients, 22 filters, red squares) at 24 h after the initial osmotic and volumetric challenge. The dashed line represents the linear regression for non-CF cultures. The relationship between ASL and DTPA absorption previously demonstrated with IR (Figure 3.4) is not apparent after HR addition ($r = 0.09$).

permeabilities in both the CF and non-CF cases were similar to those reported by Matsui and colleagues [123].

Because ion transport defects and airway surface liquid dehydration both play key roles in CF lung disease, it is important to be able to characterize liquid and solute transport. Our model demonstrates that the main factor contributing to differences in absorption dynamics between CF and non-CF epithelia are transcellular hydraulic permeabilities (Figure 3.5A, B; Table 2), which it predicts as being nearly 3-fold higher in CF. The model-predicted paracellular hydraulic permeabilities were not significantly increased in CF (Figure 3.5C). This suggests that transcellular permeability has a larger role in the observed decreased ASL volume in CF than paracellular permeability. Our model also corroborates previous reports, both in vitro [32] and *in vivo* [30], that radiolabeled DTPA conjugates absorption is increased in the CF airway. While ASL can be transported through trans- or paracellular pathways, Tc-DTPA can only be cleared paracellularly, either through diffusive or convective transport. Since the convective component of Tc-DTPA absorption is directly driven by ASL absorption, the relationship between Tc-DTPA and ASL absorption can be used to illustrate the relative contributions of convection and diffusion. For example, the increased Tc-DTPA absorption observed in Figure 3.4 C for CF cultures, relative to the non-CF trendline, suggests a Tc-DTPA absorption rate increase that is independent of liquid movement (i.e. through diffusion). Using our mathematical description of Tc-DTPA absorption from the ASL, we are able to probe the relative contributions of diffusion and convection that lead to increased solute absorption in CF. The model predicts that diffusive transport accounts for approximately 60% of all Tc-DTPA absorption seen in CF, a significant increase relative to the 49% predicted for non-CF cells, which is close to experimentally observed values [110]. It is likely that diffusion transport rates are increased in CF due to the decreased initial ASL volume and identical added Tc-DTPA counts in both CF and non-CF experiments. Thus, the concentration, and therefore the diffusive driving force, was slightly increased in CF over the course of the experiments.

Additionally, the model-determined ion channel permeabilities were within parametric ranges previously published in a model of HBE under Ussing Chamber conditions [174]. These model-predicted parameters also corroborate previous results describing the function

of epithelial ion channels. For instance, the model estimated that ENaC permeability is significantly increased in CF cell cultures (Figure **??**), which is in agreement with the findings of previous experimental and modeling studies [138, 209]. Furthermore, the model predicted a significant increase in the constitutively active (i.e. not CFTR) chloride channel permeability in our model, P_{ACC}, in non-CF cell cultures (Figure S1). These results are in line with the findings of Bertrand and colleagues, who have reported that SLC26A9, a constitutively active Cl^- channel expressed in the apical membrane of airway epithelia, shows diminished expression and functional levels in the presence of dysfunctional CFTR [8, 9]. Overall, our model describes hyperabsorptive liquid and solute dynamics in CF that are associated with a loss of CFTR function and the subsequent loss of ENaC flux and decreased constitutive Cl^- transport.

Previous mathematical models of airway epithelia have considered liquid and solute transport in varying degrees of mechanistic detail. The majority of these models have been designed for non-physiological conditions where the extracellular compartment volumes are static. A more recent model includes dynamic apical and basolateral compartments and thin film conditions [168]. These conditions recreate the conditions in the human airway, allowing the modeled epithelium to establish a homeostatic ASL at an air-liquid interface. Our model further accounts for paracellular transport and includes dynamic apical, basolateral, and cellular compartments under thin-film conditions. Airway epithelia are also known to transport solutes beyond Na^+, Cl^-, and K^+ that can play a role in the regulation of ion and liquid transport (e.g., Nucleotides, $HCO3^-$, H^+, Ca^{2+}). However, in an effort to minimize parameter uncertainty and complexity, these were not included herein as explicit model states. Instead, the model is focused on further developing the description of paracellular solute transport. It is recognized that purinergic, pH and Ca^{2+} fluctuations can have meaningful effects on the function of several ion channels, transporters, and consequently, transepithelial water transport or possibly even MCC [47, 63, 103, 221]. However, previously published work also suggests that under baseline conditions (i.e. in the absence of a purinergic/mechanical stimuli) the homeostatic levels of nucleotides and nucleosides are largely unchanged, even in the presence of large ASL volume differences [63]. As a result, we postulate that these signaling dynamics do not play a significant role under conditions

that do not explicitly induce a change in their respective baseline values. As such, they were not explicitly included in the model structure. Rather, our model considers the effects that ASL and cell volume have on regulating solute and liquid flux in an HNE culture system. It is quite possible that both mechanisms (purinergic and volumetric) are related, or a consequence of one another. However, the volumetric effect modeled herein captures the available experimental data in a structurally simple manner.

Our model also includes a more descriptive understanding of paracellular ion fluxes. Current literature describes paracellular ionic transport using Goldmans constant field equation, the same expression used for transcellular ion channel fluxes [62, 168]. This approximation fails to account for the contributions of diffusive transport along the entire paracellular pathway and convective transport due to fluid drag. Previous work from our group has shown that convective transport can account for approximately 50% of Tc-DTPA transport across primary HBE cell cultures [110]. This suggests convection could also play a significant role in the paracellular transport of ionic species. Specifically, we compared predicted paracellular electrolyte fluxes in the electroosmotic versus the combined convection plus diffusion case. Our results suggest that electrical contributions are effectively negligible after the inclusion of convective driving forces (Na^+: $9.83x10^{-9}$ vs. $2.01x10-7$; Cl^-: $8.07x10^{-9}$ vs. $1.81x10^{-7}$; K^+: $9.59x10^{-10}$ vs. $5.18x10^{-8}$; respectively, $mmol/min$). This distinction is particularly important under conditions of non-homeostatic hydraulic flux, such as those following a volumetric or tonicity challenge of the ASL. Our group has previously shown that in HBE cultures, an apical to basolateral osmotic, but not chemical, equilibrium abolished approximately 50% of Tc-DTPA transport in CF HNEs [32]. Furthermore, while electroosmotic transport is likely representative of charged solute transport across the tight junction, it does not account for the effects that the inherent paracellular pathway tortuosity and length of an epithelial membrane are likely to have on the effective solute permeabilities of larger, uncharged molecules such as Tc-DTPA, or the charge selectivity function that some tight junction proteins may exert on ionic solutes [217]. A detailed understanding of the dynamic nature of these effects is a largely underexplored area and could warrant further study.

We validated the model using 6 non-CF and 5 CF cultures from the cell lines included in the training set but exposed to different experimental conditions. Validation testing

was performed by measuring ASL and Tc-DTPA response following the addition of $10\mu L$ of HR with Tc-DTPA to the ASL. Model simulations were carried out using line-specific parameter data obtained during training (IR) experiments. Only initial apical volumes, Tc-DTPA counts, and ionic concentrations were changed to reflect experimental conditions. Model predictions obtained from simulations from the top 100 parameter sets of experimental results recapitulated data within the 95% confidence intervals in both the CF and non-CF cases overall. The model was able to capture the maximum observed ASL volume increase following the osmotic challenge, and the final steady state (Figure 3.9 A). However, the model struggled to recapitulate reabsorption dynamics for non-CF cultures in particular. This may suggest a possible shift in the expression or functional regulation profile of aquaporins as a result of the hyperosmotic challenge. This type of behavior has been observed in epithelial tissues in both the gut and urinary tract [77, 220]. HR reduced the percent of Tc-DTPA absorbed in CF cultures to levels comparable to those of non-CF cultures under IR conditions. A similar shift, however, was not observed in non-CF cultures (Figure 3.11 A). Since ASL absorption was largely abrogated with HR, Tc-DTPA absorption under these conditions is likely caused by diffusion. This is supported by the loss of the correlation between ASL and Tc-DTPA absorption following HR treatment, which is driven by the convective transport (Figure 3.11 C). Further investigation revealed that the reduction in Tc-DTPA absorption observed in CF cultures following HR treatment was primarily driven by changes in apical Tc-DTPA concentration. Because of their increased transcellular water transport, CF cultures experience a higher degree of apical solute dilution ($\sim$ 7-fold change) than non-CF cultures ($\sim$ 2-fold change) under HR conditions relative to IR ones (Figure 3.11 B). The dilution of apical Tc-DTPA leads to a corresponding reduction of chemical driving force. This loss, alongside the higher Tc-DTPA permeability predicted by the model (Figure 3.6 D), results in an abrogated Tc-DTPA diffusive transport rates in CF under hypertonic conditions. This finding is particularly important, because it provides a better mechanistic understanding of radio-labeled DTPA absorption as a biomarker of CF liquid hyperabsorptive phenotype both *in vitro* and *in vivo*.

HR acts as a direct *in vitro* surrogate for hypertonic saline (HS) [110]. Inhaled HS is a vital therapy for patients with CF and is prescribed to approximately 72% of CF patients age

6 or older [38]. Because of its tonicity when inhaled, HS acts as a mucus thinning agent that temporarily rescues the airway hyperabsorption phenotype, promoting MCC [31, 46, 48, 82]. Chronic treatment with inhaled HS has also been linked with higher lung function and reduced rates of pulmonary exacerbation among CF patients [53]. More recently, the FDA has approved the use of inhaled powder mannitol as an alternative osmotic therapy to HS in the treatment of CF patients [8]. Mannitol has a similar mechanism of action to HS, but since it is only transported paracellularly, its residence time in the ASL, and therefore its effective window thought to be prolonged [11, 20, 26, 120, 162]. Due to its similar transport pathways, DTPA transport studies in the airway both *in vitro*, as the ones described here, and *in vivo* are vital in order to understand the dynamics of inhaled osmotic therapeutics. This approach could also be extended to the development of new therapeutics, or the optimization of novel dosing strategies for other categories of inhaled therapeutics, such a bronchodilators and antibiotics, both in CF and other airway pathologies [2, 132].

Ultimately, we envision the development of *in silico* models that are informed by data relating in vitro cell physiology and therapeutic response to *in vivo* organ physiology and therapeutic response, and eventually clinical outcomes. These models could be applied to develop personalized therapeutic strategies for CF patients. They could also provide new parameters for phenotyping CF subjects and a better understanding of the physiological effects of CFTR function and specific genotypes. This notion is particularly relevant because our model is able to track the different modes of liquid and Tc-DTPA transport in HNE cultures grown from cells harvested from specific patients. This connection would suggest the in vitro and *in silico* descriptors of Tc-DTPA dynamics implemented here could correlate with their corresponding In-DTPA absorption (ABS) measurements, a DTPA-based *in vivo* biomarker of airway absorption. Current studies are underway to characterize nasal cell culture physiology, organ level physiology, and clinical outcomes in cohorts of CF subjects, single CFTR mutation Carriers who are parents of CF patients, and healthy controls (NCT02947126), that are intended to inform such models. These studies include nuclear imaging studies to measure mucociliary clearance and ABS in the lungs. We have previously observed and modeled MCC and DTPA absorption in the lungs of subjects with and without CF [110, 111, 120]. These previous studies provide a quantitative and mechanistic

description of ABS, and MCC. Similarly, this work represents a mechanistic description of DTPA and liquid transport that is relevant at a sub-scale of our previous work. Whole-organ model development based on this scan data is ongoing. Ultimately, the multi-scale linkage of *in vitro* models to the whole-organ model, including patient-specific disease mechanism and clinical performance data, will facilitate the design and use of multi-scale models in patient-tailored and population-scale interventions for CF patients.

4.0 A Multi-Scale Study of Cystic Fibrosis Airway Physiology

Therapeutic development is largely dependent on the availability of model systems that can be used to test and optimize therapies ahead of clinical use. The concept of a model can be extended to include studies of human disease that describe both the pathogenic and therapy-related components of a system. Examples of classic biomedical models would include cell-based assays and animal models of disease. These models often need to span multiple spatio-temporal scales in order to accommodate different stages of research, disease progression, and to properly describe changes in pathophysiology through quantifiable biomarkers. However, the transition from cell or animal-based model experimentation to clinically meaningful information is rarely simple, and, in fact, is often not practical due to ethical or logistical limitations.

Multiple physiological processes interact within each of these models. In the case of CF lung disease, these models include networks of interactive elements that work jointly to regulate everything from cellular electrophysiology and epithelial hydration to whole organ absorptive and clearance profiles. These networks tend to inherently be too complex to exhaustively explore experimentally. However, they can be represented through *in silico* models that provide insight into the contribution of individual mechanisms to experimental outcomes. As shown in the previous chapters, this *in silico* approach can be applied to the characterization and validation of experimental models, as well as to identify nuanced, physiologically-meaningful disease mechanisms that are not easily accessible in the lab.

Similarly, linking cellular level mechanisms to organ or system level therapeutic response through mathematically-robust and physiologically-inspired models would allow for enhanced prediction of therapeutic efficacy from *in vitro* studies. This provides novel opportunities for personalized medicine, where cells sampled and cultured from individuals could be used to determine an optimal therapeutic regimen.

4.1 Study design

The study has recruited 20 subjects ages 12 and older with CF (labeled as CF), 12 subjects who are biological parents of the CF subjects and thus are single CFTR mutation carriers (labeled as Carriers), and 14 healthy subjects (labeled as Non-CF). All subjects will undergo a nasal brushing to obtain HNE cells, nuclear imaging studies to measure baseline mucociliary clearance (MCC) and DTPA absorption (ABS) following treatment with inhaled isotonic saline, pulmonary function testing (spirogram), and inert gas washout studies to measure lung clearance index (LCI) and fractional rate clearance (FRC). In addition, CF subjects will undergo a second imaging day including inhalation of an osmotic therapy (7% hypertonic saline) to characterize their therapeutic response. CFTR genotyping was performed in all groups, if not already available. Single mutation carriers were excluded as controls. Table 4.1 provides a detailed summary of the different measurements included in the study for each group. Similarly, Tables 4.2, 4.3, and 4.4 provide summaries of the relevant demographic information for all subjects (Non-CF, Carrier, and CF) enrolled in the study at the time of writing.

It should be noted that one subject from the CF group, CF 7, was removed from the analysis due to lack of genetic confirmation of CF. This subject's genotype includes a CF-causing variation (3849+10kbc>T) and a non-CF causing CFTR variation (R668C), and shows normal levels of sweat Cl^- (13.2 mmol/L). This CFTR variant combination does not lead to the development of CF, based on both clinical evaluations of patients with similar CFTR variant combinations and laboratory experiments performed on this variant as verified through `www.cftr2.org`.

4.1.1 *In vitro* methods and measurements

4.1.1.1 HNE Sampling and Culturing HNE cultures will be developed using previously described methods developed for HBE and HNE cultures. Briefly, cells are detached from epithelial tissue in a protease solution, suspended in epithelial growth media, and initially seeded onto sterile tissue culture flasks pre-coated with human collagen. After several

Table 4.1: Summary of organ-level, cellular level (*in vitro*), and clinical endpoints included in the study protocol. *X* signals a particular measurement will be performed by a respective group.

	Measurement	**Non-CF**	**CF**	**Carriers**
Clinical Endpoints	CFTR Genotype	X	X	X
	Pulmonary Function Test	X	X	X
	Multi-breath Washout Test	X	X	X
	Sweat Chloride	X	X	X
Organ level Physiology	MCC/ABS (baseline)	X	X	X
	MCC/ABS (hypertonic saline)		X	
In vitro level Physiology	Nasal Sampling	X	X	X
	Epithelial Resistance	X	X	X
	Ussing Chamber	X	X	X
	Thin Film Dynamics	X	X	X
	CFTR protein expression	X	X	X

passages, they are seeded onto collagen coated transwell filters at a density of approximately 2×10^6 cells/cm^2. When confluent, the cells are maintained at an air-liquid interface and the differentiation media is added. Cells are allowed to fully differentiate prior to experimentation. For more detailed please refer to **Appendix A**. HNE cultures will be characterized through measurements of: (1) CFTR expression, (2) epithelial electrophysiology, (3) ASL liquid absorption, and (4) paracellular solute (Tc-DTPA) transport.

4.1.1.2 Measurements of CFTR expression in HNE cells Expression and maturation status of CFTR is performed through Western blotting. A minimum of 6 individual cultures are required for sufficient total protein. To harvest proteins, cultures are washed

3x with ice cold PBS, then cells are lysed with addition of RIPA buffer to the apical compartment. The lysate is removed from the culture support and centrifuged at 10,000g for 10 min, then quantified for total protein content. $\sim$100 μg of total protein is subject to SDS-PAGE, transferred to PVDF membrane, and probed with a CFTR primary antibody (CFFT 596). After labeling with secondary antibody and chemiluminescent substrate, total CFTR protein is imaged, and quantified by comparison to total actin protein in the sample. CFTR typically presents at two molecular weights, consistent with an immature form (band B, localized to the endoplasmic reticulum), and a mature form (band C, indicative of complex glycosylation at the plasma membrane). In HBE, the majority of CFTR protein presents as band C in non-CF, and as band B in CF patients harboring the ΔF508 mutation. The ratio of band B to C is a marker of CFTR maturation. However, since some CFTR mutations impact function rather than maturation, functional CFTR expression must be confirmed with electrophysiology.

4.1.1.3 Measurements of epithelial cell electrophysiology Individual cultures are placed in the Ussing chamber with Ringers solution aerated with 5% CO_2-95% O_2 in both apical and basolateral compartments. The culture is continuously short circuited with an automatic voltage clamp. Transepithelial resistance is calculated from the current deflection resulting from a 2-mV pulse applied every $90s$ via an automated pulse generator. Key measurements include Na^+ absorption via the ENaC channel (increased in CF) and Cl^- secretion through CFTR (generally absent in CF), which together establish the primary osmotic gradients driving liquid transport across the epithelium. Amiloride-sensitive Na^+ current is measured by adding $10\mu M$ Amiloride to the apical side of the Ussing chamber. CFTR-associated Cl^- current is measured by first stimulating cAMP production with addition of 10 μM Forskolin to the basolateral chamber, and then by inhibiting basolateral NKCC transport through the addition of $100\mu M$ Bumetanide.

4.1.1.4 Measurements of ASL and Paracellular Solute Transport Rates HNE ASL dynamics were assessed under thin film conditions using an optical meniscus method. Under thin film conditions, the thickness of the meniscus associated with the ASL layer of

an epithelial culture is visible when examining the apical surface of individual cultures. This method utilizes an optical scanner to measure the refraction pattern of transmitted light through that meniscus. Previous studies have demonstrated a robust linear relationship between the AUC of the gray scale light intensity curve generated by the meniscus and ASL volume on the cultures [130]. Absorption rate measurements were made by comparing ASL volume over 24 hours following the addition of 10 μL of Ringer's solution. Measurements of paracellular solute absorption can be performed in parallel to measurements of ASL absorption by adding the radiolabeled small molecule Tc^{99m}-DTPA (Tc-DTPA, $\sim 500Da$) to the Ringers volume challenge. Radioactivity is measured in filters containing the ASL and the cells after removing it briefly from the basolateral media.

4.1.2 *In vivo* Methods and Measurements

4.1.2.1 Functionalized Scans of Airway Absorptive and Clearance Dynamics : This procedure involves the inhalation of a nebulized aerosol containing two radiopharmaceuticals, $Indium^{111}$-DTPA (In-DTPA) and $Technetium^{99m}$ sulfur colloid (Tc-SC). In-DTPA is a small molecule that is cleared from the lungs by mucociliary clearance and absorption while Tc-Sc is a particle probe ($\sim$300 nm) that is cleared only by mucociliary clearance. Tc-SC clearance is used to measure MCC, while the difference in clearance rates between In-DTPA and Tc-SC is used to measure DTPA absorption (ABS). Previous studies have demonstrated a relationship between epithelial DTPA and liquid absorption rates [32]. A very specific breathing pattern is used to deliver the aerosol that provides increased airway deposition rates and measurement repeatability [7]. Subjects are imaged continuously using nuclear medicine gamma cameras that allow for independent tracking of the aerosolized particles for 80 minutes. Use of this dual isotope method is unique to our center [30, 32, 110, 111]. Measurements of MCC using similar methods have received extensive use in CF therapy development [46, 162, 165].

4.1.2.2 Multi-breath Washout (Lung Clearance Index) Single and multi-breath inert gas washout techniques are used to measure of ventilation heterogeneity in the lungs.

The presence of obstructive disease in the airways increases this heterogeneity and is reflected in measurements of exhaled gas concentration versus volume or time, which indicate reduced mixing. Lung clearance index (LCI) is a specific multi-breath measurement representing the number of ventilations required to clear an inert gas from the lungs. It has been shown to predict pulmonary exacerbations and to correlate with validated quality of life assessments [59, 201]. Standardized methods have been established for LCI and devices are available commercially that allow for its measurement [163].

Table 4.2: Summary of the relevant demographic information for all **Non-CF** subjects enrolled in the study. Family ID is an index that relates subjects in the carrier groups with their respective relative in the CF cohort.

ID	**Age**	**Gender**	**Family ID**	**CFTR Allele 1**	**CFTR Allele 2**
NCF 1	23	M	-	wt	wt
NCF 2	20	M	-	wt	wt
NCF 3	20	M	-	wt	wt
NCF 4	20	M	-	wt	wt
NCF 5	22	M	-	wt	wt
NCF 6	23	M	-	wt	wt
NCF 7	23	M	-	wt	wt
NCF 8	22	M	-	wt	wt
NCF 9	20	M	-	wt	wt
NCF 10	25	F	-	wt	wt
NCF 11	22	F	-	wt	wt
NCF 12	23	F	-	wt	wt
NCF 13	21	F	-	wt	wt
NCF 14	19	F	-	wt	wt

Table 4.3: Summary of the relevant demographic information for all **Carrier** subjects enrolled in the study. Family ID is an index that relates subjects in the carrier groups with their respective relative in the CF cohort. CFTR modulator therapy is coded such that: (0) means no CFTR corrector treatment used (True for all Non-CF), (1) means Kalydeco, (2) means Orkambi, and (3) means Symdeko. Sputum Culture is classified such that a positive (+) signals the subject has had a verified *Pseudomonas Aeruginosas* positive sputum or throat culture within 1 year prior to the day of functional airway testing, and a negative (-) signals the complementary situation.

ID	**Age**	**Gender**	**Family ID**	**CFTR Allele 1**	**CFTR Allele 2**	**CFTR Corrector**	**Sputum Culture**
P 1	47	F	1	F508del	wt	0	-
P 2	36	F	2	P574H	wt	0	-
P 3	35	M	3	F508del	wt	0	-
P 4	41	F	4	del exon 22,33	wt	0	-
P 5	48	F	5	F508del	wt	0	-
P 6	47	M	6	F508del	wt	0	-
P 7	48	M	7	F508del	wt	0	-
P 8	72	F	8	F508del	wt	0	-
P 9	73	M	8	F508del	wt	0	-
P 10	64	F	9	F508del	wt	0	-
P 11	53	F	10	F508del	wt	0	-
P 12	56	F	11	2184insA	wt	0	-

Table 4.4: Summary of the relevant demographic information for all **CF** subjects enrolled in the study. Family ID is an index that relates subjects in the carrier groups with their respective relative in the CF cohort. CFTR modulator therapy is coded such that: (0) means no CFTR corrector treatment used, (1) means Kalydeco, (2) means Orkambi, and (3) means Symdeko. Sputum Culture is classified such that a positive (+) signals the subject has had a verified *Pseudomonas Aeruginosas* positive sputum or throat culture within 1 year prior to the day of functional airway testing, and a negative (-) signals the complementary situation.

ID	**Age**	**Gender**	**Family ID**	**CFTR Allele 1**	**CFTR Allele 2**	**CFTR Corrector**	**Sputum Culture**
CF 1	21	M	1	F508del	F508del	2	+
CF 2	15	M	2	P574H	F508del	0	-
CF 3	13	M	3	F508del	N1303K	0	-
CF 4	25	F		c.1585-2A>G	G551D	1	-
CF 5	26	F	4	del e22,33	F508del	0	
CF 6	29	M	5	F508del	S549N	1	+
CF 7	61	F		3849+10kbc>T	R668C	0	-
CF 8	31	M		F508del	del e2,3	0	+
CF 9	24	F		F508del	N1303K	0	-
CF 10	67	M		F508del	D1152H	1	-

Table 4.4 (Continued)

ID	Age	Gender	Family ID	CFTR Allele 1	CFTR Allele 2	CFTR Corrector	Sputum Culture
CF 11	14	F	6	F508del	F508del	2	-
CF 12	39	F		F508del	W1282X	0	+
CF 13	31	F		F508del	F508del	0	+
CF 14	40	M		F508del	F508del	3	+
CF 15	17	M	7	F508del	F508del	3	-
CF 16	21	M		F508del	F508del	2	+
CF 17	25	F	8	F508del	F508del		
CF 18	39	F	9	F508del	F508del	3	+
CF 19	29	F	10	F508del	D579G	0	
CF 20	18	F	11	F508del	2184insA		
CF 21	55	M		F508del	R117H	1	

4.2 Results

4.2.1 Carriers show mild changes in baseline ion and liquid transport function, but no significant respiratory impairment

In order to assess the degree to which subjects in the carrier group differed or resembled both the CF and non-CF groups, we performed Wilcoxon rank sum tests across the three groups for all clinical endpoint measurements, and both *in vivo* and *in vitro* measures of liquid and solute transport. The Wilcoxon rank sum test is a non-parametric test that evaluates the likelihood of the population medians of two independent samples of different sizes to be equal to each other. It is equivalent to a Mann-Whitney U-test.

We first evaluated pulmonary function through the lenses of spirometry and multi-breath washout measurements. Analysis revealed consistently lower pulmonary function assessments for the CF group relative to both the Carrier (CF vs. Carrier; %FEV1: 71.27 ± 6.57 vs. 101.09 ± 4.86, p = 0.0053; FVC: 87.72 ± 5.92 vs. 105.72 ± 3.10, p = 0.0364; $FEF_{25\%-75\%}$: 50.55 ± 9.60 vs. 112.72 ± 18.23, p = 0.003; MBWFRC: 2.07 ± 0.21 vs. 2.83 ± 0.17, p = 0.027, MBWLCI: 9.41 ± 0.8 vs. 7.41 ± 0.26, p = 0.044) and non-CF groups (Non-CF; %FEV1:101.83 ± 3.41, p = 0.0025; FVC: 106.75 ± 3.67, p = 0.0234; $FEF_{25\%-75\%}$: 85.83 ± 6.03, p = 0.005; MBWFRC: 7.16 ± 0.30, p = 0.019, MWBLCI: 7.16 ± 0.30, p = 0.011). All values are shown as percent predicted values ± standard error about the mean. No meaningful difference was observed between the Carrier and Non-CF groups for any of the pulmonary functional tests. These results recapitulate well established differences in pulmonary function between Non-CF and CF individuals, and suggest there is no meaningful signs of airway function impairment in Carriers. However, sweat Cl^- measurements were found to be significantly different among the three different groups (CF: 97.89 ± 4.68, Carrier: 39.81 ± 4.93, Non-CF: 21.62 ± 3.01; CF vs. Non-CF: p = 0.000721; CF vs. Carrier: 0.000279; Carrier vs. Non-CF: 0.0061). A summary of these results can be found in Figure 4.1.

Results from functionalized scans following the inhalation of isotonic saline provide a more nuanced perspective regarding liquid absorption and mucocilliary transport in the air-

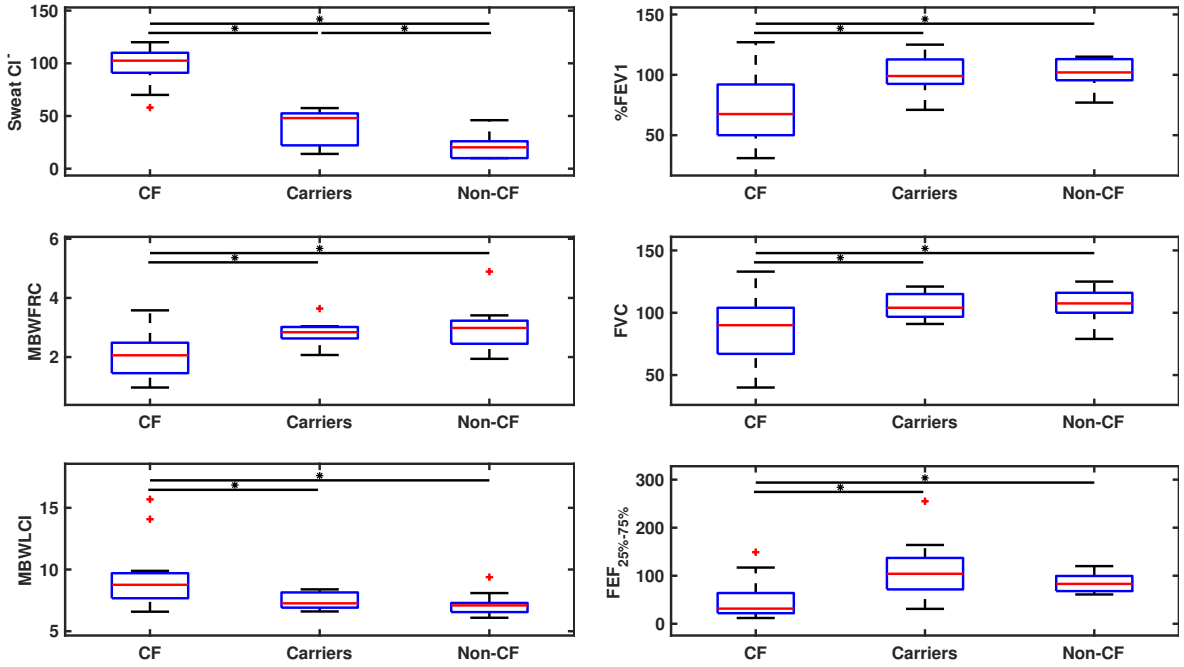

Figure 4.1: Boxplots summarizing the observed differences between the three groups in the study (Non-CF, Carriers, and CF) on the basis of common clinical endpoints used to assess Cystic Fibrosis disease progression and/or therapeutic responses. Left: (Top) Sweat Cl-, (Middle) Multi-breath washout functional residual capacity (MBWFRC), (bottom) Multi-breath washout lung clearance index (MBWLCI). Right: (Top) Percent predicted forced expiratory volume in one second (%FEV1), (Middle) Forced vital capacity (FVC), (Bottom) Forced expiratory flow at $25\% - 75\%$ ($\text{FEF}_{25\%-75\%}$). Red cross signifies a measurement found to be an outlier within its group. Statistical significance was determined through a non-parametric Wilcoxon rank sum test. *: p-values < 0.05.

way. Figure 4.2 shows the distributions for whole, central and peripheral ABS and MCC measurements stratified by subject groups in our study. The CF cohort was modified to exclude subjects that were taking ivacaftor (Kalydeco), ivacaftor/lumacaftor (Orkambi) or ivacaftor/tezacaftro (Symdeko) at the time of the study nuclear scans, to account for any possible effect on ABS measurements [31]. The analysis showed significant differences between CF and non-CF ABS (% ± SEM) levels in the whole lung (CF: 0.27 ± 0.033 vs. non-CF: 0.106 ± 0.043, $p = 0.0083$) and central lung (CF: 0.241 ± 0.038 vs. non-CF: 0.0887 ± 0.057, $p = 0.0425$), while in the peripheral lung it only approaches significance (CF: 0.27 ± 0.052 vs. non-CF: 0.133 ± 0.039, $p = 0.064$). When comparing ABS measurements between Non-CF and Carrier groups, statistical significance was only reached for the peripheral lung (Carrier: 0.254 ± 0.0482, $p = 0.041$). Whole lung (Carrier: 0.236 ± 0.048, $p = 0.072$) and central lung (Carrier: 0.218 ± 0.058, $p = 0.192$) ABS do not reach statistical significance between these two groups. No meaningful difference was observed between CF and Carrier ABS measurements in any of the regions of interest.

MCC measurements (% ± SEM) revealed no statistical difference between any of the groups in any of the regions of interest (Whole Lung; CF: 0.346±0.044; Carrier: 0.342±0.076; Non-CF: 0.250 ± 0.040; Central Lung; CF: 0.357 ± 0.054; Carrier: 0.369 ± 0.082; Non-CF: 0.272±0.055; Non-CF; CF: 0336±0.040; Carrier: 0336±0.060; Non-CF: 0.265±0.032). These analyses also excluded patients currently taking Kalydeco, Orkambi or Symdeko during the imaging day, as well as patients with a Tc^{99m}-Sc percent central deposition above 55 percent, see Figure 4.2. Previous work from our group has shown CF patients with confirmed *Pseudomonas aeruginosa* (PA) cultures have significantly lower MCC rates than CF patients without such a result [31, 111]. In order to further explore this within our study, a CF subset was created by excluding CF subjects without a positive sputum or throat PA culture within 1 year of the imaging day. These exclusion criteria resulted in only 3 CF subjects remaining within the analysis subgroup. However, no meaningful change was identified either. We believe that the relatively small cohort size and the higher percent of subjects under a CFTR modulator may act as confounding factors in these results.

Given the observed difference between the Carriers and CF groups, we wanted to explore whether these trends remain true at the cellular level. We performed ASL and Tc-DTPA

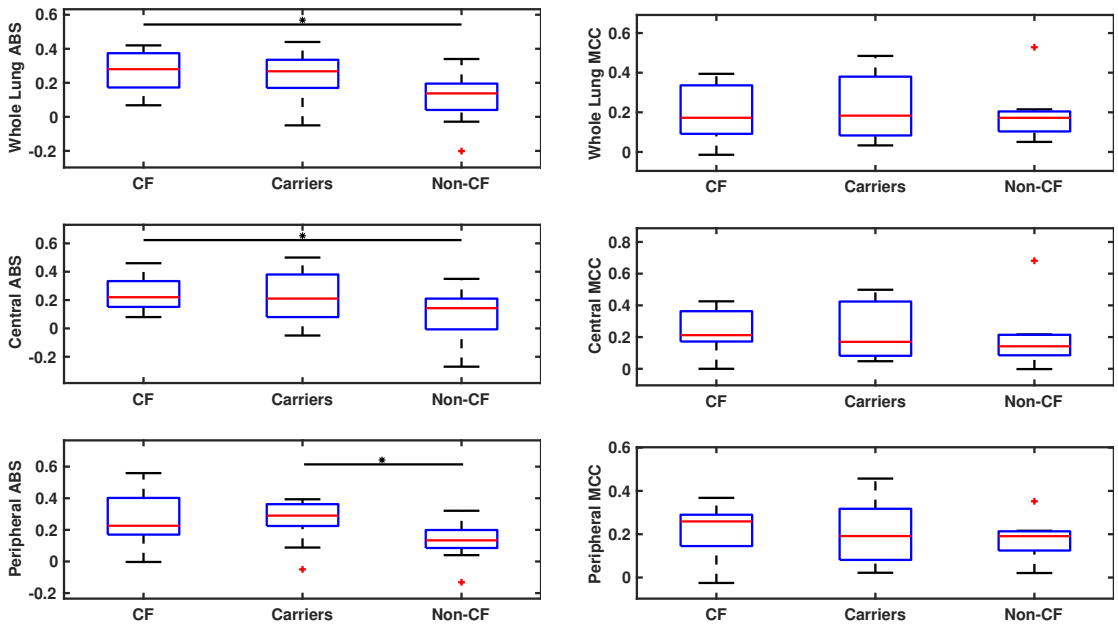

Figure 4.2: Boxplots summarizing the observed differences between the three groups in the study (Non-CF, Carriers, and CF) on the basis of functionalized scans of airway absorptive and clearance dynamics. This procedure involves the inhalation of a nebulized aerosol containing two radiopharmaceuticals, Indium111 DTPA (In-DTPA) and Technetium99m sulfur colloid (Tc-SC). In-DTPA is a small molecule that is cleared from the lungs by mucociliary clearance (MCC) and absorption while Tc-Sc is a particle probe (∼300 nm) that is cleared only by mucociliary clearance. Tc-SC clearance is used to measure MCC while the difference in clearance rates between In-DTPA and Tc-SC is used to measure DTPA absorption (ABS). Left: (Top) whole lung, (Middle) central, and (Bottom) peripheral ABS, respectively. Right: (Top) whole lung, (Middle) central, and (Bottom) peripheral MCC, respectively. Red cross signal a measurement found to be a statistical outlier within its group. Statistical significance was determined through a non-parametric Wilcoxon rank sum test. *: p-values $<$ 0.05.

dynamic experiments in HNE cultures treated with 10 μL of either isotonic Ringer's (IR), or hypertonic Ringer's (HR = IR + 200 mM NaCl) from subjects in all groups. In particular, we calculated the total % Tc-DTPA (± SEM) absorbed over 24 hours ($\%DTPA_{24h}$), the total change in ASL volume (μL ± SEM) over 24 hours (ΔASL_{24h}), and the baseline ASL volume prior to the apical volumetric challenge. This last value was used as a measured of culture quality and baseline control across the different groups and experimental conditions, see Figure 4.3. No differences were observed between any of the groups for the baseline ASL volume. CF cultures were found to be slightly drier than either the Carrier or Non-CF groups in both the isotonic (CF: -3.139 ± 0.571; Carrier: 1.434 ± 2.257; Non-CF: 0.165 ± 1.157) and the hypertonic cases (CF: -2.451 ± 0.878; Carrier: −1.033 ± 1.619; Non-CF: −3.319 ± 2.751).

Isotonic experiments also showed an increase in $\%DTPA_{24h}$ for CF HNE cultures relative to the Non-CF group (CF: 50.84 ± 2.283 vs. Non-CF: 33.51 ± 3.414, p = 0.000381), but no change was observed between the Carrier group and either the CF or Non-CF groups (Carrier: 37.68 ± 9.05; Carrier vs CF: p = 0.1623; Carrier vs. Non-CF: p = 0.6816) (Figure 4.3). The results suggest that Carriers show a much broader variance than the other groups, and effectively "split the difference" between healthy and CF. This is further supported by the results from the hypertonic experiments. HR treatment of the three groups showed no change in the $\%DTPA_{24h}$ between the three groups (CF: 33.38 ± 2.28; Carrier: 21.21 ± 5.72; Non-CF: 32.50 ± 2.77). However, HR was able to significantly reduce $\%DTPA_{24h}$ when comparing the CF (∼34%, p = 0.0034) and Carrier (∼44%, p = 0.0061) groups across the two experimental conditions. No meaningful change was observed in $\%DTPA_{24h}$ for the Non-CF group between the two groups (p = 0.894) (Figure 4.3). This suggests that at the cellular level, cultures derived from carriers of a single CFTR-causing mutation present a similar, yet milder, version of the liquid transport defect observed for CF cellular cultures, as described in Chapter 3.

In order to further inform these findings, we also measured ASL_{24h} for all groups under both IR and HR conditions. For these measurements, it should be mentioned that IR tends to promote an absorptive phenotype, while HR promotes a secretory phenotype due to reversal of the transepithelial osmotic gradient. IR experiments showed Carriers reached similar ASL volume to Non-CF samples after 24 hours (Carriers: 5.63 ± 1.719 vs. Non-CF:

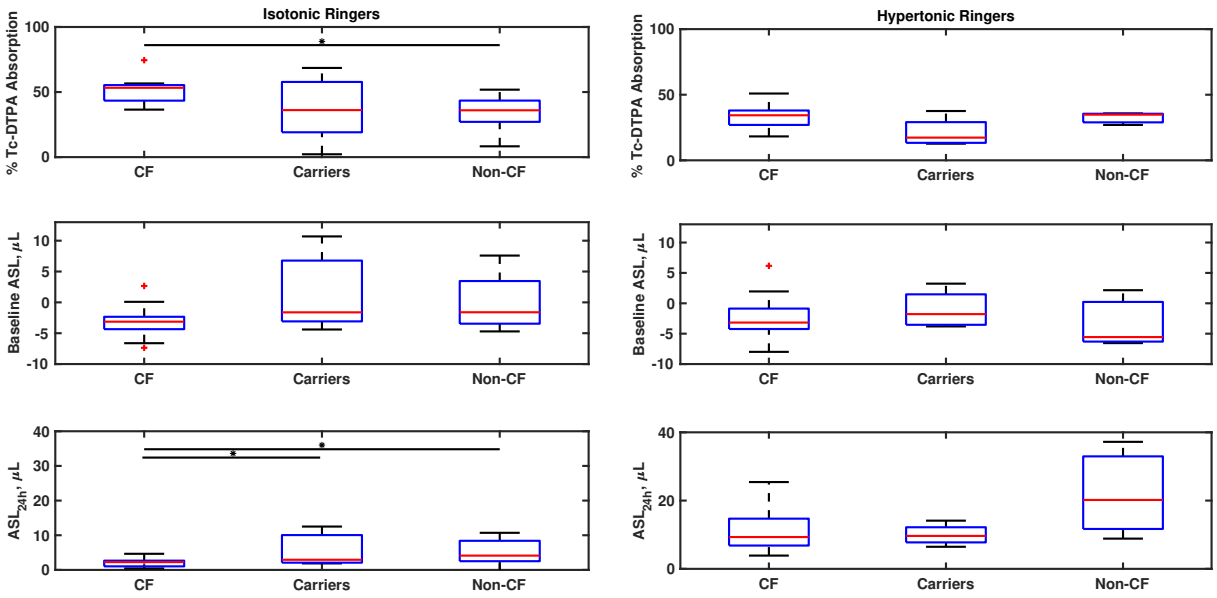

Figure 4.3: Boxplots summarizing the observed differences between the three groups in the study (CF, Carriers, and Non-CF) on the basis of *in vitro* ASL and paracellular solute transport dynamics. These experiments measure ASL volume and absorption of Technetium99m DTPA (Tc-DTPA) over 24 hours following a challenge of 10 μL of either isotonic (Left) or hypertonic (Right, isotonic + 200mM NaCl). Tc-DTPA is an *in vitro* analogue of In-DTPA an can only be cleared paracellularly. (Top) percent Tc-DTPA absorption after 24 hours, (Middle) baseline ASL at time 0, and (Bottom) Change in ASL after 24 hours. Red cross signifies a measurement found to be an outlier within its group. Statistical significance was determined through a non-parametric Wilcoxon rank sum test. *: p-values < 0.05.

5.10 ± 0.930; p = 0.852), but significantly higher than the CF group (CF: 2.163 ± 0.289, p = 0.0093). Following the treatment with IR, however, all groups show a significantly increased ASL_{24h}. The Carrier group was found to be statistically equivalent to both the CF and Non-CF groups (Carrier: 9.969 ± 1.59; Non-CF: 22.08 ± 8.23; CF: 11.08 ± 1.499). Relative to their IR levels, Non-CF cells showed the highest increase in ASL_{24h} (∼5-fold), followed by Non-CF (∼4-fold) and Carriers (∼2-fold). Immediately following the addition of HR, all groups secreted liquid into the ASL. However, following the ASL peak (∼4-6 h), only the CF and Carrier groups trend towards their initial baseline levels. Given the similar initial increase in ASL volume achieved for all three groups, the difference observed at 24 hours suggests the difference may be due to a longer duration of the osmotic effect of HR. This could be due to CF, and, to a lesser degree, Carrier cell lines decreased ability to secrete Cl^- or regulate its Na^+ intake, possibly leading to a more rapid clearing of the excess salt ions through diffusion in the paracellular space. It is important to acknowledge the limited size of the data set in these experiments (Non-CF: N = 3, n = 18; Carrier: N = 4, n = 24; CF: N = 7, n = 42), since the lower number of Non-CF and Carrier samples may skew the results. Here N represents the number of subjects, and n is the number of total individual cultures evaluated. It would be of great interest to examine the response profile as a function of stimuli with different tonicity levels and longer time points.

4.2.2 Cystic Fibrosis pathophysiology: a study between parent and child

4.2.2.1 CFTR Expression and Functional Levels We have shown so far that carriers of a single CF-causing mutation exhibit physiologically meaningful differences versus both CF and Non-CF individuals at both the cell and organ levels. UC studies in Chapter 2 showed Carriers have statistically different baseline, CFTR, and ENaC associated short circuit currents in the absence of a transepithelial chemical gradient. Similarly, we have shown that whole cell protein samples harvested from fully differentiated Carrier HNE cultures expressed approximately two-thirds as much mature CFTR as those obtained from Non-CF samples (Figure 4.4). This is further supported by a different study that showed approximately a one-third reduction of CFTR expression Carrier samples vs. Non-CF [3].

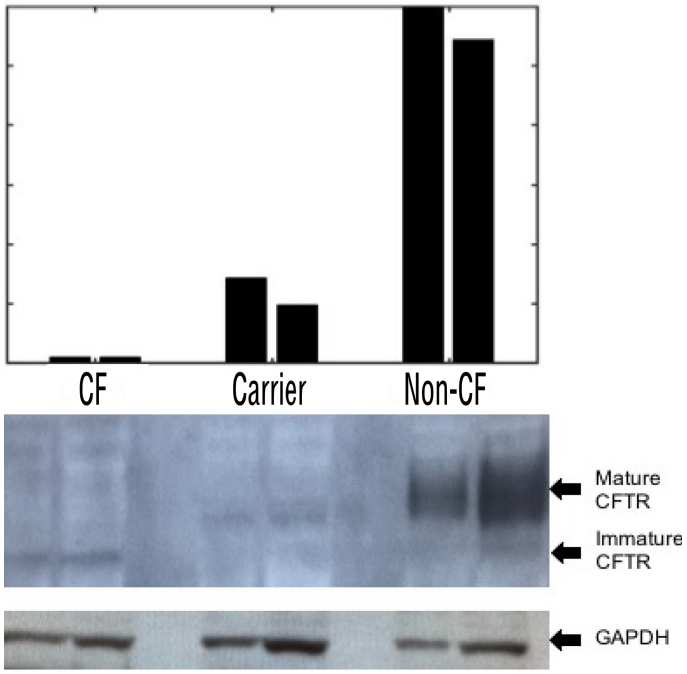

Figure 4.4: Western blot showing the whole-cell CFTR protein expression for two representative primary HNE cell lines from each group: CF, Carriers, and Non-CF. A minimum of 6 individual filters where harvested for each cell line. Protein samples were probed for CFTR (middle panel), stripped, and re-probed for GAPDH to use as a reference protein (bottom panel)

Reduced values for both $\Delta I_{Forskolin}$ and mature CFTR protein expression suggest that the lack of a functional CFTR allele does leads to quantifiable changes in cellular electrophysiology. Results shown in the previous sections also support this claim. In particular, Carriers showed approximately half as much Forskolin-stimulated ($\Delta I_{Forskolin}, \mu A/cm^2$) current than non-CF subjects (3.78 ± 0.7 vs. 7.33 ± 0.75). In order to explore this difference, we tested the I_{SC} of a subset of Carrier HNE primary cultures from the group shown in Chapter 2 following the treatment with CFTR modulators (Ivacaftor/Lumacaftor) (Figure 4.5).

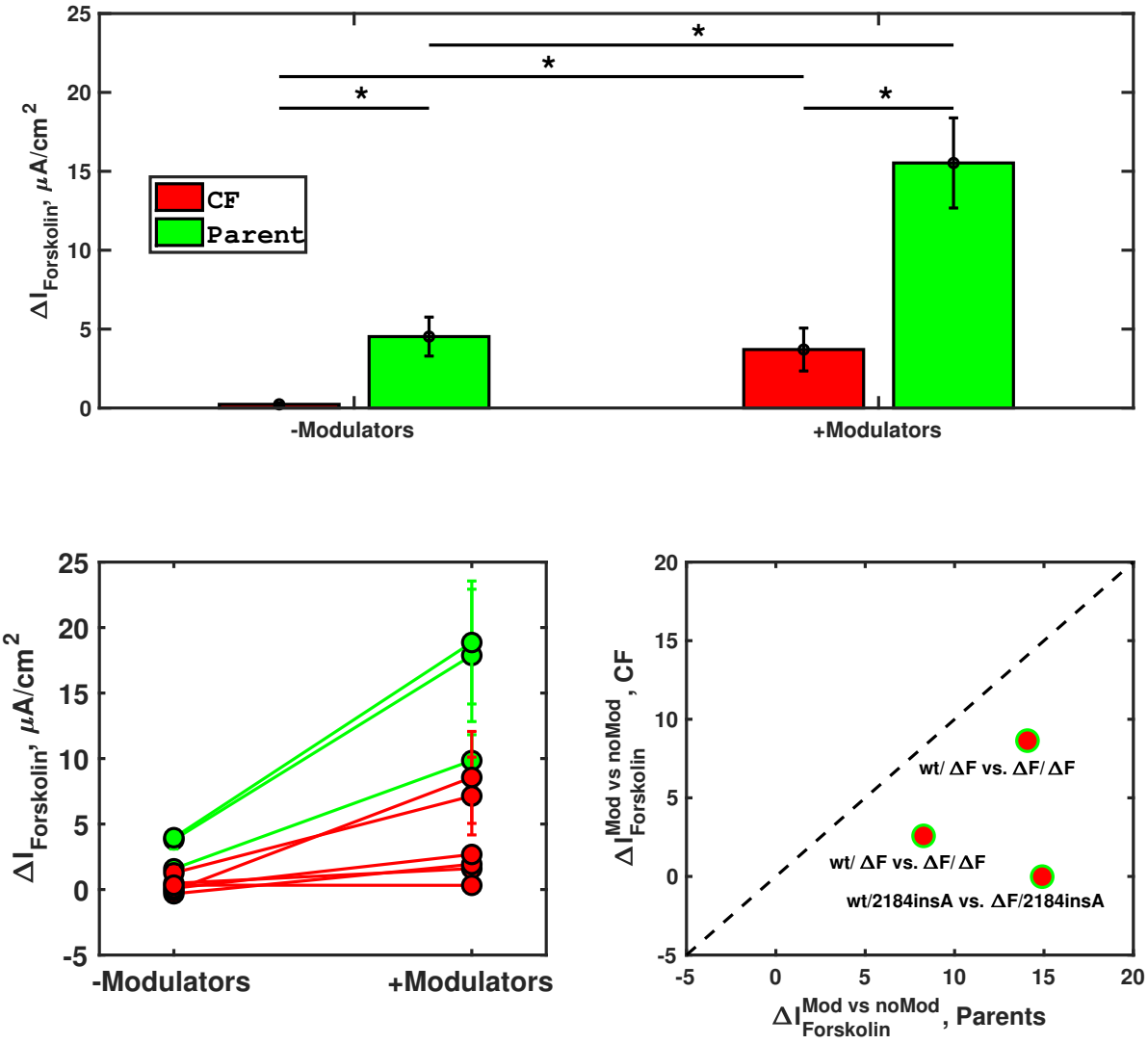

Figure 4.5: (Top) Bar plots showing the $\Delta I_{Forskolin}$ ($\mu A/cm^2$) results for CF (red) and Carriers (green) following treatment with CFTR modulators (lumacaftor/ivacaftor) or no treatment. (Bottom left) Line plot showing the subject-specific $\Delta I_{Forskolin}$ at baseline and following modulator treatment. (Bottom right) Scatter plot showing change of $\Delta I_{Forskolin}$ between the two conditions, plotted as child (CF subject) vs. parent (Carrier) pairs.

The results revealed that Carrier cultures treated with the modulator combo showed a 5-fold increase in $\Delta I_{Forskolin}$ response relative to their untreated response. This corresponds to a total increase of 11.82 $\pm$ 0.747 $\mu A/cm^2$. By comparison, CF cultures exposed to the same treatment exhibited a nearly 20-fold increase, but with a much lower over all current change of 4.29 $\pm$ 0.57 $\mu A/cm^2$ (Figure 4.5). When examining the subject-specific response to the modulator treatment, it was revealed that CF cultures showed a larger inter-subject variability of treatment response than the Carrier group. This is possibly due to their genotypes. Out of the three CF lines that exhibited less than 2 $\mu A/cm^2$ $\Delta I_{Forskolin}$, two posses a genotype not approved for treatment with Orkambi, the clinical version of the modulators used: $\Delta F508/D1152H$ and $\Delta F508/2184insA$. The third line was homozygous for $\Delta F508$. Similarly, out of the three Carrier cell lines treated with correctors, the one with approximately 50% lower treatment response also expressed one of these same alleles ($2184insA$) (Figure 4.5). We also explored whether a Carrier's $\Delta I_{Forskolin}$ response to treatment exhibited any relation with their respective child's corresponding measurement. No significant relationship was identified from the the three parent/child pairs studied. However, one of the pairs studied had the non-responsive allele described above ($2184insA$). More pairs would be required in order to establish the existence of any relationship (Figure 4.5C). Lastly, since Carriers were also shown to have meaningfully elevated levels of sweat Cl^- (Figure 4.1), we also explore a possible correlation between parent and child. However, even after accounting for pairs where the CF patient is currently on a CFTR modulator therapy, no meaningful relationship was established (Figure 4.6).

4.2.2.2 Liquid and Solute Transport: *in vitro* and *in vivo*

In vitro measurements of ASL volume and Tc-DTPA absorption have been shown to be biomarkers quantifying important aspects of CF airway pathophysiology *in vitro* [32, 111]. Results from these studies in CF and Carriers suggest the two groups share similarities in their water and solute transport profiles (Figure 4.3). This is also supported by the nominal increase in ABS values of Carriers relative to Non-CF subjects (Figure 4.2). ABS has been show to be a reliable indicator of *in vivo* CF pathophysiology, and acts as an organ-level analogue to Tc-DTPA absorption [30, 31, 111]. In an effort to explore these observation, parallel

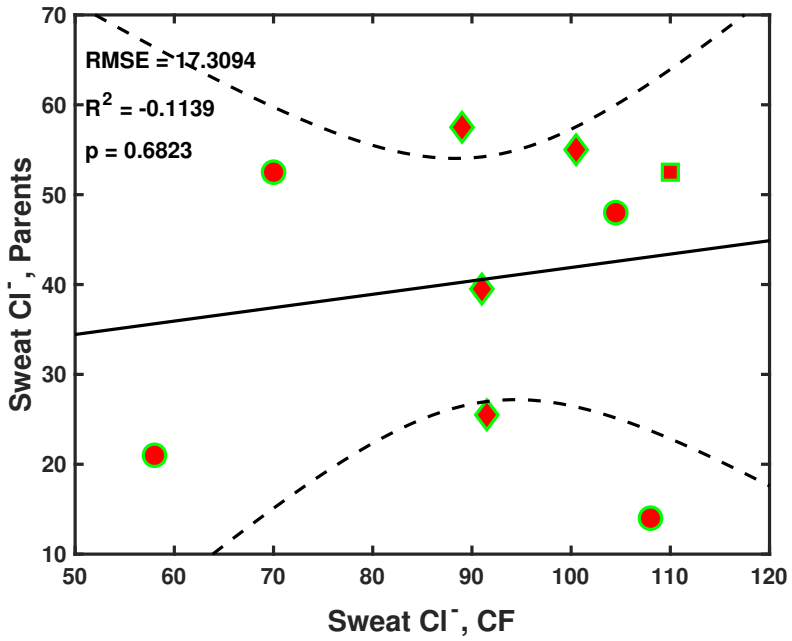

Figure 4.6: Correlation plots showing the relationship between sweat Cl^- in Parents and their CF children. A linear regression between the two groups was used to established correlation. Symbols represents current CFTR modulator status for each patient: no treatment (○), Kalydeko (square), and Orkambi/Symdeko (◇). Solid line represents the fitted regression model, and dashed lines represent the 95% confidence intervals

isotonic (pairs = 7, n = 72) and hypertonic (pairs = 4, n = 48) ASL volume and Tc-DTPA experiments were performed on CF/carrier matched pairs.

Results revealed a strong correlation between the %Tc-DTPA absorption for the two groups following the treatment with IR. This relationship is maintained, but somewhat diminished for the group treated with HR. This relationship suggests that while CF absorbed Tc-DTPA at higher rates than Carriers, the latter's paracellular transport rates are not just nominally similar, but also related to their corresponding partner in the former. This was further confirmed by calculating the change in %Tc-DTPA in the hypertonic case relative to the isotonic case, a measure of subject-specific therapeutic response. Plotting this for each parent/child pair revealed a strong linear correlation between the two groups that nearly

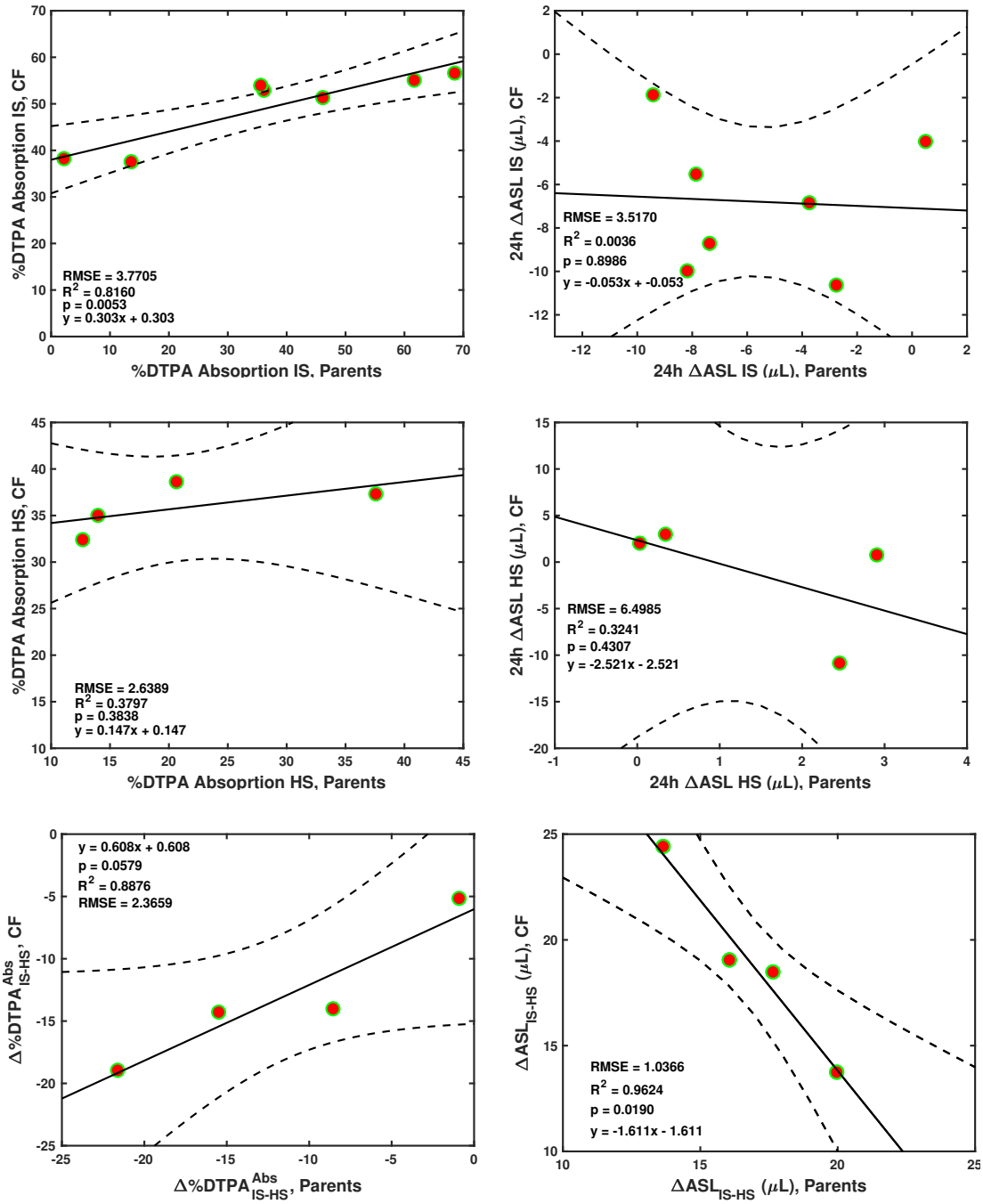

Figure 4.7: Correlation plots showing the relation between (Left) $\%DTPA$ absorption and (Right) ASL volume in Parents vs. their CF children following treatment with isotonic Ringer's (Top), hypertonic Ringer's (Center), or change from baseline (Isotonic) following hypertonic Ringer's (Bottom). A linear regression was used to established correlation. Solid line represents the fitted regression model, and dashed lines represent the 95% confidence intervals.

approached parity (Figure 4.7). Specifically, the decrease in %Tc-DTPA absorbed under hypertonic conditions relative to isotonic conditions for carriers is nearly equal to that of their respective children. This suggests that factors beyond disease progression or CFTR genotype can possibly dictate a CF patient's response to inhaled osmotic therapies.

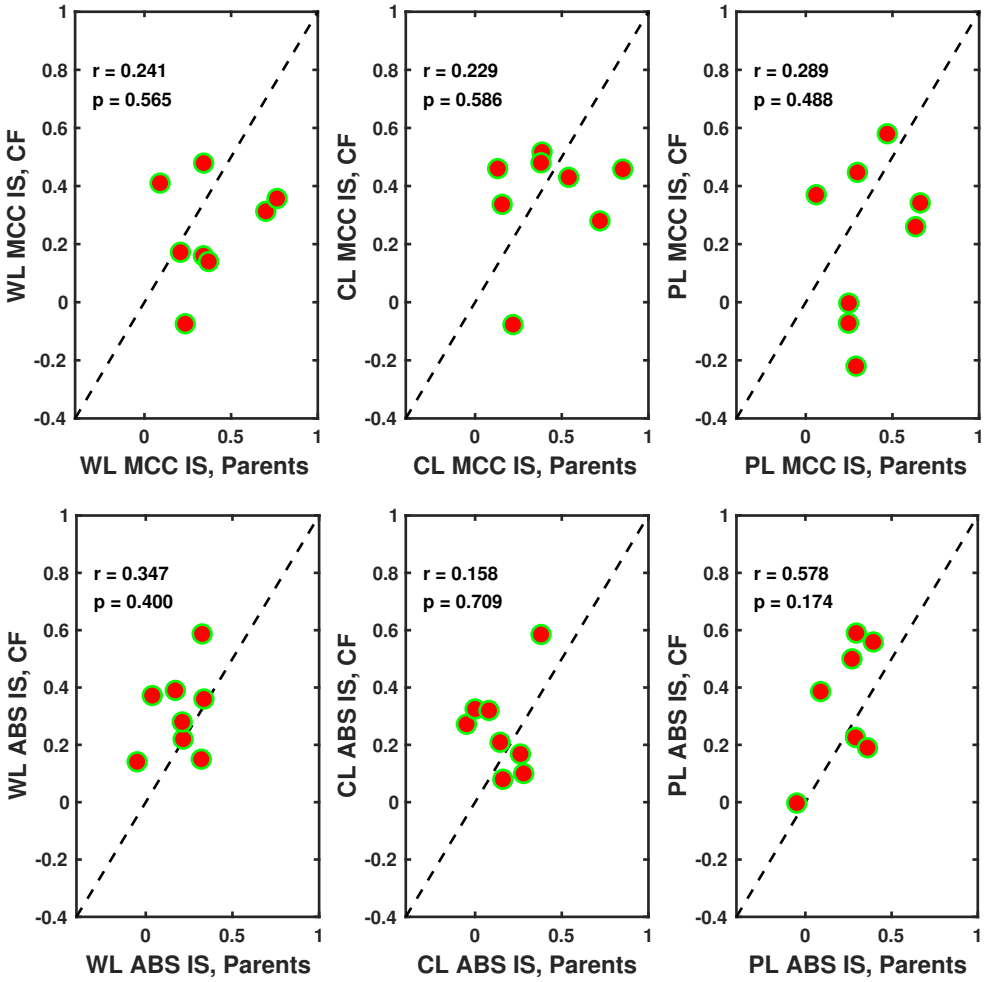

Figure 4.8: Correlation plots showing the relation between MCC (Left) and ABS (Right) in Parents vs. their CF children 24 hours following treatment with inhaled isotonic saline.

A similar analysis was carried out for ASL volume change following isotonic or hypertonic. No correlation was found between the two groups in either conditions. However, when we calculate the ASL volume therapeutic response between the two treatment conditions, we observed a strong inverse linear correlation (Figure 4.7). In this case, it appears that greater

improvement in ASL hydration following hypertonic saline for the parent corresponds with a slightly decreased ASL re-hydration profile in the CF group, with the slope significantly favoring the CF group. This falls within the predictions established in Chapter 3, which revealed that CF cells have significantly larger transepithelial hydraulic permeabilities than Non-CF. It would follow that this trend should also apply to carriers, since CF lines were shown to absorb more ASL than both Carriers and Non-CF (which were deemed equal to each other, Figure 4.3). An increased hydraulic permeability, implies that in the presence of a reverse gradient (*i.e.* apical hypertonic conditions) CF cells should secrete more ASL and thus should exhibit a larger total ASL volume change than Carriers. We also performed direct comparisons between the *in vivo* MCC and ABS measurements for the same parent/child pairs following treatment with inhaled isotonic saline. However, no meaningful correlation was found for either measurement when examining the whole lung, or either its central or peripheral regions (Figure 4.9).

4.2.3 DTPA Absorption, a Trans-scale Biomarker for Cystic Fibrosis Pathophysiology

One of the main drivers behind the use of primary HNE cell cultures as an *in vitro* model of CF is their potential to serve as a direct bench-scale analogue of a patient's possible therapeutic response. In order to fulfill this potential, we must first establish appropriate means to relate cell level mechanisms to relevant organ-level pathophysiology, and eventually clinical response. Traditionally, spirometry measurements have been used as assessments of CF airway disease progression [1, 53]. Similarly, their improvement is used as the primary endpoint for clinical trials evaluating CF therapeutics [16, 40, 92, 158]. With this in mind, we explored whether there is any link between ASL volume and Tc-DTPA clearance and common spirometry measurements: FEV1, FVC, and $FEF_{25\%-75\%}$. We have also included plots showing the same correlation analysis with respect to sweat Cl^-, a common method for CF screening and secondary clinical endpoint. This analysis included measurements from all three groups (CF, Carriers, and non-CF), and also accounted for CF patients currently on a CFTR modulator.

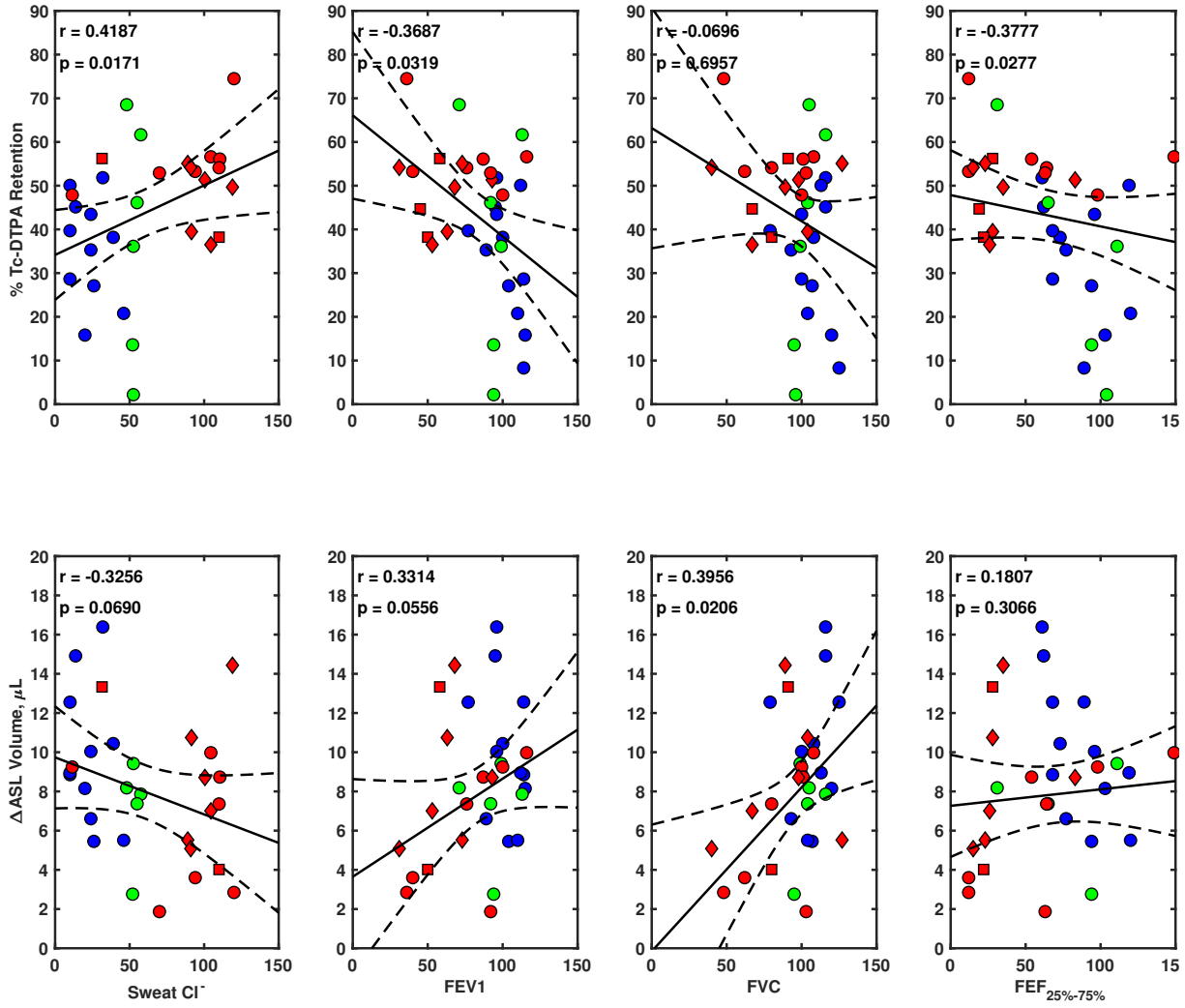

Figure 4.9: Correlation plots between the change in %Tc-DTPA clearance (Top) and ASL Volume (Bottom) versus (From left to right): Sweat Cl^- , FEV1, FVC, and $FEF_{25\%-75\%}$ for non-CF (blue), Carrier (green) and CF (red). Symbols represents current CFTR modulator status for each patient: no treatment (○), Kalydeco (square), and Orkambi/Symdeko (◇). Solid line represents the fitted regression model, and dashed lines represent the 95% confidence intervals

Sweat Cl^- was found to be directly correlated with %Tc-DTPA absorption ($p = 0.017$) and inversely correlated with ΔASL volume ($p = 0.0690$). These relationships agree with current understanding of CF pathophysiology. It is worthwhile noting that two CF patients with genotypes linked to mild CF airway disease (3849+10kbc>T/R668C and ΔF508/D1152H) showed sweat Cl^- levels on par with Non-CF subjects. No consistent meaningful improvement was observed among CF subjects on a CFTR modulator. Furthermore, this analysis revealed that while sweat Cl^- is a good measurement for distinguishing between three groups, it lacks the resolution necessary to serve as a potential link to cell level physiology on its own.

From the spirometry analysis, FEV1 was found to be directly correlated with ΔASL volume ($p = 0.0319$) and inversely correlated with %Tc-DTPA absorption, although not quite reaching statistical significance for the latter ($p = 0.0556$). Both relationships performed well when capturing the majority of the CF group, but struggle to predict some of the inter-subject variability observed among the Non-CF and Carrier groups, probably due to the scaling-related non linearities dominating the relationship between these measurements. Similar results were observed between FVC and ΔASL volume ($p = 0.0206$), and between $FEF_{25\%-75\%}$ and %Tc-DTPA absorption ($p = 0.0277$). As a whole, these results suggest that while definitely related, ASL volume and Tc-DTPA dynamics struggle to capture system level physiology with sufficient accuracy on their own.

However, it may possible to overcome this issue through the inclusion of system scale *in vivo* analogues of airway absorption dynamics in our analysis. In order to explore this, we evaluated *in vivo* absorption profiles for CF patients following treatment with either inhaled isotonic or hypertonic saline. These measurements track the airway absorption of In-DTPA, an analogue of Tc-DTPA commonly used for organ level assessments [31, 32, 111, 120]. Using this information, we calculated each subject's *in vivo* and *in vitro* therapeutic response to osmotic treatment. These values were plotted against each other, while also accounting for patients currently on a CFTR modulator.

This analysis revealed that the therapeutic response of both Tc-DTPA absorption and ASL volume change are highly correlated to the corresponding therapeutic change observed for ABS across different regions of the lung. In particular, ABS and %Tc-DTPA absorption

were found to have a very strong direct correlation in the peripheral lung ($p = 0.0001$, $R^2 = 0.7987$); this relation was lost in the central lung ($p = 0.7883$), which obfuscated the whole lung analysis ($p = 0.0633$) (Figure 4.10). Previous work in our group has shown that mucociliary clearance (MCC) dominates the dynamics in the large airway, which account for the majority of the central lung region of interest [33, 120, 176]. Since In-DTPA can also be cleared through MCC, it is reasonable to assume that the loss of correlation observed in the central and whole lung analysis is due to MCC dynamics. The peripheral lung, on the other hand, is believed to have significantly lower rates of MCC transport and higher absorptive rates [119, 120, 176], serving as an ideal link to *in vitro* Tc-DTPA clearance rates.

The opposite behavior was observed when comparing ABS with *in vitro* ASL volume change. An inverse correlation was observed between ABS therapeutic response in the whole lung and the change in ASL volume ($p = 0.0078$, $r^2 = 0.4888$). This relationship was abolished in the central ($p = 0.0854$) and peripheral ($p = 0.1459$) lung (Figure 4.10). Unlike Tc-DTPA, Δ ASL volume is not a direct analogue of ABS. ABS cannot directly account for *in vivo* transcellular liquid transport, while ΔASL volume does. The inverse nature of these correlations suggests that increased *in vitro* therapeutic response to osmotic therapies, leads to a lesser rescue of ABS. Together with findings from Chapter 3, these results suggest that following osmotic treatment, the larger transcellular water permeabilities lead to rapid, yet unsustained, hydration of the ASL. The transient increase in ASL volume favors MCC and decreases the paracellular driving force for the absorption of In-DTPA, lowering ABS. This behavior is more pronounced in the peripheral lung, which likely has larger rates of hydraulic permeability than the large airways in the central lung region of interest.

The relations established from this data set have been evaluated through both their statistical significance, as well as their overall meaning within the context of known CF airway disease mechanisms. Figure 4.11 shows the results from an univariate, combinatorial, non-linear ranked correlation matrix illustrating the resulting relations between patient-specific *in vitro*, *in vivo*, clinical measurements, and predicted *in silico* parameters from both the cell- and lung-scale models for subjects already enrolled in our trial. The results suggest there are several measurements with some degree of predictive power. Further analysis is required in other to identify optimal predictors of clinical measurements of airway function.

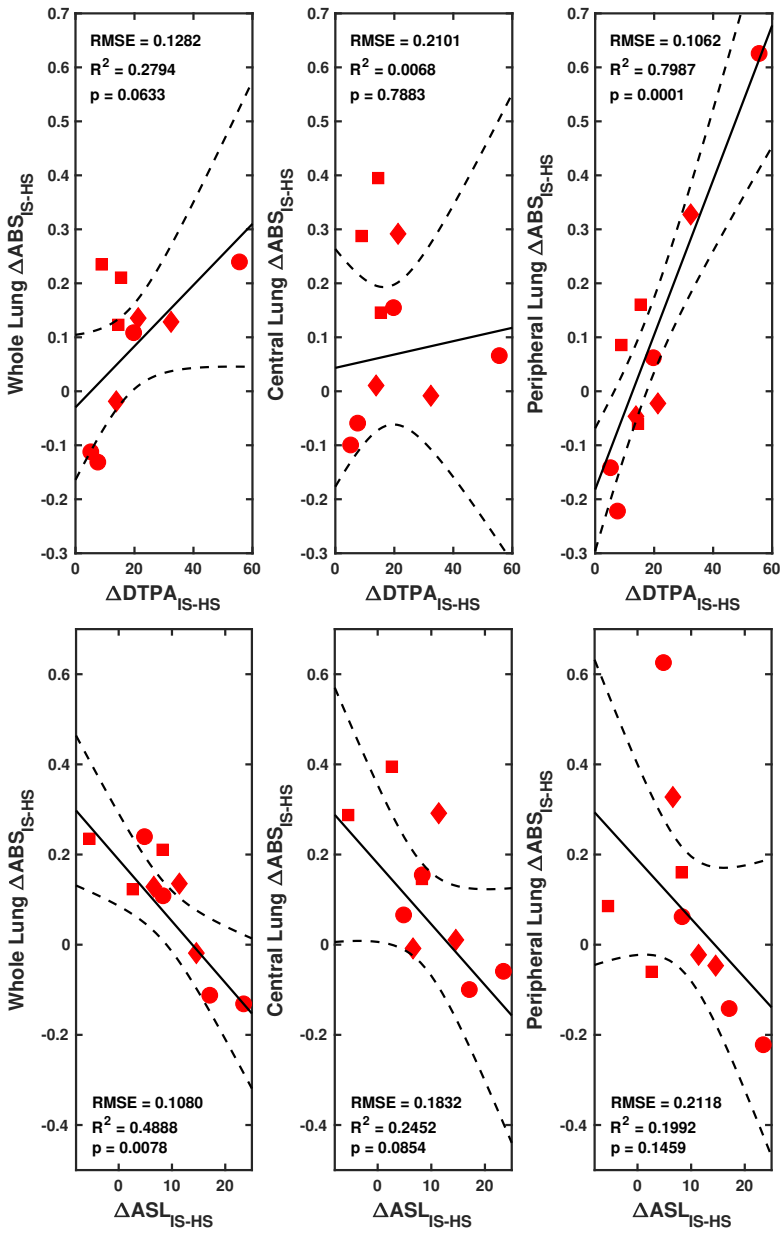

Figure 4.10: Isotonic to hypertonic change in %Tc-DTPA clearance (Top) or ASL Volume (Bottom) versus the change in In-DTPA absorption (ABS) in the whole (Left), central (Center), or peripheral (Right) lung for CF patients. Symbols represents current CFTR modulator status for each patient: no treatment (○), ivacaftor (square), and lumacaftor/tezacafor (◇). Solid line represents the fitted regression model, and dashed lines represent the 95% confidence intervals.

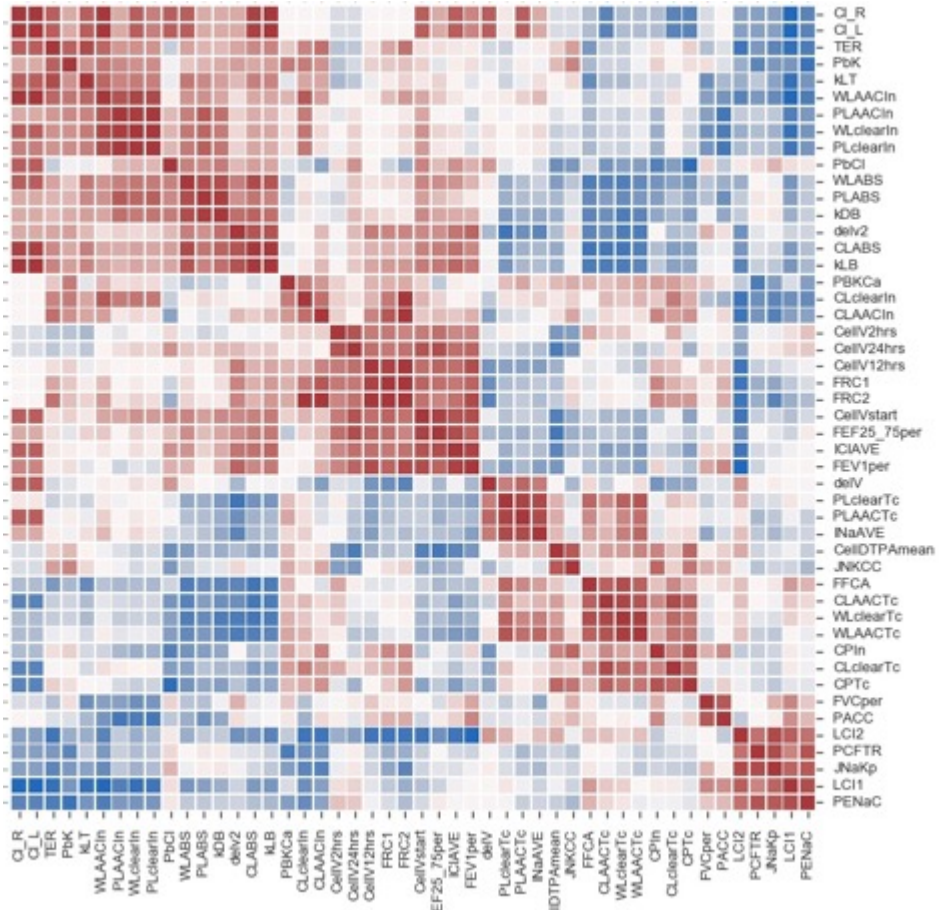

Figure 4.11: Ranked correlation matrix showing all inter-parametric correlation coefficients for all clinical, and *in vitro* measurements, as well as the *in silico* estimated parameters obtained from fitting patient-specific data through our cell-scale models.

In order to do this, we develop a series of linear regression models that leveraged ASL and DTPA measurements under isotonic and hypertonic conditions alongside common patient clinical information such as sweat Cl^-, gender, CFTR modulator usage, and airway microbiology results. The models all followed a similar format as described by Equation 4.1.

$$\mathbf{y} = \sum_{i=1}^{k} (\alpha_i \mathbf{x}_i) + \beta \tag{4.1}$$

Here $\mathbf{y}$ represents the vector of predicted variables for all subjects being studied, α_i is the estimated coefficient associated with predictor variable i, $\mathbf{x}_i$ is the vector of measured values for all subjects associated with predictor variable i, and β is the predicted model intersect, a measure of model bias.

These regressions were run following a feature selection analysis that narrowed down the data set to variables with significant univariate predictive power prior to a full 3-fold and 5-fold internal cross-validation analysis. This analysis reduced the number of variables from 55 down to a total of 6 distinct variables including: gender, presence of a *Pseudomonas aeruginosas* culture within the last year, CFTR modulator status (no use, Kalydeco, or Orkambi/Symdeko), percent of Tc-DTPA absorbed following isotonic Ringer's stimuli ($\%DTPA^{IS}_{ABS}$), baseline ASL volume (ASL^{IS}_{0h}), and sweat Cl^-. The regression models for the prediction of MCC and ABS following hypertonic saline treatment, also included their respective isotonic counterparts as predictive variables. The resulting regression models for ABS and MCC predictions following either isotonic and hypertonic saline treatment are shown in Figure 4.12. A summary of all the predicted coefficients, their associated errors and significance, as well as the over all model statistics and variance are summarized in Table 4.5 for the isotonic case, and Table 4.6 for the hypertonic case.

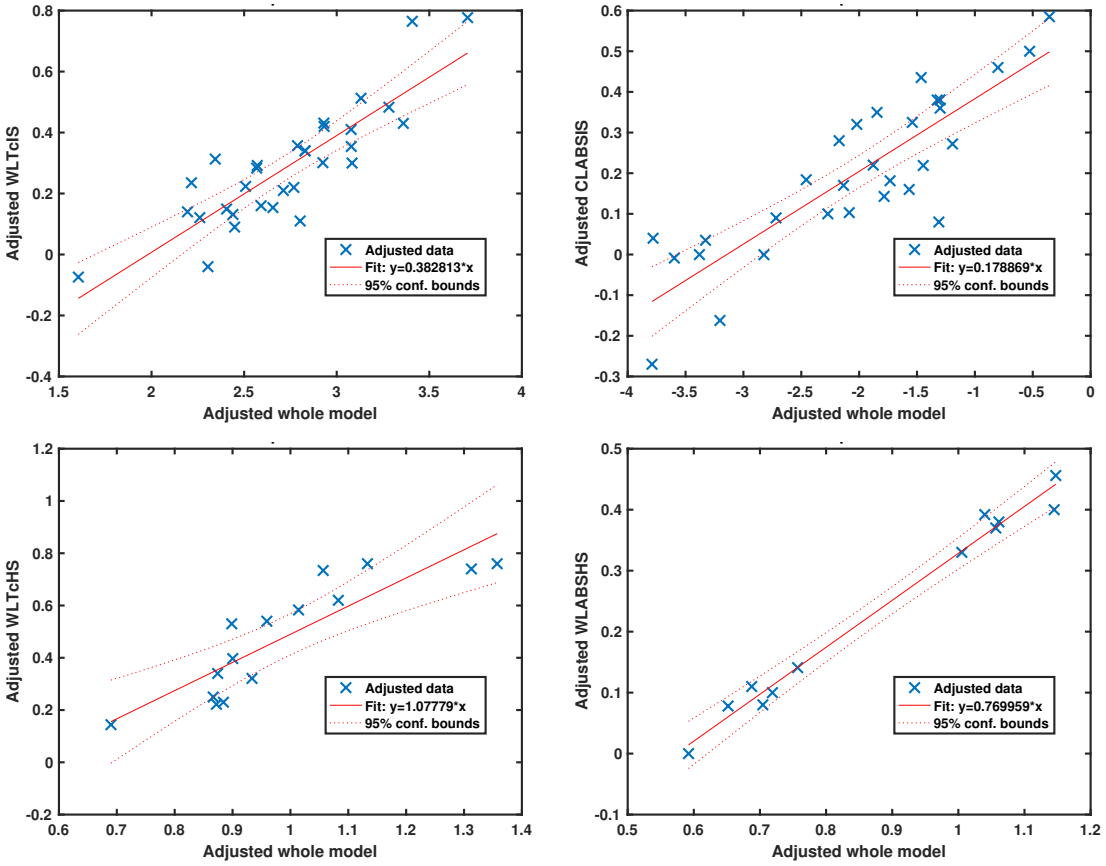

Figure 4.12: Adjusted regression models for the prediction of whole lung MCC (Top left) and ABS (Top right) following inhaled isotonic saline for Non-CF, Carrier, and CF subjects from *in vitro* and demographic data. Similarly, regression model for whole lung MCC and ABS following treatment with hypertonic saline for CF subjects. Predictors, coefficients and statistical information about model fitness can be found in Table 4.5 for the isotonic saline case, and Table 4.6 for the hypertonic saline case.

Table 4.5: Summary of regressions models developed for the prediction of MCC and ABS measurements following treatment with inhaled isotonic saline.

	Predicted Variable							
Treatment	**MCC**				**ABS**			
	Predictor	**Coefficient**	**SE**	**p-Value**	**Predictor**	**Coefficient**	**SE**	**p-Value**
	Intercept	-0.7582	0.1710	0.0002	Intercept	0.5622	0.1115	3.36E-5
	Gender (F)	0.1215	0.0422	0.0087	Gender (F)	-0.1780	0.0436	0.0047
	$\%\text{DTPA}_{ABS}^{IS}$	0.0026	0.0012	0.0546	$\%\text{DTPA}_{ABS}^{IS}$	-0.0058	0.0013	0.0002
	PA+	-0.1561	0.0549	0.0094	ASL_{0h}^{IS}	-0.0154	0.0061	0.0179
Isotonic	No Modulator	-0.2814	0.0881	0.0042	Sweat Cl^-	0.0023	0.0006	0.0018
Saline	Ivacaftor	0.0661	0.7815	0.0406				
	Luma/Teza	-0.1530	0.0756	0.0555				
	Model Statistics				**Model Statistics**			
	RMSE	0.111	**F-stat**	9.4	**RMSE**	0.106	**F-stat**	18.2
	$\mathbf{R}^2$	0.741	**p-Value**	1.74E-5	$\mathbf{R}^2$	0.745	**p-Value**	4.0E-5
	5-fold MSE	0.0256	**10-fold MSE**	0.0291	**5-fold MSE**	0.0305	**10-fold MSE**	0.0286

Table 4.6: Summary of regressions models developed for the prediction of MCC and ABS measurements following treatment with inhaled hypertonic saline.

	Predicted Variable							
Treatment	**MCC**				**ABS**			
	Predictor	**Coefficient**	**SE**	**p-Value**	**Predictor**	**Coefficient**	**SE**	**p-Value**
	Intercept	-0.5879	0.2829	0.0726	Intercept	-0.4415	0.1001	0.0069
	$\%DTPA_{ABS}^{HS}$	-0.0119	0.0045	0.0283	$\%DTPA_{ABS}^{IS}$	0.0059	0.0010	0.0023
	MCC_{WL}^{IS}	0.9249	0.2125	0.00018	ABS_{WL}^{IS}	0.7575	0.1254	0.0017
Hypertonic	No Modulator	0.3556	0.1123	0.0114	No Modulator	0.0426	0.0605	0.5124
Saline	Ivacaftor	0.3777	0.1106	0.0076	Ivacaftor	0.0745	0.0308	0.0603
	Luma/Teza	0.1919	0.1131	0.1240	Luma/Teza	0.1073	0.0370	0.0023
					Sweat Cl^-	0.0023	0.0008	0.0482
	Model Statistics				**Model Statistics**			
	RMSE	0.135	**F-stat**	5.59	**RMSE**	0.030	**F-stat**	54.0
	R^2	0.756	**p-Value**	0.012	**R^2**	0.985	**p-Value**	2.0E-4
	3-fold MSE	0.0317	**5-fold MSE**	0.0302	**3-fold MSE**	0.0360	**5-fold MSE**	0.0677
	3-fold MCR	0.4807	**5-fold MCR**	0.4807	**3-fold MCR**	0.1893	**5-fold MCR**	0.1786

4.3 Discussion

The clinical study described above has provided us with a robust data set that we have then significantly expanded to identify the parametric axes that best describe the aforementioned link. Patients with CF display a wide range of pathophysiology, even among similarly genotyped patients. These variations among the patient population are believed to be due to epigenetic differences in modifier genes of CF disease, as well as the contribution from multiple environmental influences [35, 115]. As such, developing a mathematically formalized representation of the link between cell-level mechanisms to organ-level dynamics, and potentially therapeutic response, requires ample knowledge of the physiological processes that drive these differences.

Analysis of multibreath washout studies and spirometry measurements found no meaningful decrease in airway function in Carriers relative to Non-CF individuals. However, sweat Cl^- measurements were significantly elevated, though not as much as those of CF individuals. Measurements of DTPA absorption *in vivo*, ABS, and *in vitro*, %Tc-DTPA$_{ABS}$, showed Carriers clear DTPA at nominally higher rates than Non-CF, but not as rapid as CF subjects. No statistical difference was found between Carrier and either of the other two groups. No difference was observed in MCC or baseline ASL values between any of the groups. At the cellular level, however, UC studies showed Carriers have statistically different baseline, CFTR, and ENaC associated short circuit currents. In particular, Carriers showed approximately half as much Forskolin-stimulated current as non-CF subjects, with significant changes to their model-predicted channel and transporter permeabilities.

Functional imaging based biomarkers of lung clearance have recently received extensive development in CF. MCC measurements have been used to develop inhaled osmotic therapies and more recently the CFTR potentiator Ivacaftor [165]. Previous work in our group developed a nuclear imaging method to measure ASL absorption along with measurements of MCC, based on the absorption rate of a small molecule probe (In-DTPA) from the lungs. These biomarkers demonstrate a clear, quantifiable signature of CF lung disease that changes substantially in response to therapy [31, 110]. The multiple variables developed through this work describe therapeutic response both *in vitro* and *in vivo*, and serve to

develop *in silico* system models of the organ level physiology depicted through MCC/ABS scans [119, 120, 176], and the cell level physiology depicted through cell studies [174].

This work has made significant progresses towards the development of a crucial link between cell and organ level models of airway absorption dynamics, and their dysregulation in CF. Collection of trans-scale, paired DTPA clearance data has allowed us to evaluate potential links between cell and organ level physiology. This provides us with a more mechanistic understanding of therapeutic effects on a cellular level, and allows cell level effects to be related to organ level outcomes. In particular, this work has identified a direct relationship between the osmotic effect of hypertonic Ringer's in CF HNE cultures, and the analogue therapeutic effect observed in CF individuals after treatment with inhaled hypertonic saline. This was further validated by statistical models that revealed that both ASL and DTPA can be used to predict organ-level physiology when combined with common clinical data such as gender, airway microbiology, and CFTR modulator usage.

5.0 Summary and Future Work

5.1 Contributions

5.1.1 Model of Airway Electrophysiology for Expediting of Experimental Work-Flow

The work in this dissertation presented a general model of airway epithelial electrophysiology capable of meeting both numerical tractability and physiological relevance. This work required the development of a custom parameter estimation strategy capable of circumventing the discontinuities observed in the parametric space of the model. This model was validated through the prediction of known parametric and state changes to complex experimental stimuli such as CFTR modulator therapies and inflammatory citokines.

Furthermore, the model was used to explore the electrophysiology of primary human nasal epithelial (HNE) relative to their human bronchial epithelial (HBE) counterparts. HBE cell cultures have provided a simple and robust model of airway epithelial physiology. HBEs from CF lungs mimic the epithelial pathophysiology of CF and have received extensive use in the study of CF lung disease. HNE cell cultures sampled by nasal brushing have been shown to have similar properties to the HBE cultures, allow for basic studies in cultures from subjects not undergoing lung transplant. Recent improvements to HNE culture protocols have allowed their more practical use in research applications [41, 197, 211, 215], however, little information is currently available about the possible differences between HNE and HBEs, or the impact that any possible difference may have in CF pathophysiology. The model was capable of successfully recapitulating the short-circuit dynamics observed for both types of tissues, and identify potential differences in the homeostatic levels of transepithelial Cl^- transport Non-CF HNE cell cultures relative to HBE ones. In particular, the model predicted a shift in basolateral Cl^- permeability from NKCC to bicarbonate-dependent flux.

5.1.2 Cell-Scale Model of Airway Liquid and Solute Transport

The thin-film extension of the epithelial transport model accurately captures ASL and Tc-DTPA dynamics within biologically-meaningful parametric ranges allowing for a mechanistic exploration of the physiological differences between CF and non-CF epithelia, highlighting differences in absorption kinetics between the non-CF and CF cultures. Non-CF cells rapidly reabsorbed liquid and return to homeostasis while CF cells demonstrated a slower rate, but longer duration, of liquid absorption that ultimately leads to a decreased standing apical volume. The model also predicted the main factor contributing to differences in absorption dynamics between CF and non-CF epithelia are transcellular hydraulic permeabilities ($\sim$3-fold higher in CF) and not paracellular permeability.

Our model also corroborates previous reports, both in vitro [32] and *in vivo* [30], that radiolabeled DTPA conjugates absorption is increased in the CF airway. While ASL can be transported through trans- or paracellular pathways, Tc-DTPA can only be cleared paracellularly, either through diffusive or convective transport. Since the convective component of Tc-DTPA absorption is directly driven by ASL absorption, the relationship between Tc-DTPA and ASL absorption can be used to illustrate the relative contributions of convection and diffusion. Using our mathematical description of Tc-DTPA absorption from the ASL, we were able to probe the relative contributions of diffusion and convection that lead to increased solute absorption in CF. The model predicted that diffusive transport accounts for approximately 60% of all Tc-DTPA absorption seen in CF, a significant increase relative to the 49% predicted for non-CF cells, which is close to experimentally observed values [110]. It is likely that diffusion transport rates are increased in CF due to the decreased initial ASL volume and identical added Tc-DTPA counts in both CF and non-CF experiments.

A significant contribution of the model is the use of a more mechanistic understanding of paracellular ion fluxes. Current literature describes paracellular ionic transport using Goldmans constant field equation, the same expression used for transcellular ion channel fluxes [62, 168]. This approximation fails to account for the contributions of diffusive transport along the entire paracellular pathway and convective transport due to fluid drag. Previous work from our group has shown that convective transport can account for approximately

50% of Tc-DTPA transport across primary HBE cell cultures [110]. This suggests convection could also play a significant role in the paracellular transport of ionic species. Specifically, we compared predicted paracellular electrolyte fluxes in the electroosmotic versus the combined convection plus diffusion case. Our results suggest that electrical contributions are effectively negligible after the inclusion of convective driving forces. This distinction is particularly important under conditions of non-homeostatic hydraulic flux, such as those following a volumetric or tonicity challenge of the ASL, which are highly relevant for inhaled osmotic therapies commonly used by CF patients.

5.1.3 Insight into the Physiology of Carriers of a Single CF-Causing Mutations

The work here was able to show that carriers of a single CF-causing mutation exhibit physiologically meaningful differences with both CF and non-CF individual at both the cell and organ level. Analysis of showed no meaningful airway function differences in Carriers relative to Non CF individuals. However, solute absorption rates appeared to be elevated in both *in vivo*and *in vitro* measurements never reaching levels observed in CF.

At the cellular level, this work has shown significant electrophysiological differences between Carrier sand both CF and non-CF subjects. In particular, Carriers showed approximately half as much Forskolin-stimulated current than non-CF subjects. Similarly, we have shown that both whole cell protein and CFTR modulators are statistically lower in Carriers than Non-CF lines. This study is the first comprehensive look at CFTR function in Carriers, and the degree to which a single mutation can affect the proper function of airway epithelium. This also provides an avenue to identify just how much CFTR is required in order to avoid CF pathogenesis.

5.1.4 DTPA as a Multi-Scale Biomarker of CF Pathophysiology

Functional imaging based biomarkers of lung clearance have recently received extensive development in CF. MCC measurements have been used to develop inhaled osmotic therapies and more recently the CFTR potentiator Ivacaftor [165]. In order to better understand the multiple factors contributing to therapeutic response *in vitro* and *in vivo*, we have developed

in silico systems models of the organ level physiology depicted through MCC/ABS scans [119, 120, 176], and the cell level physiology depicted through cell studies [174].

This work has made significant progresses towards the development of a crucial link between cell and organ level models of airway absorption dynamics, and their dysregulation in CF. In particular, identifying direct relationships between the therapeutic effect of hypertonic Ringer's in CF HNE cultures, and the analogue effect observed in CF individuals following treatment with inhaled hypertonic saline. Statistical models revealed that both ASL and DTPA can be used to predict organ-level physiology. This models provide a unique opportunity to evaluate organ level physiology and therapeutic response *a priori* through standard patient demographic information and HNE-based measurements. This measurements could serve as valuable tools for the pre-screening of non-responders for the purposes of clinical trials.

5.2 Future Work

The above work represents a summary of a project that bridges the quantitative and design utility of systems medicine with biological and clinical expertise relevant to the field of CF research. It is intended to serve as a means to improve our understanding of CF pathophysiology, and as a basis for the further development of novel, patient-specific treatment options for patients with CF. The following section outlines potential avenues to further advance this work.

5.2.1 Additional Applications of the Cystic Fibrosis Electrophysiology Model

5.2.1.1 Modeling of Bicarbonate and H^+ in Airway Epithelium One of the most favorable traits of the electrophysiology model presented in this work is its balance between physiological-relevance and numerical parsimony. As we have described above, the electrochemical transport of ionic solutes across biological membranes is an inherently nonlinear and numerically complex phenomenon. The models described in Chapters 2 and 3 include

descriptions of most relevant transport pathways for the three major electrolytes: Na^+, Cl^-, and K^+. However, these models also implement significant assumptions in order to circumvent the numerical issues described.

There are other ions that also play an important role in epithelial osmolarity, polarization, cell volume and ASL regulation, both in health and disease. For example, many of the cellular ion transport pathways are pH dependent [84]. Characterization of pH would require the addition of H^+ and HCO_3^- as model states. The inclusion of these components would need to account for intracellular chemical reactions that facilitate the pH regulation of the cell. At the same time, it would facilitate the explicit modeling of additional transporters such as anion exchangers (AEs), Na^+-Bicarbonate co-transporter (NBC), Na^+-Proton-exchanger (NHE), the K^+-Proton ATPAse (KHP), TMEM16A, and SLC26A9 (Figure 5.1) [1, 8, 9, 60].

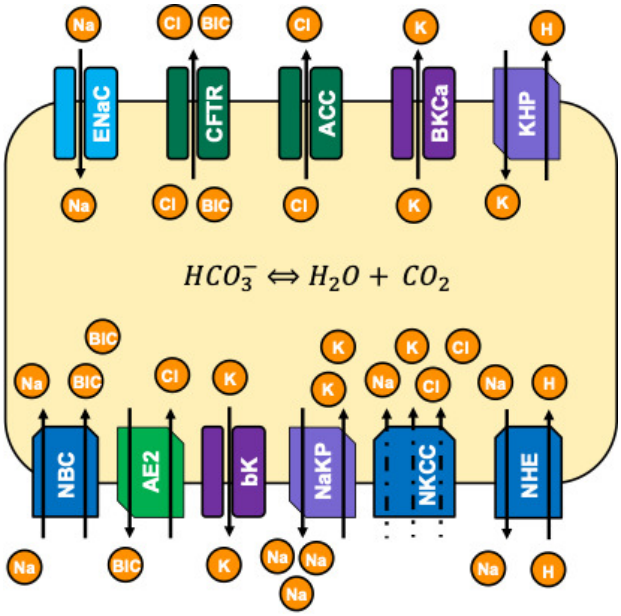

Figure 5.1: Diagram of potential Ussing Chamber model structure extension to include the addition of bicarbonate and proton transport.

Addition of some of these channels would further expand the model's ability to aid in *in silico* experimentation, particularly for the analysis of more nuanced experimental set

ups and the study of inflammatory responses in both CF or in other disease states like asthma [116, 117, 178, 212]. However, it should be noted that inclusion of these extra states would require significant effort in order to ensure model identifiability and numerical stability alongside physiological state dynamics. The difficulty of this task is evident in simulation results that used the basic descriptions of ion transport from the cell-scale models in the literature [54, 75, 135, 207]. However, our groups recent work has led up to developed a data set rich in Bicarbonate-dependent ion transport mechanisms. Thus providing us with a solid launching platform for the addition of extra pathways without necessarily compromising the numerical tractability of our model.

5.2.1.2 Electrophysiology in Cystic Fibrosis-Related Diabetes Pathophysiology

The electrophysiology model could also provide an avenue for the study of CF pathophysiology in other tissues, particularly in pancreatic cells. The recent advances in CFTR modulators and our understanding of airway microbiology and inflammation has led to significant increases in the life expectancy of CF patients. However, this has also lead to an increase in the fraction of the CF population with other meaningful comorbidities such as Cystic Fibrosis related diabetes (CFRD) [91]. This increase has led to a significant push for the study of CF "below the diaphragm".

It has been established that CFTR is widely expressed in both pancreatic α and β cells in several experimental models, where it appears to contribute to the proper polarization of islet tissue. [10, 13]. Several studies have hypothesized that CFTR dysfunction gives way to cellular hyper-polarization due to reduced glucose-sensitive depolarization and insulin release [69, 137, 214] (Figure 5.2). The electrophysiological mechanism behind this process are largely unknown, and could benefit from a biophysical model capable of tracking the relationship between transmembrane ionic transport, membrane potential, and insulin and glucose dynamics. From a model structure point of view, this system could be much more numerically tractable than airway epithelia, since it would not require the inclusion of epithelial polarization or Ussing chamber short-circuit constraints. It would also benefit from a rich library of *in silico* models of islet cell glucose/insulin dynamics and inflammatory signals in glucose response [122, 124, 155, 202].

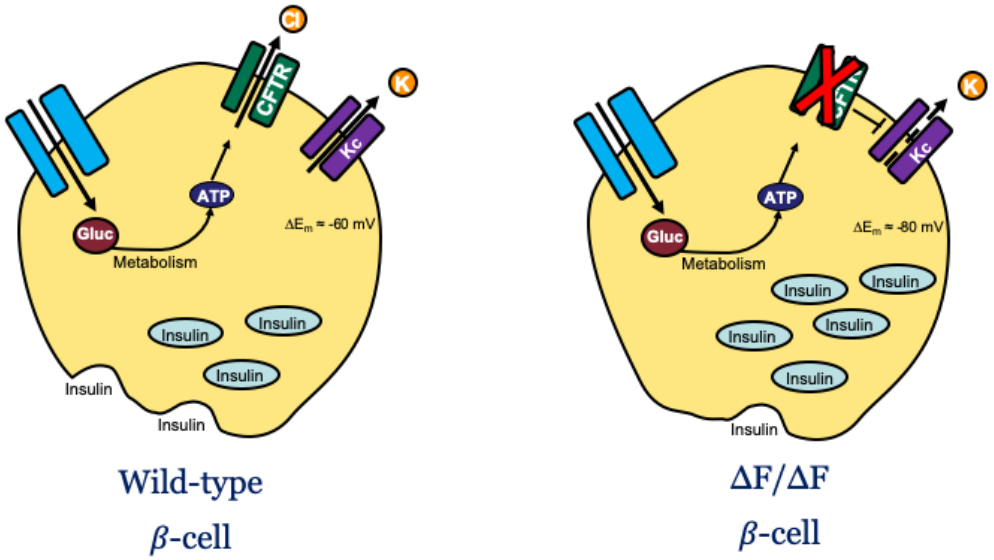

Figure 5.2: Diagram describing a potential $\beta-$cell electrophysiological mechanism leading to the pathogenesis Cystic Fibrosis-related diabetes.

5.2.2 Optimal Treatment Design at the Cell-Scale

Previous studies of have shown that both ASL reabsorption and ABS begins immediately following the treatment with isotonic therapies [31, 110]. In this work, we have established that there exits a direct relationship between *in vitro* therapeutic response of ASL and Tc-DTPA dynamics and ABS following a hypertonic stimulus. It is possible that this relationship can be used to study cell-to-organ dose response behavior. For example, it should be possible to regulate the degree of ASL hydration in primary cultures as a function of apical osmolarity challenges. Furthermore, we can assume there is a range of ASL volumes at which MCC can occur. If a greater than minimum necessary hydration level is achieved with a given dose, then there will be a period of time that MCC will be improved even as ASL volume recedes.

We have a mathematical model of the ASL volume regulatory system, a treatment objective, a body of relevant *in vitro* and *in vivo* data, and extensive knowledge and experience with airway physiology at multiple scales to generate heuristics that can serve as formal

mathematical constraints in such a way that retains clinical and logistical meaning. Given this information, a dose scheduling problem can be posed. Equation 5.1 shows a possible formulation of this problem.

$$
\begin{aligned}
\boldsymbol{min}_{N,t_k,\omega} & \left\{ \sum_{t=0}^{t_\infty} \frac{1}{\sigma_{t_k}^2} \left(\hat{V}_{CF}^{ASL}(t,\theta,u(t_k,\omega)) - V_{NCF}^{ASL}(\infty) + \lambda \right)^2 + \Gamma N \right\} \\
& \frac{dX}{dt} = \mathbf{f}(\dot{x},t,\theta) + u(t_k,\omega) \\
& Y(t) = \mathbf{g}(x,t,\theta) \\
s.\ t.\ & \lambda_l \leq \lambda \leq \lambda_u, \\
& N \leq d_D, N \in \mathbb{Z}, \\
& t_k - t_{k-1} \geq d_L, t \in \mathbb{Q}\ and \\
& \omega^{IS} \leq \omega \leq \omega^{15\%HS}, \omega \in \mathbb{Q}
\end{aligned}
\tag{5.1}
$$

Here, $\hat{V}_{CF}^{ASL}$ is the control variable, λ is a slack variable that defines the acceptable therapeutic target as referenced by the Non-CF steady state ASL volume, $V_{NCF}^{ASL}(\infty)$, and delimited by an upper , λ_l, and an lower, λ_u, bound. N is the number of treatments per day, which cannot exceed a certain number, d_D. t_k is a vector of size N containing the dosage times, such that a given dose, k, can not be less than d_L time units from dose $k-1$. ω is the total osmolarity of the solution being dosed. It is defined such that it cannot be lower than the osmolarity of isotonic saline, w^{IS}, or higher than the osmolarity of 15% hypertonic saline, $\omega^{15\%HS}$ (Figure 5.3). This formulation is similar to the one proposed by Markovetz *et. al* [119]. However, this iteration leverages the findings from Chapter 4 regarding our ability to track DTPA clearance dynamics across multiple physiological scales.

It is important to highlight that the ODE model and its the decision variables relating to dosage timing and osmolarity are highly nonlinear and continuous in nature. However, the number of doses is an integer variable, making this a mixed-integer nonlinear programming problem. It should be possible to leverage the versatility of Pyomo as well as common open source nonlinear and mix-integer solvers such as IpOpt, GLPK, and CBC to solve problems

of this class efficiently and rigorously. Kronqvist, *et. al.* recently published an extensive review covering both the formulation and implementation of these type of problems [98].

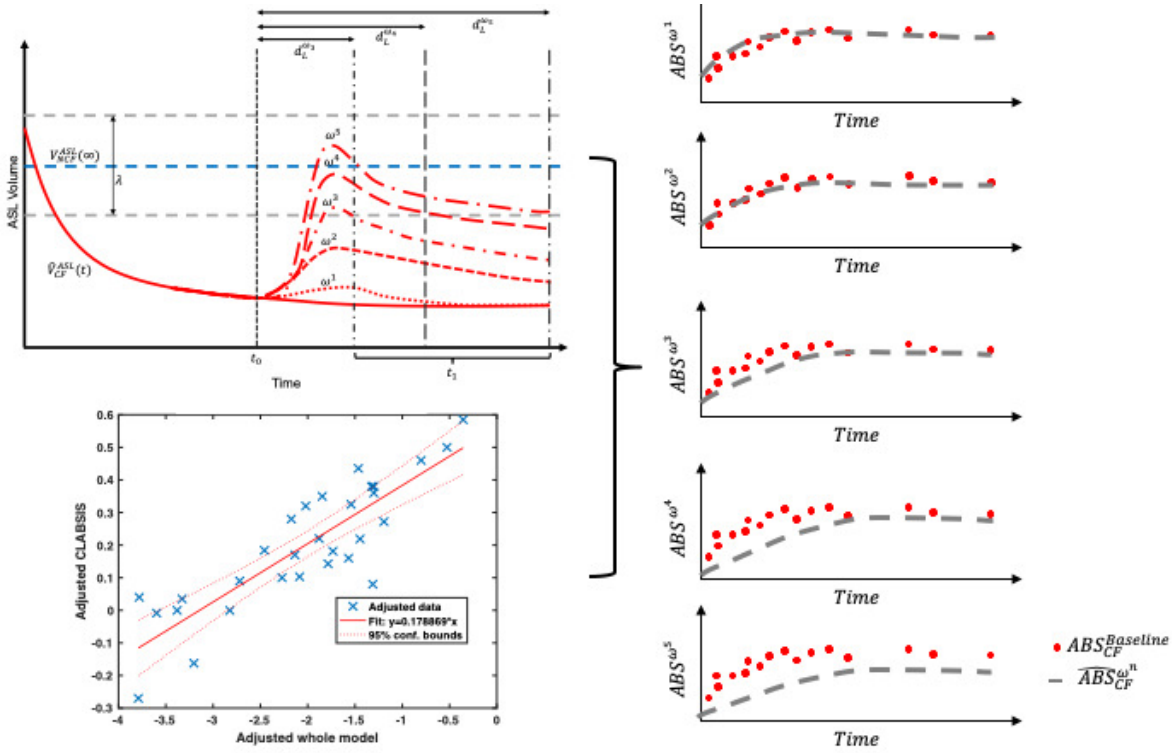

Figure 5.3: Diagram of steps necessary for the development of a therapy design framework at the cell-scale. The project would required the development of a library of dose-response osmotic therapy ASL volume changes *in vitro*, use the responses and the resulting correlations to inform a non-linear, mix integer optimization problem that can be translate to *in vivo*-level response.

5.2.3 Development of a CF Clinical Decision Support System

Current trends in CF therapeutics development indicate that future therapies are likely to be genotype specific, possibly even patient specific, and that patients may require different combinations of medications designed to both potentiate CFTR channels and ameliorate existing airway damage [16, 40, 64, 92, 158, 164, 191]. In fact, there has been significant

progress in theratyping of rare CF mutations. Theratyping focuses in evaluating the clinical response to different treatments on an individual basis. This overcomes the limitations of genotype to predict response to individual therapies and includes all patients regardless of CFTR variations. For example, the use of organoids from rectal biopsies in high throughput screening has allowed numerous compounds to be tested on patient-specific tissue pre-clinically [37, 147]. Similarly, recent work has led to the better understanding of the pharmacological mechanism different CFTR modulators used to correct distinct CF-causing variants, including rare combinations [4, 139, 149, 186]. This could lead to the extension of theratyping beyond CFTR modulators. Specifically, creating a push for the design of more targeted prophylactic or ameliorative therapies. Recognition of the clinical importance of CF theratypic variants could potentially extend to the formal definition of CF disease endotypes.

In fact, there has recently been a concerted effort in the optimization and full characterization of novel *in vitro* models of CF pathophysiology [147]. Human nasal epithelial cultures are one of these models, and the work presented in this dissertation provides a strong foundation for the better understanding of its physiological relevance in CF airway disease. Furthermore, recent studies have demonstrated the viability of recovering HNE cells from infants [129]. This provides a glimpse to a future where *in vitro* samples and clinical measurements are acquired and used to inform computational clinical decision support systems (DSS) with the ultimate goal of designing prophylactic strategies early in life, before clinical pathology is demonstrated, potentially stalling disease progression or even pathogenesis.

Furthermore, the availability of more sophisticated, interlinking models that provide a better indication of therapeutic efficacy based on *in vitro* studies would facilitate the more rapid development of these therapies. They could provide a much needed bridge between exploratory studies performed on sampled nasal cell cultures or through functionalized *in vivo* imaging and the design of more optimized and personalized medication choices and dosing schedules, as described in the previous section. A general framework for such a platform is depicted in Figure 5.4. The development and integration of the models described here is a key step in realizing this vision.

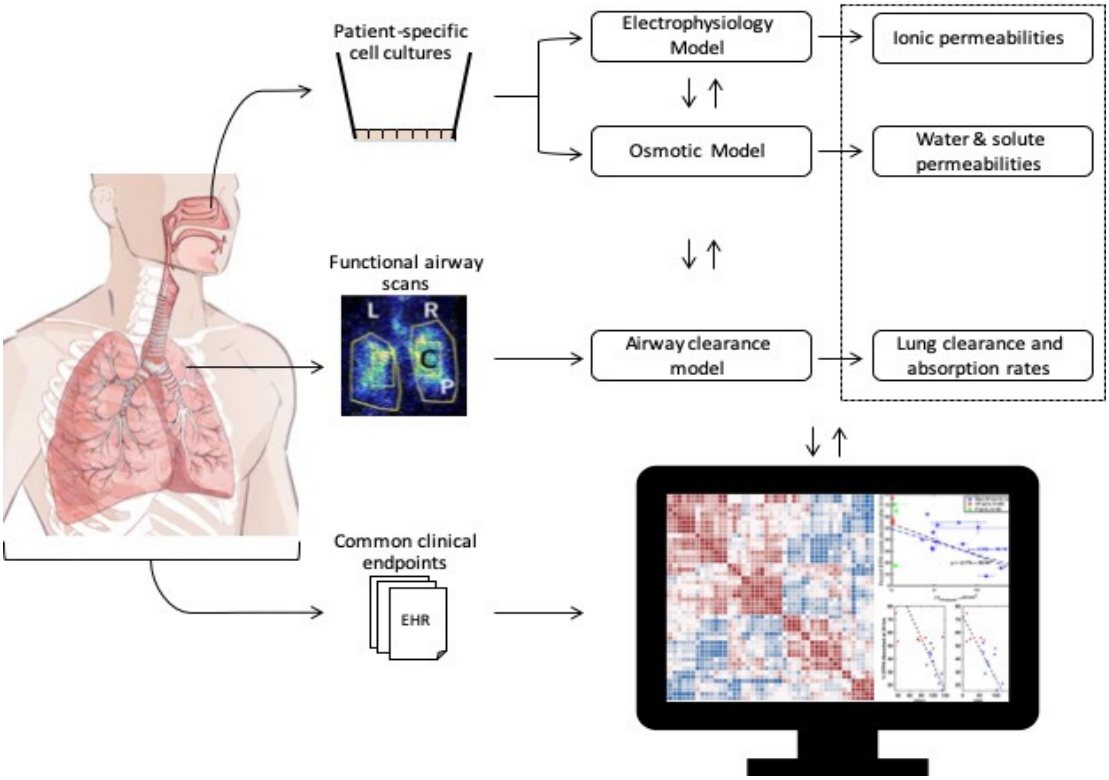

Figure 5.4: Diagram of potential Cystic Fibrosis clinical decision support system (DSS) incorporating a combination of genetic, *in vitro*, *in vivo*, and *in silico* physiological measurements to predict clinical outcomes for individual patients.

Appendix A

Human Nasal Epithelia (HNE) Cell Cultures

A.1 Protocol

A.1.1 Processing

Ussing a 1000uL pipette tip, scrape pipette tip across the brush to harvested cells. Rinse brush and pipette tip with 1-2 mL of sterile PBS to remove cells. Centrifuge sample at 300G at 4C for 5 min. Resuspend cell pellets in 5 mL Accusate, incubate at 37C with occasional agitation until pellet disperses, approximately 5-10 min. Centrifuge sample at 300G at 4C for 5 min. Resuspend pellet in 10 mL PBS and centrifuge at 300G at 4C for 5 min. Remove supernatant and resuspend each cell pellet in media for culture as below.

A.1.2 Expansion: Co-Culture Method

Pre-seed feeder cells (irradiated 3T3-J2, mouse fibroblast cell line) for 24 hours in the well of a 6 well plate with complete growth media (CGM). Typically, you will seed 400,000 3T3-J2 cells per well the day before receiving the nasal sample. Immediately prior to seeding epithelial cells, aspirate CGM and wash with sterile PBS. Resuspend epithelia cells in Georgetown media (GM), then place onto feeder cell plate. Use 2.5 mL of GM per well; seed a minimum of 500,000 epithelial cells per well for initial seed. Leave undisturbed for 48 hours. Co-culture should be checked, and media changed daily, with at least one DPBS wash per week. For further passages, 1:3 to 1:4 ratio of epithelia to feeder cells yields a co-culture that is ready for subsequent passage in 3-5 days. Ideally, cells should be passaged when the epithelial cells reach 70% confluence. If confluence exceeds 70%, multiple trypsinization (see below, 5-8 minutes each) need to be performed to optimize viability of the cells.

A.1.3 Trypsinization

Wash the plates with PBS once. Add a 1.5 mL of warm dark trypsin solution per per well of 6 well plate to remove the feeders. Swirl gently to coat and incubate the 37C for exactly 2 minute. Observe cells in microscope to verify that feeder cells have fully detached. Swirl/tap gently, if necessary. GENTLY add PBS, swirl and tilt dish to aspirate feeders. If performed too forcefully, epithelial cells can be dislodged and lost. Add 3 mL of trypsin solution per well of 6 well plate and incubate at 37C for 8-10 minutes to detach the remaining epithelial cells. Add an equal amount of TNS and collect mixture in a labeled 50 mL conical tube and place on ice. Centrifuge at 900rpm at 4C for 5 minutes. Remove supernatant and re-suspend cells in GM with a target of 1 x 106 cells per mL. Typical volumes range from 1-5mL. Count and determine the volume of cell suspension needed for plating on filters for re-differentiation and/or reseeding as co-culture Remaining cells not used for platting can be centrifuged and resuspended in DMEM/F-12 media to be frozen.

A.1.4 ALI Culture

Coat filters (Transwell) with Human placental collagen. Seed cells on filters at a seeding density of up to 300-250K cells per cm^2 (P3) or 300K cells per cm^2 (P4+). Submerged cultures in GM on filters for 24-48 hours (or until confluent) changing media every 24 hours. After cells are ¿90% confluent, remove GM media and culture cells submerged UNC media for 24 hours, then switch to ALI conditions. Culture at ALI for 28 days before evaluating electrophysiology and/or epithelial transport. Change media as appropriate, minimum is every other day basolaterally during early stages and 3X times weekly once established, with weekly sterile DPBS apical wash of approximately 50-100uL per filter.

A.2 Media Recipes

A.2.1 Complete Growth Media (CGM)

: 500 mL DMEM (H) (Gibco: 11965-092) + 50 mL fetal bovine serum (Gibco: 16140-071) + 5.5 mL 100x glutamine (Gibco: 25030-081) + 5.5 mL pen/strep (Gibco: 15140-122). Sterile. Store at 4C.

A.2.2 Georgetown Media (GM)

: 373 mL DMEM (H) (Gibco: 11965-092) + 125mL F12 nutirent mix (Gibco: 11765-054) + 0.5 mL Hydrocortizone/EGF mix (Dissolve hydrocortisone (Sigma H0888) in 100% ethanol at 0.5mg/ml. Mix 1mL of this with 19 mL DMEM containing 2.5 ug EGF (Invitrogen PHG0311 or PHG0311L)) + 0.5 mL insulin (Dissolve 100 mg insulin (Sigma I5500 or I2643) in 20 mL distilled water containing 200 uL glacial acetic acid) +0.5 mL Fungizone/Amphotericin B (Fisher: BP264550) + 0.5 Gentamicin (Gibco: 15710-064) + 4.3 L cholera toxin (Dissolve 1 mg vial of cholera toxin (Sigma C8052) in 1 mL distilled water and filter sterilize) + 0.5 mL Y-27632 (Axxora: ALX-270-333-M025. Dissolve 25 mg with sterile water to a concentration of 5 mM).

Appendix B

Ussing Chamber characterization of CF Primary Airway Epithelial Cell Cultures Following CFTR Modulator treatments

B.1 Protocol

1. Wash the apical side of the membrane for 15 minutes with $20\mu L$ of warm (37 degrees) DPBS solution at least 2 days prior to the experiments. Make sure to not disturb the monolayer when suctioning the apical wash. DPBS is used in order to minimize any disruption to the tight junctions during the wash.
2. VX-809 (or VX-661 if applicable) should be added to the basolateral media at a $3\mu M$ final concentration. Filters should be fed with freshly made VX-809 in media 48 and 24 hours prior to the chamber run. Prior testing has shown that in HBEs $\Delta I_{Forskolin}$ peaks after 48-72 hours of corrector treatment. However, it also showed longer treatment times abrogate this effect, possibly due to excessive exposure to DMSO. When using VX-809, I advise to check the cell line's genotype before starting the treatment. Experience suggest that filters with even a single nonsense or frameshift mutation (those producing no CFTR at all) tend to show negligible to no response to the treatment.
3. The potentiator, VX-770, is added acutely during the Ussing chamber run. It is prepared in DMSO and added to obtain a final chamber concentration of 100 nM. Stock solution is usually prepared at a 1000x concentration in order to facilitate addition during the run. For the purposes of data incorporation into the model, try to add VX770 at the same time as Forskolin.
4. The bath solutions should be normal Ringers with Bicarb on both the apical and basolateral sides of the cell. Some experiments will be run on the presence of a Cl^- gradient (High Cl- Ringers basolaterally and Normal Cl^- Ringers apically). 5 mL of solution should be added to both the apical and the basolateral chambers and bubbled with 5%-

CO2 95% air bubbled through for mixing purposes. In cases were the experiments are ran in the absence of Bicarbonate, use the fish pump to bubble the chambers. This will remove the CO_2 and make sure the chambers solutions do not produce bicarbonate from it.

5. It is important to allow sufficient time in between different drug additions during the run, so the filter can re-stabilize and reach a new steady state. 5 minutes is typically sufficient. Similarly, it is important to allow the baseline current to stabilize prior to the addition of any drugs. This process varies across cell-lines and can take as long as 30 minutes.
6. Please verified the specific drug additions for each experiment. A traditional corrector Ussing Chamber uses the following addition order: Amiloride → Forskolin → VX-770 → CFIhn172 → Bumetanide

B.1.1 Other chemicals used

- Amiloride: 5 L at 10mM concentration, to achieve a chamber concentration of 10 M is added directly to the apical chamber once the current has stabilized. The stock is prepared and kept in aluminum foil to eliminate exposure to light.
- Forskolin: 5 L at 10 mM concentration to achieve a chamber concentration of 10 M is added directly to the basolateral after the current has stabilized from the Amiloride addition usually 5 minutes after the Amiloride addition.
- CF Inh 172: 5 L at 20 mM concentration to achieve a chamber concentration of 20 M is added directly to the apical chamber after the current has stabilized from the VX-770/Forskolin addition.
- Bumetanide: 5 L at 50 mM concentration to achieve a chamber concentration of 50 M is added directly to the basolateral chamber after the current has stabilized from the CF172 addition usually 5 minutes.

Appendix C

Experimental Protocol to Assess Apical ASL and Tc-DTPA Retention

C.1 DTPA Experimental Protocol

1. Day before the experiment, call Cardinal Health to order radioactive material (412-227-0911), tell them its for the Corcoran Lab. Order 5 mCi sodium pertechnetate in a 1mL solution and 1 DTPA cold kit. There are a few spares in the hot lab if needed (quite rarely). Replace the spares every couple of months as they do expire.
2. Day of experiment, collect your radioactive material and DTPA cold kit from nuclear medicine in Presby.
3. In the hot lab, over an absorbent blue pad, carefully add the 1mL of 5mCi sodium pertechnetate to the DTPA cold kit vial.
4. Add 4mL of saline to the DTPA cold kit vial. The final volume of DTPA-Tc to be 5mL so if they give you the sodium pertechnetate at a different volume, just adjust the amount of saline to add so you have a final volume of 5mL (which is 1mCi/mL).
5. Allow the DTPA and sodium pertechnetate to bind for 15 minutes.
6. While you are waiting, scan the plates of cells for time point = -1.
7. After 15 minutes, remove a small sample of the DTPA-Tc into a separate microtube.
8. Perform QC by obtaining one red and one black chromatography strip. Place a 1.5uL drop of DTPA-Tc at the bottom line of the strip. Place the red strip in a glass vial with a small amount of acetone and the black strip in a glass vial with a small amount of saline. NOTE: you do not want the strip to touch the sides of the glass vial, simply place the strip in the vial so that the bottom is in the solution and the top of the strip leans against the top of the glass vial (if the strip touches the sides, it can throw off your result).
9. Place microtube with DTPA-Tc in a lead container to test the QC.

10. Cut the strips so each number is separate.

11. Check the radioactivity for each strip 1 and 4 should be high, 2 and 3 should be low. If your results are not correct, your kit failed and you must start again with fresh sodium pertechnetate.

12. Mix $10\mu L$ of the DTPA-Tc with $990\mu L$ of ringers made the previous day.

13. Add $10\mu L$ of the ringers + DTPA-Tc to the apical side of each filter

14. At the start of reading each plate, check the background (place the plate behind the lead sheet).

15. Read the radioactivity on each filter keeping the remainder of the plate behind the lead sheet.

16. Once complete, scan the plate for ASL volume.

17. Keep the plate in the incubator between time points.

18. Repeat read/scan for time 2, 4, 6, 8, 12, 24 hours.

C.1.1 Tips and Tricks

- When starting the experiment, treat one plate at a time. So treat a plate, do the reading/scan, then start the next one. Otherwise, your first time point is not truly time zero.
- When taking the plates out of the incubator, take one plate at a time. The change in temperature and gas does have an affect.
- When adding the Ringers + DTPA-Tc to the cells, you want to slowly dispense the solution to form a ball at the end of the pipet. That way only the ball of solution touches the cells and it will help to avoid disturbing the cell layer.
- Ringers should be used warm, so if you stored in the fridge overnight, place it in the water bath prior to use.

C.2 Using the Scanner for ASL volume measurement

1. Open the Scanner program on the computer
   a. EPSON scan
   b. bottom left icon on desktop
2. When the screen pops up, under SETTING Name Setting 2
3. Click Preview
4. Once the preview happens, click on Scan
5. A third screen will pop up
   a. Navigate to location → other → browse, and select the folder for which you want to place your images
   b. File name: Cell type prefix + 3 digit line number → Prefix → how you want to save your images. The standard lab practice for labeling is "date−cell line−experimental conditions−timepoint−".
   c. Place the plate on the scanner with the rounded edges toward you
   d. Slide the plate down and to the right within the template
   e. OK
6. When the scanner is done scanning the image, the folder you saved the image in will pop up and you can check your image.

C.2.1 Tips and Tricks

- Clean the condensation off the top of the filter plate (in the hood if you are keeping the cells sterile).
- Wipe any unnecessary smudges off the top and bottom of the plate.
- If the scanner stops connecting with the computer, check the connections in the back of the scanner. Tighten them and then restart the program.
- Check the images after scanning to ensure they are of good quality.

Appendix D

Code for Models

D.1 Thin Film Model of Airway Epithelial Liquid and Solute Transport

```
import aptmodel as apt
import numpy as np
import importlib
importlib.reload(apt)

# Initialize model
model = apt.aptmodel()
model.set_include_path('/usr/local/include')
model.set_lib_path('/usr/local/lib')

# Parameters
model.add_par('Pwca', 10200, 18000) #cellular-apical water permeability
model.add_par('Pwcb', 8000, 18000) #cellular-basolateral water permeability
model.add_par('Pwab', 72000, 120000) #paracellular water permeability
model.add_par('Penac', 0.06, 6) #ENaC permeability
model.add_par('Pcftr', 0.06, 6) #CFTR permeability
model.add_par('Pacc', 0.06, 6) #CaCC permeability
model.add_par('Pbk', 0.06, 6) #basolateral potassium permeability
model.add_par('Pbcl', 0.06, 6) #basolateral chloride permeability
model.add_par('Pbkca', 0.06, 6) #BKCa permeability
model.add_par('Jnakp', 0.6, 60) #NaKP flux
model.add_par('Jnkcc', 0.6, 60) #NKCC flux
model.add_par('Ppna', 0.06, 6) #Na paracellular permeability
model.add_par('Ppcl', 0.06, 6) #Cl paracellular permeability
model.add_par('Ppk', 0.06, 6) #K paraceullar permeability
model.add_par('Ppdt', 6, 10) #6-10 micrometers per second

# States
model.add_states('Vap')
model.add_states('Naap')
model.add_states('Clap')
model.add_states('Kap')
model.add_states('dtpa')
model.add_states('Vb')
model.add_states('Nab')
model.add_states('Clb')
model.add_states('Kb')
model.add_states('dtpb')
model.add_states('Vc')
model.add_states('Nac')
model.add_states('Clc')
model.add_states('Kc')
model.add_states('Ema')
model.add_states('Emb')

# Constants

model.ODE['Constants'].add_helper('Oapn = 0.0375') #apical nonperm. osmolarity (mosmol/min)
model.ODE['Constants'].add_helper('Obn = 0.0625') #basolateral nonperm. osmolarity (mosmol/min)
model.ODE['Constants'].add_helper('Ocn = 0.145') #cellular nonperm. osmolarity (mosmol/min)
model.ODE['Constants'].add_helper('Dtj = 0.006') #tight junction diameter (microns)
model.ODE['Constants'].add_helper('Dc = 8') #cell diameter (microns)
model.ODE['Constants'].add_helper('Atj = 0.000494238') #tight junction area (cm2)
```

```
69   model.ODE['Constants'].add_helper('Ama = 0.329505742') #apical cell area (cm2)
70   model.ODE['Constants'].add_helper('Amb = 3.295057417') #basolateral cell area (cm2)
71   model.ODE['Constants'].add_helper('hc0 = 0.00302') #cell hight (cm)
72   model.ODE['Constants'].add_helper('T = 310') #temperature (K)
73   model.ODE['Constants'].add_helper('F = 96485') #Faraday's constant (C/mol)
74   model.ODE['Constants'].add_helper('R = 8.314') #ideal gas constant (J/molK)
75   model.ODE['Constants'].add_helper('Vnakp_na = 0.0157') #half max [Na] to bind to nakp (mmol/ml)
76   model.ODE['Constants'].add_helper('Vnakp_k = 0.0019') #half max [K] to bind to nakp (mmol/ml)
77   model.ODE['Constants'].add_helper('Vnkcc_na = 0.105') #half max [Na] to bind to nkcc (mmol/ml)
78   model.ODE['Constants'].add_helper('Vnkcc_k = 0.00122') #half max [K] to bind to nkcc (mmol/ml)
79   model.ODE['Constants'].add_helper('Vnkcc_cl1 = 0.103') #half max [Cl1] to bind to nkcc (mmol/ml)
80   model.ODE['Constants'].add_helper('Vnkcc_cl2 = 0.0239') #half max [Cl2] to bind to nkcc (mol/ml)
81   model.ODE['Constants'].add_helper('Vw = 0.018') #molar volume of water (ml/mmol)
82   model.ODE['Constants'].add_helper('zna = 1') #charge of Na
83   model.ODE['Constants'].add_helper('zk = 1') #charge of K
84   model.ODE['Constants'].add_helper('zcl = -1') #charge of Cl
85   model.ODE['Constants'].add_helper('u = 37.43588') #F/TR (C/J)
86   model.ODE['Constants'].add_helper('Vcplus = 0.00125') #max cell vol
87   model.ODE['Constants'].add_helper('Vcminus = 0.0008') #min cell vol
88   model.ODE['Constants'].add_helper('Cap = 3.23') #muF/cm2
89   model.ODE['Constants'].add_helper('eta = 50')
90   model.ODE['Constants'].add_helper('M = 10') #muF/cm2
91   model.ODE['Constants'].add_helper('VapHalf = 10.5*pow(10,-3)')
92   model.ODE['Constants'].add_helper('n = 2') #muF/cm2
93   model.ODE['Constants'].add_helper('Cb = 33.14')
94   model.ODE['Constants'].add_helper('ee = 2.71828182845904523536')
95
96
97   #note: add_helper can be used to define
98
99   #flux term definitions
100  # Jpnac --> ((Naap/Vap*Vw*Pwab*((Nab + Kb + Clb)/Vb + Obn - (Naap + Kap + Clap)/Vap - Oapn)*(1./(1+ex
101  # Jpclc --> ((Clap/Vap*Vw*Pwab*((Nab + Kb + Clb)/Vb + Obn - (Naap + Kap + Clap)/Vap - Oapn)*(1./(1+ex
102  # Jpkc  --> ((Kap/Vap*Vw*Pwab*((Nab + Kb + Clb)/Vb + Obn - (Naap + Kap + Clap)/Vap - Oapn)*(1./(1+exp
103  #Jdtpc -->  ((dtpa/Vap*Vw*Pwab*((Nab + Kb + Clb)/Vb + Obn - (Naap + Kap + Clap)/Vap - Oapn)*(1./(1+ex
104
105  #    EnacHill = (Vap/(VapHalf+1))**n
106  # Jenac --> ((Penac*zna*u*Ema*(Naap/Vap-Nac/Vc*exp(zna*u*Ema)) / (exp(zna*u*Ema)-1))/10**4)*Ama*pow((
107  # Jcftr --> ((Pcftr*zcl*u*Ema*(Clap/Vap-Clc/Vc*exp(zcl*u*Ema)) / (exp(zcl*u*Ema)-1))/10**4)*Ama
108  # Jacc --> ((Pacc*zcl*u*Ema*(Clap/Vap-Clc/Vc*exp(zcl*u*Ema)) / (exp(zcl*u*Ema)-1))/10**4)*Ama
109  # Jbkca --> ((Pbkca*zk*u*Ema*(Kap/Vap-Kc/Vc*exp(zk*u*Ema)) / (exp(zk*u*Ema)-1))/10**4)*Ama
110  # Jbcl --> ((Pbcl*zcl*u*Emb*(Clb/Vb-Clc/Vc*exp(zcl*u*Emb)) / (exp(zcl*u*Emb)-1))/10**4)*Amb
111  # Jbk -->  ((Pbk*zk*u*Emb*(Kb/Vb-Kc/Vc*exp(zk*u*Emb)) / (exp(zk*u*Emb)-1))/10**4)*Amb
112  # Jnakpf --> Jnakp*Amb/10**4*(5*Emb+1.25)/(((Vnakp_na*Vc/Nac)**3+1)*((Vnakp_k*Vb/Kb)**2+1))
113  #    Nhillf = ((Vnkcc_na*Vb/Nab+1)*(Vnkcc_k*Vb/Kb+1) * (Vnkcc_cl1*Vb/Clb+1)*(Vnkcc_cl2*Vb/Clb+1))
114  # Jnkccf = Jnkcc*Amb/10**4/((Vnkcc_na*Vb/Nab+1)*(Vnkcc_k*Vb/Kb+1) * (Vnkcc_cl1*Vb/Clb+1)*(Vnkcc_cl2*V
115
116
117  # Qrvd = (Jnkcc*Amb/10**4)*(1+(M/(1+exp(-eta*(Vc-Vcplus)))))
118  # Qrvi = (Jnkcc*Amb/10**4)*(1+(M/(1+exp(-eta*(Vcminus-Vc)))))
119
120  # Diff Eqs
121
```

```
122
123   model.ODE['Vap'].set('(-Pwca*Vw*Ama*((Nac+Kc+Clc)/Vc + Ocn - (Naap + Kap + Clap)/Vap - Oapn) - Pwab*V
124   # dNaap/dt = Jpnac - Jpnad - Jenac
125
126   model.ODE['Naap'].set('-((Naap/Vap*Vw*Pwab*((Nab + Kb + Clb)/Vb + Obn - (Naap + Kap + Clap)/Vap - Oap
127
128   #dClap/dt = Jpclc - Jpcld - Jcftr - Jacc
129
130   model.ODE['Clap'].set('-((Clap/Vap*Vw*Pwab*((Nab + Kb + Clb)/Vb + Obn - (Naap + Kap + Clap)/Vap - Oap
131
132   #dKap/dt = Jpkc - Jpkd - Jbkca
133
134   model.ODE['Kap'].set('-((Kap/Vap*Vw*Pwab*((Nab + Kb + Clb)/Vb + Obn - (Naap + Kap + Clap)/Vap - Oapn)
135
136   #ddpta/dt = Jdtpc - Jdtpd
137
138   model.ODE['dtpa'].set('-((dtpa/Vap*Vw*Pwab*((Nab + Kb + Clb)/Vb + Obn - (Naap + Kap + Clap)/Vap - Oap
139
140   model.ODE['Vb'].set('(Pwcb*Vw*Amb*((Nab + Kb + Clb)/Vb + Obn - (Nac + Kc + Clc)/Vc - Ocn) + Pwab*Vw*A
141
142   #DNab/dt = Jpnac + Jpnad - Jnkccf +3Jnakpf - Qrdi
143
144   model.ODE['Nab'].set('((Naap/Vap*Vw*Pwab*((Nab + Kb + Clb)/Vb + Obn - (Naap + Kap + Clap)/Vap - Oapn)
145
146   #dClb/dt = Jpclc + Jpcld -2Jnkccf -Jbcl +Qrvd
147
148   model.ODE['Clb'].set('((Clap/Vap*Vw*Pwab*((Nab + Kb + Clb)/Vb + Obn - (Naap + Kap + Clap)/Vap - Oapn)
149
150   #dKb/dt = Jpkc + Jpkd - Jnkccf -2Jnakpf - Jbk
151
152   model.ODE['Kb'].set('((Kap/Vap*Vw*Pwab*((Nab + Kb + Clb)/Vb + Obn - (Naap + Kap + Clap)/Vap - Oapn)*(
153
154   #ddptab/dt = Jdtpc + Jdtpd
155
156   model.ODE['dtpb'].set('((dtpa/Vap*Vw*Pwab*((Nab + Kb + Clb)/Vb + Obn - (Naap + Kap + Clap)/Vap - Oapn
157
158   model.ODE['Vc'].set('(Pwca*Vw*Ama*((Nac + Kc + Clc)/Vc + Ocn - (Naap + Kap + Clap)/Vap - Oapn) - Pwcb
159
160   #dNac/dt = Jenac + Jnkccf - 3Jnakpf + Qrvi
161
162   model.ODE['Nac'].set('((Penac*zna*u*Ema*(Naap/Vap-Nac/Vc*exp(zna*u*Ema)) / (exp(zna*u*Ema)-1))/pow(10
163
164   #dClc/dt = Jcftr + Jacc + 2Jnkccf + Jbcl - Qrvd
165
166   model.ODE['Clc'].set('((Pcftr*zcl*u*Ema*(Clap/Vap-Clc/Vc*exp(zcl*u*Ema)) / (exp(zcl*u*Ema)-1))/pow(10
167
168   #dKc/dt = Jbkca + Jnkccf + 2Jnakpf + Jbk
169
170   model.ODE['Kc'].set('((Pbkca*zk*u*Ema*(Kap/Vap-Kc/Vc*exp(zk*u*Ema)) / (exp(zk*u*Ema)-1))/pow(10,4))*A
171
172   # dEa/dt = (Ipar + Iap)/(Cap*Ama)/1000000
173   # dEb/dt = (Ipar - Ibl)/(Cb*Amb)/1000000
174
```

```
model.ODE['Ema'].set('((zna*(((Naap/Vap*Vw*Pwab*((Nab + Kb + Clb)/Vb + Obn - (Naap + Kap + Clap)/Vap

model.ODE['Emb'].set('((zna*(((Naap/Vap*Vw*Pwab*((Nab + Kb + Clb)/Vb + Obn - (Naap + Kap + Clap)/Vap


model.showpar()
model.showstates()

# data loading

from scipy.io import loadmat
import numpy as np

voldata = loadmat('CFMultiExperimentData.mat')['p1'] #RENAME WITH ACTUAL FILE NAMES
dtpa = loadmat('CFMultiExperimentData.mat')['dtpa1']
timedata = loadmat('CFMultiExperimentData.mat')['time']
#experiment
experiment1 = apt.experiment('Experiment1')

#aptdata object
aptdata = apt.data(voldata,states=['Vap'], time=timedata, isLog=False)
experiment1.add_data(aptdata)

aptdata = apt.data(dtpa, states=['dtpa'], time = timedata, isLog=False)
experiment1.add_data(aptdata)

initcond = apt.data([107.5*0.0189/pow(10,3), 125*0.0189/pow(10,3), 30*0.0189/pow(10,3), 0.4, 107.5*0.
experiment1.add_data(initcond)

model.add_experiment(experiment1)

voldata = loadmat('CFMultiExperimentData.mat')['p2'] #RENAME WITH ACTUAL FILE NAMES
dtpa = loadmat('CFMultiExperimentData.mat')['dtpa2']
timedata = loadmat('CFMultiExperimentData.mat')['time']
#experiment
experiment2 = apt.experiment('Experiment2')

#aptdata object
aptdata = apt.data(voldata,states=['Vap'], time=timedata, isLog=False)
experiment2.add_data(aptdata)

aptdata = apt.data(dtpa, states=['dtpa'], time = timedata, isLog=False)
experiment2.add_data(aptdata)

initcond = apt.data([107.5*0.0189/pow(10,3), 125*0.0189/pow(10,3), 30*0.0189/pow(10,3), 0.4, 107.5*0.
experiment2.add_data(initcond)

model.add_experiment(experiment2)

voldata = loadmat('CFMultiExperimentData.mat')['p3'] #RENAME WITH ACTUAL FILE NAMES
dtpa = loadmat('CFMultiExperimentData.mat')['dtpa3']
timedata = loadmat('CFMultiExperimentData.mat')['time']
#experiment
```

```
experiment3 = apt.experiment('Experiment3')

#aptdata object
aptdata = apt.data(voldata,states=['Vap'], time=timedata, isLog=False)
experiment3.add_data(aptdata)

aptdata = apt.data(dtpa, states=['dtpa'], time = timedata, isLog=False)
experiment3.add_data(aptdata)

initcond = apt.data([107.5*0.0189/pow(10,3), 125*0.0189/pow(10,3), 30*0.0189/pow(10,3), 0.4, 107.5*0.
experiment3.add_data(initcond)

model.add_experiment(experiment3)

voldata = loadmat('CFMultiExperimentData.mat')['p4'] #RENAME WITH ACTUAL FILE NAMES
dtpa = loadmat('CFMultiExperimentData.mat')['dtpa4']
timedata = loadmat('CFMultiExperimentData.mat')['time']
#experiment
experiment4 = apt.experiment('Experiment4')

#aptdata object
aptdata = apt.data(voldata,states=['Vap'], time=timedata, isLog=False)
experiment4.add_data(aptdata)

aptdata = apt.data(dtpa, states=['dtpa'], time = timedata, isLog=False)
experiment4.add_data(aptdata)

initcond = apt.data([107.5*0.0189/pow(10,3), 125*0.0189/pow(10,3), 30*0.0189/pow(10,3), 0.4, 107.5*0.
experiment4.add_data(initcond)

model.add_experiment(experiment4)

voldata = loadmat('CFMultiExperimentData.mat')['p5'] #RENAME WITH ACTUAL FILE NAMES
dtpa = loadmat('CFMultiExperimentData.mat')['dtpa5']
timedata = loadmat('CFMultiExperimentData.mat')['time']
#experiment
experiment5 = apt.experiment('Experiment5')

#aptdata object
aptdata = apt.data(voldata,states=['Vap'], time=timedata, isLog=False)
experiment5.add_data(aptdata)

aptdata = apt.data(dtpa, states=['dtpa'], time = timedata, isLog=False)
experiment5.add_data(aptdata)

initcond = apt.data([107.5*0.0189/pow(10,3), 125*0.0189/pow(10,3), 30*0.0189/pow(10,3), 0.4, 107.5*0.
experiment5.add_data(initcond)

model.add_experiment(experiment5)

voldata = loadmat('CFMultiExperimentData.mat')['p6'] #RENAME WITH ACTUAL FILE NAMES
dtpa = loadmat('CFMultiExperimentData.mat')['dtpa6']
timedata = loadmat('CFMultiExperimentData.mat')['time']
```

```
#experiment
experiment6 = apt.experiment('Experiment6')

#aptdata object
aptdata = apt.data(voldata,states=['Vap'], time=timedata, isLog=False)
experiment6.add_data(aptdata)

aptdata = apt.data(dtpa, states=['dtpa'], time = timedata, isLog=False)
experiment6.add_data(aptdata)

initcond = apt.data([107.5*0.0189/pow(10,3), 125*0.0189/pow(10,3), 30*0.0189/pow(10,3), 0.4, 107.5*0.
experiment6.add_data(initcond)

model.add_experiment(experiment6)

voldata = loadmat('CFMultiExperimentData.mat')['p7'] #RENAME WITH ACTUAL FILE NAMES
dtpa = loadmat('CFMultiExperimentData.mat')['dtpa7']
timedata = loadmat('CFMultiExperimentData.mat')['time']
#experiment
experiment7 = apt.experiment('Experiment7')

#aptdata object
aptdata = apt.data(voldata,states=['Vap'], time=timedata, isLog=False)
experiment7.add_data(aptdata)

aptdata = apt.data(dtpa, states=['dtpa'], time = timedata, isLog=False)
experiment7.add_data(aptdata)

initcond = apt.data([107.5*0.0189/pow(10,3), 125*0.0189/pow(10,3), 30*0.0189/pow(10,3), 0.4, 107.5*0.
experiment7.add_data(initcond)

model.add_experiment(experiment7)

voldata = loadmat('CFMultiExperimentData.mat')['p8'] #RENAME WITH ACTUAL FILE NAMES
dtpa = loadmat('CFMultiExperimentData.mat')['dtpa8']
timedata = loadmat('CFMultiExperimentData.mat')['time']
#experiment
experiment8 = apt.experiment('Experiment8')

#aptdata object
aptdata = apt.data(voldata,states=['Vap'], time=timedata, isLog=False)
experiment8.add_data(aptdata)

aptdata = apt.data(dtpa, states=['dtpa'], time = timedata, isLog=False)
experiment8.add_data(aptdata)

initcond = apt.data([107.5*0.0189/pow(10,3), 125*0.0189/pow(10,3), 30*0.0189/pow(10,3), 0.4, 107.5*0.
experiment8.add_data(initcond)

model.add_experiment(experiment8)

voldata = loadmat('CFMultiExperimentData.mat')['p9'] #RENAME WITH ACTUAL FILE NAMES
dtpa = loadmat('CFMultiExperimentData.mat')['dtpa9']
```

```
timedata = loadmat('CFMultiExperimentData.mat')['time']
#experiment
experiment9 = apt.experiment('Experiment9')

#aptdata object
aptdata = apt.data(voldata,states=['Vap'], time=timedata, isLog=False)
experiment9.add_data(aptdata)

aptdata = apt.data(dtpa, states=['dtpa'], time = timedata, isLog=False)
experiment9.add_data(aptdata)

initcond = apt.data([107.5*0.0189/pow(10,3), 125*0.0189/pow(10,3), 30*0.0189/pow(10,3), 0.4, 107.5*0.
experiment9.add_data(initcond)

model.add_experiment(experiment9)

voldata = loadmat('CFMultiExperimentData.mat')['p10'] #RENAME WITH ACTUAL FILE NAMES
dtpa = loadmat('CFMultiExperimentData.mat')['dtpa10']
timedata = loadmat('CFMultiExperimentData')['time']
#timedata2 = loadmat('CFMultiExperimentData.mat')['time']
#experiment
experiment10 = apt.experiment('Experiment10')

#aptdata object
aptdata = apt.data(voldata,states=['Vap'], time=timedata, isLog=False)
experiment10.add_data(aptdata)

aptdata = apt.data(dtpa, states=['dtpa'], time = timedata, isLog=False)
experiment10.add_data(aptdata)

initcond = apt.data([107.5*0.0189/pow(10,3), 125*0.0189/pow(10,3), 30*0.0189/pow(10,3), 0.4, 107.5*0.
experiment10.add_data(initcond)

model.add_experiment(experiment10)

voldata = loadmat('CFMultiExperimentData.mat')['p11'] #RENAME WITH ACTUAL FILE NAMES
dtpa = loadmat('CFMultiExperimentData.mat')['dtpa11']
timedata = loadmat('CFMultiExperimentData')['time']
#timedata2 = loadmat('CFMultiExperimentData.mat')['time']
#experiment
experiment11 = apt.experiment('Experiment11')

#aptdata object
aptdata = apt.data(voldata,states=['Vap'], time=timedata, isLog=False)
experiment11.add_data(aptdata)

aptdata = apt.data(dtpa, states=['dtpa'], time = timedata, isLog=False)
experiment11.add_data(aptdata)

initcond = apt.data([107.5*0.0189/pow(10,3), 125*0.0189/pow(10,3), 30*0.0189/pow(10,3), 0.4, 107.5*0.
experiment11.add_data(initcond)

model.add_experiment(experiment11)
```

```
387
388   voldata = loadmat('CFMultiExperimentData.mat')['p12'] #RENAME WITH ACTUAL FILE NAMES
389   dtpa = loadmat('CFMultiExperimentData.mat')['dtpa12']
390   timedata = loadmat('CFMultiExperimentData.mat')['time']
391   #experiment
392   experiment12 = apt.experiment('Experiment12')
393
394   aptdata = apt.data(voldata,states=['Vap'], time=timedata, isLog=False)
395   experiment12.add_data(aptdata)
396
397   aptdata = apt.data(dtpa, states=['dtpa'], time = timedata, isLog=False)
398   experiment12.add_data(aptdata)
399
400   initcond = apt.data([107.5*0.0189/pow(10,3), 125*0.0189/pow(10,3), 30*0.0189/pow(10,3), 0.4, 107.5*0.
401   experiment12.add_data(initcond)
402
403   model.add_experiment(experiment12)
404   #aptdata object
405
406
407   '''voldata = loadmat('CFMultiExperimentData.mat')['p13'] #RENAME WITH ACTUAL FILE NAMES
408   dtpa = loadmat('CFMultiExperimentData.mat')['dtpa13']
409   timedata = loadmat('CFMultiExperimentData.mat')['time2']
410   #timedata2 = loadmat('CFMultiExperimentData.mat')['time']
411   #experiment
412   experiment13 = apt.experiment('Experiment13')
413
414   #aptdata object
415   aptdata = apt.data(voldata,states=['Vap'], time=timedata, isLog=False)
416   experiment13.add_data(aptdata)
417
418   aptdata = apt.data(dtpa, states=['dtpa'], time = timedata2, isLog=False)
419   experiment13.add_data(aptdata)
420
421   initcond = apt.data([107.5*0.0189/pow(10,3), 125*0.0189/pow(10,3), 30*0.0189/pow(10,3), 0.4, 107.5*0.
422   experiment13.add_data(initcond)'''
423
424   #model.add_experiment(experiment13)
425
426   #voldata = loadmat('CFMultiExperimentData.mat')['p14'] #RENAME WITH ACTUAL FILE NAMES
427   #dtpa = loadmat('CFMultiExperimentData.mat')['dtpa14']
428   #timedata = loadmat('CFMultiExperimentData.mat')['time']
429   #experiment
430   experiment14 = apt.experiment('Experiment14')
431
432   #aptdata object
433   aptdata = apt.data(voldata,states=['Vap'], time=timedata, isLog=False)
434   experiment14.add_data(aptdata)
435
436   aptdata = apt.data(dtpa, states=['dtpa'], time = timedata, isLog=False)
437   experiment14.add_data(aptdata)
438
439   initcond = apt.data([107.5*0.0189/pow(10,3), 125*0.0189/pow(10,3), 30*0.0189/pow(10,3), 0.4, 107.5*0.
```

```
449
450   #aptdata object
451   aptdata = apt.data(voldata,states=['Vap'], time=timedata, isLog=False)
452   experiment15.add_data(aptdata)
453
454   aptdata = apt.data(dtpa, states=['dtpa'], time = timedata, isLog=False)
455   experiment15.add_data(aptdata)
456
457
458   initcond = apt.data([107.5*0.0189/pow(10,3), 125*0.0189/pow(10,3), 30*0.0189/pow(10,3), 0.4, 107.5*0.
459   experiment15.add_data(initcond)
460
461   model.add_experiment(experiment15)
462
463   # Create an options variable for model
464   options = apt.aptoptions(maxThr=16)
465   options.nSwap= 1e2
466   options.nTemp = 8
467   options.filename = "IonTransModel_CFMultiExperiment"
468
469   options.show()  # Should run this and double check things are okay before generating
470
471   model.output('IonTransModel_CFMultiExperiment')
472   model.generate(options)
473
```

D.2 Code for Ussing Chamber Electrophysiology Model

```
import math
from pyomo.environ import *
from pyomo.opt import SolverFactory
from pyomo.dae import *
from pyomo.dae.plugins.finitedifference import Finite_Difference_Transformation
from pyomo.dae.plugins.colloc import Collocation_Discretization_Transformation
import pylab
import numpy as np
import scipy as sp
import scipy.io as sio

def UC_PyomoSyst(solver, nfe, stepsize, pfixed, par0):


    #specify the number of finite element
#    mult = 1

#    n_finite_elements = nfe*mult

#   specify the stepsize (in time) for each finite element
#    stepsize = stepsize/mult

    tdata = []
    #tdata.extend([i for i in range(0,3501,1)])
    tdata.extend([i for i in range(0,1010,10)])

    #Create ODE Model
    model = ConcreteModel()
    model.t = ContinuousSet(initialize = tdata)
    model.time = Set(initialize = tdata, within = model.t, ordered = True)


    Nac0 = par0[0]
    Clc0 = par0[1]
    Kc0 = par0[2]
    Vc0 = par0[3]
    Oc0 = par0[4]

    Fenac0 = par0[5]
    Fcftr0 = par0[6]
    Facc0 = par0[7]
    Fbkca0 = par0[8]
    Fbk0 = par0[9]
    Fbcl0 = par0[10]
    Fnkccr0 = par0[11]
    Fnkccf0 = par0[12]
    Fnakp0 = par0[13]
    Fae0 = par0[14]
    Fnhe0 = par0[15]
    Fnbc0 = par0[16]
    Fkhp0 = par0[17]

    Ema0 = par0[18]
```

```
56      Emb0 = par0[19]
57
58
59
60  #    p  = [Penac, Pcftr, Pacc, Pbkca, Pbk, Pbcl,\
61  #          Jnkcc, Jnakp, Jnhe, Jae, Jnbc, Jkhp,  Pw,
62  #          Naa, Cla, Ka, Va, Oa0, Nab, Clb, Kb, Vb, Ob0, Oic0,\
63  #           Venac, Vcftr, Vtmem, Vbkca, Vnkcc_na, Vnkcc_k,\
64  #          Vnkcc_cl1, Vnkcc_cl2, Vnakp_na, Vnakp_k, Vnhe_na, Vae_cl, Vnbc_na,\
65  #          Amil, Forsk, But]
66
67      #Cellular states
68      model.Nac = Var(model.t, bounds=(Nac0*0.75,Nac0*1.5), initialize=(Nac0)) #guessed bounds, mM
69      model.dNacdt = DerivativeVar(model.Nac, wrt = model.t)
70
71      model.Clc = Var(model.t, bounds=(Clc0*0.75,Clc0*1.5), initialize=(Clc0)) #guessed bounds, mM
72      model.dClcdt = DerivativeVar(model.Clc, wrt = model.t)
73
74      model.Kc = Var(model.t, bounds=(Kc0*0.75,Kc0*1.5), initialize=(Kc0)) #Guess bounds, mM
75      model.dKcdt = DerivativeVar(model.Kc, wrt = model.t)
76
77      model.Vc = Var(model.t, bounds=(0.85,1.25), initialize=(Vc0)) #Guess Bounds, Check! ul
78      model.dVcdt = DerivativeVar(model.Vc, wrt = model.t)
79
80      model.Oc = Var(model.t, bounds=(250,350), initialize=(Oc0)) #Guess Bounds, mOsmls
81      model.dOcdt = DerivativeVar(model.Oc, wrt = model.t)
82
83      #Channel states
84      #model.Fenac = Var(model.FE, initialize=(Fenac0))
85      model.dFenacdt = Var(model.t)
86
87      #model.Fcftr = Var(model.FE, initialize=(Fcftr0))
88      model.dFcftrdt = Var(model.t)
89
90      #model.Facc = Var(model.FE, initialize=(Facc0))
91      model.dFaccdt = Var(model.t)
92
93      #model.Fbkca = Var(model.FE, initialize=(Fbkca0))
94      model.dFbkcadt = Var(model.t)
95
96      #model.Fbk = Var(model.FE, initialize=(Fbk0))
97      model.dFbkdt = Var(model.t)
98
99      #model.Fbcl = Var(model.FE, initialize=(Fbcl0))
100     model.dFbcldt = Var(model.t)
101
102     #model.Fnkccr = Var(model.FE, initialize=(Fnkccr0))
103     model.dFnkccrdt = Var(model.t)
104
105     #model.Fnkccf = Var(model.FE, initialize=(Fnkccf0))
106     model.dFnkccfdt = Var(model.t)
107
108     #model.Fnakp = Var(model.FE, initialize=(Fnakp0))
```

```
    model.dFnakpdt = Var(model.t)

    #model.Fae = Var(model.FE, initialize=(Fae0))
    #model.dFaedt = Var(model.t)

    #model.Fnhe = Var(model.FE, initialize=(Fnhe0))
    #model.dFnhedt = Var(model.t)

    #model.Fnbc = Var(model.FE, initialize=(Fnbc0))
    #model.dFnbcdt = Var(model.t)

    #model.Fkhp = Var(model.FE, initialize=(Fkhp0))
    model.dFkhpdt = Var(model.t)

    #channel states
    # model.Penac = Var(bounds=(1e-9,9e-7), initialize=(pfixed[0]))
    # model.Pcftr = Var(bounds=(1e-9,9e-7), initialize=(pfixed[1]))
    # model.Pacc = Var(bounds=(1e-9,9e-7), initialize=(pfixed[2]))
    # model.Pbkca = Var(bounds=(1e-9,9e-7), initialize=(pfixed[3]))
    # model.Pbk = Var(bounds=(1e-9,1e-8), initialize=(pfixed[4]))
    # model.Pbcl = Var(bounds=(1e-9,1e-8), initialize=(pfixed[5]))
    # model.Jnkcc = Var(bounds=(1e-7,1e-6), initialize=(pfixed[6])) #reduced upper boudsn 10fold....
    # model.Jnakp = Var(bounds=(1e-7,1e-6), initialize=(pfixed[7]))
    # model.Jnhe = pfixed[8]#Var(bounds=(1e-9,1e-7), initialize=(pfixed[8]))
    # model.Jae = pfixed[9]#Var(bounds=(1e-9,1e-7), initialize=(pfixed[9]))
    # model.Jnbc = pfixed[10]#Var(bounds=(1e-9,1e-7), initialize=(pfixed[10]))
    # model.Jkhp = Var(bounds=(1e-9,5e-7), initialize=(pfixed[11]))
    #
    #
    model.Penac = Var(bounds=(1e-11,1e-5), initialize=(pfixed[0]*1.2))
    model.Pcftr = 1e-19; #Var(bounds=(1e-10,1e-5), initialize=(pfixed[1]*0.8))
    model.Pacc = Var(bounds=(1e-11,1e-5), initialize=(pfixed[2])*1.1)
    model.Pbkca = Var(bounds=(1e-11,1e-5), initialize=(pfixed[3]*0.8))
    model.Pbk = Var(bounds=(1e-11,1e-6), initialize=(pfixed[4]))
    model.Pbcl = Var(bounds=(1e-11,1e-6), initialize=(pfixed[5]))
    model.Jnkcc = Var(bounds=(1e-9,1e-5), initialize=(pfixed[6])) #reduced upper boudsn 10fold....
    model.Jnakp = Var(bounds=(1e-9,1e-5), initialize=(pfixed[7]))
    model.Jnhe = pfixed[8]#Var(bounds=(1e-9,1e-7), initialize=(pfixed[8]))
    model.Jae = pfixed[9]#Var(bounds=(1e-9,1e-7), initialize=(pfixed[9]))
    model.Jnbc = pfixed[10]#Var(bounds=(1e-9,1e-7), initialize=(pfixed[10]))
    model.Jkhp = Var(bounds=(1e-11,5e-6), initialize=(pfixed[11]))

    #water permeabilities
    model.Pw = Var(bounds=(200,230), initialize=(pfixed[12]))
    model.Vw = pfixed[49]  #m^3/mol

    #Membrane potentials
    model.Ema = Var(model.t, bounds=(-0.1, -0.003), domain = Reals) #, initialize = Ema0
    model.Emb = Var(model.t, bounds=(0.003, 0.1), domain = Reals) # , initialize = Emb0

    #Membrane Currents
    model.Iap = Var(model.t, bounds=(1,100))
    model.Ibl = Var(model.t, bounds=(1,100))
```

```
162
163     #Apical and Basolateral chamber conditions, ten dto be constant
164     model.Naa = pfixed[13]
165     model.Cla = pfixed[14]
166     model.Ka = pfixed[15]
167     model.Va = pfixed[16]
168     model.Oa0 = pfixed[17]
169     model.Nab = pfixed[18]
170     model.Clb = pfixed[19]
171     model.Kb = pfixed[20]
172     model.Vb = pfixed[21]
173     model.Ob0 = pfixed[22]
174
175
176     #Hill half-permeabilities, and coefficients
177     model.Venac = pfixed[23]
178     model.Vcftr = pfixed[24]
179     model.Vacc = pfixed[25]
180     model.Vbkca = pfixed[26]
181
182     model.Vnkcc_na = pfixed[27]
183     model.Vnkcc_k = pfixed[28]
184     model.Vnkcc_cl1 = pfixed[29]
185     model.Vnkcc_cl2 = pfixed[30]
186
187     model.Vnakp_na = pfixed[31]
188     model.Vnakp_k = pfixed[32]
189
190     model.Vnhe_na = pfixed[33]
191     model.Vae_cl = pfixed[34]
192     model.Vnbc_na = pfixed[35]
193
194     model.Vae_hco = pfixed[36]
195     model.Vnhe_h = pfixed[37]
196     model.Vnbc_hco = pfixed[38]
197
198     model.Kp_ae = pfixed[39]
199     model.Kp_nhe = pfixed[40]
200     model.Kp_nbc = pfixed[41]
201
202     model.HCOc = pfixed[42]
203     model.Hc = pfixed[43]
204     model.HCOb = pfixed[44]
205
206     model.pHc = pfixed[45]
207     model.ap_nbc = pfixed[46]
208     model.ap_nhe = pfixed[47]
209     model.ap_ae = pfixed[48]
210
211     model.Ama = pfixed[50]
212     model.Amb = pfixed[51]
213
214
```

```
215     #Valence
216     model.zna = 1
217     model.zcl = -1
218     model.zk = 1
219
220     #Electric Constants
221     model.F = 96485 # mA/mmol
222     model.R = 8.314 # J/Mol K
223     model.T = 310 # K
224     model.u = model.F/(model.R*model.T)
225
226     # Nak pump
227     #def Nakhill_fun(m, fe):
228     #    return Nakhill[fe] == (((m.Vnakp_na*m.Vc[fe]/m.Nac[fe])**3+1)*((m.Vnakp_k/m.Kb)**2+1))
229
230     # Nkcc Hill factors
231     #def Nhillf_fun(m, fe):
232     #    return Nhillf[fe] == ((m.Vnkcc_na/m.Nab+1)*(m.Vnkcc_k*m.Kb+1)*(m.Vnkcc_cl1/m.Clb+1)*(m.Vnkcc_
233
234     #def Nhillr_fun(m, fe):
235     #    return Nhillr[fe] == ((m.Vnkcc_na*m.Vc[fe]/m.Nac[fe]+1)*(m.Vnkcc_k*m.Vc[fe]/m.Kc[fe]+1)*(m.V
236
237     # Vol Regulations
238     #def NregD_fun(m, fe):
239     #    return NregD[fe] == (1+(100/(1+np.exp(-50*(m.Vc[fe]*1e6-1)))))
240
241     #def NregI_fun(m, fe):
242     #    return NregI[fe] == (1+(100/(1+np.exp(-50*(0.7-m.Vc[fe]*1e6)))))
243
244     # Other Cotransporters
245
246     # Define the RHS rules for the differential equations
247     # Channel states
248     def Amiloride(m, fe):
249         if fe in range(1,220):
250             return 1
251         else:
252             return 1e-20
253
254     def Forsk(m, fe):
255         if fe in range(1,660):
256             return 1
257         else:
258             return 3
259
260     def dFenacdt_rule(m, fe):
261         #print "dFenacdt_rule was called for i=",fe
262         return m.dFenacdt[fe]  == Amiloride(m, fe)*m.Penac*m.zna*m.u*m.Ema[fe]*(m.Naa-m.Nac[fe]*1e6/m
263     model.dFenacdt_RHS = Constraint(model.t, rule = dFenacdt_rule)
264
265     def dFcftrdt_rule(m, fe):
266         #print "dFcftrdt_rule was called for i=",fe
267         return m.dFcftrdt[fe]  == Forsk(m, fe)*m.Pcftr*m.zcl*m.u*m.Ema[fe]*(m.Cla-m.Clc[fe]*1e6/m.Vc[
```

```
    #Valence
    model.zna = 1
    model.zcl = -1
    model.zk = 1

    #Electric Constants
    model.F = 96485 # mA/mmol
    model.R = 8.314 # J/Mol K
    model.T = 310 # K
    model.u = model.F/(model.R*model.T)

    # Nak pump
    #def Nakhill_fun(m, fe):
    #    return Nakhill[fe] == (((m.Vnakp_na*m.Vc[fe]/m.Nac[
    fe])**3+1)*((m.Vnakp_k/m.Kb)**2+1))

    # Nkcc Hill factors
    #def Nhillf_fun(m, fe):
    #    return Nhillf[fe] == ((m.Vnkcc_na/m.Nab+1)*(m.Vnkcc_k*m.Kb+1
    )*(m.Vnkcc_cl1/m.Clb+1)*(m.Vnkcc_cl2/m.Clb+1))

    #def Nhillr_fun(m, fe):
    #    return Nhillr[fe] == ((m.Vnkcc_na*m.Vc[fe]/m.Nac[
    fe]+1)*(m.Vnkcc_k*m.Vc[fe]/m.Kc[fe]+1)*(m.Vnkcc_cl1*model.Vc[
    fe]/m.Clc[fe]+1)*(m.Vnkcc_cl2*m.Vc[fe]/m.Clc[fe]+1))

    # Vol Regulations
    #def NregD_fun(m, fe):
    #    return NregD[fe] == (1+(100/(1+np.exp(-50*(m.Vc[
    fe]*1e6-1)))))

    #def NregI_fun(m, fe):
    #    return NregI[fe] == (1+(100/(1+np.exp(-50*(0.7-m.Vc[
    fe]*1e6)))))

    # Other Cotransporters

    # Define the RHS rules for the differential equations
    # Channel states
    def Amiloride(m, fe):
        if fe in range(1,220):
            return 1
        else:
            return 1e-20

    def Forsk(m, fe):
        if fe in range(1,660):
            return 1
        else:
            return 3

    def dFenacdt_rule(m, fe):
        #print "dFenacdt_rule was called for i=",fe
```

```
262         return m.dFenacdt[fe]  == Amiloride(m, fe)*m.Penac*m.zna*m.u*
                m.Ema[fe]*(m.Naa-m.Nac[fe]*1e6/m.Vc[fe]*exp(m.zna*m.u*m.
                Ema[fe]))/(exp(m.zna*m.u*m.Ema[fe])-1)
263     model.dFenacdt_RHS = Constraint(model.t, rule = dFenacdt_rule)
264
265     def dFcftrdt_rule(m, fe):
266         #print "dFcftrdt_rule was called for i=",fe
267         return m.dFcftrdt[fe]  == Forsk(m, fe)*m.Pcftr*m.zcl*m.u*m.
                Ema[fe]*(m.Cla-m.Clc[fe]*1e6/m.Vc[fe]*exp(m.zcl*m.u*m.Ema
                [fe]))/(exp(m.zcl*m.u*m.Ema[fe])-1)
268     model.dFcftrdt_RHS = Constraint(model.t, rule = dFcftrdt_rule)
269
270     def dFaccdt_rule(m, fe):
271         #print "dFaccdt_rule was called for i=",fe
272         return m.dFaccdt[fe]  == m.Pacc*m.zcl*m.u*m.Ema[fe]*(m.Cla-m.
                Clc[fe]*1e6/m.Vc[fe]*exp(m.zcl*m.u*m.Ema[fe]))/(exp(m.zcl
                *m.u*m.Ema[fe])-1)
273     model.dFaccdt_RHS = Constraint(model.t, rule = dFaccdt_rule)
274
275     def dFbkcadt_rule(m, fe):
276         #print "dFbkcadt_rule was called for i=",fe
277         return m.dFbkcadt[fe]  == m.Pbkca*m.zk*m.u*m.Ema[fe]*(m.Ka-m.
                Kc[fe]*1e6/m.Vc[fe]*exp(m.zk*m.u*m.Ema[fe]))/(exp(m.zk*m.
                u*m.Ema[fe])-1)
278     model.dFbkcadt_RHS = Constraint(model.t, rule = dFbkcadt_rule)
279
280     def dFbkdt_rule(m, fe):
281         #print "dFbkdt_rule was called for i=",fe
282         return m.dFbkdt[fe]  == m.Pbk*m.zk*m.u*m.Emb[fe]*(m.Kc[fe]*
                1e6/m.Vc[fe]-m.Kb*exp(m.zk*m.u*m.Emb[fe]))/(exp(m.zk*m.u*
                m.Emb[fe])-1)
283     model.dFbkdt_RHS = Constraint(model.t, rule = dFbkdt_rule)
284
285     def dFbcldt_rule(m, fe):
286         #print "dFbcldt_rule was called for i=",fe
287         return m.dFbcldt[fe]  == Forsk(m,fe)*m.Pbcl*m.zcl*m.u*m.Emb[
                fe]*(m.Clc[fe]*1e6/m.Vc[fe]-m.Clb*exp(m.zcl*m.u*m.Emb[fe]
                ))/(exp(m.zcl*m.u*m.Emb[fe])-1)
288     model.dFbcldt_RHS = Constraint(model.t, rule = dFbcldt_rule)
289
290     def dFnakpdt_rule(m, fe):
291         Nakhill = (((m.Vnakp_na*m.Vc[fe]*1e-6/m.Nac[fe])**3+1)*((m.
                Vnakp_k/m.Kb)**2+1))
292         #print "dFnakpdt_rule was called for i=",fe
293         return m.dFnakpdt[fe]  == m.Jnakp*(5*m.Emb[fe]+1.25)/Nakhill
294     model.dFnakpdt_RHS = Constraint(model.t, rule = dFnakpdt_rule)
295
296     def dFnkccrdt_rule(m, fe):
297         Nhillr = ((m.Vnkcc_na*m.Vc[fe]*1e-6/m.Nac[fe]+1)*(m.Vnkcc_k*m
                .Vc[fe]*1e-6/m.Kc[fe]+1)*(m.Vnkcc_cl1*model.Vc[fe]*1e-6/m
                .Clc[fe]+1)*(m.Vnkcc_cl2*m.Vc[fe]*1e-6/m.Clc[fe]+1))
298         NregD = (1+(100/(1+exp(-50*(m.Vc[fe]-1)))))
299         #print "dFnkccfdt_rule was called for i=",fe
```

```
300         return m.dFnkccrdt[fe]  == m.Jnkcc*NregD/Nhillr
301     model.dFnkccrdt_RHS = Constraint(model.t, rule = dFnkccrdt_rule)
302
303     def dFnkccfdt_rule(m, fe):
304         Nhillf = ((m.Vnkcc_na/m.Nab+1)*(m.Vnkcc_k*m.Kb+1)*(m.
                Vnkcc_cl1/m.Clb+1)*(m.Vnkcc_cl2/m.Clb+1))
305         NregI = (1+(100/(1+exp(-50*(0.7-m.Vc[fe])))))
306         #print "dFnkccrdt_rule was called for i=",fe
307         return m.dFnkccfdt[fe]  == m.Jnkcc*NregI/Nhillf
308     model.dFnkccfdt_RHS = Constraint(model.t, rule = dFnkccfdt_rule)
309
310     # def dFaedt_rule(m, fe):
311     #     Aehill = ((model.Vae_cl/model.Clb+1)*(model.Vae_hco/
        model.HCOc+1)*(10**((model.Kp_ae-model.pHc)/model.ap_ae)+1))
312     #     #Keep in mind that the AE channel is regulated by pH and
        is possibly not well defined by a simple first order Michealis
        Menten term
313     #     #print "dFaedt_rule was called for i=",fe
314     #     return m.dFaedt[fe]  == m.Jae/Aehill
315     # model.dFaedt_RHS = Constraint(model.t, rule = dFaedt_rule)
316
317     # def dFnhedt_rule(m, fe):
318     #     Nhehill = ((model.Vnhe_na/model.Nab+1)*(model.Vnhe_h/
        model.Hc+1)*(10**((model.Kp_nhe-model.pHc)/model.ap_nhe)+1))
319     #     #print "dFnhedt_rule was called for i=",fe
320     #     return m.dFnhedt[fe]  == m.Jnhe/Nhehill
321     # model.dFnhedt_RHS = Constraint(model.t, rule = dFnhedt_rule)
322
323     # def dFnbcdt_rule(m, fe):
324     #     Nbchill = ((model.Vnbc_na/model.Nab+1)*(model.Vnbc_hco/
        model.HCOb+1)*(10**((model.Kp_nbc-model.pHc)/model.ap_nbc)+1))
325     #     #print "dFnbcdt_rule was called for i=",fe
326     #     return m.dFnbcdt[fe]  == m.Jnbc/Nbchill
327     # model.dFnbcdt_RHS = Constraint(model.t, rule = dFnbcdt_rule)
328
329     def dFkhpdt_rule(m, fe):
330         #Khphill = 0.2 #I need to get info on this transporter
331         #Not sure if this will be needed on terms of a thin film
            model... re-evaluate the need based on the ability to
            maintain intracellular K homeostasis
332         #print "dFkhpdt_rule was called for i=",fe
333         return m.dFkhpdt[fe]  == m.Jkhp#/Khphill
334     model.dFkhpdt_RHS = Constraint(model.t, rule = dFkhpdt_rule)
335
336     # Cellular states
337     def dNacdt_rule(m, fe):
338         #print "dNacdt_rule was called for i=",fe
339         return m.dNacdt[fe]  == m.dFenacdt[fe] + m.dFnkccfdt[fe] - m.
                dFnkccrdt[fe] - 3*m.dFnakpdt[fe] #+ m.dFnbcdt[fe] +
            m.dFnhedt[fe]
340     model.dNacdt_RHS = Constraint(model.t, rule = dNacdt_rule)
341
342     def dClcdt_rule(m, fe):
```

```
343             #print "dClcdt_rule was called for i=",fe
344             return m.dClcdt[fe]  == m.dFcftrdt[fe] + 2*(m.dFnkccfdt[fe] -
                     m.dFnkccrdt[fe]) + m.dFbcldt[fe] + m.dFaccdt[fe] #+
                m.dFaedt[fe]
345         model.dClcdt_RHS = Constraint(model.t, rule = dClcdt_rule)
346
347         def dKcdt_rule(m, fe):
348             #print "dKcdt_rule was called for i=",fe
349             return m.dKcdt[fe]  == m.dFbkcadt[fe] + m.dFnkccfdt[fe] - m.
                    dFnkccrdt[fe] + 2*m.dFnakpdt[fe] + m.dFkhpdt[fe] + m.
                    dFbkdt[fe]
350         model.dKcdt_RHS = Constraint(model.t, rule = dKcdt_rule)
351
352         def dVcdt_rule(m, fe):
353             #print "dVcdt_rule was called for i=",fe
354             return m.dVcdt[fe]  == (m.Pw*m.Vw**m.Ama*(m.Oc[fe]-m.Oa0)-m.
                    Pw*m.Vw*m.Amb*(m.Ob0-m.Oc[fe]))*1e-1
355         model.dVcdt_RHS = Constraint(model.t, rule = dVcdt_rule)
356
357         def dOcdt_rule(m, fe):
358             #print "dOcdt_rule was called for i=",fe
359             return m.dOcdt[fe]  == ((m.dNacdt[fe] + m.dKcdt[fe] + m.
                    dClcdt[fe])*m.Vc[fe]*1e-6 - m.dVcdt[fe]*(155 + m.Nac[fe]
                    + m.Clc[fe] + m.Kc[fe]))*(1e6)**2/m.Vc[fe]**2 #85 used
                to be m.Oc[fe]
360         model.dOcdt_RHS = Constraint(model.t, rule = dOcdt_rule)
361
362         #Membrane Currents
363         def ApCurrent_rule(m, fe):
364             Ina_ap = 100*m.dFenacdt[fe]*m.zna*m.F
365             Icl_ap = 100*(m.dFcftrdt[fe] + m.dFaccdt[fe])*m.zcl*m.F
366             Ik_ap = 100*m.dFbkcadt[fe]*m.zk*m.F
367             #print "dIap_rule was called for i=",fe
368             return m.Iap[fe] == Ina_ap + Icl_ap + Ik_ap
369         model.Iap_RHS = Constraint(model.t, rule = ApCurrent_rule)
370
371         def BlCurrent_rule(m, fe):
372             Icl_bl = 100*m.dFbcldt[fe]*m.zcl*m.F
373             Ik_bl = 100*m.dFbkdt[fe]*m.zk*m.F
374             Ipump = 1000*m.dFnakpdt[fe]*m.zna*m.F
375             #print "dIbl_rule was called for i=",fe
376             return m.Ibl[fe] == Icl_bl + Ik_bl + Ipump
377         model.Ibl_RHS = Constraint(model.t, rule = BlCurrent_rule)
378
379     # #####
380     #     def ACC_CFTR(m, fe):
381     #         return m.Pcftr >= m.Pacc
382     #     model.ACC_CFTR_rel = Constraint(model.t, rule = ACC_CFTR)
383     # ######
384
385
386         # Kirchhoff Law's
387         def kirchlaw1_rule(m, fe):
```

```
388         #print "Kirch1_rule was called for i=",fe
389         return m.Iap[fe] - m.Ibl[fe] <= 0.0001
390         #return m.Iap[fe] == m.Ibl[fe]
391     model.kirchlaw1 = Constraint(model.t, rule = kirchlaw1_rule)
392
393     def kirchlaw2_rule(m, fe):
394         #print "Kirch2_rule was called for i=",fe
395         return m.Ema[fe] + m.Emb[fe] <= 0.01 #<= 0.0001
396         #return m.Ema[fe] == m.Emb[fe]
397     model.kirchlaw2 = Constraint(model.t, rule = kirchlaw2_rule)
398
399     def _obj(m):
400
401         CurrObj = 0.0
402         #ncol = len(data[0,:])-1
403
404         dummy = sio.loadmat('CFHNEUCperPatient.mat')
405         data = dummy['UCF10']
406         ncol = len(data[0,])-1
407         datacols = np.arange(1,ncol+1)
408         a=data[:,[datacols]]
409
410
411         for j in range(ncol):
412             nrow = 0
413             for i in np.arange(0,1010,10):
414                 CurrObj = CurrObj + ((3*m.Iap[i]- data[nrow,j+1])**2)
                        /(np.std(a[nrow,])/np.sqrt(len(a[nrow,])))
415                 CurrObj = CurrObj + ((3*m.Ibl[i]- data[nrow,j+1])**2)
                        /(np.std(a[nrow,])/np.sqrt(len(a[nrow,])))
416                 nrow = nrow + 1
417         return CurrObj
418
419
420       #tdat1 = [30, 60, 120, 240, 500, 700, 900, 1100, 1500, 2000,
          2500, 3000, 3500]
421       #tdat1 = [30, 60, 90, 120, 180, 240, 300, 360, 420, 480,
          520, 600, 800, 1000]
422       #tdat1 = []
423       #tdat1.extend([i for i in range(0,1001,50)])
424
425       #for i in m.time: #tdat1:
426       #  if i < 300:
427       #      CurrObj = CurrObj + (3*m.Iap[i] - 30 )**2
428       #  elif ( i >= 300 and i < 600):
429       #      CurrObj = CurrObj + (3*m.Iap[i] - 12 )**2
430       #  else:
431       #      CurrObj = CurrObj + (3*m.Iap[i] - 21 )**2
432
433
434       #for j in range(ncol):
435 #             CurrObj = CurrObj + ((m.Iap[i] - HBEdata[tdat1.index(
    i),j+1])**2/np.std(HBEdata[tdat1.index(i),1:]))
```

D.3 Driver for Ussing Chamber Model

```
import numpy as np
import math as m
import multiprocessing
from itertools import product
from scipy.optimize import *
import least_squares as ls
import TicToc as t
from pyDOE import *
from pyomo.environ import *
from pyomo.opt import SolverFactory, SolverStatus, TerminationCondition
import pandas as pd
from pandas import *


import pylab
import numpy as np
import scipy as sp
import scipy.io as sio
import pickle
from scipy.stats.distributions import chi2
#from UCSim_DAE_wObj import UC_PyomoSyst
#from UCSim_DAE_wObj import UC_PyomoSyst
#from UCSim_PyomoImplementation import UC_PyomoSyst
#from UCSim_PyTest_Amil2 import UC_PyomoSyst
#from UCSim_PyTest_HighK_NomrCl import UC_PyomoSyst
#from UCSim_PyTest_OpenParBounds import UC_PyomoSyst
#from UCSim_PyTest_OpenPar_nopH import UC_PyomoSyst
#from UCSim_PyTest_OpenParBounds_CF import UC_PyomoSyst_Open
##from UCSim_PyTest_OpenBar_HNE import UC_PyomoSyst
#from UCSim_PyTest_OpenBar_UPHNE import UC_PyomoSyst
#from UCSim_PyTest_OpenBar_CFHNE import UC_PyomoSyst
#from UCSim_PyTest_OpenBar_UPHNE import UC_PyomoSyst
#from UCSim_PyTest_OpenBar_CFHBE import UC_PyomoSyst
#from UCSim_PyTest_OpenBar_HNE_noKpump import UC_PyomoSyst
#from UCSim_PyTest_OpenBar_HBE_noKpump import UC_PyomoSyst
#from UCSim_PyTest_OpenBar_CFHBE_noKpump import UC_PyomoSyst
#from UCSim_PyTest_CF254_CorrectorTest import UC_PyomoSyst
#from UCSim_PyTest_Amil import UC_PyomoSyst
#from UCSim_PyomoImplementation import UC_PyomoSyst
#from UCSim_PyTest_OpenBar_HNE_testing import UC_PyomoSyst
#from UCSim_PyTest_CFHNE_perPatient import UC_PyomoSyst
from UCSim_PyTest_OpenBar_UPHNE import UC_PyomoSyst
from matplotlib import pyplot as plt
from itertools import repeat


def pyUCSimTest(parParams):

    Va = 4.5
    Naa = 127.5#*(Va/1e3) #mmol NaCl + NaHCO3
```

```
58      Cla = 125#*(Va/1e3) #mmol NaCl + others
59      Ka = 5#*(Va/1e3) #mmol KCl ******
60      Oa0 = 300#(300*(Va/1e3) - (Naa + Cla + Ka)) # mOsmol
61      Ema0= -0.03747 # Initial guess apical potential
62
63      ## Basolateral Compartment
64      Vb = 4.5 #mean(vdat(1,:)); %ml
65      Nab = 127.5#*(Vb/1e3)  #mmol NaCl + NaHCO3
66      Clb = 125#*(Vb/1e3) #mmol NaCl + others
67      Kb = 5#*(Vb/1e3) #mmol KCl
68      Ob0 = 300#(300*(Vb/1e3) - (Nab + Clb + Kb))  # mOsmol
69      Emb0 = 0.03747 # Initial guess basolateral potential
70
71       ## Cellular Compartment
72      Dtj = 6e-7 # cm
73      Dc  = 8e-4 # cm
74      Atj = 0.33*(2*Dtj*Dc)/(Dtj+Dc)**2 # cm^2
75      Ac  = 0.33-Atj #cm^2
76      hc0 = 30.2e-4 # cm
77      Vc0 = Ac*hc0*1000 #ul # 1.92ul
78      Nac0 = 20*(Vc0/1e6) # mmol (15)*(Vc0/1e6); %mmole Na+
79      Clc0 = 55*(Vc0/1e6) # mmol  9*(Vc0/1e6); %mmole Cl-
80      Kc0 = 80*(Vc0/1e6) # mmol  150*(Vc0/1e6); %mmole K+
81      #Oc0 = (300*(Vc0/1e6) - (Nac0 + Clc0 + Kc0)) # mmol
82      Oc0 = 300# - (20 + 55 + 140)
83      T = 310 #K
84      F = 96485  #Faraday's constant, C/mol
85      R = 8.314  #Ideal gas, J/K mol
86
87      #params = product(Penac_list, Pcftr_list, Jnkcc_list, Jnakp_list, Pbkca_list, Pbk_list, Pbcl_list
        Jnkcc_list, Jnakp_list, Pacc_list)
88      #Passive Ion Channels Permeabilities, related to  abundance of channel expression
89      Penac = parParams[0] #7.11e-8 #9.55e-8 #m/s ENaC Permeability
90      Pcftr = parParams[1] #3.7e-8 #2.98e-8 m/s CFTR Permeability
91      Pacc = parParams[7] #1e-8#8e-8  #m/s CaCC Permeability
92      Pbk = parParams[5] #5e-9 #%8e-8 #m/s Basolateral Potassium permeability
93      Pbcl = parParams[6] #3e-8 #5.2e-8 #m/s Basolateral Cloride
94      Pbkca = parParams[4] #1.05e-8#7.05e-8 #m/s BKCa permeability **GUESS***
95
96      #Ion Fluxes for pump, and transporters
97      Jnakp = parParams[3] #1.1e-5 #mol/m^2s, maximun flux for NaK pump
98      Jnkcc = parParams[2] #1.6e-5#mol/m^2s, maximun flux for NaKCl cotransporter
99      Jnhe = 1.6e-7#1.6e-6 #1.6e-5 #mol/m^2s;
100     Jae = 5.5e-7#5.5e-6 #mol/m^2s
101     Jnbc = 1.25e-7#1.25e-6 #mol/m^2s
102     Jkhp = 1.25e-7#1.25e-6#1.25e-5 #mol/m^2s
103
104     #Paracellular fluxes
105     Ppna = 2.8e-8 #m/s
106     Ppcl = 3.0e-8 #m/s
107     Ppk = 1.47*Ppna #m/s
108
```

```
    # Half max Concentrations for substrates binding to ion channels
    Venac  = 1 #2.3e-6; % m^3 Half-Max ENaC Permeability
    Vcftr  = 1 #1.88e-6; % m^3 Half-Max CFTR Permeability
    Vacc = 1 #5e-6; %mM
    Vbkca = 3e-6 #mM ***Guess***
    Vnakp_k = 1.9 #mM Falkenberg
    Vnakp_na = 15.7 #mM Falkenberg
    Vnkcc_na = 105 #mM
    Vnkcc_k = 1.22 #mM
    Vnkcc_cl1 = 103 #mM
    Vnkcc_cl2 = 23.9 #mM
    Vbkca_v = 20 #mV

    Vnhe_na = 15 #mM
    Vae_cl = 5.6 #mM
    Vnbc_na = 24  #mM

    Pw = 220 #um/s
    Vw = 1.8e-5   #m^3/mol

    Ama = 0.33  #9.5; %cm^2 chnaged from 0.33;%
    Amb = 0.33*10  #*5cm^2

    Vnhe_h = 4.5e-4 #mM
    Kp_nhe = 10**-3
    ap_nhe = 1

    Vae_hco = 10**-4 #mM
    Kp_ae = 6.85
    ap_ae = 0.17

    Vnbc_hco = 19  #mM
    Kp_nbc = 10**-3
    ap_nbc = 1

    pHc = 7.5

    Hc = 4.2e-5 #mM
    HCOc = 13 #mM
    HCOb = 25 #mM

    #Channel initial fluxes
    Fenac0 = 0.0
    Fcftr0 = 0.0
    Facc0 = 0.0
    Fbkca0 = 0.0
    Fbk0 = 0.0
    Fbcl0 = 0.0
    Fnkccr0 = 0.0
    Fnkccf0 = 0.0
    Fnakp0 = 0.0
    Fae0 = 0.0
```

```
    Fnhe0 =0.0
    Fnbc0 = 0.0
    Fkhp0 = 0.0

    ## Parameter Structure to pass
    pfixed  = [Penac, Pcftr, Pacc, Pbkca, Pbk, Pbcl,\
            Jnkcc, Jnakp, Jnhe, Jae, Jnbc, Jkhp,  Pw,\
            Naa, Cla, Ka, Va, Oa0, Nab, Clb, Kb,  Vb, Ob0,\
            Venac, Vcftr, Vacc, Vbkca, Vnkcc_na, Vnkcc_k, Vnkcc_cl1, Vnkcc_cl2,\
            Vnakp_na, Vnakp_k, Vnhe_na, Vae_cl, Vnbc_na, Vae_hco, Vnhe_h, Vnbc_hco,\
            Kp_ae, Kp_nhe, Kp_nbc, HCOc, Hc, HCOb, pHc, ap_nbc, ap_nhe, ap_ae, Vw, Ama, Amb]

    par0 = [Nac0, Clc0, Kc0, Vc0, Oc0, Fenac0, Fcftr0, Facc0, Fbkca0, Fbk0,\
             Fbcl0, Fnkccr0, Fnkccf0, Fnakp0, Fae0, Fnhe0, Fnbc0, Fkhp0, Ema0,  Emb0]


    #   p  = [Penac, Pcftr, Pacc, Pbkca, Pbk, Pbcl,\
    #         Jnkcc, Jnakp, Jnhe, Jae, Jnbc, Jkhp,  Pw,
    #         Naa, Cla, Ka, Va, Oa0, Nab, Clb, Kb, Vb, Ob0, Oic0,\
    #         Venac, Vcftr, Vtmem, Vbkca, Vnkcc_na, Vnkcc_k,\
    #         Vnkcc_cl1, Vnkcc_cl2, Vnakp_na, Vnakp_k, Vnhe_na, Vae_cl, Vnbc_na,\
    #         Amil, Forsk, But]

    Parname = ['Penac', 'Pcftr', 'Pacc', 'Pbkca', 'Pbk', 'Pbcl', 'Jnkcc', 'Jnakp', 'Jnhe', 'Jae', 'Jnl
        Jkhp', 'Pw']
    ParList = [Penac, Pcftr, Pacc, Pbkca, Pbk, Pbcl, Jnkcc, Jnakp, Jnhe, Jae, Jnbc, Jkhp, Pw]

    #Solver Problems
    solver = 'ipopt'
    nfe = 500
    stepsize = 1

    print(params)

    #Flag is a output varible that signals the convergence condition of the run.
    #0: Optimization crashed
    #1: Optimal condition found
    #2: Infeasible condition found
    #3: I dont know

    try:

        instance, results = UC_PyomoSyst(solver, nfe, stepsize, pfixed, par0)
        print((results.solver.termination_condition == TerminationCondition.infeasible))
        print((results.solver.termination_condition == TerminationCondition.optimal))
        #instance.load(results)
        if  (results.solver.status == SolverStatus.ok) and (results.solver.termination_condition ==
            TerminationCondition.optimal):
            flag = 1
        elif (results.solver.termination_condition == TerminationCondition.infeasible):
            flag = 2
        else:
            flag = 3
```

```
212
213     except:
214         print('++++++++++++++++++++++ERROR--------ERROR----------ERROR---------ERROR+++++++++++++++++')
215
216         par_dict = {}
217
218         for i in range(len(Parname)):
219             par_dict[Parname[i]] = ParList[i]
220
221         par_dict[len(Parname)] = 'ERROR Throw Initial values'
222         flag = 0
223         return par_dict
224
225     #output = open('PyomoFirstRun.pkl', 'wb')
226     #pickle.dump(instance, output)
227     #output.close()
228
229     #Unpacking model instance
230     Penac = value(instance.Penac)
231     Pcftr = value(instance.Pcftr)
232     Pacc = value(instance.Pacc)
233     Pbkca = value(instance.Pbkca)
234     Pbk = value(instance.Pbk)
235     Pbcl = value(instance.Pbcl)
236     Jnkcc = value(instance.Jnkcc)
237     Jnakp = value(instance.Jnakp)
238     Jnhe = value(instance.Jnhe)
239     Jae = value(instance.Jae)
240     Jnbc= value(instance.Jnbc)
241     #Jkhp= value(instance.Jkhp)
242     Pw = value(instance.Pw)
243
244     #equate initial value for results array
245     t = [0.0]
246     #cell states
247     Nac = [Nac0]
248     Clc = [Clc0]
249     Kc = [Kc0]
250     Vc = [Vc0]
251     Oc = [Oc0]
252     #cell state differentials
253     dNacdt = []
254     dClcdt = []
255     dKcdt = []
256     dVcdt = []
257     dOcdt = []
258     #ion Fluxes
259
260     Fenac = []
261     Fcftr = []
262     Facc = []
263     Fbkca = []
264     Fbk = []
```

```
    Fbcl = []
    Fnkccr = []
    Fnkccf = []
    Fnakp = []
    Fae = [0]
    Fnhe = [0]
    Fnbc = [0]
    Fkhp = []
    #electrophys states
    Ema = []
    Emb = []
    Iap = []
    Ibl = []

    tdata = []
    tdata.extend([i for i in range(0,100,2)])

    for fe in instance.time:
        t.append(fe)
        #Cellular states
        Nac.append(value(instance.Nac[fe]))
        Clc.append(value(instance.Clc[fe]))
        Kc.append(value(instance.Kc[fe]))
        Vc.append(value(instance.Vc[fe]))
        Oc.append(value(instance.Oc[fe]))
        #Derivatives of cell states
        dNacdt.append(value(instance.dNacdt[fe]))
        dClcdt.append(value(instance.dClcdt[fe]))
        dKcdt.append(value(instance.dKcdt[fe]))
        dVcdt.append(value(instance.dVcdt[fe]))
        dOcdt.append(value(instance.dOcdt[fe]))
        #Ion channels, and cotransporter Fluxes
        Fenac.append(value(instance.dFenacdt[fe]))
        Fcftr.append(value(instance.dFcftrdt[fe]))
        Facc.append(value(instance.dFaccdt[fe]))
        Fbkca.append(value(instance.dFbkcadt[fe]))
        Fbk.append(value(instance.dFbkdt[fe]))
        Fbcl.append(value(instance.dFbcldt[fe]))
        Fnkccr.append(value(instance.dFnkccrdt[fe]))
        Fnkccf.append(value(instance.dFnkccfdt[fe]))
        Fnakp.append(value(instance.dFnakpdt[fe]))
        #Fae.append(value(instance.dFaedt[fe]))
        #Fnhe.append(value(instance.dFnhedt[fe]))
        #Fnbc.append(value(instance.dFnbcdt[fe]))
        #Fkhp.append(value(instance.dFkhpdt[fe]))
        #Electrophysiology variables
        Ema.append(value(instance.Ema[fe]))
        Emb.append(value(instance.Emb[fe]))
        Iap.append(value(instance.Iap[fe]))
        Ibl.append(value(instance.Ibl[fe]))
```

```
317         RList = [parParams, t, Nac, Clc, Kc, Vc, Oc, Fenac, Fcftr, Facc, Fbkca, Fbk, Fbcl, Fnkccr, \
318           Fnkccf, Fnakp, Fae, Fnhe, Fnbc, Fkhp, Ema, Emb, Iap, Ibl, Penac, Pcftr, Pacc, Pbkca, Pbk, Pbcl,
                Jnakp, Jnhe, Jae, Jnbc, Jkhp, Pw, flag]
319         KeyList = ['par0', 'time','Nac', 'Clc', 'Kc', 'Vc', 'Oc', 'Fenac', 'Fcftr', 'Facc', 'Fbkca', 'Fbk
              , 'Fnkccr', \
320           'Fnkccf', 'Fnakp', 'Fae', 'Fnhe', 'Fnbc', 'Fkhp', 'Ema', 'Emb', 'Iap', 'Ibl', 'Penac', 'Pcftr',
                'Pbkca', \
321            'Pbk', 'Pbcl', 'Jnkcc', 'Jnakp', 'Jnhe', 'Jae', 'Jnbc', 'Jkhp', 'Pw','flag']
322
323         params2 = np.array([Penac, Pcftr, Jnkcc, Jnakp, Pbkca, Pbk, Pbcl, Pacc])
324         print(params2)
325         print('++++++++++++++++++++++++++++++++++++++++++++++++++++++++++++++++++++++++++++++++++++++++')
326         #print(Iap)
327
328         #print(Ibl)
329     #   ParList = [Penac, Pcftr, Pacc, Pbkca, Pbk, Pbcl, Jnkcc, Jnakp, Jnhe, Jae, Jnbc, Jkhp, Pw]
330     #   Parname = ['Penac', 'Pcftr', 'Pacc', 'Pbkca', 'Pbk', 'Pbcl', 'Jnkcc', 'Jnakp', 'Jnhe', 'Jae', 'Jnl
    'Jkhp', 'Pw']
331
332         results_dict = {}
333     #   par_dict = {}
334
335         for i in range(len(KeyList)):
336             results_dict[KeyList[i]] = RList[i]
337
338     #   for i in range(len(Parname)):
339     #       par_dict[Parname[i]] = ParList[i]
340             #model = parmodel.parmodel()
341
342         return results_dict
343
344     #Latin HyperCube Sampling
345     #numDim = 8
346     #numSamp = 2
347
348
349     ##Regular Parameters
350     Penac = 7.11e-8 #9.55e-8 #m/s ENaC Permeability
351     Pcftr = 3.7e-8 #2.98e-8 m/s CFTR Permeability
352     Pacc = 8e-8  #m/s CaCC Permeability
353     Pbk = 5e-9 #%8e-8 #m/s Basolateral Potassium permeability
354     Pbcl = 3e-8 #5.2e-8 #m/s Basolateral Cloride
355     Pbkca = 7.05e-8 #m/s BKCa permeability **GUESS***
356     Jnakp = 1.1e-5 #mol/m^2s, maximun flux for NaK pump
357     Jnkcc = 1.6e-5#mol/m^2s, maximun flux for NaKCl cotransporter
358     Jnhe = 1.6e-5 #mol/m^2s;
359     Jae = 5.5e-6 #mol/m^2s
360     Jnbc = 1.25e-6 #mol/m^2s
361     Jkhp = 1.25e-5 #mol/m^2s
362     #######
363
364
365     tictoc2 = t.TicTocGenerator()
```

```
366
367 #max_numProcesses = 1
368 #pool = multiprocessing.Pool(max_numProcesses)
369 #soltemp = { 'Header' : 'Header'}
370 #sio.savemat('ParSearchPyomo_UCSimTenshi.mat', soltemp) #Create save
371 results = []
372
373 #Latin HyperCube Sampling
374 numDim = 8
375 numSamp = 15
376
377 #Enac, CFTR, BKCa, BK, BCl, NKCC, NakP
378 # lb = np.array([1e-10, 1e-10, 1e-10, 1e-10, 1e-9, 1e-9, 1e-10, 1e-10])
379 # ub = np.array([9e-6, 9e-6, 9e-6, 1e-7, 1e-7, 1e-7, 1e-7, 9e-8])
380
381 # Tentative HNE range
382 lb = np.array([1e-11, 1e-14, 1e-11, 1e-11, 1e-10, 1e-10, 1e-9, 1e-9])
383 ub = np.array([1e-5, 1e-7, 1e-5, 1e-5, 1e-6, 1e-6, 1e-5, 1e-5])
384 bdiff = ub - lb
385
386 lhsmatrix = lhs(numDim, samples = numSamp)
387 lhsmatrix_ad = lhsmatrix * bdiff #chnage index depending on value being varied
388 lhsmatrix_fin = lhsmatrix_ad + lb  #chnage index depending on value being varied
389 # Penac_list = lhsmatrix_fin[:,0]
390 # Pcftr_list = lhsmatrix_fin[:,1]
391 # Pbkca_list = lhsmatrix_fin[:,2]
392 # Pbk_list = lhsmatrix_fin[:,3]
393 # Pbcl_list = lhsmatrix_fin[:,4]
394 # Jnkcc_list = lhsmatrix_fin[:,5]
395 # Jnakp_list = lhsmatrix_fin[:,6]
396 # Pacc_list = lhsmatrix_fin[:,7]
397
398 for i in range(numSamp):
399     t.tic(tictoc2)
400
401     soldict = {}
402     soltemp = {}
403     #params = [Penac_list, Pcftr_list, Jnkcc_list, Jnakp_list, Pbkca_list, Pbk_list, Pbcl_list, Pacc_
404     params = lhsmatrix_fin[i,:]
405     results.append(pyUCSimTest(params))
406     soltemp = results[i]
407     InitialGuess = {"InitialGuess%d" %i: params for i in range(len(params))}
408     soldict ={"ParSearch_Run%d" %i: soltemp for i in range(len(soltemp))}#Change list based on parame
        being varied
409     j = i
410     print(i)
411     #with open('ParSearchPyomo_UCSimTenshi.mat','ab') as f:
412     #sio.savemat('ParSearchPyomo_UCSimTenshi_CF_%d.mat' %j, soldict)
413     t.toc(tictoc2)
414
415
416 sollist = []
417 for item in results:
```

```
416 sollist = []
417 for item in results:
418     sollist.append(item)
419
420 soldic = {"Run%d" %(i) : sollist[i] for i in range(len(sollist)) }
421 #optdict = {"Run%d_optinfo" %i: results[i-1][2] for i in range(len(results))}
422
423 #Chnage file name, depenidng on channel
424 sio.savemat("MultiVarLHS_PyomoParSearchTest_TitanUP9_NaivePool_wFeasibilityCheck", soldic)
```

Bibliography

[1] Frank J. Accurso, Steven M. Rowe, J.P. Clancy, Michael P. Boyle, Jordan M. Dunitz, Peter R. Durie, Scott D. Sagel, Douglas B. Hornick, Michael W. Konstan, Scott H. Donaldson, Richard B. Moss, Joseph M. Pilewski, Ronald C. Rubenstein, Ahmet Z. Uluer, Moira L. Aitken, Steven D. Freedman, Lynn M. Rose, Nicole Mayer-Hamblett, Qunming Dong, Jiuhong Zha, Anne J. Stone, Eric R. Olson, Claudia L. Ordoñez, Preston W. Campbell, Melissa A. Ashlock, and Bonnie W. Ramsey. Effect of VX-770 in Persons with Cystic Fibrosis and the G551D-CFTR Mutation. *New England Journal of Medicine*, 2010.

[2] Penny Agent and Helen Parrott. Inhaled therapy in cystic fibrosis: Agents, devices and regimens. *Breathe*, 11(2):111–118, 2015.

[3] Margarida D Amaral. Processing of CFTR: Traversing the cellular mazeHow much CFTR needs to go through to avoid cystic fibrosis? *Pediatric Pulmonology*, 39(6):479–491, 2005.

[4] Felice Amato, Paolo Scudieri, Ilaria Musante, Valeria Tomati, Emanuela Caci, Marika Comegna, Sabrina Maietta, Francesca Manzoni, Antonella Miriam Di Lullo, Elke De Wachter, Eef Vanderhelst, Vito Terlizzi, Cesare Braggion, Giuseppe Castaldo, and Luis J.V. Galietta. Two CFTR mutations within codon 970 differently impact on the chloride channel functionality. *Human Mutation*, 40(6):742–748, 2019.

[5] Anita Balázs and Marcus A. Mall. Role of the SLC26A9 chloride channel as disease modifier and potential therapeutic target in cystic fibrosis. *Frontiers in Pharmacology*, 9(OCT):1–9, 2018.

[6] CN Belcher and N Vij. Protein processing and Inflammatory Signaling in Cystic Fibrosis. *Current Molecular Medicine*, (10):82–94, 2010.

[7] William D. Bennett, Beth L. Laube, Timothy Corcoran, Kirby Zeman, Gail Sharpless, Kristina Thomas, Jihong Wu, Peter J. Mogayzel, Joseph Pilewski, and Scott Donaldson. Multisite Comparison of Mucociliary and Cough Clearance Measures Using Standardized Methods. *Journal of Aerosol Medicine and Pulmonary Drug Delivery*, 26(3):157–164, 2013.

[8] Carol A. Bertrand, Shalini Mitra, Sanjay K. Mishra, Xiaohui Wang, Yu Zhao, Joseph M. Pilewski, Dean R. Madden, and Raymond A. Frizzell. The CFTR trafficking mutation F508del inhibits the constitutive activity of SLC26A9. *American Journal of Physiology - Lung Cellular and Molecular Physiology*, 312(6):L912–L925, 2017.

[9] Carol A. Bertrand, Ruilin Zhang, Joseph M. Pilewski, and Raymond A. Frizzell. SLC26A9 is a constitutively active, CFTR-regulated anion conductance in human bronchial epithelia. *The Journal of General Physiology*, 133(4):421–438, 2009.

[10] Len Best. Glucose-induced electrical activity in rat pancreatic β-cells: Dependence on intracellular chloride concentration. *Journal of Physiology*, 568(1):137–144, 2005.

[11] Diana Bilton, Gregory Tino, Alan F Barker, Daniel C Chambers, Anthony De Soyza, Lieven J A Dupont, Conor O'Dochartaigh, Eric H J van Haren, Luis Otero Vidal, Tobias Welte, Howard G Fox, Jian Wu, and Brett Charlton. Inhaled mannitol for non-cystic fibrosis bronchiectasis: a randomised, controlled trial. *Thorax*, 2014.

[12] Susan E. Birket, Kengyeh K. Chu, Linbo Liu, Grace H. Houser, Bradford J. Diephuis, Eric J. Wilsterman, Gregory Dierksen, Marina Mazur, Suresh Shastry, Yao Li, John D. Watson, Alexander T. Smith, Benjamin S. Schuster, Justin Hanes, William E. Grizzle, Eric J. Sorscher, Guillermo J. Tearney, and Steven M. Rowe. A functional anatomic defect of the cystic fibrosis airway. *American Journal of Respiratory and Critical Care Medicine*, 190(4):421–432, 2014.

[13] Alain Boom, Pascale Lybaert, Jean François Pollet, Paul Jacobs, Hassan Jijakli, Philippe E. Golstein, Abdullah Sener, Willy J. Malaisse, and Renaud Beauwens. Expression and localization of cystic fibrosis transmembrane conductance regulator in the rat endocrine pancreas. *Endocrine*, 32(2):197–205, 2007.

[14] R C Boucher. Regulation of airway surface liquid volume by human airway epithelia. *Pflügers Archiv : European journal of physiology*, 445(4):495–8, January 2003.

[15] Richard C Boucher. Cystic fibrosis: a disease of vulnerability to airway surface dehydration. *Trends in molecular medicine*, 13(6):231–40, June 2007.

[16] Michael P Boyle, Scott C Bell, Michael W Konstan, Susanna A Mccolley, Steven M Rowe, Ernst Rietschel, Xiaohong Huang, and David Waltz. Articles A CFTR corrector (lumacaftor) and a CFTR potentiator (ivacaftor) for treatment of patients with cystic fi brosis who have a phe508del CFTR mutation : a phase 2 randomised controlled trial. *The Lancet Respiratory*, 2(7):527–538, 2014.

[17] John J Brewington, Lauren M Strecker, John P Clancy, John J Brewington, Erin T Filbrandt, F J Larosa Iii, Jessica D Moncivaiz, and Alicia J Ostmann. Brushed nasal epithelial cells are a surrogate for bronchial epithelial CFTR studies Find the latest version : Brushed nasal epithelial cells are a surrogate for bronchial epithelial CFTR studies. *JCI Insight*, 3(13), 2018.

[18] Robert J Bridges. Mechanisms of Bicarbonate Secretion : Lessons from the Airways. pages 1–10, 2012.

[19] C J Britto. Splunc1 Dysregulation In The Sputum Of Stable Adult Cystic Fibrosis Subjects. *Am J Respir Crit Care Med*, 193:A2881, 2016.

[20] Celeste B Burness and Gillian M Keating. Mannitol Dry Powder for Inhalation. *Drugs*, 72(10):1411–1421, 2012.

[21] Kelly Burrowes and Merryn Tawhai. Computatio al predictions of pulmonary blood flow gradients: gravity versus structure. *Respiratory Physiology and Neurobiology*, 154(3), 2006.

[22] K.S Burrowes, A.J Swan, N.J Warren, and M.H Tawhai. Towards a virtual lung: multi-scale, multi-physics modelling of the pulmonary system. *Philosophical Transactions of the Royal Society A: Mathematical, Physical and Engineering Sciences*, 366(1879):3247–3263, 2008.

[23] Brian Button, Seiko F Okada, Charles Brandon Frederick, William R Thelin, and Richard C Boucher. Mechanosensitive ATP release maintains proper mucus hydration of airways. *Science signaling*, 6(279):ra46, 2013.

[24] C. Castellani, C. Quinzii, S. Altieri, G. Mastella, and B.M. Assael. A Pilot Survey of Cystic Fibrosis Clinical Manifestations in CFTR Mutation Heterozygotes . *Genetic Testing*, 5(3):249–254, 2002.

[25] CFTR2. CFTR2 Variant List history.

[26] Chiesi. BRONCHITOL FOR MANAGEMENT OF CYSTIC FIBROSIS IN ADULT PATIENTS PULMONARY-ALLERGY DRUGS ADVISORY COMMITTEE MEETING DATE : MAY 8 , 2019 ADVISORY COMMITTEE BRIEFING MATERIALS :. Technical report, 2019.

[27] Do Yeon Cho, Peter H. Hwang, Beate Illek, and Horst Fischer. Acid and base secretion in freshly excised nasal tissue from cystic fibrosis patients with delF508 mutation. *International Forum of Allergy and Rhinology*, 1(2):123–127, 2011.

[28] Jonathan A Cohn, Kenneth Friedman, Peadar Noone, Michael R Knowles, Lawrence M. Silverman, and Paul S. Jowell. Relation Between Mutations of the Cystic Firbosis Gene and Idiopathic Pancreatistis. *The New England Journal of Medicine*, 339(10):781–790, 1998.

[29] D. I. Cook and J. A. Young. Effect of K+ channels in the apical plasma membrane on epithelial secretion based on secondary active Cl- transport. *The Journal of Membrane Biology*, 110(2):139–146, 1989.

[30] T. E. Corcoran, K. M. Thomas, M. M. Myerburg, A. Muthukrishnan, L. Weber, R. Frizzell, and J. M. Pilewski. Absorptive clearance of DTPA as an aerosol-based biomarker in the cystic fibrosis airway. *European Respiratory Journal*, 35(4):781–786, 2010.

[31] Timothy E Corcoran, Alex S Huber, Michael M Myerburg, Daniel J Weiner, Landon W Locke, Ryan T Lacy, Lawrence Weber, Michael R Czachowski, Darragh J

Johnston, Ashok Muthukrishnan, Alison T Lennox, and Joseph M Pilewski. Multi-probe Nuclear Imaging of the Cystic Fibrosis Lung as a Biomarker of Therapeutic Effect. *Journal of Aerosol Medicine and Pulmonary Drug Delivery*.

[32] Timothy E Corcoran, Kristina M Thomas, Stefanie Brown, Michael M Myerburg, Landon W Locke, and Joseph M Pilewski. Liquid hyper-absorption as a cause of increased DTPA clearance in the cystic fibrosis airway. *EJNMMI Research*, 3(1):14, 2013.

[33] Timothy E Corcoran, Kristina M Thomas, Stefanie Brown, Michael M Myerburg, Landon W Locke, and Joseph M Pilewski. Liquid hyper-absorption as a cause of increased DTPA clearance in the cystic fibrosis airway. *EJNMMI research*, 3(1):14, January 2013.

[34] Harriet Corvol, Julie Mésinèle, Isman Hassan Douksieh, Lisa J. Strug, Pierre Yves Boëlle, and Loïc Guillot. SLC26A9 gene is associated with lung function response to ivacaftor in patients with cystic fibrosis. *Frontiers in Pharmacology*, 9(JUL):1–11, 2018.

[35] Scott Corvol, Harriet; Blackman and Michael Knowles. Genome-wide association meta-analysis identifies five modifier loci of lung disease severity in cystic fibrosis. *Nature Communications*, 6, 2015.

[36] Carolyn B Coyne, Miriam K Vanhook, Todd M Gambling, L Johnny, Richard C Boucher, Larry G Johnson, Chapel Hill, Chapel Hill, and North Carolina. Proinflammatory Cytokines. (September):3218–3234, 2002.

[37] Kathryn J. Crawford and Damian G. Downey. Theratyping in cystic fibrosis. *Current opinion in pulmonary medicine*, 24(6):612–617, 2018.

[38] Cystic Fibrosis Foundation (CFF). 2017 Patient Registry: Annual Data Report. Technical report, 2017.

[39] H. Danahay. Membrane capacitance and conductance changes parallel mucin secretion in the human airway epithelium. *AJP: Lung Cellular and Molecular Physiology*, 290(3):L558–L569, 2005.

[40] Jane C Davies, Samuel M Moskowitz, Cynthia Brown, Alexander Horsley, Marcus A Mall, Edward F McKone, Barry J Plant, Dario Prais, Bonnie W Ramsey, Jennifer L Taylor-Cousar, Elizabeth Tullis, Ahmet Uluer, Charlotte M McKee, Sarah Robertson, Rebecca A Shilling, Christopher Simard, Fredrick Van Goor, David Waltz, Fengjuan Xuan, Tim Young, and Steven M Rowe. VX-659TezacaftorIvacaftor in Patients with Cystic Fibrosis and One or Two Phe508del Alleles. *New England Journal of Medicine*, 379(17):1599–1611, 2018.

[41] F. de Courcey, A. V. Zholos, H. Atherton-Watson, M. T. S. Williams, P. Canning, H. L. Danahay, J. S. Elborn, and M. Ennis. Development of primary human nasal

epithelial cell cultures for the study of cystic fibrosis pathophysiology. *AJP: Cell Physiology*, 303(11):C1173–C1179, 2012.

[42] P. a. de Jong, Y. Nakano, M. H. Lequin, J. R. Mayo, R. Woods, P. D. Paré, and H. a W M Tiddens. Progressive damage on high resolution computed tomography despite stable lung function in cystic fibrosis. *European Respiratory Journal*, 23(1):93–97, 2004.

[43] Daniel C. Devor and Joseph M. Pilewski. UTP inhibits Na + absorption in wild-type and ΔF508 CFTR-expressing human bronchial epithelia . *American Journal of Physiology-Cell Physiology*, 276(4):C827–C837, 2017.

[44] Daniel C Devor, Ashvani K Singh, Linda C Lambert, Arthur Deluca, Raymond A Frizzell, and Robert J Bridges. Bicarbonate and Chloride Secretion in Calu-3 Human Airway Epithelial Cells. 113(May), 1999.

[45] Thomas E. Dick, Yaroslav I. Molkov, Gary Nieman, Yee Hsee Hsieh, Frank J. Jacono, John Doyle, Jeremy D. Scheff, Steve E. Calvano, Ioannis P. Androulakis, Gary An, and Yoram Vodovotz. Linking inflammation, cardiorespiratory variability, and neural control in acute inflammation via computational modeling. *Frontiers in Physiology*, 3 JUL, 2012.

[46] Scott H. Donaldson, William D. Bennett, Kirby L. Zeman, Michael R. Knowles, Robert Tarran, and Richard C. Boucher. Mucus Clearance and Lung Function in Cystic Fibrosis with Hypertonic Saline. *New England Journal of Medicine*, 354(3):241–250, 2006.

[47] Scott H Donaldson and Richard C Boucher. Therapeutic Applications for Nucleotides in Lung Disease BT - The P2 Nucleotide Receptors. pages 413–424. Humana Press, Totowa, NJ, 1998.

[48] Scott H Donaldson, Timothy E Corcoran, Beth L Laube, and William D Bennett. Mucociliary clearance as an outcome measure for cystic fibrosis clinical research. *Proceedings of the American Thoracic Society*, 4(4):399–405, August 2007.

[49] Graham M. Donovan. Multiscale mathematical models of airway constriction and disease. *Pulmonary Pharmacology and Therapeutics*, 24(5):533–539, 2011.

[50] Mitchell L Drumm, Michael W Konstan, Mark D Schluchter, Allison Handler, Rhonda Pace, Fei Zou, Maimoona Zariwala, David Fargo, Airong Xu, John M Dunn, Rebecca J Darrah, Ruslan Dorfman, Andrew J Sandford, Mary Corey, Julian Zielenski, Peter Durie, Katrina Goddard, James R Yankaskas, Fred A Wright, and Michael R Knowles. Genetic Modifiers of Lung Disease in Cystic Fibrosis. *n engl j med School of Medicine School of Public HealthBiotechnology Center for Bioinformatics Chapel Hill; the Program in Integrative Biology N Engl J Med*, 35314353(353):1443–53, 2005.

[51] Patricia J Dubin and Jay K Kolls. IL-23 mediates inflammatory responses to mucoid Pseudomonas aeruginosa lung infection in mice. *American journal of physiology. Lung cellular and molecular physiology*, 292(2):L519–L528, 2007.

[52] Paul D W Eckford, Mohabir Ramjeesingh, Steven Molinski, Stan Pasyk, Johanna F. Dekkers, Canhui Li, Saumel Ahmadi, Wan Ip, Timothy E. Chung, Kai Du, Herman Yeger, Jeffrey Beekman, Tanja Gonska, and Christine E. Bear. VX-809 and related corrector compounds exhibit secondary activity stabilizing active F508del-CFTR after its partial rescue to the cell surface. *Chemistry and Biology*, 21(5):666–678, 2014.

[53] Mark R Elkins, M H Sc, Michael Robinson, D Ph, Barbara R Rose, Colin Harbour, Carmel P Moriarty, Guy B Marks, Elena G Belousova, M Appl Sc, and Wei Xuan. new england journal. *New England Journal of . . .*, 354(3):229–240, 2006.

[54] Cibele V Falkenberg and Eric Jakobsson. A biophysical model for integration of electrical, osmotic, and pH regulation in the human bronchial epithelium. *Biophysical journal*, 98(8):1476–1485, 2010.

[55] J. W. Fernandez, P. Mithraratne, Tawhai Thrupp, S., and P. J. M. H. Hunter. Anatomically based geometric modelling of the musculo-skeletal system and other organs. *Biomech. Model. Mechanobiol.*, 2:139–155., 2004.

[56] J. Fischbarg, F. P J Diecke, P. Iserovich, and a. Rubashkin. The role of the tight junction in paracellular fluid transport across corneal endothelium. Electro-osmosis as a driving force. *Journal of Membrane Biology*, 210(2):117–130, 2006.

[57] Jeffry a Florian, Julie L Eiseman, and Robert S Parker. Nonlinear model predictive control for dosing daily anticancer agents using a novel saturating-rate cell-cycle model. *Computers in biology and medicine*, 38(3):339–47, March 2008.

[58] Cystic Fibrosis Foundation. Patient Registry Annual Data Report. Technical report, 2016.

[59] Andrew Fretzayas, Konstantinos Douros, and Ioanna Loukou. Application of Lung Clearance Index in Monitoring Children with Cystic Fibrosis. *World Journla of Clinical Pediatrics*, 8(2):15–23, 2019.

[60] L E Friberg, A Henningson, H Maas, and \it et al. Model of Chemotherapy-induced Myelosuppression with Parameter Consistency Across Drugs. *Cancer Res.*, 20:523–527, 2002.

[61] I. Galeva. Cystic fibrosis related diabetes mellitus. *Pediatriya*, 52(2):10–14, 2012.

[62] Guilherme J M Garcia, Richard C. Boucher, and Timothy C. Elston. Biophysical model of ion transport across human respiratory epithelia allows quantification of ion permeabilities. *Biophysical Journal*, 104(3):716–726, feb 2013.

[63] Guilherme J. M. Garcia, Maryse Picher, Peiying Zuo, Seiko F. Okada, Eduardo R. Lazarowski, Brian Button, Richard C. Boucher, and Tim C. Elston. Computational Model for the Regulation of Extracellular ATP and Adenosine in Airway Epithelia. pages 51–74. 2011.

[64] Martina Gentzsch and Marcus A. Mall. Ion Channel Modulators in Cystic Fibrosis. *Chest*, 154(2):383–393, 2018.

[65] D. J. Gillie, A. J. Pace, R. J. Coakley, B. H. Koller, and P. M. Barker. Liquid and ion transport by fetal airway and lung epithelia of mice deficient in sodium-potassium-2-chloride transporter. *American Journal of Respiratory Cell and Molecular Biology*, 25(1):14–20, 2001.

[66] D. E. Goldman. POTENTIAL, IMPEDANCE, AND RECTIFICATION IN MEMBRANES. *The Journal of General Physiology*, 1943.

[67] Jiafen Gong, Fan Wang, Bowei Xiao, Naim Panjwani, Fan Lin, Katherine Keenan, Julie Avolio, Mohsen Esmaeili, Lin Zhang, Gengming He, David Soave, Scott Mastromatteo, Zeynep Baskurt, Sangook Kim, Wanda K. O'Neal, Deepika Polineni, Scott M. Blackman, Harriet Corvol, Garry R. Cutting, Mitchell Drumm, Michael R. Knowles, Johanna M. Rommens, Lei Sun, and Lisa J. Strug. *Genetic association and transcriptome integration identify contributing genes and tissues at cystic fibrosis modifier loci*, volume 15. 2019.

[68] Jonathan Goodman, Jonathan. Weare. *Communication in Applied Mathematics and Computational Science*, volume 5. 2010.

[69] Jing Hui Guo, Hui Chen, Ye Chun Ruan, Xue Lian Zhang, Xiao Hu Zhang, Kin Lam Fok, Lai Ling Tsang, Mei Kuen Yu, Wen Qing Huang, Xiao Sun, Yiu Wa Chung, Xiaohua Jiang, Yoshiro Sohma, and Hsiao Chang Chan. Glucose-induced electrical activities and insulin secretion in pancreatic islet 2-cells are modulated by CFTR. *Nature Communications*, 5:1–10, 2014.

[70] Sanjana Gupta, Liam Hainsworth, Justin Hogg, Robin Lee, and James Faeder. Evaluation of Parallel Tempering to Accelerate Bayesian Parameter Estimation in Systems Biology. *Proceedings - 26th Euromicro International Conference on Parallel, Distributed, and Network-Based Processing, PDP 2018*, pages 690–697, 2018.

[71] Iram J Haq, Michael A Gray, James P Garnett, Christopher Ward, and Malcolm Brodlie. Airway surface liquid homeostasis in cystic fibrosis: pathophysiology and therapeutic targets. *Thorax*, pages thoraxjnl–2015–207588, 2015.

[72] John M. Harrold, Julie L. Eiseman, Erin Joseph, Sandra Strychor, William C. Zamboni, and Robert S. Parker. Control-relevant modeling of the antitumor effects of 9-nitrocamptothecin in SCID mice bearing HT29 human colon xenografts. *Journal of Pharmacokinetics and Pharmacodynamics*, 32(1):65–83, 2005.

[73] William E. Hart, Carl D. Laird, Jean-Paul Watson, David L. Woodruff, Gabriel A. Hackebeil, Bethany L. Nicholson, and John D. Siirola. *Pyomo - Optimization Modeling in Python*. Springer, 2017.

[74] William E Hart, Jean-paul Watson, and David L Woodruff. Pyomo : modeling and solving mathematical programs in Python. *Mathematical Programming Computing*, 3(219):219–260, 2011.

[75] T Hartmann and a S Verkman. Model of ion transport regulation in chloride-secreting airway epithelial cells. Integrated description of electrical, chemical, and fluorescence measurements. *Biophysical journal*, 58(2):391–401, 1990.

[76] Peter R. Harvey, Robert Tarran, Stephen Garoff, and Mike M. Myerburg. Measurement of the airway surface liquid volume with simple light refraction microscopy. *American Journal of Respiratory Cell and Molecular Biology*, 45(3):592–599, 2011.

[77] U. Hasler. Dual Effects of Hypertonicity on Aquaporin-2 Expression in Cultured Renal Collecting Duct Principal Cells. *Journal of the American Society of Nephrology*, 16(6):1571–1582, 2005.

[78] Gregory Herschlag, Guilherme J M Garcia, Brian Button, Robert Tarran, Brandon Lindley, Benjamin Reinhardt, Timothy C. Elston, and M. Gregory Forest. A mechanochemical model for auto-regulation of lung airway surface layer volume. *Journal of Theoretical Biology*, 325:42–51, 2013.

[79] David B. Hill, Paula a. Vasquez, John Mellnik, Scott a. McKinley, Aaron Vose, Frank Mu, Ashley G. Henderson, Scott H. Donaldson, Neil E. Alexis, Richard C. Boucher, and M. Gregory Forest. A biophysical basis for mucus solids concentration as a candidate biomarker for airways disease. *PLoS ONE*, 9(2):1–11, 2014.

[80] Thang Ho, Gilles Clermont, and Robert S. Parker. A model of neutrophil dynamics in response to inflammatory and cancer chemotherapy challenges. *Computers and Chemical Engineering*, 51:187–196, 2013.

[81] Mark J Hoegger, Maged Awadalla, Eman Namati, Omar a Itani, Anthony J Fischer, Alexander J Tucker, Ryan J Adam, Geoffrey McLennan, Eric a Hoffman, David a Stoltz, and Michael J Welsh. Assessing mucociliary transport of single particles in vivo shows variable speed and preference for the ventral trachea in newborn pigs. *Proceedings of the National Academy of Sciences of the United States of America*, 111(6):2355–60, 2014.

[82] Lucas R. Hoffman and Bonnie W. Ramsey. Cystic fibrosis therapeutics: The road ahead. *Chest*, 143(1):207–213, 2013.

[83] Justin S. Hogg. Advances in Rule-Based Modeling : Compartments , Energy , and Hybrid Simulation , With Application To Sepsis and Cell Signaling. page 260, 2013.

[84] Monika I. Hollenhorst, Katrin Richter, and Martin Fronius. Ion transport by pulmonary epithelia. *Journal of biomedicine & biotechnology*, 2011:174306, 2011.

[85] Junwei Huang, Jiajie Shan, Dusik Kim, Jie Liao, Alexandra Evagelidis, Seth L Alper, and John W Hanrahan. Basolateral chloride loading by the anion exchanger type 2 : role in fluid secretion by the human airway epithelial cell line Calu-3. 21:5299–5316, 2012.

[86] N S Huang and J D Hellums. A theoretical model for gas transport and acid/base regulation by blood flowing in microvessels. *Microvasc Res*, 48(3):364–388, 1994.

[87] Jacky Jacquot, Olivier Tabary, Philippe Le Rouzic, and Annick Clement. Airway epithelial cell inflammatory signalling in cystic fibrosis, 2008.

[88] S Jayaraman, N S Joo, B Reitz, J J Wine, and a S Verkman. Submucosal gland secretions in airways from cystic fibrosis patients have normal [Na(+)] and pH but elevated viscosity. *Proceedings of the National Academy of Sciences of the United States of America*, 98(14):8119–8123, 2001.

[89] Jin Hyeok Jeong, Nam Soo Joo, Peter H Hwang, and Jeffrey J Wine. Mucociliary clearance and submucosal gland secretion in the ex vivo ferret trachea. *American journal of physiology. Lung cellular and molecular physiology*, (650):83–93, 2014.

[90] P. Jourdain, F. Becq, S. Lengacher, C. Boinot, P. J. Magistretti, and P. Marquet. The human CFTR protein expressed in CHO cells activates aquaporin-3 in a cAMP-dependent pathway: study by digital holographic microscopy. *Journal of Cell Science*, 127(3):546–556, 2014.

[91] Kayani Kayani, Raihan Mohammed, and Hasan Mohiaddin. Cystic fibrosis related diabetes. *Pediatriya*, 52(2):10–14, 2012.

[92] Dominic Keating, Gautham Marigowda, Lucy Burr, Cori Daines, Marcus A Mall, Edward F McKone, Bonnie W Ramsey, Steven M Rowe, Laura A Sass, Elizabeth Tullis, Charlotte M McKee, Samuel M Moskowitz, Sarah Robertson, Jessica Savage, Christopher Simard, Fredrick Van Goor, David Waltz, Fengjuan Xuan, Tim Young, and Jennifer L Taylor-Cousar. VX-445TezacaftorIvacaftor in Patients with Cystic Fibrosis and One or Two Phe508del Alleles. *New England Journal of Medicine*, 379(17):1612–1620, 2018.

[93] M S Kelker, I a Wilson, J M Fine, A Drilhon, P Amouch, G W Litman, J Finstad, J Howell, R a Good, W a Hendrickson, J L Smith, M Karplus, R L Stanfield, C Sander, L Teyton, G Johnson, E a Kabat, P D Mcneill, S Hakomori, F a Quiocho, X Dai, J Paulson, R Mcbride, J Vanhnasy, and B Droese. Disruption of the CFTR Gene Produces. (September):1837–1841, 2008.

[94] Adrian Kis, Stefanie Krick, Nathalie Baumlin, and Matthias Salathe. Airway Hydration, Apical K Secretion, and the Large-Conductance, Ca-activated and Voltage-dependent Potassium (BK) Channel. pages 163–168, 2014.

[95] Hiroaki Kitano, Kanae Oda, Tomomi Kimura, Yukiko Matsuoka, Marie Csete, John Doyle, and Masaaki Muramatsu. Metabolic syndrome and robustness tradeoffs. *Diabetes*, 53 Suppl 3(December):S6–S15, dec 2004.

[96] Timothy D. Knab, Gilles Clermont, and Robert S. Parker. Zone Model Predictive Control and Moving Horizon Estimation for the Regulation of Blood Glucose in Critical Care Patients. In *ADCHEM 2015*, page paper 224, Whistler, BC.

[97] Michael W Konstan, Jeffrey S Wagener, and Donald R VanDevanter. Characterizing aggressiveness and predicting future progression of CF lung disease. *Journal of cystic fibrosis : official journal of the European Cystic Fibrosis Society*, 8 Suppl 1(0 1):S15–9, 2009.

[98] Jan Kronqvist, David E Bernal, Andreas Lundell, and Ignacio E Grossmann. A Review and Comparison of Solvers for Convex MINLP. *Optimization and Engineering*, 20(2):397–455, 2019.

[99] Mauri E Krouse, Jason F Talbott, Martin M Lee, Nam Soo Joo, Jeffrey J Wine, E Mauri, Jason F Talbott, Martin M Lee, Nam Soo, and Jeffrey J Wine Acid. Acid and base secretion in the Calu-3 model of human serous cells. 94305:1274–1283, 2004.

[100] P. Kurbatova, N. Bessonov, V. Volpert, H. A.W.M. Tiddens, C. Cornu, P. Nony, and D. Caudri. Model of mucociliary clearance in cystic fibrosis lungs. *Journal of Theoretical Biology*, 372:81–88, 2015.

[101] Jessica Larusch, Jinsei Jung, Ignacio J General, Michele D Lewis, Hyun Woo, Randall E Brand, Andres Gelrud, Michelle A Anderson, Peter A Banks, Darwin Conwell, Christopher Lawrence, Joseph Romagnuolo, John Baillie, Samer Alkaade, Gregory Cote, Timothy B Gardner, Stephen T Amann, Adam Slivka, Bimaljit Sandhu, and Amy Aloe. Mechanisms of CFTR Functional Variants That Impair Regulated Bicarbonate Permeation and Increase Risk for Pancreatitis but Not for Cystic Fibrosis. 10(7), 2014.

[102] Gillian M. Lavelle, Michelle M. White, Niall Browne, Noel G. McElvaney, and Emer P. Reeves. Animal Models of Cystic Fibrosis Pathology: Phenotypic Parallels and Divergences. *BioMed Research International*, 2016, 2016.

[103] Robert J. Lee and J. Kevin Foskett. Ca2+ signaling and fluid secretion by secretory cells of the airway epithelium. *Cell Calcium*, 55(6):325–336, 2014.

[104] Ching-Long Lin, Merryn Tawhai, and Eric A. Hoffman. Multiscale image-based modeling and simulation of gas flow and particle transport in the human lungs. *Wiley interdiscio Rev Syst Biol Med*, 5(5), 2013.

[105] Jessica Lin, Normy N Razak, Christopher G Pretty, Aaron Le Compte, Paul Docherty, Jacquelyn D Parente, Geoffrey M Shaw, Christopher E Hann, and J Geoffrey Chase. A physiological Intensive Control Insulin-Nutrition-Glucose (ICING) model validated in critically ill patients. *Computer methods and programs in biomedicine*, 102(2):192–205, may 2011.

[106] B. Lindemann. Hans Ussing, experiments and models. *Journal of Membrane Biology*, 184(3):203–210, 2001.

[107] W Lissens. Cystic Fibrosis and infertility caused by congenital bilateral absence of the vas deferens and related clinical entities. *Human Reproduction*, 4, 1996.

[108] CH Liu, SC Niranjan, JW Clarck, and KY San. Airway mechanics, gas exchange, and blood flow in a nonlinear model of the normal human lung. *J Appl Physiol*, 84:1447:1469, 1998.

[109] Linbo Liu, Kengyeh K Chu, Grace H Houser, Bradford J Diephuis, Yao Li, Eric J Wilsterman, Suresh Shastry, Gregory Dierksen, Susan E Birket, Marina Mazur, Suzanne Byan-Parker, William E Grizzle, Eric J Sorscher, Steven M Rowe, and Guillermo J Tearney. Method for quantitative study of airway functional microanatomy using micro-optical coherence tomography. *PloS one*, 8(1):e54473, January 2013.

[110] Landon W. Locke, Michael M. Myerburg, Matthew R. Markovetz, Robert S. Parker, Lawrence Weber, Michael R. Czachowski, Thomas J. Harding, Stefanie L. Brown, Joseph A. Nero, Joseph M. Pilewski, and Timothy E. Corcoran. Quantitative imaging of airway liquid absorption in cystic fibrosis. *European Respiratory Journal*, 44(3):675–684, 2014.

[111] Landon W. Locke, Michael M. Myerburg, Daniel J. Weiner, Matthew R. Markovetz, Robert S Parker, Ashok Muthukrishnan, Lawrence Weber, Michael R Czachowski, Ryan T. Lacy, Joseph M. Pilewski, and Timothy E. Corcoran. Pseudomonas infection and mucociliary and absorptive clearance in the cystic fibrosis lung. *European Respiratory Journal*, 47(5):1392–1401, 2016.

[112] Dan L. Longo, David a. Stoltz, David K. Meyerholz, and Michael J. Welsh. Origins of Cystic Fibrosis Lung Disease. *New England Journal of Medicine*, 372(4):351–362, 2015.

[113] Author Nilceia Lopez-souza, Pedro C Avila, Jonathan H Widdicombe, Nilceia Lopez-Souza, Pedro C Avila, Jonathan H Widdicombe, Author Nilceia Lopez-souza, Pedro C Avila, Jonathan H Widdicombe, and Nilceia Lopez-Souza. Polarized cultures of human airway epithelium from nasal scrapings and bronchial brushings. *In vitro cellular & developmental biology. Animal*, 39(7):266–269, 2003.

[114] Todd MacKenzie, Alex H. Gifford, Kathryn A. Sabadosa, Hebe B. Quinton, Emily A. Knapp, Christopher H. Goss, and Bruce C. Marshall. Longevity of patients with

cystic fibrosis in 2000 to 2010 and beyond: Survival analysis of the Cystic Fibrosis Foundation Patient Registry. *Annals of Internal Medicine*, 161(4):233–241, 2014.

[115] Milena Magalhães, Isabelle Rivals, Mireille Claustres, Jessica Varilh, Mélodie Thomasset, Anne Bergougnoux, Laurent Mely, Sylvie Leroy, Harriet Corvol, Loïc Guillot, Marlène Murris, Emmanuelle Beyne, Davide Caimmi, Isabelle Vachier, Raphaël Chiron, and Albertina De Sario. DNA methylation at modifier genes of lung disease severity is altered in cystic fibrosis. *Clinical Epigenetics*, 9(1):19, 2017.

[116] Dahis Manzanares, Carlos Gonzalez, Pedro Ivonnet, Ren Shiang Chen, Monica Valencia-Gattas, Gregory E. Conner, H. Peter Larsson, and Matthias Salathe. Functional apical large conductance, Ca2+-activated, and voltage-dependent K+ channels are required for maintenance of airway surface liquid volume. *Journal of Biological Chemistry*, 286(22):19830–19839, 2011.

[117] Dahis Manzanares, Stefanie Krick, Nathalie Baumlin, John S. Dennis, Jean Tyrrell, Robert Tarran, and Matthias Salathe. Airway surface dehydration by transforming growth factor β (TGF-β) in cystic fibrosis is due to decreased function of a voltage-dependent potassium channel and can be rescued by the drug pirfenidone. *Journal of Biological Chemistry*, 290(42):25710–25716, 2015.

[118] Veronica Marcos, Zhe Zhou-Suckow, Ali Önder Yildirim, Alexander Bohla, Andreas Hector, Ljubomir Vitkov, Wolf Dietrich Krautgartner, Walter Stoiber, Matthias Griese, Oliver Eickelberg, et al. Free dna in cystic fibrosis airway fluids correlates with airflow obstruction. *Mediators of inflammation*, 2015, 2015.

[119] Matthew R. Markovetz. MULTISCALE MATHEMATICAL MODELING OF THE ABSORPTIVE AND MUCOCILIARY PATHOPHYSIOLOGY OF CYSTIC FIBROSIS LUNG DISEASE. *PhD Dissertation*, 2017.

[120] Matthew R. Markovetz, Timothy E. Corcoran, Landon W. Locke, Michael M. Myerburg, Joseph M. Pilewski, and Robert S. Parker. A physiologically-motivated compartment-based model of the effect of inhaled hypertonic saline on mucociliary clearance and liquid transport in cystic fibrosis. *PLoS ONE*, 9(11), 2014.

[121] Kelly M. Martinovich, Thomas Iosifidis, Alysia G. Buckley, Kevin Looi, Kak Ming Ling, Erika N. Sutanto, Elizabeth Kicic-Starcevich, Luke W. Garratt, Nicole C. Shaw, Samuel Montgomery, Francis J. Lannigan, Darryl A. Knight, Anthony Kicic, and Stephen M. Stick. Conditionally reprogrammed primary airway epithelial cells maintain morphology, lineage and disease specific functional characteristics. *Scientific Reports*, 7(1):1–13, 2017.

[122] Shibin Mathew, John Barterls, Ipsita Banerjee, and Yoram Vodovotz. Global Sensitivity Analysis of a Mathematical Model of Acute Inflammation Identifies Nonlinear Dependence of Cumulative Tissue Damage on Host Interleukin-6 Responses. *J Theor Biol*, 358:132–148, 2014.

[123] Hirotoshi Matsui, C William Davis, Robert Tarran, and Richard C Boucher. Osmotic water permeabilities of cultured , well-differentiated normal and cystic fibrosis airway epithelia. (May):1419–1427, 2000.

[124] Shibin Matthew and Ipsita Banerjee. Quantitative Analysis of Robustness of Dynamic Response and Signal Transfer in Insulin mediated PI3K/AKT Pathway. *Comput Chem Eng*, 71(2):715–727, 2014.

[125] Catherine M. McDougall, Morgan G. Blaylock, J. Graham Douglas, Richard J. Brooker, Peter J. Helms, and Garry M. Walsh. Nasal epithelial cells as surrogates for bronchial epithelial cells in airway inflammation studies. *American Journal of Respiratory Cell and Molecular Biology*, 39(5):560–568, 2008.

[126] P. M. McIlwaine, L. T. Wong, D. Peacock, and a. G F Davidson. Long-term comparative trial of conventional postural drainage and percussion versus positive expiratory pressure physiotherapy in the treatment of cystic fibrosis. *Journal of Pediatrics*, 131(4):570–574, 1997.

[127] Pierre Miossec and Jay K. Kolls. Targeting IL-17 and TH17 cells in chronic inflammation. *Nature Reviews Drug Discovery*, 11(10):763–776, 2012.

[128] Natalia Molenda, Katarina Urbanova, Nelly Weiser, Kristina Kusche-Vihrog, Dorothee Gunzel, and Hermann Schillers. Paracellular transport through healthy and cystic fibrosis bronchial epithelial cell lines - Do we have a proper model? *PLoS ONE*, 9(6), 2014.

[129] Katharina Mosler, Christelle Coraux, Konstantina Fragaki, Jean Marie Zahm, Odile Bajolet, Katia Bessaci-Kabouya, Edith Puchelle, Michel Abély, and Pierre Mauran. Feasibility of nasal epithelial brushing for the study of airway epithelial functions in CF infants. *Journal of Cystic Fibrosis*, 7(1):44–53, 2008.

[130] Michael M. Myerburg, Peter R. Harvey, Elisa M. Heidrich, Joseph M. Pilewski, and Michael B. Butterworth. Acute regulation of the epithelial sodium channel in airway epithelia by proteases and trafficking. *American Journal of Respiratory Cell and Molecular Biology*, 43(6):712–719, 2010.

[131] Mike M Myerburg, Joseph D Latoche, Erin E Mckenna, Laura P Stabile, Jill S Siegfried, Carol A Feghali-bostwick, and Joseph M Pilewski. Hepatocyte growth factor and other fibroblast secretions modulate the phenotype of human bronchial epithelial cells. *Lung Cellular and Molecular Physiology*, 292:1352–1360, 2007.

[132] Dave P. Nichols, Anthony G. Durmowicz, Ann Field, Patrick A. Flume, Donald R. VanDevanter, and Nicole Mayer-Hamblett. Developing Inhaled Antibiotics in Cystic Fibrosis: Current Challenges and Opportunities. *Annals of the American Thoracic Society*, 16(5):534–539, 2019.

[133] Bethany Nicholson. *Applications , Modeling Tools , and Parallel Solution Algorithms for Dynamic*. PhD thesis, Carnegie Mellon University, 2016.

[134] H. Frederik Nijhout, Janet A. Best, and Michael C. Reed. Using mathematical models to understand metabolism, genes, and disease. *BMC Biology*, 13(1):79, 2015.

[135] Janet A Novotny and Eric Jakobsson. Computational studies of ion-water flux coupling in the airway epithelium. I. Construction of model. *The American journal of physiology*, 270(6 Pt 1):C1751–C1763, 1996.

[136] Janet A Novotny and Eric Jakobsson. Computational studies of ion-water flux coupling in the airway epithelium. II. Role of specific transport mechanisms. *The American journal of physiology*, 270(6 Pt 1):C1764–C1772, 1996.

[137] Thierry Ntimbane, Geneviève Mailhot, Schohraya Spahis, Remi Rabasa-Lhoret, Marie-Laure Kleme, Danielle Melloul, Emmanuelle Brochiero, Yves Berthiaume, and Emile Levy. CFTR silencing in pancreatic β-cells reveals a functional impact on glucose-stimulated insulin secretion and oxidative stress response. *American Journal of Physiology-Endocrinology and Metabolism*, 310(3):E200–E212, 2015.

[138] Donal L. O'Donoghue, Vivek Dua, Guy W. J. Moss, and Paola Vergani. Increased apical Na + permeability in cystic fibrosis is supported by a quantitative model of epithelial ion transport. *The Journal of Physiology*, 591(15):3681–3692, 2013.

[139] Tsukasa Okiyoneda, Guido Veit, Johanna F. Dekkers, Miklos Bagdany, Naoto Soya, Haijin Xu, Ariel Roldan, Alan S. Verkman, Mark Kurth, Agnes Simon, Tamas Hegedus, Jeffrey M. Beekman, and Gergely L. Lukacs. Mechanism-based corrector combination restores ΔF508-CFTR folding and function. *Nat Chem Biol.*, 9(7), 2013.

[140] OLLI M. PITKÄNEN, DAVID SMITH, HUGH O'BRODOVICH, GAIL OTULAKOWSKI, and The. Expression of alpha -, beta-, and gamma-hENaC mRNA in the Human Nasal, Bronchial, and Distal Lung Epithelium. *Am J Respir Crit Care Med*, 163(15):273–276, 2001.

[141] Ruth O'Reilly and Heather E. Elphick. Development, clinical utility, and place of ivacaftor in the treatment of cystic fibrosis, 2013.

[142] Daniel J. Orestein, David M.; Spahr, Jonathan E.; Weiner. *Cystic Fibrosis: A Guide for Patient and Family*. Lippincott Williams & Wilkins, fourth edi edition, 2012.

[143] Brian P. O'Sullivan and Steven D. Freedman. Cystic fibrosis. *The Lancet*, 373(9678):1891–1904, 2009.

[144] G Otulakowski, S Flueckiger-Staub, L Ellis, K Ramlall, O Staub, D Smith, P Durie, and O Brodovich H. Relation between alpha, beta, and gamma human amiloride-sensitive epithelial Na+ channel mRNA levels and nasal epithelial potential difference in healthy men. *Am J Respir Crit Care Med*, 158(4):1213–1220, 1998.

[145] Art B. Owen. A Central Limit Theorem for Latin Hypercube Sampling. *Journal of the Royal Statistical Society. Series B (Methodological)*, 54(2):541–551, 1991.

[146] R S Parker. *Model-Based Analysis and Control for Biosystems*. PhD thesis, Department of Chemical Engineering, University of Delaware, 1999.

[147] John Paul, Calvin U Cotton, Scott H Donaldson, George M Solomon, Donald R Vandevanter, Michael P Boyle, Martina Gentzsch, Jerry A Nick, Beate Illek, John C Wallenburg, Eric J Sorscher, Margarida D Amaral, Jeffrey M Beekman, Anjaparavanda P Naren, Robert J Bridges, Philip J Thomas, Garry Cutting, Steven Rowe, Anthony G Durmowicz, Martin Mense, Kris D Boeck, William Skach, Christopher Penland, Elizabeth Joseloff, Hermann Bihler, John Mahoney, Drucy Borowitz, and Katherine L Tuggle. CFTR modulator theratyping : Current status , gaps and future directions . *Journal of Cystic Fibrosis*, 18(1):22–34, 2019.

[148] Alejandro a. Pezzulo, Xiao Xiao Tang, Mark J. Hoegger, Mahmoud H. Abou Alaiwa, Shyam Ramachandran, Thomas O. Moninger, Phillip H. Karp, Christine L. Wohlford-Lenane, Henk P. Haagsman, Martin van Eijk, Botond Bánfi, Alexander R. Horswill, David a. Stoltz, Paul B. McCray, Michael J. Welsh, and Joseph Zabner. Reduced airway surface pH impairs bacterial killing in the porcine cystic fibrosis lung. *Nature*, 487(7405):109–113, 2012.

[149] Puay-Wah Phuan, Jung-Ho Son, Joseph-Anthony Tan, Clarabella Li, Ilaria Musante, Lorna Zlock, Dennis W. Nielson, Walter E. Finkbeiner, Mark J. Kurth, Luis J. Galietta, Peter M. Haggie, and Alan S. Verkman. COMBINATION POTENTIATOR (CO-POTENTIATOR') THERAPY FOR CF CAUSED BY CFTR MUTANTS, INCLUDING N1303K, THAT ARE POORLY RESPONSIVE TO SINGLE POTENTIATORS Puay-Wah. *J Cyst Fibrosis*, 17(5):595–606, 2018.

[150] P F Pignatti, C Bombieri, C Marigo, M Benetazzo, and M Luisetti. Increased incidence of cystic fibrosis gene mutations in adults with disseminated bronchiectasis. *Human molecular genetics*, 4(4):635–639, apr 1995.

[151] J. M. Pilewski and R. A. Frizzell. Role of CFTR in airway disease. *Physiological reviews*, 79(1):S215–55, 1999.

[152] Paola Prandini, Francesco De Logu, Camilla Fusi, Lisa Provezza, Romina Nassini, Giulia Montagner, Serena Materazzi, Silvia Munari, Eliana Gilioli, Valentino Bezzerri, Alessia Finotti, Ilaria Lampronti, Anna Tamanini, Maria Cristina Dechecchi, Giuseppe Lippi, Carla M. Ribeiro, Alessandro Rimessi, Paolo Pinton, Roberto Gambari, Pierangelo Geppetti, and Giulio Cabrini. Transient receptor potential ankyrin 1 channels modulate inflammatory response in respiratory cells from patients with cystic fibrosis. *American Journal of Respiratory Cell and Molecular Biology*, 55(5):645–656, 2016.

[153] Iwona M. Pranke, Aurélie Hatton, Juliette Simonin, Jean Philippe Jais, Françoise Le Pimpec-Barthes, Ania Carsin, Pierre Bonnette, Michael Fayon, Nathalie Stremler-Le

Bel, Dominique Grenet, Matthieu Thumerel, Julie Mazenq, Valerie Urbach, Myriam Mesbahi, Emanuelle Girodon-Boulandet, Alexandre Hinzpeter, Aleksander Edelman, and Isabelle Sermet-Gaudelus. Correction of CFTR function in nasal epithelial cells from cystic fibrosis patients predicts improvement of respiratory function by CFTR modulators. *Scientific Reports*, 7(1), 2017.

[154] Michelle A Pressly, Matthew D Neal, Gilles Clermont, and Robert S Parker. Dynamic Modeling of Thromboelastography To Inform State of Coagulopathy in Trauma Patients. In *Conference Paper 105 for the Foundations of Computer Aided Process Operations/Chemical Process Control Conference*, Tuscan, AZ, 2017.

[155] A. Pritchard-Bell, G. Clermont, T.D. Knab, J. Maalouf, M. Vilkhovoy, and R.S. Parker. Subcutaneous Insulin Dynamics in a Critical Care Population. *Control Engineering Practice (IFAC 2014 Special Issue)*, 58:268–275, 2017.

[156] Andras Rab, Rafal Bartoszewski, Asta Jurkuvenaite, John Wakefield, James F. Collawn, and Zsuzsa Bebok. Endoplasmic reticulum stress and the unfolded protein response regulate genomic cystic fibrosis transmembrane conductance regulator expression. *Am J Physiol Cell Physiol*, 0005(292):756–766, 2007.

[157] B W Ramsey, S J Astley, M L Aitken, W Burke, a a Colin, H L Dorkin, J D Eisenberg, R L Gibson, I R Harwood, and D V Schidlow. Efficacy and safety of short-term administration of aerosolized recombinant human deoxyribonuclease in patients with cystic fibrosis. *The American review of respiratory disease*, 148(1):145–151, 1993.

[158] Bonnie W. Ramsey. A CFTR Potentiator in Patients with Cystic Fibrosis and the G551D Mutation Bonnie. 365(18):1663–1672, 2012.

[159] Andreas Raue, C. Kreutz, T. Maiwald, J. Bachmann, M. Schilling, U. Klingmüller, and J. Timmer. Structural and practical identifiability analysis of partially observed dynamical models by exploiting the profile likelihood. *Bioinformatics*, 25(15):1923–1929, 2009.

[160] Andreas Raue, Marcel Schilling, Julie Bachmann, Andrew Matteson, Max Schelke, Daniel Kaschek, Sabine Hug, Clemens Kreutz, Brian D. Harms, Fabian J. Theis, Ursula Klingmüller, and Jens Timmer. Lessons Learned from Quantitative Dynamical Modeling in Systems Biology. *PLoS ONE*, 8(9), 2013.

[161] M M Reddy and P M Quinton. Control of dynamic CFTR selectivity by glutamate and ATP in epithelial cells. *Nature*, 423(6941):756–760, 2003.

[162] M. Robinson, E. Daviskas, S. Eberl, J. Baker, H. K. Chan, S. D. Anderson, and P. T P Bye. The effect of inhaled mannitol on bronchial mucus clearance in cystic fibrosis patients: A pilot study. *European Respiratory Journal*, 14(3):678–685, 1999.

[163] Paul D Robinson, Philipp Latzin, Sylvia Verbanck, Graham L Hall, Alexander Horsley, Monika Gappa, Cindy Thamrin, Hubertus G M Arets, Paul Aurora, Susanne I

Fuchs, Gregory G King, Sooky Lum, Kenneth Macleod, Manuel Paiva, Jane J Pillow, Sarath Ranganathan, Felix Ratjen, Florian Singer, Samatha Sonnappa, Janet Stocks, Padmaja Subbarao, Bruce R Thompson, and Per M Gustafsson. Consensus statement for inert gas washout measurement using multiple- and single- breath tests. *European Respiratory Journal*, 41(3):507–522, 2013.

[164] Steven M. Rowe, Cori Daines, Felix C. Ringshausen, Eitan Kerem, John Wilson, Elizabeth Tullis, Nitin Nair, Christopher Simard, Linda Han, Edward P. Ingenito, Charlotte McKee, Julie Lekstrom-Himes, and Jane C. Davies. TezacaftorIvacaftor in Residual-Function Heterozygotes with Cystic Fibrosis. *New England Journal of Medicine*, 377(21):2024–2035, 2017.

[165] Steven M. Rowe and Alan S. Verkman. Cystic fibrosis transmembrane regulator correctors and potentiators. *Cold Spring Harbor Perspectives in Biology*, 5(8), 2013.

[166] A Roy and R S Parker. Dynamic Modeling of Free Fatty Acids, Glucose, and Insulin: An Extended Minimal Model. *Diabetes Tech. Theraput.*, 8:617–626, 2006.

[167] Claudia Rückes, Ulrike Blank, Karin Möller, Jens Rieboldt, Hermann Lindemann, Gerd Münker, Wolfgang Clauss, and Wolf-Michael Weber. Amiloride-Sensitive Na+Channels in Human Nasal Epithelium Are Different from Classical Epithelial Na+Channels. *Biochemical and Biophysical Research Communications*, 237(3):488–491, 1997.

[168] Conner I. Sandefur, Richard C. Boucher, and Timothy C. Elston. Mathematical model reveals role of nucleotide signaling in airway surface liquid homeostasis and its dysregulation in cystic fibrosis. *Proceedings of the National Academy of Sciences*, 114(35):E7272–E7281, 2017.

[169] Conner I. Sandefur, Richard C. Boucher, and Timothy C. Elston. Mathematical model reveals role of nucleotide signaling in airway surface liquid homeostasis and its dysregulation in cystic fibrosis. *Proceedings of the National Academy of Sciences*, 114(35):E7272–E7281, 2017.

[170] Bob J. Scholte, William H. Colledge, Martina Wilke, and Hugo de Jonge. Cellular and animal models of cystic fibrosis, tools for drug discovery. *Drug Discovery Today: Disease Models*, 3(3):251–259, 2006.

[171] Rainer Schreiber, Roland Nitschke, Rainer Greger, and Karl Kunzelmann. The cystic fibrosis transmembrane conductance regulator activates aquaporin 3 in airway epithelial cells. *The Journal of biological chemistry*, 274(17):11811–11816, 1999.

[172] Bruce D. Schultz. Airway epithelial cells: 'Bicarbonate in''Bicarbonate out'. *Journal of Physiology*, 590(21):5263–5264, 2012.

[173] Bruce D. Schultz and Robert J Bridges. The Effects of CFTR Variants on Chloride and Bicarbonate Secretion and Their Responsiveness to CFTR Modulators. In

William R Skach and Katherine L Tuggle, editors, *Cystic Fibrosis Foundation Research Conference: Pushing Frontiers*, page 13, Stowe, VT, 2019.

[174] Florencio Serrano Castillo, Carol A. Bertrand, Timothy E. Corcoran, Monica E. Shapiro, and Robert S. Parker. A Dynamic Model of Cystic Fibrosis Airway Epithelium Electrophysiology. *IFAC-PapersOnLine*, 51(19):94–97, 2018.

[175] Jiajie Shan, Jie Liao, Junwei Huang, Renaud Robert, Melissa L. Palmer, Scott C. Fahrenkrug, Scott M. O'Grady, and John W. Hanrahan. Bicarbonate-dependent chloride transport drives fluid secretion by the human airway epithelial cell line Calu-3. *The Journal of Physiology*, 590(21):5273–5297, 2012.

[176] M.E. Shapiro, T.E. Corcoran, C.A. Bertrand, F. Serrano Castillo, and R.S. Parker. Physiologically-Based Model of Fluid Absorption and Mucociliary Clearance in Cystic Fibrosis. *IFAC-PapersOnLine*, 51(19), 2018.

[177] Nicholas Sharer, Martin Schwarz, Geraldine Malone, Andrea Howarth, Johm Painter, Maurice Super, and Joan Braganza. Mutations of the Cystic Fibrosis Gene in Patients with Chronic Pancreatitis. *The New England Journal of Medicine*, 339(10):645–6520, 1998.

[178] J. H. Shin, E. J. Son, H. S. Lee, S. J. Kim, K. Kim, J. Y. Choi, M. G. Lee, and J. H. Yoon. Molecular and functional expression of anion exchangers in cultured normal human nasal epithelial cells. *Acta Physiologica*, 191(2):99–110, 2007.

[179] Peter D. Sly, Siobhain Brennan, Catherine Gangell, Nicholas De Klerk, Conor Murray, Lauren Mott, Stephen M. Stick, Philip J. Robinson, Colin F. Robertson, and Sarath C. Ranganathan. Lung disease at diagnosis in infants with cystic fibrosis detected by newborn screening. *American Journal of Respiratory and Critical Care Medicine*, 180(2):146–152, 2009.

[180] Steven M. Snodgrass, Kristine M. Cihil, Pamela K. Cornuet, Michael M. Myerburg, and Agnieszka Swiatecka-Urban. Tgf-??1 Inhibits Cftr Biogenesis and Prevents Functional Rescue of ??F508-Cftr in Primary Differentiated Human Bronchial Epithelial Cells. *PLoS ONE*, 8(5), 2013.

[181] J Strieter, J L Stephenson, L G Palmer, and a M Weinstein. Volume-activated chloride permeability can mediate cell volume regulation in a mathematical model of a tight epithelium. *The Journal of general physiology*, 96(August):319–344, 1990.

[182] Lisa J. Strug, Tanja Gonska, Gengming He, Katherine Keenan, Wan Ip, Pierre-Yves Boëlle, Fan Lin, Naim Panjwani, Jiafen Gong, Weili Li, David Soave, Bowei Xiao, Elizabeth Tullis, Harvey Rabin, Michael D. Parkins, April Price, Peter C. Zuberbuhler, Harriet Corvol, Felix Ratjen, Lei Sun, Christine E. Bear, and Johanna M. Rommens. Cystic fibrosis gene modifier SLC26A9 modulates airway response to CFTR-directed therapeutics . *Human Molecular Genetics*, 25(20):ddw290, 2016.

[183] Robert Sturm. An advanced stochastic model for mucociliary particle clearance in cystic fibrosis lungs. *Journal of Thoracic Disease*, 4(1):48–57, 2012.

[184] M. Stutts, C. Canessa, J. Olsen, M. Hamrick, J. Cohn, B. Rossier, and R. Boucher. CFTR as a cAMP-dependent regulator of sodium channels. *Science*, 269(5225):847–850, 1995.

[185] Rami Subhi, Rachel Ooi, Felicity Finlayson, and Satish Warrier. Distal Intestinal Obstruction Syndorme in cystic Fibrosis: presentation, outcome and management in a tertiary hospital (2007-2012). *Anz Journal of Surgery*, 2013.

[186] Paolo Sudieri, Ilaria Musante, Ariana Venturini, Daniela Guidone, Michele Genovese, Mario Renda, Alessandra Montalbano, Virgiania Spano, Marilia Barreca, Paola Barraja, and Luis Galietta. Pharmacological Approached for Rare CF Mutations. In *Cystic Fibrosis Foundation Research Conference: Pushing Frontiers*, 2019.

[187] Hongtao Sun, William T. Harris, Stephanie Kortyka, Kavitha Kotha, Alicia J. Ostmann, Amir Rezayat, Anusha Sridharan, Yan Sanders, Anjaparavanda P. Naren, and John P. Clancy. TGF-beta downregulation of distinct chloride channels in cystic fibrosis-affected epithelia. *PLoS ONE*, 9(9), 2014.

[188] Xingshen Sun, Hongshu Sui, John T Fisher, Ziying Yan, Xiaoming Liu, Hyung-ju Cho, Nam Soo Joo, Yulong Zhang, Weihong Zhou, Yaling Yi, Joann M Kinyon, Diana C Lei-butters, Michelle a Griffin, Paul Naumann, Meihui Luo, Jill Ascher, Kai Wang, Timothy Frana, Jeffrey J Wine, David K Meyerholz, and John F Engelhardt. Technical advance Disease phenotype of a ferret CFTR -knockout model of cystic fibrosis. 120(9):3149–3160, 2010.

[189] Lin Tang, Mohammad Fatehi, and Paul Linsdell. Mechanism of direct bicarbonate transport by the CFTR anion channel. *Journal of Cystic Fibrosis*, 8(2):115–121, 2009.

[190] Robert Tarran, Brian Button, and Richard C. Boucher. REGULATION OF NORMAL AND CYSTIC FIBROSIS AIRWAY SURFACE LIQUID VOLUME BY PHASIC SHEAR STRESS. *Annual Review of Physiology*, 68(1):543–561, 2006.

[191] Jennifer L. M.D. Taylor-Cousar, Anne M.D. Munck, Edward F. M.D. McKone, M.D. Cornelis K. van der Ent, M.D., Ph.D., Alexander Moeller, M.D. Christopher Simard, Ph.D. Linda T. Wang, M.D. Edward P. Ingenito, M.D., M.D. Charlotte McKee, Ph.D. Yimeng Lu, M.D. Julie Lekstrom-Himes, and M.D. J. Stuart Elborn. TezacaftorIvacaftor in Patients with Cystic Fibrosis Homozygous for Phe508del. *The New England journal of medicine*, 377(21):2013–2023, 2017.

[192] The Cystic Fibrosis Foundation. About Cystic Fibrosis.

[193] Kendra Tosoni, Diane Cassidy, Barry Kerr, Stephen C. Land, and Anil Mehta. Using drugs to probe the variability of trans-epithelial airway resistance. *PLoS ONE*, 11(2), 2016.

[194] Katherine L. Tuggle, Susan E. Birket, Xiaoxia Cui, Jeong Hong, Joe Warren, Lara Reid, Andre Chambers, Diana Ji, Kevin Gamber, Kengyeh K. Chu, Guillermo Tearney, Li Ping Tang, James a. Fortenberry, Ming Du, Joan M. Cadillac, David M. Bedwell, Steven M. Rowe, Eric J. Sorscher, and Michelle V. Fanucchi. Characterization of defects in ion transport and tissue development in Cystic Fibrosis Transmembrane Conductance Regulator (CFTR)-knockout rats. *PLoS ONE*, 9(3):1–14, 2014.

[195] F. Van Goor, S. Hadida, P. D. J. Grootenhuis, B. Burton, D. Cao, T. Neuberger, A. Turnbull, A. Singh, J. Joubran, A. Hazlewood, J. Zhou, J. McCartney, V. Arumugam, C. Decker, J. Yang, C. Young, E. R. Olson, J. J. Wine, R. A. Frizzell, M. Ashlock, and P. Negulescu. Rescue of CF airway epithelial cell function in vitro by a CFTR potentiator, VX-770. *Proceedings of the National Academy of Sciences*, 106(44):18825–18830, 2009.

[196] F. Van Goor, S. Hadida, P. D. J. Grootenhuis, B. Burton, J. H. Stack, K. S. Straley, C. J. Decker, M. Miller, J. McCartney, E. R. Olson, J. J. Wine, R. A. Frizzell, M. Ashlock, and P. A. Negulescu. Correction of the F508del-CFTR protein processing defect in vitro by the investigational drug VX-809. *Proceedings of the National Academy of Sciences*, 108(46):18843–18848, 2011.

[197] Marit Arianne van Meegen, Suzanne Willemina Julia Terheggen-Lagro, Kirsten Judith Koymans, Cornelis Korstiaan van der Ent, and Jeffrey Matthijn Beekman. Apical CFTR Expression in Human Nasal Epithelium Correlates with Lung Disease in Cystic Fibrosis. *PLoS ONE*, 2013.

[198] E. Vazquez, M. Nobles, and M. A. Valverde. Defective regulatory volume decrease in human cystic fibrosis tracheal cells because of altered regulation of intermediate conductance Ca2+-dependent potassium channels. *Proceedings of the National Academy of Sciences*, 98(9):5329–5334, 2001.

[199] A S Verkman. Role of aquaporin water channels in kidney and lung. *Am J Med Sci*, 316(5):310–320, 1998.

[200] A. S. Verkman. Role of aquaporins in lung liquid physiology. *Respiratory Physiology and Neurobiology*, 159(3):324–330, 2007.

[201] François Vermeulen, Marijke Proesmans, Mieke Boon, Trudy Havermans, and Kris De Boeck. Lung clearance index predicts pulmonary exacerbations in young patients with cystic fi brosis. pages 39–45, 2014.

[202] M. Vilkhovoy, A. Pritchard-Bell, G. Clermont, and R.S. Parker. A Control-Relevant Model of Subcutaneous Insulin Absorption. In *Proc. 19th IFAC World Congress on Automatic Control*, Cape Town, South Africa, 2014.

[203] Andreas Wachter and Lorenz T. Biegler. On the implementation of an interior-point filter line-search algorithm for large-scale nonlinear programming. *Mathematical Programming*, 57(1):25–26, 2006.

[204] Nancy M. Walker, Michael Flagella, Lara R. Gawenis, Gary E. Shull, and Lane L. Clarke. An alternate pathway of cAMP-stimulated Cl secretion across the NKCC1-null murine duodenum. *Gastroenterology*, 123(2):531–541, 2002.

[205] Xin Jing Wang, Jean Kim, Rita McWilliams, and Garry R. Cutting. Increased prevalence of chronic rhinosinusitis in carriers of a cystic fibrosis mutation. *Archives of Otolaryngology - Head and Neck Surgery*, 131(3):237–240, 2005.

[206] Xin Jing Wang, Birgitta Moylan, Donald A. Leopold, Jean Kim, Ronald C. Rubenstein, Alkis Togias, David Proud, Pamela L. Zeitlin, and Garry R. Cutting. Mutation in the gene responsible for cystic fibrosis and predisposition to chronic rhinosinusitis in the general population. *Journal of the American Medical Association*, 284(14):1814–1819, 2000.

[207] N. J. Warren, M. H. Tawhai, and E. J. Crampin. A mathematical model of calcium-induced fluid secretion in airway epithelium. *Journal of Theoretical Biology*, 259(4):837–849, 2009.

[208] Mark Thomas Shaw Williams, Francine de Courcey, David Comer, Joseph S. Elborn, and Madeleine Ennis. Bronchial epithelial cell lines and primary nasal epithelial cells from cystic fibrosis respond differently to cigarette smoke exposure. *Journal of Cystic Fibrosis*, 15(4):467–472, 2016.

[209] N J Willumsen and R C Boucher. Sodium transport and intracellular sodium activity in cultured human nasal epithelium. *American Journal Of Physiology*, 261:C319–31, 1991.

[210] N J Willumsen and R C Boucher. Transcellular sodium transport in cultures cystic fibrosis human nasal epithelium. *Am J Physiol*, 30:C332–C341, 1991.

[211] Niels J Willumsen, C William Davis, and Richard C Boucher. Intracellular Cl-activity and cellular Cl-pathways in cultured human airway epithelium.

[212] Jeffrey J. Wine, Gunnar C. Hansson, Peter König, Nam Soo Joo, Anna Ermund, and Mario Pieper. Progress in understanding mucus abnormalities in cystic fibrosis airways. *Journal of Cystic Fibrosis*, 17(2):S35–S39, 2018.

[213] Jiusheng Yan and Richard W. Aldrich. LRRC26 auxiliary protein allows BK channel activation at resting voltage without calcium. *Nature*, 466(7305):513–516, 2010.

[214] Shao-Nian Yang and Per-Olof Berggren. β-Cell Ca V channel regulation in physiology and pathophysiology . *American Journal of Physiology-Endocrinology and Metabolism*, 288(1):E16–E28, 2004.

[215] James R Yankaskas, Calvin U Cotton, Michael R Knowles, John T Gatzy, and Richard C Boucher. Culture of Human Nasal Epithelial Cells on Collagen Matrix Supports. *American Review of Respiratory Disease*, 132(6):1281–1287, 1985.

[216] Makoto Yasuda, Naomi Niisato, Hiroaki Miyazaki, Yoshinobu Iwasaki, Takemitsu Hama, Kenji Dejima, Yasuo Hisa, and Yoshinori Marunaka. Epithelial Na+ channel and ion transport in human nasal polyp and paranasal sinus mucosa. *Biochemical and Biophysical Research Communications*, 2007.

[217] Dan Yu, Christopher R. Weber, Le Shen, Jerrold R. Turner, and David R. Raleigh. Tight Junction Pore and Leak Pathways: A Dynamic Duo. *Annual Review of Physiology*, 73(1):283–309, 2011.

[218] Li Ang Zhang, Alisa Urbano, Gilles Clermont, David Swigon, Ipsita Banerjee, and Robert S. Parker. APT-MCMC, a C++/Python implementation of Markov Chain Monte Carlo for parameter identification. *Computers and Chemical Engineering*, 110:1–12, 2018.

[219] Yun Zhang, Charles A Phillips, Gary L Rogers, Erich J Baker, Elissa J Chesler, and Michael A Langston. On finding bicliques in bipartite graphs: a novel algorithm and its application to the integration of diverse biological data types. *BMC bioinformatics*, 15(1):110, jan 2014.

[220] B. Zhou, D. K. Ann, X. Li, K.-J. Kim, H. Lin, P. Minoo, E. D. Crandall, and Z. Borok. Hypertonic induction of aquaporin-5: novel role of hypoxia-inducible factor-1. *AJP: Cell Physiology*, 292(4):C1280–C1290, 2006.

[221] Peiying Zuo, Maryse Picher, Seiko F. Okada, Eduardo R. Lazarowski, Brian Button, Richard C. Boucher, and Timothy C. Elston. Mathematical model of nucleotide regulation on airway epithelia: Implications for airway homeostasis. *Journal of Biological Chemistry*, 283(39):26805–26819, 2008.